274 7-22-85 W.B. ①

DOE/ER-0046/21

I-21956 Dn. # 1143-6

Damage Analysis and Fundamental Studies

Quarterly Progress Report
January-March 1985

May 1985

U.S. Department of Energy
Office of Energy Research
Office of Fusion Energy
Washington, DC 20545
B&R No. AT-15-02-03-04

MASTER

DISTRIBUTION OF THIS DOCUMENT IS UNLIMITED

DO NOT MICROFILM
COVER

Printed in the United States of America
Available from
National Technical Information Service
U.S. Department of Commerce
5285 Port Royal Road
Springfield, VA 22161

NTIS price codes
Printed copy: A 08
Microfiche copy: A01

DOE/ER--0046/21

DE85 014864

Damage Analysis and Fundamental Studies

Quarterly Progress Report
January-March 1985

May 1985

U.S. Department of Energy
Office of Energy Research
Office of Fusion Energy
Washington, DC 20545
B&R No. AT-15-02-03-04

MASTER

2b

FOREWORD

This report is the twenty-ninth in a series of Quarterly Technical Progress Reports on *Damage Analysis and Fundamental Studies* (DAFS), which is one element of the Fusion Reactor Materials Program, conducted in support of the Magnetic Fusion Energy Program of the U.S. Department of Energy (DOE). The first eight reports in this series were numbered DOE/ET-0065/1 through 8. Other elements of the Fusion Materials Program are:

- Alloy Development for Irradiation Performance (ADIP)
- Plasma-Materials Interaction (PMI)
- Special Purpose Materials (SPM).

The DAFS program element is a national effort composed of contributions from a number of National Laboratories and other government laboratories, universities, and industrial laboratories. It was organized by the Materials and Radiation Effects Branch, DOE/Office of Fusion Energy, and a Task Group on *Damage Analysis and Fundamental Studies,* which operates under the auspices of that branch. The purpose of this series of reports is to provide a working technical record of that effort for the use of the program participants, the fusion energy program in general, and the DOE.

This report is organized along topical lines in parallel to a Program Plan of the same title so that activities and accomplishments may be followed readily, relative to that Program Plan. Thus, the work of a given laboratory may appear throughout the report. A chapter has been added on Reduced Activation Materials to accommodate work on a topic not included in the early program plan. The Contents is annotated for the convenience of the reader.

This report has been compiled and edited by N. E. Kenny under the guidance of the Chairman of the Task Group on *Damage Analysis and Fundamental Studies,* D. G. Doran, Hanford Engineering Development Laboratory (HEDL). Their efforts, those of the supporting staff of HEDL, and the many persons who made technical contributions are gratefully acknowledged. T. C. Reuther, Fusion Technologies Branch, is the DOE counterpart to the Task Group Chairman and has responsibility for the DAFS program within DOE.

G. M. Haas, Chief
Fusion Technologies Branch
Office of Fusion Energy

CONTENTS

Foreword — Page

CHAPTER 1: IRRADIATION TEST FACILITIES — 1

1. RTNS-II IRRADIATIONS AND OPERATIONS (LLNL) — 2

Irradiations were performed on 13 different experiments during this quarter. Target vacuum system modifications were completed on the right and left machines. The target chilled water system upgrade was complete.

CHAPTER 2: DOSIMETRY AND DAMAGE PARAMETERS — 4

1. FISSION REACTOR DOSIMETRY - HFIR-CTR 30, 36, 46 (ANL) — 5

Dosimetry measurements and damage calculations are reported for the CTR 30, 36, and 46 experiments in HFIR. CTR 30 has the highest exposure to date with a fluence of 1.95 x 10^{23} n/cm^2 producing 44 dpa and 2613 appm helium in a 316 stainless steel.

2. ANALYSIS OF DAMAGE EXPOSURE RATES IN THE MATERIALS OPEN TEST ASSEMBLY OF THE FAST FLUX TEST FACILITY (HEDL) — 10

The axial distribution of dpa/sec in stainless steel (Fe18Cr10Ni) and flux $E > 0$ MeV and $E > 0.1$ MeV were determined from the analysis of dosimetry measurements made during MOTA Cycles 1A and 1B.

3. ACTIVATION CROSS-SECTION MEASUREMENTS AT RTNS-II (ANL, LLNL, RI) — 15

Cross sections are reported for 22 reactions measured at RTNS-II in the angular range from 0-60° for neutron energies between 14.5-14.9 MeV. Results are compared to ENDF/B-V and other data.

4. ISOTOPIC TAILORING WITH NICKEL-59 TO ENHANCE HELIUM PRODUCTION IN FISSION REACTOR IRRADIATIONS (HEDL) — 19

Three heats of austenitic steel doped with Ni-59 have been prepared for irradiation in out-of-core locations in the Fast Flux Test Facility (FFTF).

5. ON THE USE OF ISOTOPIC AND SPECTRAL TAILORING TO SIMULATE FUSION IRRADIATION VARIABLES IN FISSION REACTORS (U. of California, Santa Barbara) — 23

It is shown that by using various isotopic ratios of ^{58}Ni/^{60}Ni, single variable experiments on the effect of helium to displacement-per-atom ratios (He/dpa) can be carried out in ferritic and austenitic alloys. Further, additions of small amounts of ^{59}Ni result in the elimination of the low fluence transient, resulting in an approximately constant He/dpa ratio in the range up to 100 dpa.

6. HELIUM PRODUCTION CROSS SECTIONS FOR 14.8-MeV NEUTRONS (RI) — 34

Total helium production cross sections were measured for eleven separate isotopes of lead and tin irradiated in the ~14.8-MeV T(d,n) neutron environment of RTNS-II.

5. EARLY DEVELOPMENT OF SPINODAL DECOMPOSITION IN NEUTRON-IRRADIATED Fe-35Ni-7.5Cr AT 550°C (HEDL) 92

In Fe-35Ni-7.5Cr irradiated at 550°C to 2.5 x 10^{22} n/cm^2 (E > 0.1 MeV), the spinodal decomposition observed at higher irradiation temperatures and higher neutron exposures is just beginning to form.

6. OWR/RTNS-II LOW EXPOSURE SPECTRAL EFFECTS EXPERIMENT (HEDL) 99

The first leg of the RTNS-II portion of this experiment was completed at a peak fluence of 2.4 x 10^{18} n/cm^2. An excellent fit to the dosimetry data has been obtained.

7. RADIATION-INDUCED PRECIPITATION IN Ti-64 (U. of Wisconsin-Madison) 102

The alloy Ti-64 was irradiated with 9-MeV Al ion to 2 dpa at 500-700°C. The density of the radiation-induced β precipitate decreased at high temperature while the size increased. The total fraction of bcc phase present is drastically altered by irradiation.

8. HEAVY ION IRRADIATION OF Ti-6242S (U. of Wisconsin-Madison) 117

After 2 dpa of 9-MeV Al ion irradiation, Ti-6242S displayed extensive precipitation of a bcc phase at all temperatures in the range 450-700°C. The morphology below 600°C was highly unusual; it consisted of the apparent agglomeration of small (~20 nm) precipitates into some form of array or cluster.

9. THE EFFECT OF DENSITY CHANGES ON THE ENERGY AND ION DEPOSITION PROFILES (U. of Wisconsin-Madison) 130

Using transport theory to calculate the distribution of deposited energy or deposited ions, it is shown that the effect of density changes on these distribution profiles can be obtained in a medium with constant density by a simple coordinate transformation, provided the distribution functions depend only on one spatial coordinate.

10. STABILITY OF VACANCY CLUSTERS IN COPPER AND OTHER METALS (U. of Wisconsin-Madison) 134

The energies of voids, stacking fault tetrahedra and vacancy loops in aluminum, copper, nickel and stainless steel have been determined as a function of size using established equations from elasticity theory. Stacking fault tetrahedra and vacancy loops are the most stable small cluster morphologies in the absence of gas. Small amounts of oxygen or helium cause the void to be the most stable.

11. A NOTE ON REACTIVE GAS CHARGING DURING PRE-IRRADIATION SPECIMEN PREPARATION (U. of Wisconsin-Madison) 148

The common misconception of hydrogen introduction during the pre-irradiation specimen electropolish has been addressed. It is shown that hydrogen cannot enter the specimen, but that the ingress of oxygen may occur during the electropolishing step. Hydrogen can, however, enter the specimen in the absence of the applied voltage if the sample, without a passive film layer, remains in the electrolyte.

CHAPTER 6: FUNDAMENTAL STUDIES OF SPECIAL PURPOSE MATERIALS 151

1. RADIATION-ENHANCED RECRYSTALLIZATION IN COPPER ALLOYS (U. of Wisconsin-Madison) 152

AMZIRC and AMAX-MZC exhibit signs of radiation-enhanced recrystallization following ion irradiation to 10 dpa at temperatures above 300°C. A simplified analysis suggests that the accelerated recrystallization kinetics is due to radiation-enhanced diffusion.

CHAPTER 1

IRRADIATION TEST FACILITIES

RTNS-II IRRADIATIONS AND OPERATIONS

C.M. Logan and D. W. Heikkinen (Lawrence Livermore National Laboratory)

1.0 Objective

The objectives of this work are operation of RTNS-II (a 14-MeV neutron source facility), machine development, and support of the experimental program that utilizes this facility. Experimenter services include dosimetry, handling, scheduling, coordination, and reporting. RTNS-II is supported jointly by the U.S. and Japan and is dedicated to materials research for the fusion power program. Its primary use is to aid in the development of models of high-energy neutron effects. Such models are needed in interpreting and projecting to the fusion environment, engineering data obtained in other spectra.

2.0 Summary

Irradiations were performed on 13 different experiments during this quarter.
Target vacuum system modifications were completed on the right and left machines.
The target chilled water system upgrade was completed.

3.0 Program

Title: RTNS-II Operations (WZJ-16)
Principal Investigator: D. W. Heikkinen
Affiliation: Lawrence Livermore National Laboratory

4.0 Relevant DAFS Program Plan Task/Subtask

TASK II.A.2,3,4.
TASK II.B.3,4
TASK II.C.1,2,6,11,18.

5.0 Irradiation - C. M. Logan, D. W. Heikkinen and M. W. Guinan

During this quarter, irradiations (both dedicated and add-on) were done for the following people.

Experimenter	P or A*	Sample Irradiated
D. Heikkinen (LLNL)	A	Nb - dosimetry calibration
P. Cannon (HEDL)	P	Thermocouples and ceramic-metal seals - neutron damage
C. Snead (BNL) and M. Guinan (LLNL)	A	Nb_3Sn-Ti alloys (mono-filaments) critical field, current and temperature
R. Flukiger (Karlsruhe) and M. Guinan (LLNL)	A	Nb_3Sn various multifilamentary alloys - critical field, current and temperature

Experimenter	P or A*	Sample Irradiated
J. S. Huang and M. Guinan (LLNL)	A	Al, Cu, Fe, Ni-Si, NiAl and Ni_3Al defect cluster formation and phase transformation
J. S. Huang and M. Guinan (LLNL)	A	BN - evaluate coating for high temperature furnace
R. Borg	A	$K_3Fe(CN)_6$ - K cross sections
M. Nakazawa (Tokyo)	P	Nb, Zr, Au, Al, Ni, Co, TLD600 & TLD700 - neutron spectra and flux distributions
Y. Tabata (Tokyo)	A	Polymer materials - tensile strength
K. Abe (Tohoku)	A	Sc and Mo - induced activity
E. Kuramoto (Kyushu) M. Kiritani (Hokkaido) H. Matsui (Tohoku) K. Abe (Tohoku) S. Ishino (Tokyo) M. Shimotomai (Tokyo) Y. Shimomura (Hiroshima) N. Yoshida (Kyushu)	P	Metals - displacement damage & mechanical properties - irradiated at 60°C and 150°C
H. Heinisch (HEDL) G. Pells (Harwell) F. Clinard (LANL) M. Kiritani (Hokkaido) R. Ohshima (Osaka) H. Yoshida (Kyoto) K. Abe (Tohoku) H. Matsui (Tohoku) H. Kayano (Tohoku) H. Kawanishi (Tokyo) N. Igata (Tokyo) Y. Shimomura (Hiroshima) N. Yoshida (Kyushu)	P	Metals - displacement damage & mechanical properties. Ceramics - neutron damage - irradiated at 90°C and 290°C
S. Iwasaki (Tohoku)	A	$^{27}Al(n,2n)$ - cross section

*P = primary, A = Add-on

5.1 RTNS-II Status - C. M. Logan and D. W. Heikkinen

The vertical turbo pumps in the target rooms are being replaced with Balzer's turbo pumps as part of the vacuum system modification.

The target chilled water system upgrade was completed.

6.0 Future Work

Irradiations will be continued for D. Heikkinen (LLNL), C. Snead (BNL)/M. Guinan (LLNL), R. Flukiger (Karlsruhe)/M. Guinan (LLNL), H. Heinisch et al. (HEDL), J. Huang/M. Guinan (LLNL), R. Borg (LLNL), S. Iwasaki (Tohoku), K. Abe (Tohoku). Also during this period, irradiations for M. Guinan/P. Hahn (LLNL), J. Huang/M. Guinan (LLNL), E. Dalder (LLNL), D. Tucker (LANL), E. Franco (Aracor), R. Jalbert (LANL), S. Iwasaki (Tohoku) and J. McDonald (HEDL) will be initiated.

CHAPTER 2

DOSIMETRY AND DAMAGE PARAMETERS

FISSION REACTOR DOSIMETRY - HFIR-CTR 30, 36, 46

L. R. Greenwood (Argonne National Laboratory)

1.0 Objective

To characterize neutron irradiation experiments in terms of neutron fluence, spectra, and damage parameters (dpa, gas generation, transmutation).

2.0 Summary

Dosimetry measurements and damage calculations have been completed for the CTR 30, 36, and 46 experiments in HFIR. CTR 30 and 36 have the highest exposures seen to date with fluences of $1.95 \times 10^{23} n/cm^2$ and $1.61 \times 10^{23} n/cm^2$, respectively. Work is in progress on the RB2 and T3 experiments in HFIR and a prototype of the Japanese experiments in ORR.

The status of all other experiments is summarized in Table I.

Table I. Status of Dosimetry Experiments

Facility/Experiment		Status/Comments
ORR	- MFE 1	Completed 12/79
	- MFE 2	Completed 06/81
	- MFE 4A1	Completed 12/81
	- MFE 4A2	Completed 11/82
	- MFE 4B	Completed 04/84
	- TBC 07	Completed 07/80
	- TRIO-Test	Completed 07/82
	- TRIO-1	Completed 12/83
	- HF Test	Completed 03/84
	- JP Test	Samples Received 03/85
	- J6, J7	Samples Sent 02/85
HFIR	- CTR 32	Completed 04/82
	- CTR 31, 34, 35	Completed 04/83
	- T2, RB1	Completed 09/83
	- T1, CTR 39	Completed 01/84
	- CTR 40-45	Completed 09/84
	- CTR 30, 36, 46	Completed 03/85
	- RB2, T3	Samples Received 11/84
	- CTR 47-56	Irradiations in Progress
	- JP 1-8	Irradiations in Progress
Omega West	- Spectral Analysis	Completed 10/80
	- HEDL1	Completed 05/81
	- HEDL2	Samples Sent 05/83
	- LANL 1	Completed 08/84
EBR II	- X287	Completed 09/81
IPNS	- Spectral Analysis	Completed 01/82
	- LANL1 (Hurley)	Completed 06/82
	- Hurley	Completed 02/83
	- Coltman	Completed 08/83

3.0 Program

Title: Dosimetry and Damage Analysis
Principal Investigator: L. R. Greenwood
Affiliation: Argonne National Laboratory

4.0 Relevant DAFS Program Plan Tasks/Subtask

Task II.A.1 Fission Reactor Dosimetry

5.0 Accomplishments and Status

Dosimetry measurements and damage calculations have been completed for the CTR 30, 36, and 46 experiments in the peripheral target position of the High Flux Isotopes Reactor (HFIR) at Oak Ridge National Laboratory.

The present experiments are designed to study PCA, ferritic alloys, long-range ordered alloys, titanium alloys, and high nickel alloys in CTR 30; fatigue specimens of austenitic stainless steels in CTR 36; and the impact properties of 12 Cr - 1 MoVW steel in CTR 46. The exposure histories are as follows:

Experiment	Dates	Exposure, MWD
30	07/80 - 11/81	43,316
36	11/82 - 04/84	38,069
46	02/83 - 06/83	10,620

Dosimetry capsules were located at six vertical positions in CTR 30 and at five positions in CTR 36 and 46. Each capsule contained Fe, Ti, Co-Al, and Mn-Cu dosimetry wires; CTR 30 also contained additional helium samples in Cu, Fe, and Nb which could also be used for dosimetry.

The measured activities are listed in Tables II-III. The values are normalized to 100 MW and have been corrected for burnups. The very long exposures on CTR 30 and 36 necessitated rather sizeable burnup corrections of nearly 60% for the ^{59}Co(n,γ)^{60}Co reaction. In fact, the ^{60}Co activity level was found to actually be declining with further exposure due to burnout of the cobalt sample. In the case of ^{54}Mn produced by the ^{54}Fe(n,p) and ^{55}Mn(n,2n) reactions, burnup corrections are also hampered by our lack of information concerning the thermal cross section of ^{54}Mn. Previous work indicated a value of about 10b for thermal capture in ^{54}Mn. With these present higher exposure data, we can now determine the proper value more accurately to be 14.6±1.5b. We were also able to determine a better thermal cross section for ^{94}Nb of about 15.6b (to ^{95g}Nb) in good agreement with the ENDF/B-V value[2] of 14.9±1.0b. A paper is now being written describing these new cross section determinations. In any case, these new values permit us to correct the activities in Table I with an estimated uncertainty of about ±2% for all reactions except ^{59}Co(n,γ) which has a larger uncertainty of about ±5%.

All of the data in Tables II-III agree quite well with previous data[1] and the vertical gradients can be described by the following equation:

$$f(z) = a\,(1 + bz + cz^2) \tag{1}$$

where a = midplane value, $b = 5.02\times10^{-4}$, $c = 1.00\times10^{-3}$, and z = height in cm. This equation has been slightly revised from previous work since it represents a global fit to all of the available data. The b term indicates only a small asymmetry and is not significant near midplane. Some of the data is shown in Fig. 1.

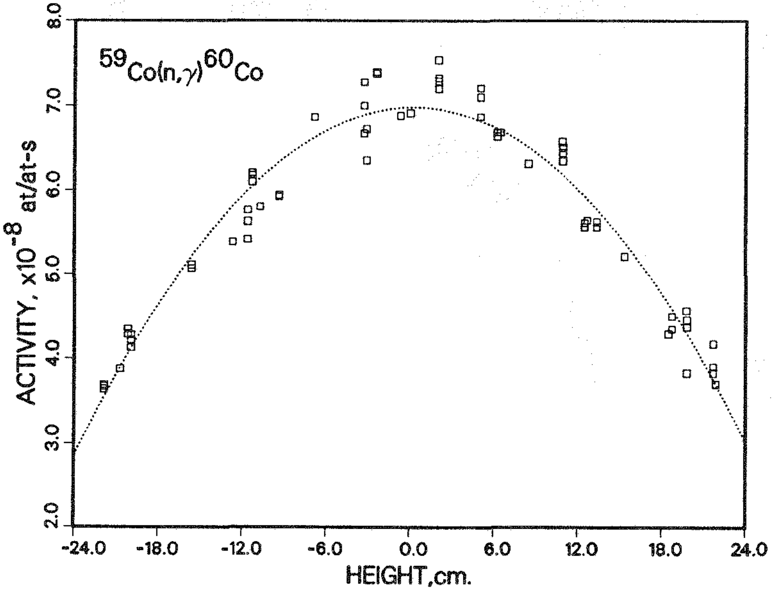

FIGURE 1. Activation Measurements of the ^{59}Co(n,γ)^{60}Co Reaction are Shown for 63 Locations in HFIR During 14 Different Materials Experiments. The Dotted Line Represents a Least Square Fit to the Data. The Scatter of 5% is Partially Due to Uncertanties in the Burnup Corrections and Partially Due to Physical Differences in the Flux Levels and Experimental Assemblies.

Table II. Measured Activities for HFIR-CTR 30

Values at 100 MW With Burnup Corrections
Accuracy ±2% Unless Noted

Height, cm[a]	Activation Rate, at/at-s					
	^{59}Co(n,γ)[b]	^{93}Nb(n,γ)	^{54}Fe(n,p)	^{46}Ti(n,p)	^{55}Mn(n,2n)	^{63}Cu(n,α)
	($\times10^{-8}$)	($\times10^{-9}$)	($\times10^{-11}$)	($\times10^{-12}$)	($\times10^{-13}$)	($\times10^{-13}$)
20.8	3.83	1.66	4.46	5.94	1.38	2.81
16.7	-	-	5.27	-	-	-
12.5	5.62	2.53	6.20	8.56	1.76	3.86
8.3	-	-	-	-	-	4.44
4.2	6.87	3.03	7.55	10.38	2.27	5.01
0.0	-	-	-	10.72	-	-
-4.2	7.00	3.07	7.40	10.54	2.16	5.04
-8.3	-	-	6.79	-	-	-
-12.5	5.41	2.36	6.89	9.04	1.83	4.63
-20.8	4.13	1.66	4.13	5.61	1.25	3.07
-25.0	-	-	-	4.41	-	-

---

[a] Height to bottom of capsule; samples may vary by 1 cm.
[b] Co values ±5% due to large burnup corrections.

Table III. Measured Activities for HFIR-CTR36,46

Values at 100 MW with Burnup Corrections
Accuracy ±2% Unless Noted

Height, cm	^{59}Co(n,γ)[a]	^{58}Fe(n,γ)[a]	^{54}Fe(n,p)	^{55}Mn(n,2n)
CTR 36:	(10^{-8})	(10^{-9})	(10^{-11})	(10^{-13})
18.5	4.29	1.22	4.55	1.40
8.5	6.31	1.68	6.49	2.10
-0.7	6.88	1.92	7.27	2.23
-10.7	5.80	1.68	6.43	1.93
-20.7	3.88	1.17	4.36	1.36

CTR 46:	^{59}Co(n,g)	^{58}Fe(n,g)b	^{54}Fe(n,p)	^{46}Ti(n,p)	^{55}Mn(n,2n)
	(10^{-8})	(10^{-9})	(10^{-11})	(10^{-12})	(10^{-13})
21.9	3.70	1.06	3.93	5.48	1.14
12.7	5.61	1.56	6.10	8.26	1.80
0.0	6.91	1.91	7.40	9.71	2.13
-12.7	5.38	1.45	6.28	8.64	1.79
-21.9	3.64	1.32	3.13	5.10	1.07

---

a ^{59}Co and ^{58}Fe(n,γ) values ±5% due to large burnup corrections for CTR 36.
b ^{58}Fe(n,γ) values ±5% on CTR 46.

Neutron fluence and damage parameters are listed in Table IV. These gradients are also described by equation (1) except for helium production in nickel which listed separately in Table IV. The methods used to determine the helium and dpa from nickel are well described in recent papers.[3,4]

In the case of CTR 30, selected samples have been sent to Rockwell International for helium analysis.

Table IV. Neutron Fluence and Damage Parameters - HFIR-CTR 30, 36, 46

Values at midplane; gradients use equation (1)

Energy	Neutron Fluence, x 10^{22} n/cm^2		
	CTR 30	CTR 36	CTR 46
Total	19.5	16.1	4.44
Thermal (<.5 eV)[a]	7.89	6.51	1.79
Fast (>.11 MeV)	5.23	4.31	1.20

Element	CTR 30		CTR 36		CTR 46	
	DPA	He, appm	DPA	He, appm	DPA	He, appm
Al	68.8	31.8	56.7	27.9	15.8	7.62
Ti	43.7	22.1	36.1	18.6	10.1	5.22
V	48.9	1.08	40.3	0.94	11.3	0.26
Cr	43.2	7.39	35.6	6.41	10.0	1.76
Mn[b]	47.4	6.44	39.1	5.65	10.9	1.54
Fe	38.2	13.0	31.5	11.38	8.84	3.12
Co[b]	47.7	6.38	39.4	5.60	11.0	1.53
Fast [c]	41.0	176.	33.9	151.	9.46	42.
Ni ^{59}Ni	35.0	19,848.	28.5	16,178.	5.02	2845.
Total	76.0	20,024.	62.4	16,329.	14.48	2887.
Cu	37.2	11.6	30.7	10.1	8.59	2.77
Nb	36.9	2.38	30.5	2.08	8.51	0.57
Mo	27.4	-	22.6	-	6.32	-
316SS[d]	44.0	2613.	36.2	2131.	9.75	378.

---

[a] Multiply X0.866 for 2200 m/s value; temperature effect not included.
[b] Thermal self-shielding important for Mn and Co.
[c] See Table IV for Ni gradients.
[d] 316SS: Fe(.645), Ni(.13), Cr(.18), Mn(.019), Mo(.026).

The damage parameters listed in Tables IV and V show rather large helium effects for the thermal nickel reactions. For CTR 30, the helium production has reached 2 atom percent and the extra displacements from the ^{59}Fe recoils (He/567) produce 35 dpa, nearly equal to the fast displacements.

Table V. Helium and Displacement Damage for 316SS*

Helium Includes ^{59}Ni and Fast Reactions
DPA Includes Extra Thermal Kick (He/567)

	CTR 30		CTR 36		CTR 46	
Height, cm	He, appm	DPA	He, appm	DPA	He, appm	DPA
0	2613	44.0	2131	36.2	378	9.75
3	2588	43.5	2109	35.9	372	9.66
6	2515	42.4	2046	34.9	356	9.38
9	2391	40.4	1939	33.3	330	8.93
12	2214	37.6	1786	30.9	295	8.30
15	1983	34.0	1590	28.0	250	7.48
18	1693	29.6	1344	24.2	199	6.48
21	1343	24.3	1052	19.9	144	5.32
24	935	18.2	718	14.9	88	3.99

*316SS: Fe(.645), Ni(.13), Cr(.18), Mn(.019), Mo(.026).

6.0 References

1. L. R. Greenwood, Damage Analysis and Fundamental Studies Quarterly Progress Report, DOE/ER-0046/13, pp. 17-26, May 1983; DOE/ER-0046/14, pp. 9-18, August 1983.

2. S. F. Mughabgbab, M. Divadeenam, and N. E. Holden, Neutron Cross Sections, Vol. I, Academic Press, New York, 1981.

3. L. R. Greenwood, A. New Calculation of Thermal Neutron Damage and Helium Production in Nickel, J. Nucl. Mater. 115, 137-142 (1983).

4. L. R. Greenwood, D. W. Kneff, R. P. Skowronski, and F. M. Mann, A Comparison of Measured and Calculated Helium Production in Nickel Using Newly Evaluated Neutron Cross Sections for ^{59}Ni, J. Nucl. Mater. 122, 1002-1010 (1984).

5. D. W. Kneff, B. M. Oliver, R. P. Skowronski, and L. R. Greenwood, Damage Analysis and Fundamental Studies Quarterly Progress Report, DOE/ER-0046/20, pp. 13-16, February 1985.

7.0 Future Work

Recent dosimetry measurements and helium measurements for copper also indicate that a thermal helium effect is present.[5] This effect is now being studied and is not included in Table IV. Since the effect in copper requires three successive thermal captures, the effect is much smaller than seen for nickel. For CTR 30, we predict that the effect may produce about 75 appm helium and 0.2 dpa in addition to the 12 appm helium and 37.2 dpa produced by fast neutrons. A joint paper with Rockwell International is now being written describing this effect.

8.0 Publications

L. R. Greenwood, A. New Calculation of Thermal Neutron Damage and Helium Production in Nickel, J. Nucl. Mater. 115, 137-142 (1983).

L. R. Greenwood, D. W. Kneff, R. P. Skowronski, and F. M. Mann, A Comparison of Measured and Calculated Helium Production in Nickel Using Newly Evaluated Neutron Cross Sections for ^{59}Ni, J. Nucl. Mater. 122, 1002-1010 (1984).

ANALYSIS OF DAMAGE EXPOSURE RATES IN THE MATERIALS OPEN TEST ASSEMBLY OF THE FAST FLUX TEST FACILITY

R. L. Simons (Hanford Engineering Development Laboratory)

1.0 Objective

The objective of this effort is to calculate the irradiation damage parameters for the Materials Open Test Assembly (MOTA) in the Fast Flux Test Facility (FFTF).

2.0 Summary

The axial distribution of dpa/sec in stainless steel (Fe18Cr10Ni) and flux $E > 0$ MeV and $E > 0.1$ MeV were determined from the analysis of dosimetry measurements made during MOTA Cycles 1A and 1B.

3.0 Program

Title: Irradiation Effects Analysis (AKJ)
Principal Investigator: D. G. Doran
Affiliation: Hanford Engineering Development Laboratory

4.0 Relevant DAFS Program Plan Task/Subtask

Subtask II.A.1 Fission Reactor Dosimetry

5.0 Accomplishments and Status

5.1 Introduction

The FFTF MOTA is an excellent facility for materials irradiation experiments for a number of reasons including: 1) high displacement rate and subsequent dpa, 2) large test volumes, 3) controlled and measured irradiation temperatures, and 4) quick recharging of metallurgical specimens between reactor cycles.

Dosimetry monitors irradiated in MOTA cycles 1A and 1B were analyzed and axial distribution of dpa/sec and flux >0 MeV and >0.1 MeV were determined for MOTA.

5.2 Analysis and Results

The dosimetry in MOTA-1A consisted of seven spectral sets and nine gradient sets which were distributed axially and radially to obtain neutron spectra and flux gradient information. MOTA-1B dosimetry consisted of three spectral sets (two in the below core canister) and five gradient sets distributed axially. For the most part, the dosimetry in MOTA-1A was used to characterize the neutron environment in MOTA, and the dosimetry in MOTA-1B was used to normalize the characterized environment. The normalization is justifiable because the neutron environment is expected to change little between reactor operating cycles.

The FFTF power time history (obtained from operations reports) was used as input to the TIMWH code(1) to determine saturation factors and the total effective full power exposure time. The reaction rates [disintegrations per second per nucleus, (dps/n)] at full power operation (400 MW) are tabulated for MOTA-1A and -1B in Tables 1 and 2, respectively. The uncertainty in the reaction rates was about 3%, but they ranged from one to seven percent on standard deviation. The irradiation time for 1A was 1.750×10^7 seconds and for 1B was 9.466×10^6 seconds.

The measured reaction rates are used to adjust the a priori neutron spectrum using the generalized least-squares code FERRET.(2) The a priori neutron spectra for MOTA are from a three-dimensional, 53-energy group-diffusion theory calculation of the FFTF for the pre-startup fuel loading condition.(3) The MOTA fluxes used in this analysis are from the subassembly 3404. Subassembly 3404 is a shim subassembly (filled with stainless steel pins) in a location with surrounding fuel and control rods that were nominally the same as those around MOTA. The diffusion theory calculations used six mesh points in each hexagonal subassembly. The fluxes used in this calculation were the average values of the six mesh points for each axial location. The calculation showed no significant radial gradient across the subassembly. The reaction cross sections and fission yields are based on ENDF/B-V nuclear data.

The fluxes (E >0.0 MeV and E >0.1 MeV) and dpa/sec in stainless steel (Fe18Cr10Ni) for MOTA-1A and -1B are shown in Figures 1 thru 3 and are tabulated in Table 3. The symbols are the adjusted values. The curve is an interpolation using the calculated values as a guide. Differences between measured and calculated exposure rates were <25% in core and above core. However, in the below core canister, the measured and calculated differed by up to 80%. The accuracy of the adjusted exposures is 5-10% ($\pm 1\sigma$) in the core (levels 1 thru 5) and 10-15% ($\pm 1\sigma$) outside the core (bcc and levels 6 and 8). The analysis of the gradient sets shows that the flux drops <5% across the MOTA subassembly at all levels except in level 6. In level 6 the gradient wires show approximately 10% higher flux on the core center side of MOTA then the core edge side. This may be affected by the mass loading in level 6 or a nearby control rod.

Differences between MOTA-1A and -1B due to cycle-to-cycle fuel loading, and control rod positioning is expected to be less than 5%. The MOTA-1B results generally fall within the one standard deviation uncertainties.

6.0 References

1. R. D. Bourquin, TIMH - A Computer Program for the Determination of Fluence with a TIMH Varying Flux, BNWL-1492, Battelle Northwest Laboratories, August 1970. TIMWH is a modified version of the TIMH program.

2. F. A. Schmittroth, FERRET Data Analysis Code, HEDL-TME 79-40, Hanford Engineering Development Laboratory, Richland, WA, Sept 1979.

3. D. W. Wooten, J. A. Rawlins, K. D. Dobbins, "Reaction Rates and Neutron Spectra in the FFTF at Full Power," Amer. Nucl. Soc., Vol. 16, 1984.

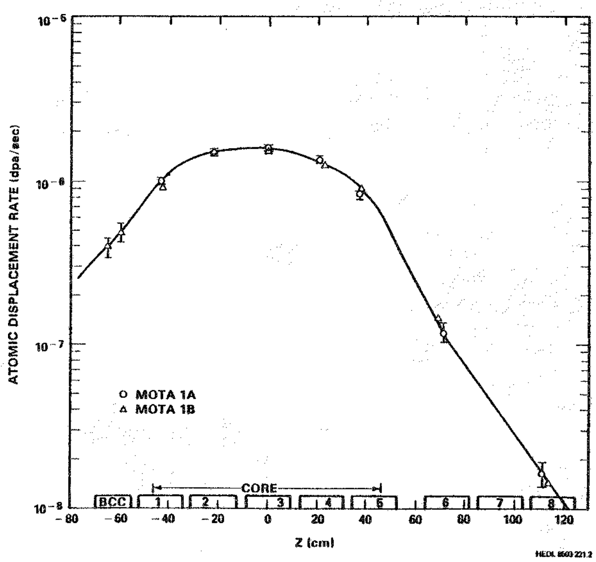

FIGURE 1. Displacement Rate for Stainless Steel (Fe18Cr10Ni) in FFTF MOTA.

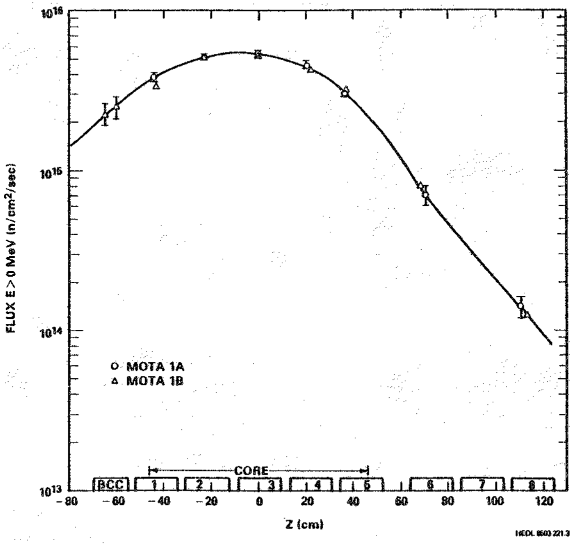

FIGURE 2. Flux E > 0 MeV in FFTF MOTA.

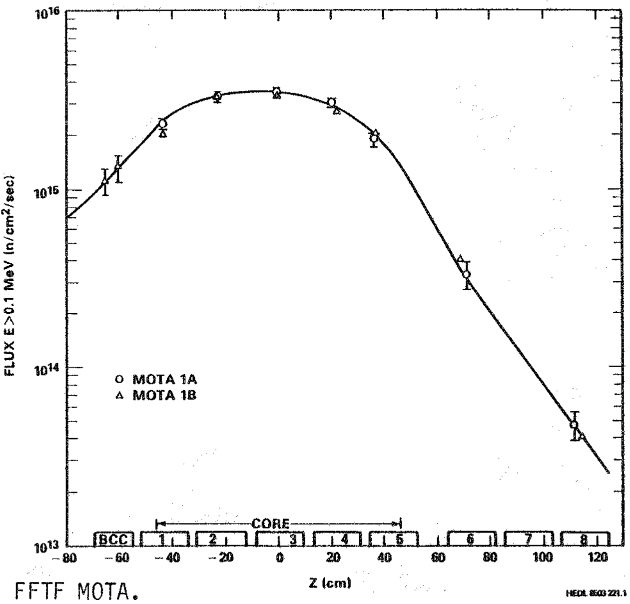

FIGURE 3. Flux E > 0.1 MeV in FFTF MOTA.

TABLE 1

REACTION RATES FROM MOTA-1A THAT WERE USED TO ADJUST THE SPECTRA AT VARIOUS AXIAL LOCATIONS

Reaction \ Axial location (cm)	Reaction Rates (dps/n) at Dosimeter locations in MOTA-1A						
	-44.27	-22.75	-0.03	+20.27	+36.78	+71.07	+111.46
^{59}Co(N,γ)^{60}Co	9.489-10	4.522-10	4.248-10	3.668-10	5.694-10	1.021+09	3.306-10
^{58}Fe(n,γ)^{59}Fe	5.152-11	5.378-11	5.861-11	4.771-11	3.503-11	1.857-11	5.128-12
^{54}Fe(n,p)^{54}Mn	2.420-11	4.205-11	4.535-11	3.802-11	2.141-11	6.885-13	3.181-14
^{63}Cu(n,γ)^{60}Co	1.386-13	2.425-13	2.579-13	2.172-13	1.227-13	3.583-15	2.386-16
^{58}Ni(n,p)^{58}Co	3.629-11	6.034-11	6.487-11	5.528-11	3.084-11	1.038-12	5.052-14
^{45}Sc(n,γ)^{46}Ti	1.757-10	2.031-10	2.152-10	1.787-10	1.237-20	6.195-11	2.015-11
^{46}Ti(n,p)^{46}Sc	3.050-12	5.385-12	5.859-12	4.883-12	2.781-12	7.963-14	2.426-15
^{237}Np(n,f)	1.433-09	2.289-09	2.613-09	2.038-09	1.166-09	1.369-10	1.393-11
^{239}Pu(n,f)	8.056-09	9.371-09	9.808-09	8.496-09	5.965-09	3.108-09	9.156-10
^{235}U (n,f)	8.354-09	9.567-09	1.004-08	8.581-09	6.208-09	3.273-09	9.784-10

TABLE 2

REACTION RATES FROM MOTA-1B THAT WERE USED TO ADJUST THE NEUTRON SPECTRA AT VARIOUS AXIAL LOCATIONS

Reaction \ Axial location (cm)	Reaction Rates (dps) at Dosimeter location in MOTA-1B								
	-65.34	-60.10	-43.17	-21.69	-2.38	21.37	+37.37	+68.99	+114.46
^{59}Co(n,γ)^{60}Co	3.099-09	3.317-09	1.160-09	4.382-10	3.904-10	3.484-10	4.420-10	1.198-09	3.324-10
^{58}Fe(n,γ)^{59}Fe	5.234-11	5.578-11	4.789-11	5.265-11	5.196-11	4.623-11	3.626-11	2.012-11	4.626-12
^{54}Fe(n,p)^{54}Mn	2.458-12	4.702-12	2.407-11	4.409-11	4.586-11	3.961-11	2.409-11	9.987-13	2.868-14
^{63}Cu(n,γ)^{60}Co	2.471-14	3.557-14							
^{58}Ni(n,p)^{58}Co	3.519-12	6.656-12							
^{46}Ti(n,p)^{46}Sc	2.814-13	5.630-13							
^{237}Np(n,f)	4.646-10	6.305-10							
^{239}Pu(n,f)	9.790-09	1.084-08							
^{235}U(n,f)	1.038-08	1.073-08							

TABLE 3

DPA/S AND FLUX E > 0 AND > 0.1 MeV IN FFTF MOTA-1A AND -1B

Z (cm)	Flux E > 0 MeV (n/cm^2-s)	Flux E > 0.1 MeV (n/cm^2-s)	dpa/s
-77.53	1.51×10^{15}	7.57×10^{14}	2.55×10^{-7}
-72.01	1.85×10^{15}	9.26×10^{14}	3.22×10^{-7}
-65.76	2.19×10^{15}	1.10×10^{15}	3.95×10^{-7}
-60.20	2.57×10^{15}	1.33×10^{15}	4.93×10^{-7}
-55.34	2.96×10^{15}	1.59×10^{15}	6.16×10^{-7}
-50.47	3.34×10^{15}	1.98×10^{15}	7.73×10^{-7}
-47.01	3.61×10^{15}	2.15×10^{15}	9.15×10^{-7}
-43.57	3.88×10^{15}	2.40×10^{15}	1.06×10^{-6}
-38.74	4.26×10^{15}	2.69×10^{15}	1.21×10^{-6}
-33.90	4.61×10^{15}	2.92×10^{15}	1.33×10^{-6}
-29.04	4.98×10^{15}	3.10×10^{15}	1.43×10^{-6}
-24.15	5.11×10^{15}	3.25×10^{15}	1.50×10^{-6}
-19.34	5.26×10^{15}	3.36×10^{15}	1.55×10^{-6}
-14.62	5.44×10^{15}	3.44×10^{15}	1.59×10^{-6}
-9.92	5.50×10^{15}	3.49×10^{15}	1.62×10^{-6}
-5.03	5.50×10^{15}	3.51×10^{15}	1.63×10^{-6}
0.00	5.39×10^{15}	3.48×10^{15}	1.61×10^{-6}
4.95	5.26×10^{15}	3.39×10^{15}	1.57×10^{-6}
9.80	5.02×10^{15}	3.27×10^{15}	1.52×10^{-6}
14.66	4.82×10^{15}	3.13×10^{15}	1.45×10^{-6}
19.51	4.50×10^{15}	2.97×10^{15}	1.35×10^{-6}
24.36	4.18×10^{15}	2.72×10^{15}	1.25×10^{-6}
29.32	3.79×10^{15}	2.47×10^{15}	1.14×10^{-6}
34.10	3.36×10^{15}	2.21×10^{15}	1.02×10^{-6}
38.98	2.91×10^{15}	1.91×10^{15}	8.75×10^{-7}
43.85	2.46×10^{15}	1.58×10^{15}	7.08×10^{-7}
47.32	2.16×10^{15}	1.33×10^{15}	5.80×10^{-7}
50.77	1.87×10^{15}	1.09×10^{15}	4.57×10^{-7}
55.63	1.50×10^{15}	8.17×10^{14}	3.27×10^{-7}
60.50	1.17×10^{15}	6.03×10^{14}	2.33×10^{-7}
67.41	8.06×10^{14}	3.95×10^{14}	1.47×10^{-7}
76.87	5.45×10^{14}	2.48×10^{14}	8.98×10^{-8}
88.33	3.42×10^{14}	1.41×10^{14}	5.01×10^{-8}
100.27	2.18×10^{14}	8.08×10^{13}	2.85×10^{-8}
111.22	1.43×10^{14}	4.77×10^{13}	1.69×10^{-8}
122.16	9.32×10^{13}	2.79×10^{13}	9.96×10^{-9}

Activation Cross-Section Measurements at RTNS-II

L. R. Greenwood (Argonne National Laboratory), M. W. Guinan (Lawrence Livermore National Laboratory), and D. W. Kneff (Rockwell International)

1.0 Objective

To measure activation cross sections for the characterization of experiments at 14 MeV neutron facilities and fusion reactors.

2.0 Summary

Cross section measurements have been completed for 22 activation reactions at RTNS-II in the angular range from 0-60° for neutron energies from 14.5-14.9 MeV. The results are compared with ENDF/B-V and other previous data. Samples of Mo, ^{94}Mo, Cu, and Fe have also been irradiated in order to look for very long-lived activation products.

3.0 Program

Title: Dosimetry and Damage Analysis
Principal Investigator: L. R. Greenwood
Affiliation: Argonne National Laboratory

4.0 Relevant DAFS Program Plan Task/Subtask

Task II.A.2 High-Energy Neutron Dosimetry
Task II.A.7 Magnetic Fusion Reactor Dosimetry

5.0 Accomplishments and Status

Activation cross sections have been measured for 22 separate reactions at the RTNS-II. The irradiations were performed in collaboration with Rockwell International and Lawrence Livermore National Laboratory during June-July 1980 as part of an effort to characterize the facility. Whereas some of this characterization work has been published previously[1,2], the angular-dependent cross sections have not been fully published and detailed helium measurements have ~~re~~cently been submitted for publication.[3]

The dosimetry foils were mounted on three thin arcs of stainless steel at 5, 15, and 30 cm from the RTNS-II target. Details of the assembly have been published previously.[7] The samples were irradiated for 123 hours with a net neutron production of 3.27×10^{17}. At the 30 cm arc, this produced a maximum neutron fluence of about 3.7×10^{14} n/cm^2. The samples were gamma counted both at Lawrence Livermore National Laboratory and at Argonne.

In order to determine cross sections, values were determined by comparison to the ^{93}Nb(n,2n)^{92m}Nb reaction with a reported value of 463 mb.[4] This reaction was chosen for two reasons. The cross section is believed to be the best known (±7%) near 14 MeV and the energy dependence is quite flat near 14.8 MeV. The latter point is very important since each sample subtended a finite solid angle over which the neutron flux and energy was slowly varying.

Corrections for absorption and finite solid angle were made in several ways. Selected foils were repeated in the thin foil stacks to measure absorption effects. Calculations were performed to average the reaction rates over a given solid angle. Checks were also made on our procedure by measuring most reactions at the three different locations from the target. Finally, a good check on the normalization procedure is provided by examining the response of reactions such as ^{197}Au(n,2n) which is quite independent of either distance or angle, as expected.

Room-return neutrons were also measured by placing dosimetry foils at 120 and 380 cm from the target at 0° to the beam. The results of these measurements indicated that the room-return neutron flux is quite isotropic throughout the target vault,[5] in good agreement with neutronics calculations. At 30 cm, the total room-return flux was found to be about 3.1% of the total. At 5 and 15 cm the effect is <1% and could not be observed in the measured activation rates.

The measured cross sections are listed in Table VI. The values are compared to ENDF/B-V[6] and other selected references in the table. In order to make this comparison meaningful, it was necessary to average the energy-dependent cross sections over the true neutron energy spectrum. The neutron energy spectra were calculated using the known properties of the TiT_2 targets, energy of the incident deuterons at 360 keV, stopping power of deuterons in TiT_2, and the measured cross sections and angular distributions of the D-T nuclear reaction.[7] The resultant spectra are shown in Fig. 1. These results are also in excellent agreement with previous calculations.[8] The average neutron energies at each angle are also listed in Table VI. The energy spread at each angle can be seen in Fig. 2 and declines from about 600 keV at 0° to about 300 keV at 30°.

As can be seen in Table I, several of the reactions have notable differences with previous data. Some of the largest differences are for $Ti(n,x)^{47}Sc$ (30%), $^{59}Co(n,p)^{59}Fe$ (26%), $^{60}Ni(n,p)^{60}Co$ (21%), $^{58}Ni(n,p)^{58}Co$ (13%), $^{58}Ni(n,2n)^{57}Ni$ (14%), and $Ti(n,x)^{46}Sc$ (10%). All of the other reactions agree with other data within 10%. One especially interesting pair of reactions are the $^{58}Ni(n,p)$ and (n,2n) cross sections. Since the (n,p) cross section is declining with increasing neutron energy while the (n,2n) cross section is rapidly increasing, the ratio has often been proposed as a monitor of the neutron energy near 14 MeV. We note that the ratio of the ENDF/B-V values is in error by 27% leading to an error of more than 0.5 MeV in the average neutron energy deduced from the ratio.

6.0 References

1. L. R. Greenwood, Neutron Source Characterization and Radiation Damage Calculations for Materials Studies, J. Nucl. Mater. 108, 21-27 (1982).

2. D. W. Kneff, B. M. Oliver, M. M. Nakata, and H. Farrar IV, Damage Analysis and Fundamental Studies Quarterly Progress Report, DOE/ER-0046/3, p. 25, October 1980.

3. D. W. Kneff, B. M. Oliver, H. Farrar IV, L. R. Greenwood, and F. M. Mann, Helium Production Cross Sections I: ^{4}He Production in Pure Elements, Isotopes, and Alloy Steels by 14.8 MeV Neutrons, submitted for publication in Nuclear Science and Engineering.

4. D. R. Nethaway, The $^{93}Nb(n,2n)^{92m}Nb$ Cross Section, J. Inorg. Nucl. Chem. 40, 1285 (1978).

5. L. R. Greenwood, Neutron Flux and Spectral Measurements to Characterize Irradiation Facilities for Fusion Materials Studies, Proc. Fourth ASTM-Euratom Symp. on Reactor Dosimetry, NUREG/CP-0029, pp. 783-792, March 1982.

6. Evaluated Neutron Data File, Version V, National Neutron Cross Section Center, Brookhaven National Laboratory (1979).

7. H. Liskien and A. Paulsen, Nuclear Data Tables 11, 569 (1979).

8. J. D. Seagrave, $D(d,n)^{3}He$ and $T(d,n)^{4}He$ Neutron Source Handbook, LAMS-2162, Los Alamos Scientific Laboratory (1958).

9. D. L. Garber and R. R. Kinsey, Neutron Cross Sections, Vol. II, BNL-325, January 1976.

10. B. P. Bayhurst, J. S. Gilmore, R. J. Prestwood, J. B. Wilhelmy, N. Jarmie, B. H. Erkkila, and R. A. Hardekopf, Phys. Rev. C12, 451 (1975).

11. R. K. Smither and L. R. Greenwood, J. Nucl. Mater. 122, 1071-1077 (1984).

12. R. K. Smither and L. R. Greenwood, Damage Analysis and Fundamental Studies Quarterly Progress Report, DOE/ER-0046/17, pp. 11-13, May 1984.

7.0 Future Work

New measurements of very long-lived isotope production cross reactions have been initiated at RTNS II. We have previously reported the production cross sections of $^{27}Al(n,2n)^{26}Al$ ($7.3x10^{5}y$)[11] and $^{54}Fe(n,2n)^{53}Fe(\beta)^{53}Mn$ ($3.8x10^{6}y$).[12] New experiments have irradiated samples of Fe, Cu, Mo, and ^{94}Mo as add-on experiments at RTNS II in collaboration with Hanford Engineering Development Laboratory. These samples have now been gamma counted along with Fe dosimetry foils. We plan to analyze these samples for various long-lived isotopes by gamma counting, liquid scintillation counting, and accelerator mass spectrometry. Such data are badly needed to accurately assess the production of long-lived isotopes at fusion reactors.

We are also collaborating with M. Nakazawa (U. Tokyo) to provide dosimetry support for Japanese experiments at RTNS II.

8.0 Publications

L. R. Greenwood, Neutron Source Characterization and Radiation Damage Calculations for Materials Studies, J. Nucl. Mater. 108, 21-27 (1982).

R. K. Smither and L. R. Greenwood, J. Nucl. Mater. 122, 1071-1077 (1984).

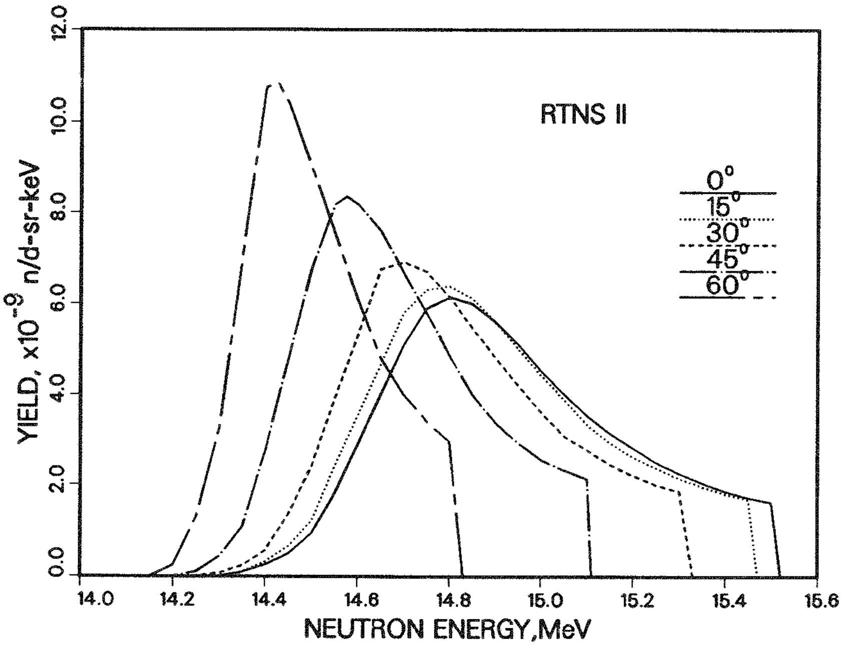

FIGURE 1. Calculated Neutron Energy Spectra are Shown for Various Angles at RTNS II.

Table I. Cross Sections Measured at RTNS-II

Values Normalized to ^{93}Nb(n,2n) = 463 mb
Geometry, Absorption Corrections Included
Accuracy +/-2% Unless Noted
ENDF/B-V Values are Spectral-Averaged at
Each Angle

Reaction	Cross Section, mb					
	0°	15°	30°	45°	60°	
<En>, MeV	14.90	14.85	14.80	14.65	14.50	
^{27}Al(n,α)^{24}Na	108.	107.	111.	113.	117.	
ENDF	113.	114.	115.	117.	119.	
^{45}Sc(n,2n)^{44}Sc	128.	-	-	-	117.	
ENDF	124.	-	-	-	112.	
^{45}Sc(n,α)^{42}K	54.	-	-	-	58.	(10%)
Ti(n,x)^{46}Sc	297.	301.	299.	298.	300.	
ENDF	324.	323.	322.	319.	315.	

Table I. (continued)

Reaction	Cross Section, mb					
	0°	15°	30°	45°	60°	
<En>, MeV	14.90	14.85	14.80	14.65	14.50	
Ti(n,x)^{46}Sc	297.	301.	299.	298.	300.	
ENDF	324.	323.	322.	319.	315.	
Ti(n,x)^{47}Sc	317.	317.	302.	287.	262.	
ENDF	246.	242.	237.	226.	214.	
^{48}Ti(n,x)^{48}Sc	66.3	67.5	67.6	69.4	66.0	
ENDF	61.9	62.1	62.2	62.6	63.0	
^{55}Mn(n,2n)^{54}Mn	840.	827.	807.	825.	791.	
ENDF	786.	784.	779.	770.	759.	
^{54}Fe(n,p)^{54}Mn	296.	298.	303.	311.	331.	
ENDF	289.	292.	298.	309.	324.	
^{54}Fe(n,α)^{51}Cr	92.7	93.3	92.6	92.5	91.2	
BNL-325	95.8	95.7	95.3	94.8	94.1	
^{59}Co(n,p)^{59}Fe	45.9	45.9	46.1	47.5	48.9	
BNL-325	62.2	62.5	62.8	63.3	63.8	
^{59}Co(n,2n)^{58}Co	803.	796.	800.	789.	771.	
ENDF	819.	818.	814.	806.	794.	
^{58}Ni(n,p)^{58}Co	295.	295.	303.	312.	329.	
ENDF	335.	339.	346.	360.	378.	
^{58}Ni(n,2n)^{57}Ni	40.9	41.2	40.0	38.2	33.1	
ENDF	36.7	36.2	35.4	33.7	31.5	
^{60}Ni(n,p)^{60}Co	132.	132.	135.	138.	142.	
ENDF	108.	109.	110.	113.	116.	
^{63}Cu(n,α)^{60}Co	40.1	38.8	38.4	40.4	41.2	(3%)
ENDF	38.4	38.7	39.1	40.0	40.9	
^{89}Y(n,2n)^{88}Y	991.	-	-	-	929.	
LASL	942.	-	-	-	887.	
^{89}Y(n,α)^{86}Rb	5.8	-	-	-	5.5	(13%)
Zr(n,X)^{89}Zr	846.	850.	824.	796.	737.	
LASL	799.	791.	776.	745.	703.	
^{96}Zr(n,2n)^{95}Zr	1593.	1599.	1581.	1580.	1608.	
^{107}Ag(n,2n)^{106}Ag	567.	-	551.	-	547.	
LASL	612.	-	605.	-	581.	
^{169}Tm(n,2n)^{168}Tm	1946.	-	-	-	1939.	
LASL	2034.	-	-	-	2022.	
^{197}Au(n,2n)^{196}Au	2174.	2172.	2171.	2154.	2151.	
ENDF	2109.	2113.	2118.	2130.	2142.	

References: ENDF - Ref. 6
BNL-325 - Ref. 9
LASL - Ref. 10

ISOTOPIC TAILORING WITH NICKEL-59 TO ENHANCE HELIUM PRODUCTION IN FISSION REACTOR IRRADIATIONS

R. L. Simons (Hanford Engineering Development Laboratory)

1.0 Objective

The objective of this effort is to isotopically tailor materials with nickel 59 so that in fission reactor experiments the ratio of helium to atomic displacements per atom is similar to that expected in magnetic fusion energy devices.

2.0 Summary

A fragment of a fracture toughness specimen of Inconel 600 was obtained after irradiation in the Engineering Test Reactor (ETR). The specimen was estimated to contain ~2.2% nickel 59/gram nickel. The nickel was successfully isolated and three heats of austenitic steel doped with Ni-59 have been prepared for irradiation in the Fast Flux Test Facility (FFTF).

3.0 Program

Title: Irradiation Effects Analysis (AKJ)
Principal Investigator: D. G. Doran
Affiliation: Hanford Engineering Development Laboratory

4.0 Relevant DAFS Plan Task/Subtask

Subtask II.C.2 Effects of Helium on Microstructure
II.C.7 Effects of Helium and Displacements on Flow

5.0 Accomplishments and Status

5.1 Introduction

Helium is known to affect the nucleation and growth of voids in metals. The voids cause dimensional changes and can produce significant hardening of the metal. Fission reactors generally produce helium at a substantially lower rate than expected in a fusion device. The exception is nickel-bearing alloys irradiated in a thermal reactor such as the High Flux Isotope Reactor (HFIR) or out-of-core in a fast reactor such as FFTF, where the nonlinear build-up of the isotope nickel 59 can lead to high levels of helium production in the metal. Initially, however, the helium production rate is at least a factor of ten lower than expected in a fusion device. It is during this transient period that nucleation of voids is taking place. The transient can be circumvented by adding an initial concentration of nickel 59 to the alloy.

This report documents the work done to secure a usable source of nickel enriched in nickel 59 and the preparation of the initial experiment for irradiation in out-of-core locations in FFTF.

5.2 Nickel Source (R. L. Simons, W. Y. Matsumoto, and F. A. Scott)

A fracture toughness specimen (ME-7) of Inconel 600 was located at the Bettis Atomic Power Laboratory. It had been sectioned from the ETR M-7 in-pile tube. The in-pile tube was irradiated from July 1967 to April 1973. It received a peak fluence (E > 1 MeV) of 1.8 x 10^{22} n/cm^2 (~25 dpa). The Inconel 600 composition is listed in Table 1. After irradiation the ME-7 specimen, which was located at the peak fluence location, contained 1.7% nickel-59/atom of Inconel or 2.2% nickel-59/atom of nickel. This is 85% of the maximum equilibrium concentration. At higher fluences the nickel 59 burns out yielding a lower concentration.

TABLE 1

CHEMICAL COMPOSITION OF ALLOY 600 IN-PILE TUBE ETR M-7

Element	Alloy W/O
Nickel	78.01
Chromium	14.81
Iron	6.63
Manganese	0.28
Carbon	0.07
Copper	0.02
Silicon	0.15
Cobalt	0.05
Sulfur	0.008
Phosphorus	0.021
Aluminum	0.11
Titanium	0.22
Magnesium	0.03
Boron	0.005

On receipt of the ME-7 specimen the dose rate at one meter was ~8 R/hr. Calculations indicated that this was nearly all due to cobalt 60. In order to work with this material out of the hot cell it was necessary to chemically remove the cobalt 60. The Inconel 600 was first dissolved in a solution of concentrated 50% HCL 50% HNO_3. The HNO_3 was removed after dissolution by alternately evaporating and bringing to solution with HCL. A three liter solution of nine molar HCL was then passed through a 350 milliliter column of DOWEX-1, X8 anion resin (100-200 mesh). Two passes through the anion exchange column were sufficient to remove nearly all of the cobalt (and iron). The dose from the remaining solution was ~50 mR/hr at contact (of the polyethylene container). The dose was primarily from Cobalt 60 and Manganese 54. The nickel solution was further purified by using a hydroxide precipitation separation method. The precipitate was washed and the procedure repeated several times. The nickel solution was finally converted to a strong ammoniacal nickel solution. This solution was electroplated onto one-inch square by 3 mil thick high purity iron cathodes. The solution was kept saturated with ammonia during electroplating by maintaining a cover of ammonia gas over the solution. The voltage was maintained so that the electrode was concentration polarized. The net nickel recovered was ~53 grams with a purity >99%. About 20 grams of nickel were lost during the chemical processing. The preparation of the nickel 59 enriched metal cost ~$500 gram. However, it is expected that future preparation would cost much less because of the experience gained to date.

A sample of nickel was examined in an Ion Microprobe Mass Analyzer to determine the isotopic composition of the nickel present. The mass ratios are summarized in Table 2. The mass 59 fraction was found to be 0.025 ± 0.003. This is considered an upper limit since an interfering mass was found at mass 59. Additional mass spectograph measurements of ultrapure nickel are presently being made to resolve the mass 59 interference problem. In addition, it is noted that the nickel 58 mass is 2.23% less than the natural abundance. The calculations indicate 2.2% nickel 59 should be present. All values are within 10% of one another.

TABLE 2

ISOTOPIC MASS ANALYSIS WITH ION MICROPROBE

Nickel Isotope Mass	Natural Abundance	Final Abundance
58	.683	.661
59	.000	.025
60	.261	.257
61	.011	.019
62	.036	.027
63	.000	.003
64	.009	.008
65	.000	>.000
	1.000	1.000

5.3 Nickel Utilization (R. L. Simons and H. R. Brager)

Three simple austenitic steels enriched with nickel 59 were designed and prepared for irradiation in FFTF. Fifty gram buttons were melted in an argon partial atmosphere in the presence of molten titanium which was used to getter H, O, and N. The buttons were normalized at 1250°C for two hours in an argon atmosphere. This was followed by a series of cold rolls and thirty minute anneals at 1030°C in argon until the alloys were given a 20% reduction in thickness with a final roll to 10 mils thick. The specimens were punched into TEM disks and miniature tensile specimens. The solution annealed specimens were heat treated at 1030°C for thirty minutes after being deburred and engraved with identification codes.

All the alloys will be irradiated side-by-side with alloys that have identical chemistry but no nickel 59. The three reference heats used nickel obtained by reducing unirradiated Inconel 600 by the same processes described above. This series of six alloys will be irradiated in both the annealed and 20% cold worked condition.

The first alloy is a ternary with the composition Fe15Cr25Ni. The nickel was split 80% radioactive nickel and 20% natural nickel. The second alloy composition is the same as the first but with 0.04% phosphorus. The phosphorus-modified alloy is designed to investigate the interaction between this high diffusivity solute and void nucleation as discussed by Garner and Brager.[1] The third alloy contains the same weight percent radioactive nickel but the total nickel concentration was increased to 45% at the expense of the iron. This alloy is designed to investigate the influence of spinodal hardening, the resistance to void nucleation in the Invar composition region, and the effect of helium/dpa on the transient regime of void nucleation. The irradiation temperatures chosen are 360, 450, 490, and 600°C. The exposure times will be approximately 200, 400, and 800 effective full power days (EFPD) in the FFTF Materials Open Test Assembly (MOTA).

The specimen locations in MOTA, the number of MOTA cycles (200 EFPD/cycle), irradiation temperature, dpa damage exposure, helium/dpa ratio and total helium (appm) are summarized in Table 3. The last column is the helium/dpa enhancement expected by using a steel enriched in nickel 59 compared to a steel without nickel 59. The level 8 location will be used to compare with a high temperature, long term RTNS-II irradiation currently planned by Japan/USA. Some extrapolation of the FFTF and RTNS-II data will be necessary because the fluences do not overlap. There will be substantial differences between the cascades produced in the two neutron spectra.

The specimen configurations are mini-tensile specimens and TEM disks. Tensile testing will be done at the irradiation temperatures for all materials and thermal/mechanical conditions. Tensile testing of the solution-annealed material will be done at room temperature also. Density, hardness, and instrumented punch tests will be performed on TEM disks in addition to TEM analysis.

TABLE 3

IRRADIATION PARAMETERS FOR THE ^{59}Ni ENRICHED TERNARY

MOTA Level	MOTA Irrad. Cycles	Temp. (°C)	Dose (dpa)	hpa/dpa (appm/dpa)	hpa (appm)	Initial hpa/dpa Enhancement
6E2	1	490	2.2	11	24	150
	2		4.4		48	
	4		8.8		97	
5D1	1	600	8.8	8	70	22
	2		18		144	
	4		35		280	
Below Core Canister (BCC)	1	360	5.2	11	57	113
	2		10		110	
	4		21		231	
8E1	1	450	.19	33	6	50
	2		.38		13	
	4		.76		25	

Thirty-three grams of the original 53 grams of nickel containing nickel 59 have been used in preparation for the FFTF irradiations. This leaves ~20 grams for additional alloys to be used in future irradiations.

5.4 Acknowledgement

The authors would like to acknowledge the persistent efforts of several members of the HEDL Analytical Chemistry group for surmounting several technical problems in order to obtain the final nickel product. These staff members include R. W. Stromatt, A. C. Leaf, and E. D. Jenson.

6.0 References

1. F. A. Garner and H. R. Brager, "The Role of Phosphorus in the Swelling and Creep of Irradiated Austenitic Alloys," DAFS Quarterly Progress Report, DOE/ER-0046/20 (Oct-Dec 1984), 56-62.

ON THE USE OF ISOTOPIC AND SPECTRAL TAILORING TO SIMULATE FUSION IRRADIATION VARIABLES IN FISSION REACTORS

G. R. Odette (University of California, Santa Barbara)

1.0 Objective

The purpose of this study is to explore means of approximating the irradiation variables found in fusion reactor environments in experiments in existing high flux fission reactors.

2.0 Summary

It is shown that by using various isotopic ratios of ^{58}Ni/^{60}Ni, single variable experiments on the effect of helium to displacement-per-atom ratios (He/dpa) can be carried out in ferritic and austenitic alloys. Further, additions of small amounts of ^{59}Ni result in the elimination of the low fluence transient, resulting in an approximately constant He/dpa ratio in the range up to 100 dpa. Further, approaches are outlined for dealing with other variables and/or confounding factors, including higher than normal nickel contents in ferritics, different sources of helium, the hydrogen generation rate, evolution of solid elemental constituents, and even differences in the primary recoil spectra. Finally, some important fundamental experiments and issues in need of resolution are noted.

3.0 Program

Title: Damage Analysis and Fundamental Studies for Fusion Reactor Materials Development
Principal Investigators: G. R. Odette and G. E. Lucas
Affiliation: University of California, Santa Barbara

4.0 Relevant DAFS Program Plan/Subtask

Subtask II.C.2 Effects of Helium on Microstructure
Subtask II.C.16 Composite Correlation Models and Experiments

5.0 Accomplishments and Status

5.1 Introduction

Irradiation damage to structural components has been identified as a major technological barrier to the realization of fusion power. Developing radiation resistant alloys for fusion applications has been hampered by the fact that test facilities with the proper combination of irradiation variables are not available. Currently, high exposure data can be obtained only in fission reactors. Efforts to develop correlations to extrapolate fission reactor data to fusion conditions are and will continue to be the basis for predicting irradiation effects in fusion environments. These so-called fission-fusion correlations are based on a combination of theory and data from an array of available irradiation facilities; ultimately, a high flux and energy neutron source will be needed to refine and validate the correlations and to provide the data base requisite for reactor design. Meanwhile, it is important to seek new and innovative means of obtaining more relevant data and to continue to improve theoretical models.

It is widely believed that the most significant environmental difference is the high rate of transmutant helium generation in fusion spectra. This environmental variable is usually characterized in terms of the helium (He) to displacement-per-atom (dpa) ratio (He/dpa), where the helium content is expressed in units of atom parts-per-million. Prototypical values of the He/dpa ratios are around 10 for iron based alloy first walls, although this number varies with reactor design, alloy type and composition, and position in the blanket. Corresponding He/dpa ratios for fast fission reactors are typically about 0.5 or less. Other potentially significant differences in fusion relative to fission environments include: the higher energy of the primary knock-on atom recoil distribution; higher concentrations of hydrogen (from both transmutant and environmental sources); and variations in solid transmutation products. Further, both damage rates and irradiation temperatures may be lower in early fusion reactors than found for the bulk of existing and anticipated fission reactor data.

It has been recognized for some time that irradiations of nickel bearing alloys in mixed spectrum fission reactors, with an appreciable thermal flux component, can produce copious amounts of helium through the two stage reaction

$$^{58}\mathrm{Ni}(n,\gamma)^{59}\mathrm{Ni}(n,\alpha)$$

This reaction is exoergic and occurs at low neutron energies with a large cross section. By adjusting the thermal to fast flux ratio (i.e., spectral tailoring), He/dpa ratios of 10 can be approximated in stainless steels containing 10 to 20% nickel. Unfortunately, practical considerations appear to restrict such irradiations to intermediate flux environments with exposure accumulations of less than about 10 dpa per year. Higher fluxes are available for some (e.g. the PTP) locations in the High Flux Isotope Reactor (HFIR) which produces about 30 dpa per year; however, significant spectral tailoring is not possible at this time in these HFIR reactor locations, and the He/dpa ratio changes with exposure, approaching an approximately constant value of 65±5 after about 10 dpa. Other important candidate alloy classes, including ferritic/ martensitic stainless steels typically contain less than 0.5 percent nickel. Hence, high He/dpa ratios do not result from mixed spectrum irradiations unless such alloys are doped with unnaturally large amounts of nickel. Unfortunately, nickel may have an influence on both the basic physical metallurgy of such alloys and their response to irradiation.

Simons has suggested the use of pre-irradiated nickel, containing a substantial initial concentration of ^{59}Ni, coupled with subsequent irradiations in intermediate spectral locations in the Fast Flux Test Facility (FFTF)[1]. Because of a large 203 eV resonance, this results in He/dpa ratios around 10 in alloys containing more than about 15% nickel, at exposure rates of about 10 dpa per year. To this end Simons and coworkers have succeeded in extracting approximately 55 grams of nickel containing about 2.1% ^{59}Ni from a nickel based alloy irradiated to high fluence in a mixed spectrum reactor[2]. As noted by Simons, it is possible to generate additional ^{59}Ni in HFIR using either natural nickel or an isotopic mix highly enriched in ^{58}Ni, thereby permitting ^{59}Ni concentrations of up to 3.5%. The major practical difficulty in obtaining ^{59}Ni in a useful form is separation of the concommital high level of ^{60}Co activity, which is on the order of 1 Ci per gram of ^{58}Ni. It has been demonstrated that this separation can be accomplished by electrochemical techniques[2].

In this report, several alternate approaches to the use of isotopic tailoring are proposed using both synthesized and separated isotopes of nickel and other elements. This strategy permits single variable experiments involving controlled He/dpa ratios in the high flux locations in HFIR for a variety of candidate alloys, including ferritics. Other single or few variable experiments in high flux fission reactors which explore the effect of recoil spectra, solid transmutants, and high levels of transmutant hydrogen as well as evaluating particular mechanisms are also possible. Finally, the combined effects of several of the important fission-fusion variables can be assessed.

The rest of this report describes the basic concepts, outlines an overall strategy based on these concepts and discusses briefly some of the important issues which need to be addressed.

5.2 Helium to dpa Ratios in Alloys Containing Tailored Isotopic Concentrations of Nickel

The production of helium from ^{59}Ni is given by the relation

$$\mathrm{He}_1/{}^{59}\mathrm{Ni}_0 = [\langle\sigma_\alpha\rangle_{59}/\langle\sigma_t\rangle_{59}]\,[1 - \exp(-\langle\sigma_t\rangle_{59}\phi t)] \qquad (1)$$

where the $\langle\sigma_\tau\rangle$ and $\langle\sigma_\alpha\rangle$ are spectral averaged total absorption and alpha emission cross sections, $^{59}\mathrm{Ni}_0$ the initial concentration of this isotope, and ϕt the total fluence. The corresponding expression for the helium production from ^{58}Ni is

$$He_2/{}^{58}Ni_o = \langle\sigma_\alpha\rangle_{59}\ [\langle\sigma_t\rangle_{59}(1-\exp[-\langle\sigma_\gamma\rangle_{58}\phi t])-\langle\sigma_t\rangle_{59}(1-\exp[-\langle\sigma_t\rangle_{59}\phi t])]/\langle\sigma_t\rangle_{59}(\langle\sigma_t\rangle_{59}-\langle\sigma_\gamma\rangle_{58})) \quad (2)$$

where $\langle\sigma_\gamma\rangle_{58}$ is the (n,γ) absorption cross section and ${}^{58}Ni_0$ the initial nickel concentration of this isotope. Helium is also produced by high energy neutron (n,α) reactions as

$$He_3/N_{steel} = \langle\sigma_{he}\rangle_{steel}\phi t \quad (3)$$

where the $\langle\sigma_{he}\rangle_{steel}$ is a function of the overall composition (including the isotopic mix) as well as the spectrum. As noted above, for the range of He/dpa of about 10, this is normally not a significant source of helium; however, the contributions from specific isotopes of iron, nickel and chromium can be significant. Contributions of other isotopes, of trace impurities such as boron and lithium, generally do not exceed a few parts per million, hence are not important at higher exposures. The total displacement damage exposure can also be calculated from the compositionally weighted spectral averaged cross section as

$$dpa = \langle\sigma_{dpa}\rangle_{steel}\phi t \quad (4)$$

As pointed out by Greenwood, the (n,α) reaction produces recoils at 340 keV which also generates displacement at a rate of about 1 per 570 parts-per-million of helium; however, while this is not normally a significant source of displacement damage, it will be shown below that this reaction can also be used to study high energy recoil effects with specially designed specimens.

Equations 1 to 4 can be used along with appropriate measured or calculated of spectral averaged cross sections to calculate the total helium concentration as a function of displacement damage for various irradiation facilities. As shown below, by changing the initial fraction of the various isotopes, it is possible to modify the He/dpa ratio. However, separate strategies are needed for the various alloy classes.

For alloys such as austenitic stainless steels which contain appreciable amounts of nickel (8 to 16%), dilution of the normal isotopic composition of ^{58}Ni (about 68 percent) and additions of small amounts of ^{59}Ni coupled with irradiations in high flux HFIR positions yields an approximately constant and controllable He/dpa ratio. Table 1 lists various spectral averaged cross sections for HFIR, EBRII core and a typical fusion first wall spectra[3-7]. The calculations which follow also assume, unless otherwise stated, a austenitic alloy composition (in atom percent) of 65 iron, 18 chromium, 14 nickel and balance other; ferritic alloys are taken as 88 iron, 10 chromium and balance other. These calculations also neglect the effects of reactions with both radioactive isotopes, other than ^{59}Ni, and trace impurities such as nitrogen and boron; further the effect of (n,2n) and (n,charged particle) reactions on the solid elemental constitutent evolution is not treated. Improved calculations will be pursued in future research.

The large total cross section for ^{59}Ni has two important consequences: the initial ^{59}Ni quickly burns out with about 10.3 of the total 12.5 percent conversion to helium occurring by 10 dpa; and the transmuted ^{59}Ni approaches rapidly secular equilibrium with ^{58}Ni achieving over 90 percent of its maximum value at this exposure at a ratio of ^{59}Ni/^{58}Ni of about 1/33. The total concentration of ^{58}Ni/^{59}Ni slowly declines following the peak due to burnout of ^{58}Ni, with a proportional decrease in the helium production rate. Hence, an isotopically tailored alloy initially containing a similar ^{59}Ni/^{58}Ni ratio will have an approximately constant value of He/dpa over a broad exposure range.

Figure 1 shows the He/dpa ratio for an alloy with 2 percent pre-irradiated natural nickel of isotopic composition 2.1 percent ^{59}Ni and about 64 percent of ^{58}Ni with the balance of higher weight nickel isotopes. The remaining 11.3 (or whatever) percent nickel is composed of isotopically separated ^{60}Ni (this isotope can be purchased for about \$350/g). There is an approximately constant He/dpa ratio of 10.5±1.5 up to a level of 100 dpa as a consequence of the compensating burn-out of ^{59}Ni and the burn-in of ^{58}Ni. The relative contributions are also shown in Figure 1. It is obvious that by changing the fraction of the ^{60}Ni isotope, the He/dpa ratio can be varied from fast reactor levels of less than 1 to about 50 or more. Hence, as discussed below, as well as providing an approximate simulation of the fusion He/dpa levels, data from such experiments could be used to refine and validate models of the synergistic interactions between helium and displacement damage in controlling microstructural evolution. In addition to controlled variations in the He/dpa ratio, alloys without the ^{59}Ni would have the transient He/dpa ratio as shown in Figure 1. Hence, side by side irradiations with and without ^{59}Ni would be useful in illuminating the role

Table 1

Spectral Averaged Cross Sections (mb)

Reaction-Isotope	Reactor Spectrum			Reaction-Isotope	Reactor Spectrum			Reaction-Isotope	Reactor Spectrum		
(n,p)	HFIR (PTP)	EBRII (5.2,0.0)	FUSION	(n,α)	HFIR (PTP)	EBRII (5.2,0.0)	FUSION	Other	HFIR (PTP)	EBRII (5.2,0.0)	FUSION
Cr	0.4	0.49	22	Cr	0.057	0.068	12	^{58}Ni(n,γ)	1625	9.4	--
^{58}Ni	17.4	22	98	^{58}Ni	1.22	1.42	20	^{59}Ni(n,γ)	29150	72.5	--
^{59}Ni	735	54.7	--	^{59}Ni	4300	14.4	--	^{54}Fe(n,γ)*	2900	--	--
^{60}Ni	0.42	0.47	32	^{60}Ni	0.14	0.16	10	^{54}Mn(n,γ)*	13300	--	--
^{54}Fe	11.9	14.6	92	^{54}Fe$_1$	0.36	0.43	25	^{54}Cr(n,γ)*	300	--	--
^{56}Fe	0.24	0.28	22	^{54}Fe$_2$	0.19	0.21	25	^{50}Cr(n,γ)*	17000	--	--
dpa	2x10^5	4.8x10^5	10^6	^{56}Fe	0.036	0.048	21	^{50}V(n,γ)*	4900	--	--

*These are cross sections for thermal neutrons in HFIR taken from Reference 4; nuclear decay data was also taken from this source.

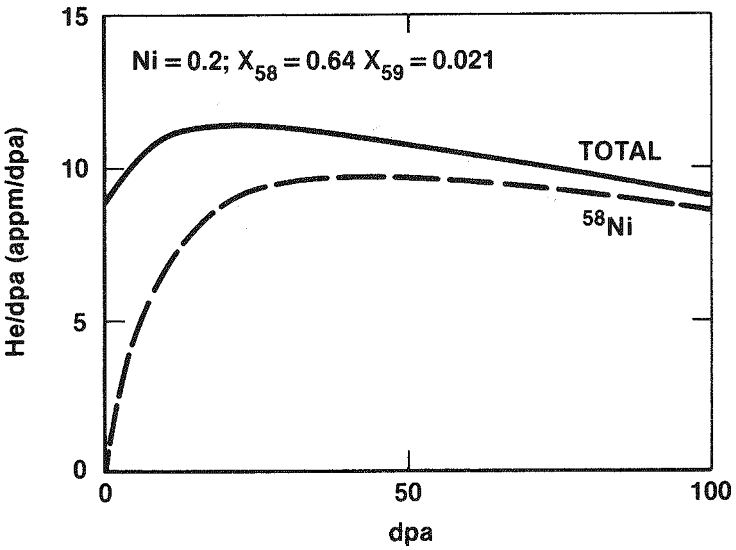

Figure 1. The He/dpa ratio variation with exposure for a ^{58}Ni/^{59}Ni/^{60}Ni isotopically tailored austenitic steel.

of helium in the early microstructural evolution, and the effect of this early evolution on the incubation and steady state swelling regimes. Further, it is noted that, in principle, manganese can be substituted for ^{60}Ni, in order to study the behavior of low activation austenitics; however, in practice somewhat higher nickel levels plus spectral tailoring to reduce thermal fluxes would be needed to limit the burnout of manganese.

Ferritic/martensitic stainless steels contain much lower amounts of nickel, typically less than 0.5 percent. Hence, high He/dpa ratios cannot be readily achieved by either isotope or spectral tailoring applicable to austenitic alloys. Simons has suggested use of isotopically separated ^{59}Ni enriched to nearly 100 percent for use in fast reactor irradiations. An alternate strategy is to evaluate the effects of nickel variations at a constant He/dpa ratio using ^{60}Ni dilution coupled with an assessment of the effect of He/dpa variations at a constant nickel content. With about 2 percent nickel, a He/dpa ratio of about 10 can be achieved with natural nickel, and the ratio can be made approximately constant by adding the ^{59}Ni as discussed above. If ^{59}Ni produced in fully enriched ^{58}Ni is used, the nominal He/dpa ratio of 10 can be achieved using only about 1.4 percent nickel. Hence, by varying both the ^{58}Ni/^{59}Ni/^{60}Ni ratio and the nickel content a response surface can be constructed to permit systematic extrapolation to the appropriate combination of He/dpa ratio and nickel content. That is nickel variations at constant He/dpa ratios and He/dpa variations at constant nickel content can be studied simultaneously. This is schematically illustrated in Figure 2. Further, by overlapping He/dpa and nickel content matrix points with alloys not containing an initial charge of ^{59}Ni, transient effects (if any) can be evaluated. Indeed, if the effect of nickel variations (in the range up to 2 percent) and the He/dpa transient are found to be minimal, a very convenient means of evaluating He/dpa ratios using only ^{58}Ni will be possible.

5.3 Confounding Factors, Other Variables and Other Isotopes

While these experiments confront directly the question of He/dpa effects, there are confounding factors which need to be considered and there are other fission-fusion variables which are not properly accounted for. The effects of higher than normal nickel levels in ferritic alloys at He/dpa ratios of about 10 is one example. Another is the variation in the transmutant hydrogen (H) production in various environments. For austenitic alloys the H/dpa ratios are: HFIR~12; EBRII~6; and fusion~30. The corresponding H/dpa values for ferritic alloys are: HFIR~5; EBRII~2.5; and fusion~25. In HFIR alloys isotopically tailored to have He/dpa ratios of about 5 to 20 there is a slight reduction in their H/dpa ratios which varies from about 4 to 6, similar to the ratio for fast reactors.

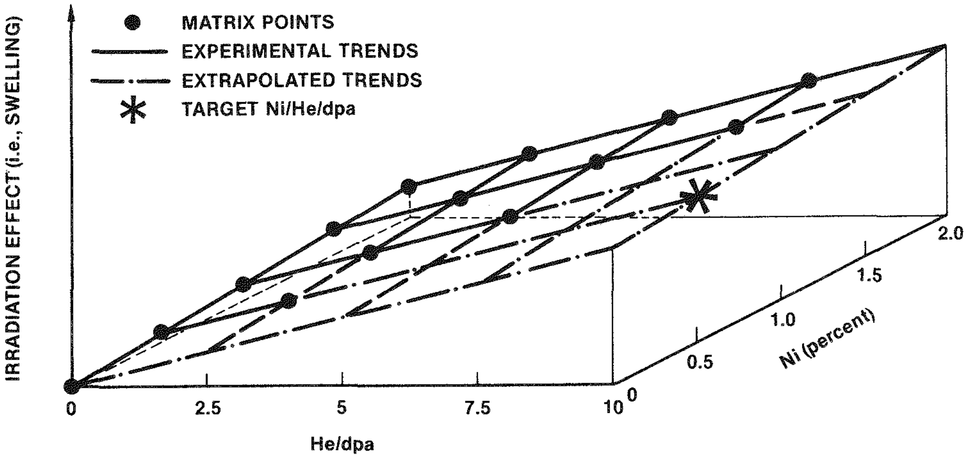

Figure 2. Schematic illustration of an irradiation response surface for He/dpa and Ni variations could be used to extrapolate to a relevant combination of material and environmental variables.

In thermal reactors with the He/dpa ratio of about 10, well over 90 percent of the helium comes from nickel; this is fairly close to the case for fast fission reactors where over 70 percent of the helium is generated from nickel reactions. The question of the source of helium becomes more serious, and indeed may be a fission-fission-fusion variable, when comparing various fission reactors with the fusion environment. In a fast spectra typical of fusion environment, the elemental sources of helium are in rough proportion to the percentages of the major alloy constituents, hence, are predominantly produced in reactions with iron. The concern over the elemental source derives from the fact that the alloy constituents segregate strongly during irradiation, hence helium generation will not be spatially uniform.

Another potential fission-fission-fusion variable is associated with solid transmutant production and elemental burnout reactions. Figure 3 shows the calculated evolution of the vanadium and manganese content in mixed and fast fission and a fusion spectrum.[5] The significance of the variations in solid minor alloy constituents (and hydrogen and the source of helium) is not known. Evaluation of limited data on the effect of these elements in fast reactor irradiations suggests that they are second order variables.

By tailoring of other isotopes of iron and chromium it may be possible to assess experimentally effects of these variables and confounding factors. Further, in combination with spectral tailoring is in principle possible to evaluate the effects of He/dpa ratios independent of the nickel tailoring. The major source of transmutant vanadium in mixed HFIR is the ^{50}Cr chain

$$^{50}\mathrm{Cr}(n,\gamma)^{51}\mathrm{Cr}(EC)^{51}\mathrm{V}(n,\gamma)^{52}\mathrm{V}(\beta^-)^{52}\mathrm{Cr}$$

The isotope ^{50}Cr is naturally 4.3 percent abundant; hence, by using chromium depleted in this isotope, the amount of transmutant vanadium in HFIR can be reduced as illustrated in Figure 3 for depletion factors of 3.6 approximating behavior in fusion spectra. At depletions factors greater than 30 to 40, the vanadium content remains low, similar to fast reactor behavior. Figure 4 shows an approach to treating the effect of manganese variations. Here, use is made of the reaction chain starting with the isotope ^{54}Fe

$$^{54}\mathrm{Fe}(n,\gamma)^{55}\mathrm{Fe}(EC)^{55}\mathrm{Mn}(n,\gamma)^{56}\mathrm{Mn}(\beta^-)^{56}\mathrm{Fe}$$

The upper dashed curve shows the results of a HFIR irradiation of an austenitic alloy fabricated from an iron enriched to 58 percent ^{54}Fe pre-irradiated to a thermal fluence of 3×10^{26}n/m^2 combined with an initial charge of 2.0 percent natural manganese. Thermal cross sections from the literature were used in these calculations[4]. The lower dashed-dotted curve is for a similar case where the ^{54}Fe enrichment is 40 percent and the initial concentration of natural manganese is 2.5 percent. These limiting cases approximate the changes in manganese for a typical austenitic alloy irradiated in a fusion and fast fission spectra respectively, as shown by the solid lines. It should be noted, however, that there may be effects due to the differences in the location of the various parent/burnout species.

The use of iron enriched in ^{54}Fe can also be used to increase both the helium and hydrogen production. Table 1 also gives estimates of the spectral averaged (n,p) and (n,α) cross sections for high flux locations in HFIR and EBRII for the isotopes of iron, nickel and chromium. The cross sections were taken from a recent critical review of Paulsen who compared existing experimental data to excitation functions calculated from nuclear models[6]. The spectra are also from the literature[7]. Two values are listed for the ^{54}Fe(n,α) cross section reflecting significant deviations between the calculated cross section and experimental values in the threshold region of 2 to 4 MeV; an average value between these limits will be used for the subsequent calculations.

In HFIR the ^{54}Fe(n,α) cross section is about 0.27 ± 0.08 mb which is about a factor of 8 times higher than the corresponding cross section for ^{56}Fe; at 100 percent enrichment this yields a He/dpa ratio of about 1.4 ± .4 mb. Thus the behavior of iron based alloys containing nickel only in the form of ^{60}Ni could be compared to those based on natural iron containing sufficient ^{58}Ni/^{60}Ni to give the same He/dpa ratio, but where most of the helium comes from the nickel. The use of ^{54}Fe in HFIR does result, however, in a significant increase in the manganese content. Moderate spectral tailoring to reduce the thermal flux could be used to diminish this effect. Alternately irradiations in fast spectra could be carried out; the He/dpa ratios obtainable are reduced by a factor of about 0.6 in a EBRII core spectra.

For HFIR irradiations of iron based austenitic steels containing a small amount of ^{58}Ni so that about two thirds of the helium is generated from nickel, the He/dpa ratio increases about 4; a comparable value for a natural elemental austenitic alloy in EBRII is about 0.5 and about 0.15* for steels containing less than 1

---

*It is noted that the low He/dpa ratio in ferritics may be one factor in their swelling resistance.

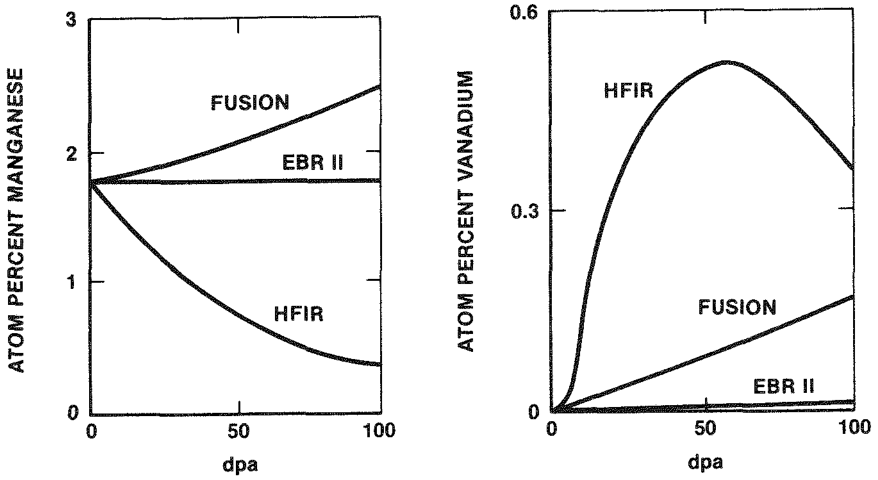

Figure 3. Calculated estimates of the evolution of elemental concentrations of manganese and vanadium in various spectra.

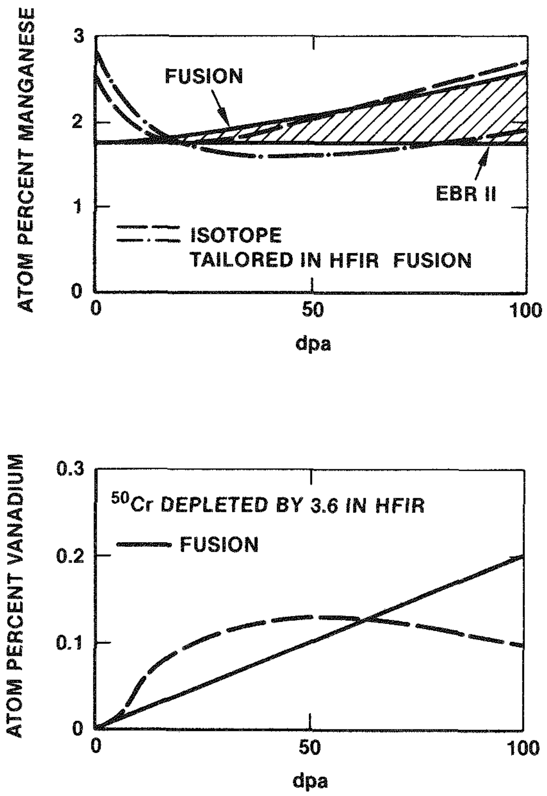

Figure 4. A comparison of the calculated evolution of elemental manganese and vanadium for isotopically tailored austenitic steels in HFIR with estimates for fast fission and fusion environments.

percent nickel. In HFIR burnout of the ^{54}Fe lowers the rate of helium production to about 50 percent at 100 dpa in alloys with only ^{60}Ni and by about 15 percent in alloys containing ^{58}Ni; again this can be reduced using spectral tailoring. Decreasing the thermal flux by a factor of 2.5 would result in reduction of the helium generation rate at 100 dpa by only about 13 and 4 percent for these cases respectively. Hence, HFIR experiments on ^{54}Fe enriched alloys can result in significant increases in the He/dpa ratio where the helium is roughly generated from the same sources as either fast fission or fusion environments. More significantly perhaps, ^{54}Fe enrichment can also be used to study the effect of intermediate He/dpa ratios in low activation austenitics and ferritics.

Independent variation of the hydrogen production rate at a constant He/dpa ratio can also be affected by enrichment in ^{54}Fe. The H/dpa for an austenitic alloy with elemental iron in HFIR can be increased from about 5 (at a He/dpa ratio of 5 to 20) to about 30 for iron 75 percent enriched in the ^{54}Fe isotope. This is close to the H/dpa ratio for a similar natural elemental alloy in fusion spectra. Hence, combinations of isotope/spectral tailoring can be used to simulate both the H/dpa and the He/dpa ratios as well as the elemental evolution which occurs in either fusion or fast fission spectra.

Other uses of isotope/spectral tailoring to study particular mechanisms and phenomena will be discussed briefly in a later section. Modifications of high flux positions in HFIR to provide lower temperatures, instrumentation and spectral tailoring, use of other HFIR lower flux reflector positions (e.g. the RBR-which can be instrumented and spectral tailored) will be needed to refine the characterization and extend the range of variables such as damage rate (comparable irradiations at about 12 versus 30 dpa per year) and temperature (below 300°C). Further, it is expected that the bulk of irradiation effects data, particularly for mechanical property changes, will continue to be generated in fast reactors such as large volume Materials Open Test Assembly (MOTA) locations in the Fast Test Reactor (FTR).

Together with the concepts and approaches outlined above, these developments will provide an effective strategy of obtaining a data base for developing fission-fusion correlations. Quasi single variable experiments can be used to evaluate the effect of particular irradiation variables and confounding factors; and the combination of the most important irradiation variables (stress, temperature, damage rate, He/dpa ratio, H/dpa ratio and elemental evolution) can be held reasonably close to conditions expected for fusion environments. However, there is one important exception to achieving a reasonable matching of important or potentially important irradiation variables, namely, the PKA recoil spectra. This will be discussed in the following section.

5.4 PKA Spectral Differences and Approaches to Simulation

The quantitative differences between primary knock-on atom recoil spectra is fission and fusion environments, and between various fission environments, have been well documented in the literature^{7}. The fusion recoil spectra can be described qualitatively in terms of a high energy component produced by the 14 MeV neutrons, which are about 20 percent of the neutron flux at the first wall. The high energy component has a mean energy in the range of a few hundred keV. It is coupled with a broadly distributed lower energy recoil distribution with a mean energy in the tens of keV generated by the collided neutron spectra (which comprises about 80 percent of the first wall flux). The latter resembles the recoil distribution produced in the core region of a fission reactor such as HFIR. Roughly 60 percent of the displacement damage is produced by the high energy neutrons; and about one out of 15 recoils have energies greater than 200 keV (above this energy the HFIR and fusion PKA spectra diverge very rapidly). Smaller differences in recoil spectra are found among the various high flux fission reactor environments; mean energies at recoils generated by fast neutrons increase from about 5 to 30 keV in ascending order for FTR, EBRII and HFIR in locations with roughly comparable total displacement rates.

Hence, the major factor which must be accounted for in developing fission-fusion correlations is the high energy recoil component. Substantial progress has been made in characterizing the initial production stage of displacement damage based on flow fluence irradiations in the RTNS-II 14 MeV facility; corresponding fission irradiations are more limited, but a number are planned which should provide a sound basis for defining net defect production parameters for the energy range of interest. Information available to date suggests that dpa is an adequate basis for correlating low temperature irradiation effects on simple mechanical and physical property changes in pure materials and model alloys. There is not sufficient data to support this conclusion for more complex alloys in general, and for property changes which are due to a significant evolution of the microstructure induced at high fluences and temperatures in particular.

This is significant, since even if the low fluence data is sufficient to rigorously establish defect production parameters, there is evidence that the form of the damage may have important effects on evolutionary processes such as void swelling. In particular, damage predominantly generated in the form of cascade clusters might yield significantly different rates and even paths of microstructural evolution than the same number of defects generated predominantly as isolated Frenkel pairs. High resolution microscopy of the primary damage structure will be useful in addressing this issue; however, these results can be translated to effects on high fluence evolutionary processes only through models. Ultimately, high flux high energy neutron irradiation facilities will provide experimental verification of the models. However, in the interim isotope and spectral tailoring experiments may permit a preliminary assessment of high energy recoil effects at high fluences.

The concept involves taking advantage of the 340 keV recoil from the ^{59}Ni(n,α) reaction. Greenwood has shown that for about every 570 ppm of helium generated there is a corresponding displacement[8]. Hence as the He/dpa ratio is increased by enrichment with the isotopes ^{59}Ni/^{58}Ni, a significant fraction of the displacements is due to 340 keV recoil. For a 20 percent nickel alloy fully enriched in these isotopes with the ratio ^{59}Ni/^{58}Ni (~ 0.033) so that the He/dpa ratio is approximately constant at about 150, the 340 keV recoils contribute about 20 percent of the displacements. In this case, however, the fraction of high energy recoils, greater than 200 KeV is about 5 times lower than in a fusion spectra.

This fraction as well as the high energy recoil contribution to the displacements can be increased by increasing the nickel content of the alloy, or by increasing the thermal to fast flux ratio. Alternately, a higher ratio of ^{59}Ni/^{58}Ni prepared by isotopic separation could be used; 33 percent enriched ^{59}Ni in a 20 percent nickel alloy would result in about 60 percent of the displacements generated by the high energy recoils, and a fraction of PKAs with energy greater than 200 keV approximately equal to that in a fusion spectra. However, burnout of the ^{59}Ni would decrease the high energy contribution to about 33 percent at 5 dpa and 14 percent at 10 dpa; hence, this approach would be useful only in a relatively low fluence or short incremental exposure experiments. Some basic mechanism studies that would be possible using this approach are discussed below.

The obvious disadvantage to this means of obtaining high energy recoil damage is that the intrinsic He/dpa ratios would be much to high. However, this problem could be mitigated by irradiating specimens in the form of thin foils (fine powders might also be considered). The alpha product has an energy of about 4.3 MeV and an equivalent range in iron of about R = 7.4 μm. As illustrated in Figure 5 in a thin foil geometry, most of the alpha particles would escape, leaving only those emitted within the shaded (solid) angle. For a foil of thickness t this fraction f_{He} can be readily calculated by the expression

$$f_{He} = 5.55\text{x}10^{-3} \int_0^t (\sin^{-1}(x/R_e) + \sin^{-1}(t-x/R_e))dx \sim .047t(\mu m) \qquad (5)$$

In this calculation the effective range of the alpha particle R_e is taken as 95% of the total range R to account for straggling. With foils of about a micron thickness, reasonable effective He/dpa ratios (< 50) can be maintained even up to actual He/dpa ratios of 1000. Formation of surface denuded zones of up to 0.5 micron and problems of fabrication and contamination may

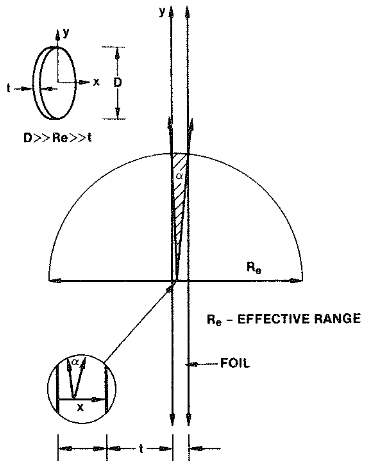

Figure 5. Illustration of the thin foil geometry needed to reduce helium retained from (n,α) reactions.

restrict minimum foil thickness to a few microns; however even a 3 μm foil isotopically tailored to produce a He/dpa of 150 would have an effective He/dpa ratio of only about 25. Further, some of these problems might be reduced at lower temperatures where the effect of cascade damage is believed to be most significant.

5.5 Discussion: Issues and Other Implications

The preceding discussion outlines a broad strategy to achieving fusion like irradiaton variables in fission reactor environments with emphasis on mixed spectrum reactors. While all the fusion variables of known or potential significance cannot be duplicated, in almost all cases it is possible to conduct quasi single variable experiments in order to systematically evaluate the effects of differences in the irradiation variables. Coupled with physical models and other information from fast reactor and dual ion bombardment experiments, significant advances in fission-fusion correlations can be anticipated.

The approaches outlined here clearly neither exhaust the possibilities nor necessarily describe an optimum approach. For example, there are a large number of mechanism studies which might be considered, which could help develop understanding of critical phenomena and refine models. To illustrate this point, consider only a few of many possibilities:

1. Helium mobility partitioning and initial kinetics of bubble formation, and partitioning under realistic conditions could be studied in relatively low fluence experiments using nickel isotope tailoring in HFIR. In particular, the dependence of the cavity density and the general scale of microstructural development as a function of the He/dpa ratio and other variables could be determined.
2. The capacity of various microstructural features to trap helium, the duration of trapping, and the effect of trapped helium on the stability of features such as MC carbides could be similarly examined.
3. The basic importance of helium in controlling the onset of rapid swelling and the validity of critical bubble models can be studied by lowering the He/dpa ration using alloys enriched in the isotopes ^{60}Ni and ^{56}Fe.
4. The effect of cascade recoil energy on point defect survival could be assessed by low fluence loop growth experiments using thin foils enriched in ^{59}Ni. Alternately, such foils might be first be irradiated in a fast reactor to initiate void swelling followed by an incremental exposure of several dpa in both the fast reactor and HFIR to measure any effects of high energy cascade damage production on the subsequent swelling rates. High energy recoil primary defect production effects on other property changes which occur at such exposures (e.g. creep) could be evaluated in a similar manner.

While these and many other possibilities exist, there are a number of potential problems to be overcome and techniques which must be developed if the full potential of the isotope/spectral tailoring approach is to be realized. The primary issues of concern include:

1. Procedures to produce ^{59}Ni in HFIR positions, and means of extracting pure nickel from isotopically modified materials. As noted by Simons, isotopic separation of ^{59}Ni would also be a useful capability.
2. Measurement of isotopic production rate of helium in various spectra of interest. Further, such measurements should be extended to measure hydrogen production and changes in solid elemental components.
3. Development and evaluation procedures to ensure reproducibility and composition-microstructural control in small slit melts. The necessity to handle radioactive stock may complicate the fabrication problem further. Developing techniques for fabricating and irradiating thin films to study recoil effects would also be required.
4. Continued efforts at developing small specimen testing procedures.
5. Improved monitoring and control of temperatures in HFIR (and EBRII if it is used). Further, development of a spectral tailoring facility in the reflector position in HFIR would be very useful.

While these developments may involve considerable effort, it seems likely that these and other related problems can be solved. As noted in the introduction, a high energy-flux-volume irradiation facility will be required for the rational development of high performance structural alloys for fusion reactors. However, in the interim, the creative use of isotope and spectral tailoring in fission reactors promises to be a rich source of information and a sound basis for preliminary data correlation for fusion reactor structural alloys.

6.0 References

1. R. L. Simons, ^{59}Ni Enrichment as a Means of Simulations the He/dpa Reaction of a Fusion Neutron Environment, Damage Analysis and Fundamental Studies Quarterly Progress Report-20, DOE/ER-0046/12, 37 (1983).

2. R. L. Simons, "Isotopic Tailoring with Nickel-59 to Enhance Helium Production in Fission Reactor Irradiation," this volume.

3. D. W. Kneff, R. P. Skowronski, B. M. Oliver and L. R. Greenwood, A Comparison of Measured and Calculated Helium Production in Nickel for Fission Reactor Irradiations, Damage Analysis and Fundamental Studies Progress Report-23, DOE/ER-0046/15, 12 (1983).

4. C. M. Lederer, J. M. Hollander and I. Perlman, Table of Isotopes - Sixth Edition, John Wiley (1967).

5. J. F. Bates, F. A. Garner and F. M. Mann, J. Nucl. Mater. 103 & 104, 999 (1981); F. A. Garner, F. M. Mann, and H. R. Brager, "Measurements and Calculation of Solid Transmutants formed in AISI 316," DAFS Quarterly Progress Report, DOE/ER-0046/7, November 1981, p. 198.

6. A. Paulsen, Status Report About Some Activation, Hydrogen and Helium Production Cross Sections of Structural Materials, Neutron Data of Structural Materials for Fast Reactors, K. H. Böckhoff, Ed. Pergamon Press, 261 (1979).

7. D. G. Doran and N. J. Graves, Displacement Cross Sections and PKA Spectra: Tables and Applications, Report, HEDL TME 76-60, Hanford Engineering Development Laboratory, Richland, WA, 1961.

8. L. R. Greenwood, J. Nucl. Mater. 115, 137 (1983).

7.0 Future Work

An initial experiment to use the isotope tailoring technique has been proposed, and a detailed plan will be developed during the next reporting period.

HELIUM PRODUCTION CROSS SECTIONS FOR 14.8-MeV NEUTRONS

B. M. Oliver, D. W. Kneff, R. P. Skowronski, and H. Farrar IV (Rockwell International)

1.0 Objective

The objective of this work is to measure helium generation rates of materials for Magnetic Fusion Reactor applications in the ~14.8-MeV T(d,n) neutron environment.

2.0 Summary

Total helium production cross sections have been measured for eleven separated isotopes of lead and tin irradiated in the ~14.8-MeV T(d,n) neutron environment of RTNS-II.

3.0 Program

Title: Helium Generation in Fusion Reactor Materials
Principal Investigators: D. W. Kneff and H. Farrar IV
Affiliation: Rockwell International

4.0 Relevant DAFS Program Plan Task/Subtask

Subtask II.A.4.2 T(d,n) Helium Gas Production Data

5.0 Accomplishments and Status

The total helium production cross sections of the separated isotopes ^{116}Sn, ^{117}Sn, ^{118}Sn, ^{119}Sn, ^{120}Sn, ^{122}Sn, ^{124}Sn, ^{204}Pb, ^{206}Pb, ^{207}Pb, and ^{208}Pb have been measured for ~14.8-MeV T(d,n) neutrons from the Rotating Target Neutron Source-II. The measurements were made by irradiating multiple samples of each separated isotope in close geometry to the RTNS-II source, and subsequently analyzing the samples for helium by high-sensitivity isotope-dilution gas mass spectrometry.(1) The irradiation was a joint Rockwell International-Argonne National Laboratory (ANL)-Lawrence Livermore National Laboratory (LLNL) experiment that also included numerous other materials for cross section measurements.(2) The neutron fluence received at each sample location was determined by detailed neutron fluence mapping of the irradiation volume using a combination of radiometric and helium accumulation dosimetry.(3,4) Various aspects of this work were supported by the Office of Fusion Energy and the Office of Basic Energy Sciences of the U.S. Department of Energy.

The irradiated isotopes were etched, to remove all possible effects of helium recoil into or out of the samples, and then analyzed using a new constant-temperature sample furnace. These samples were not segmented, as was done for most of the previously analyzed samples, because of the low helium concentrations expected. The measured helium concentrations in these samples ranged from 0.07 appb to 1.8 appb (atomic parts per billion, 10^{-9} atom fraction).

The new constant-temperature furnace was developed for the analysis of samples with small (~1 mb) helium production cross sections, and for metallic samples of large mass (≥200 mg). The furnace utilizes a large graphite crucible, maintained at a constant elevated temperature (~2000°C), into which samples are dropped remotely. This system provides a more uniform background signal than is currently obtainable by using individual resistance-heated tungsten wire crucibles. The background uncertainty is also an order-of-magnitude smaller than is currently produced when vaporizing samples in our larger resistance-heated graphite crucibles. The Pb and Sn analyses were performed in the new furnace using an empty, heated crucible. The measured oven background was $(0.4 \pm 2.1) \times 10^{8}$ atoms of helium. High-melting-point samples will utilize a

TABLE 1

TOTAL HELIUM GENERATION CROSS SECTIONS FOR ~14.8-MeV NEUTRONS[a]

Material	Cross Section (mb)	Material	Cross Section (mb)
Sn-116	3.0 ± 0.2	Pb-204	1.02 ± 0.08
Sn-117	3.0 ± 0.2	Pb-206	0.66 ± 0.06
Sn-118	1.4 ± 0.1	Pb-207	0.52 ± 0.04
Sn-119	1.2 ± 0.1	Pb-208	0.42 ± 0.04
Sn-120	0.62 ± 0.05		
Sn-122	0.34 ± 0.03		
Sn-124	0.12 ± 0.02		

(a)Preliminary values; see text.

liquid metal bath within the crucible, where the samples' helium will be released by sample dissolution. Initial tests have been conducted using nickel for the liquid metal bath, and additional tests are planned using alternative metals.

The cross section results for the eleven Sn and Pb isotopes are summarized in Table 1. These cross sections were determined by first evaluating the cross section of each irradiated isotopic material. The cross section of each isotope was then calculated by constructing a matrix of equations for all of the enriched isotopes of that element, and solving it to correct the cross section measurement of each enriched isotope for the small concentrations of each of the other isotopes in the material. The assumed isotopic compositions were those provided by the vendor (Oak Ridge National Laboratory). The effect of small impurity concentrations of the unmeasured isotopes ^{112}Sn, ^{114}Sn, and ^{115}Sn was found to be negligible, based on calculations performed using estimated values for the unknown cross sections.

These cross sections must be considered preliminary at the present time, because an independent analysis has not yet been performed to test the isotopic materials for impurity elements. Small concentrations of low-Z impurities, such as C, O, and Si, with high (n,Xα) cross sections could have an effect on these low measured cross sections. However, the elemental impurities are expected to be negligible. Spectroscopic analysis of another separated isotope originally prepared in an identical manner at Oak Ridge (reduced to metallic form and arc-melted to release all helium) indicated limited impurities only at the parts-per-million level. The measured Sn and Pb cross sections also exhibit the expected decrease in value with increasing mass number. Further evidence of a negligible impurity effect is given by the abundance-weighted averages of the measured isotopic cross sections. They give calculated pure-element cross sections of 0.51 mb for Pb and 1.4 mb for Sn. These calculated cross sections are slightly lower than, but consistent with, the previously measured pure-element cross sections of 0.62 ± 0.05 mb and 1.5 ± 0.1 mb, respectively.(3,5) Low-Z impurities would have produced relatively higher cross sections. The tin calculation used estimated cross sections of 5.3 mb, 4.2 mb, and 3.7 mb for ^{112}Sn, ^{114}Sn, and ^{115}Sn, respectively, but the results are not very sensitive to these estimates because of the low abundances of the three isotopes.

6.0 References

1. B. M. Oliver, J. G. Bradley, and H. Farrar IV, "Helium Concentration in the Earth's Lower Atmosphere," Geochim. Cosmochim. Acta, 48, 1759 (1984).
2. D. W. Kneff, B. M. Oliver, M. M. Nakata, and H. Farrar IV, "Experimental Helium Generation Cross Sections for Fast Neutrons," J. Nucl. Mater., 103 & 104, 1451 (1981).
3. D. W. Kneff, B. M. Oliver, M. M. Nakata, and H. Farrar IV, "RTNS-II Fluence Mapping and Helium Generation Cross Sections," in Damage Analysis and Fundamental Studies, Quarterly Progress Report January-March 1982, DOE/ER-0046/9, U.S. Department of Energy, 16 (1982).
4. D. W. Kneff, B. M. Oliver, M. M. Nakata, and H. Farrar IV, "Helium Production Cross Sections for 14.8-MeV Neutrons," in Damage Analysis and Fundamental Studies, Quarterly Progress Report April-June 1982, DOE/ER-0046/10, U.S. Department of Energy, 19 (1982).
5. B. M. Oliver, D. W. Kneff, M. M. Nakata, and H. Farrar IV, "Helium Generation Cross Sections for 14.8-MeV Neutrons, in Damage Analysis and Fundamental Studies, Quarterly Progress Report October-December 1981, DOE/ER-0046/8, Vol 1, U.S. Department of Energy, 31 (1982).

7.0 Future Work

A new RTNS-II irradiation is in planning, to measure the total helium production cross sections of new materials (e.g., N, Mg, W) at 14.8 MeV.

8.0 Publications

None.

HELIUM PRODUCTION IN REACTOR-IRRADIATED COPPER

D. W. Kneff, B. M. Oliver, and R. P. Skowronski (Rockwell International)

1.0 Objective

The objectives of this work are to apply helium accumulation neutron dosimetry to the measurement of neutron fluences and energy spectra in mixed-spectrum fission reactors utilized for fusion materials testing, and to measure helium generation rates of materials in these irradiation environments.

2.0 Summary

Helium generation measurements have been performed for copper samples irradiated in the High Flux Isotopes Reactor (HFIR) experiments CTR30 and CTR32, and in the Oak Ridge Research Reactor (ORR) experiment MFE4B. The high measured helium concentrations in the CTR30 samples (up to 81 appm) provide further evidence for the recently identified thermal three-stage reaction process in copper.

3.0 Program

Title: Helium Generation in Fusion Reactor Materials
Principal Investigators: D. W. Kneff and H. Farrar IV
Affiliation: Rockwell International

4.0 Relevant DAFS Program Plan Task/Subtask

Task II.A.1	Fission Reactor Dosimetry
Task II.A.4	Gas Generation Rates
Subtask II.A.5.1	Helium Accumulation Monitor Development

5.0 Accomplishments and Status

Helium generation measurements have been performed for copper samples irradiated in HFIR as part of experiments CTR30 and CTR32, and in ORR as part of experiment MFE4B. These measurements are part of a joint Rockwell-Argonne National Laboratory (ANL) program to measure total helium production rates over the range of fission reactor neutron spectra and fluences used for fusion materials testing, and to use the results to integrally test helium production cross section evaluations used in damage calculations. The present measurements were performed to extend the data base for helium generation in reactor-irradiated copper at high neutron fluences. The results will be used in the determination of those spectrum-integrated cross sections needed to predict helium generation in copper at high fluences from the thermal three-stage reaction process.(1)

The copper samples were irradiated in HFIR and ORR as bare wire segments, and were used for both helium accumulation and radiometric dosimetry measurements (the latter at ANL). The samples were etched following irradiation, to remove any helium recoil effects, and then segmented before helium analysis. The helium analyses were performed by high-sensitivity isotope-dilution gas mass spectrometry,(2) and included duplicate analyses for each sample location. Selected samples from each irradiation were also analyzed for ^{3}He, which is formed from the decay of tritium often found in reactor environments. The ^{3}He concentration in each case was measured to be less that 2 appb (10^{-9} atom fraction). The absolute uncertainty in each ^{4}He analysis was ±1-2%.

TABLE 1

HELIUM PRODUCTION MEASUREMENTS FOR COPPER IRRADIATED IN HFIR AND ORR

Experiment	Sample	Core Height(a) (cm)	Thermal Fluence (10^{22} n/cm^2)	^{4}He Concentration Measured (appm)(b)	Calculated(c) (appm)(b)	Calculated / Measured (C/E)
HFIR-CTR30	Cu-1	+21.86	3.36	24.1	6.17	0.26
	Cu-3	+ 5.20	6.12	81.3	11.32	0.14
	Cu-5	-11.46	4.96	52.4	10.01	0.19
HFIR-CTR32	Cu-1	+21.86	0.84	2.50	1.58	0.63
	Cu-5	-11.46	1.24	4.54	2.57	0.57
ORR-MFE4B	Cu-3	-13.64 inner	0.56	2.03	1.37	0.67
	Cu-4	-13.64 outer	0.61	1.99	1.38	0.69

(a) Distance above core midplane
(b) Atomic parts per million (10^{-6} atom fraction)
(c) L. R. Greenwood, Refs. 3-5. These calculations include helium production from fast-neutron reactions only.

The analyzed samples are listed in Table 1. Table 1 also gives their irradiation locations, measured helium concentrations, and comparisons between the measurements and predictions. The predictions, based on calculations by L. R. Greenwood(3-5) using ENDF/B-V cross section evaluations, include only fast-neutron helium production. Samples from Experiment CTR30 were exposed to the highest neutron fluences of any mixed-spectrum reactor samples measured to date, and exhibit significantly higher helium concentrations than previously measured copper samples.(1) Comparison of the calculated/experimental (C/E) ratios for these samples (Table 1, Column 7) demonstrates the significant increase in helium production rate at high fluences. The large discrepancy in the C/E values is attributed primarily to helium production from the three-stage reaction process

$$^{63}\mathrm{Cu}(n,\gamma)^{64}\mathrm{Cu} \longrightarrow {}^{64}\mathrm{Zn}(n,\gamma)^{65}\mathrm{Zn}(n,\alpha)^{62}\mathrm{Ni}$$

with thermal neutrons.(1) The present measurements are consistent with the copper helium concentration measurements summarized in the previous DAFS report,(1) for copper samples irradiated to different fluences in other mixed-spectrum reactor experiments, and provide further evidence for the three-stage reaction mechanism.

The present results, plus the previously-reported results, and additional data developed at ANL, are being used in a joint Rockwell-ANL effort to determine a consistent set of spectrum-integrated cross sections for both thermal- and fast-neutron helium production in copper. These results can then be used to obtain more accurate predictions of helium generation in reactor-irradiated copper at high neutron fluences.

6.0 References

1. D. W. Kneff, B. M. Oliver, R. P. Skowronski, and L. R. Greenwood, "Helium Production in Reactor-Irradiated Copper and Titanium, and Evidence for a Copper Three-Stage Reaction," in Damage Analysis and Fundamental Studies, Quarterly Progress Report October-December 1984, DOE/ER-0046/20, U.S. Department of Energy, 13 (1985).

2. B. M. Oliver, J. G. Bradley, and H. Farrar IV, "Helium Concentration in the Earth's Lower Atmosphere," Geochim. Cosmochim. Acta, 48, 1759 (1984).

3. L. R. Greenwood, "Fission Reactor Dosimetry - HFIR - CTR 31, 32, 34, and 35," in Damage Analysis and Fundamental Studies, Quarterly Progress Report April-June 1983, DOE/ER-0046/14, U.S. Department of Energy, 9 (1983).

4. L. R. Greenwood and R. K. Smither, "Dosimetry Measurements and Damage Calculations for the ORR-MFE4B Experiment," in Damage Analysis and Fundamental Studies, Quarterly Progress Report April-June 1984, DOE/ER-0046/18, U.S. Department of Energy, 5 (1985).

5. L. R. Greenwood, "Fission Reactor Dosimetry," in Damage Analysis and Fundamental Studies, Quarterly Progress Report January-March 1985, DOE/ER-0046/21 (this volume), U.S. Department of Energy (1985).

7.0 Future Work

A joint Rockwell-ANL effort is in progress to determine the spectrum-integrated cross sections for the reactions $^{64}Cu(n,\gamma)$, $^{65}Zn(n,\alpha)$, $^{65}Zn(n,\gamma)$, and $^{63}Cu(n,\alpha)$. The results will provide a basis for more accurate predictions of helium production in copper samples irradiated to high neutron fluences in mixed-spectrum reactors.

8.0 Publications

A paper entitled "Helium Production in Copper by a Thermal Three-Stage Reaction," by D. W. Kneff (Rockwell), L. R. Greenwood (ANL), B. M. Oliver, and R. P. Skowronski (Rockwell), will be presented at the International Conference on Nuclear Data for Basic and Applied Science, in Santa Fe, New Mexico in May 1985.

CHAPTER 3

REDUCED ACTIVATION MATERIALS

NEUTRON-INDUCED SWELLING OF Fe-Cr-Mn TERNARY ALLOYS

F. A. Garner and H. R. Brager (Hanford Engineering Development Laboratory)

1.0 Objective

The object of this effort is to determine those factors which control the swelling of alloy systems which have the potential for reduced activation.

2.0 Summary

It appears that the swelling of Fe-Cr-Mn alloys is remarkably insensitive to both irradiation temperature (420-600°C) and composition. The slight dependence of macroscopic swelling on manganese content is thought to be primarily the consequence of a composition-dependent densification, possibly associated with radiation-induced spinodal decomposition in the Fe-Cr-Mn Invar regime. The steady-state swelling rate of these alloys appears to be ∿1%/dpa.

3.0 Program

Title: Irradiation Effects Analysis (AKJ)
Principal Investigator: D. G. Doran
Affiliation: Hanford Engineering Development Laboratory

4.0 Relevant DAFS Program Plan Task/Subtask

Subtask II.C.1 Effects of Material Parameters on Microstructure

5.0 Accomplishments and Status

5.1 Introduction

In a previous report(1) it was shown that the swelling of simple Fe-Mn binary and Fe-Mn-Cr ternary alloys in FFTF-MOTA at 520°C and ∿14 dpa is remarkably insensitive to the chromium level and only weakly dependent on the manganese level as shown in Figure 1a. Figure 1b shows that this behavior is quite different from that of Fe-Cr-Ni alloys which are strongly sensitive to both chromium and nickel for comparable irradiation conditions.

Additional immersion density data are now becoming available for this irradiation series. The portion of the data matrix that is now complete leads us to revise somewhat our earlier conception of the parametric dependency of swelling in the Fe-Cr-Mn system.

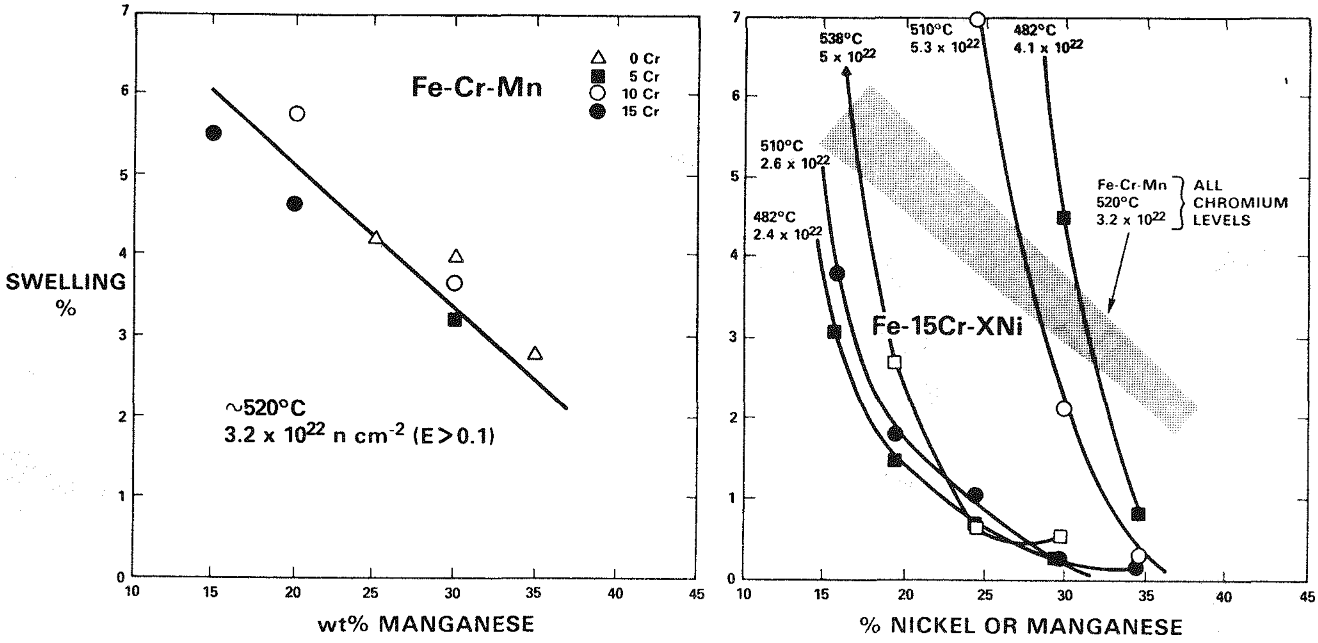

FIGURE 1. Comparison between neutron-induced swelling in Fe-Cr-Mn and Fe-Cr-Ni alloys.(1)

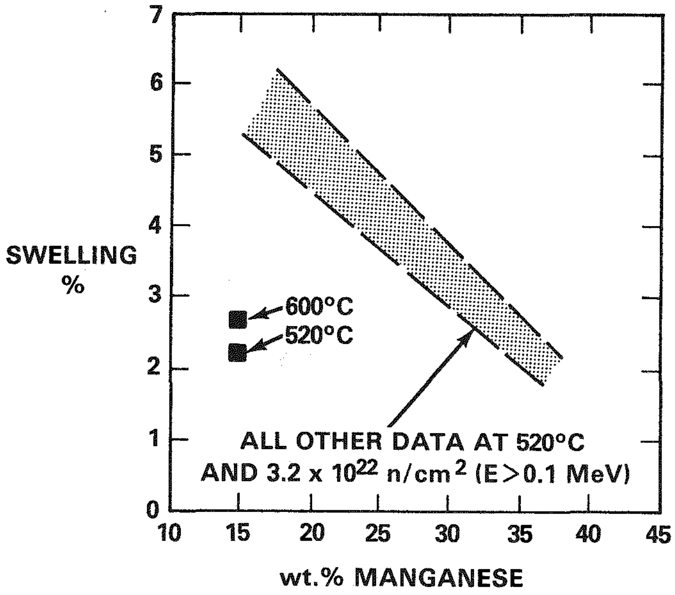

FIGURE 2. Comparison of new data on swelling of Fe-5Cr-15Mn at 14 dpa and the trend of previously published data for other Fe-Cr-Mn alloys at 520°C and 14 dpa.

5.2 New Data

Figure 2 shows that the swelling data of one alloy, Fe-5Cr-15Mn, does not fit the behavior typical of the other previously reported alloys irradiated at 520°C and 14 dpa. At 600°C and 14 dpa essentially the same swelling is observed for this alloy, however, which leads us to speculate that irradiation above 500°C has caused some relatively temperature-independent phase evolution for this alloy that is different from that of the others. Figure 3 shows that, with the exception of Fe-5Cr-15Mn, all other alloys exhibit after irradiation at 600°C and 14 dpa essentially the same swelling as observed at 520°C and 14 dpa. This implies that there is little or no dependence of swelling on temperature in the range 520-600°C. It is desired to check whether the independence of temperature extends as low as 420°C but unfortunately the data at 420°C exist only at 9 dpa, as is also shown in Figure 3. Note that at 420°C most of the specimens 'densify' but that rather large densifications are exhibited at the higher manganese levels.

At this point we can borrow from our experience on Fe-Cr-Ni alloys and remember that at low temperature there is usually no temperature dependence of swelling and thus we can plot the data ignoring the temperature.(2,3) Note in Figure 4 that we can draw lines between (420°C, 9 dpa) data and (520°C, 14 dpa) data for each alloy and that each line exhibits a slope of ~1%/dpa. This apparent swelling rate is identical to that observed for all other austenitic alloys in the post-transient regime.(2)

The densification shown in Figures 3 and 4 tends to imply that much of the previously observed composition dependence of post-irradiation density change is a reflection of a process other than void swelling. Therefore the composition dependence of swelling in the Fe-Cr-Mn system appears to be even less than previously reported.(1)

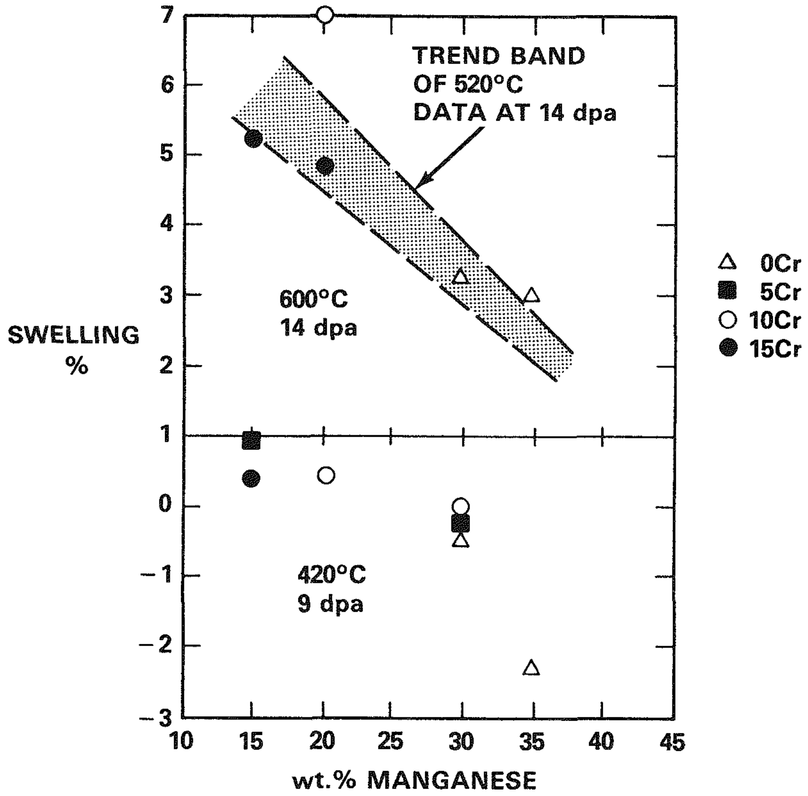

FIGURE 3. New data showing swelling of Fe-Cr-Mn alloys and 420°C and 600°C. Some alloys densify at 420°C.

5.3 Discussion

The alloys irradiated in this experiment were selected to explore the possibility that a correlation exists between anomalous Invar properties and swelling resistance.(4) Since the Fe-Cr-Mn system also exhibits Invar behavior in the range around 35% Mn(5,6,7) it was thought that there might be some advantage to developing low activation austenitic alloys which contain manganese levels of this magnitude.

Just as radiation-induced spinodaling is a consequence of the same metastability that produces anomalous properties in the Fe-Cr-Ni Invar regime, it is suggested that spinodaling also occurs in the Fe-Cr-Mn Invar regime. In order to quickly and almost completely destroy the compositional and temperature dependence of swelling, however, spinodal decomposition in the Fe-Cr-Mn system must occur faster than it does in the Fe-Cr-Ni system. The densification of 2.2% observed in Fe-35Mn is much larger than the 0.9% that occurs in the Fe-Ni-Cr system.(8) This implies a much larger driving force in the Fe-Cr-Mn

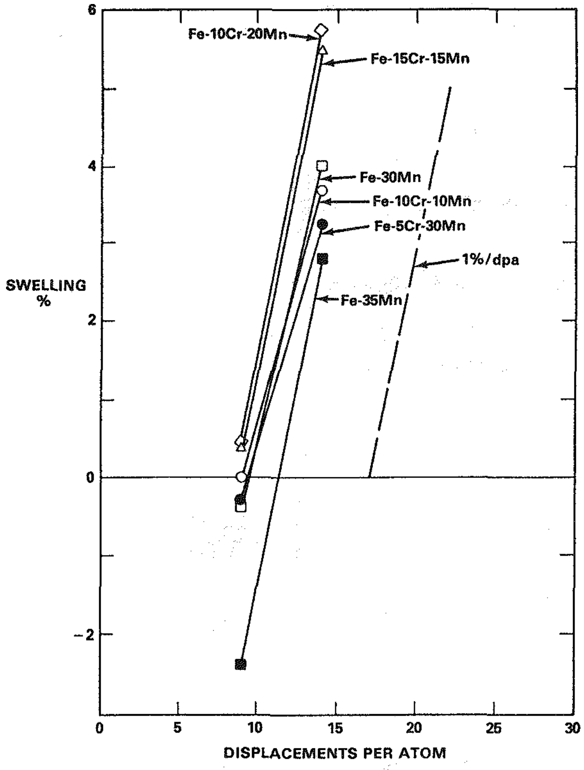

FIGURE 4. Plot of Fe-Cr-Mn swelling data assuming independence of swelling on temperature between temperatures of 420 and 520°C.

system. Figure 5 indeed shows that the rate of change with manganese content of pre-irradiation density of Fe-Cr-Mn alloys below 35% manganese is very large. If the density again rises steeply above 35% manganese, spinodal decomposition could indeed lead to a very substantial densification and a large driving force.

5.4 Conclusions

There does not appear to be any advantage to be gained at higher (>20%) manganese contents in terms of the intrinsic swelling resistance of simple Fe-Cr-Mn alloys. However, this conclusion may not apply to the solute-modified Fe-Cr-Mn alloys which have not yet been examined. If radiation-induced spinodal decomposition is causing both large densifications and the destruction of the swelling resistance, then the study of the differences between Fe-Cr-Mn and Fe-Cr-Ni Invar alloys may lead to clues as to how to suppress the spinodal process and extend the incubation period of swelling. Therefore examination of the Fe-Cr-Mn Invar alloys will continue despite the initially unsuccessful application of the Invar-swelling resistance correlation to the simple Fe-Cr-Mn system.

6.0 References

1. H. R. Brager and F. A. Garner, "Swelling of Fe-Cr-Mn Ternary Alloys in FFTF," DAFS Quarterly Progress Report, DOE/ER-0046/19, November 1984, 31-33.

2. F. A. Garner, J. Nucl. Mater., 122 & 123 (1984) 459-471.

3. F. A. Garner, "Application of High Fluence Fast Reactor Data to Fusion-Relevant Materials Problems," this volume.

4. H. R. Brager and F. A. Garner, "Fundamental Alloy Studies," DAFS Quarterly Progress Report, DOE/ER-0046/17, May 1984, 93-101.

5. Y. Endoh, Y. Noda and M. Iizumi, J. Phys. Soc. Japan, 50, No. 2 (1981), 469-475.

6. O. G. Sokolov and A. I. Mel'ker, Soviet Physics-Doklady, 9, No. 1, (1965), 1019-1021.

7. O. A. Khomenko and I. F. Khil'kevich, Met. Term. Obra. Met. 6 (1982), 42-44.

8. H. R. Brager and F. A. Garner, "Swelling of Fe-Ni-Cr Ternary Alloys at High Exposure," DAFS Quarterly Progress Report, DOE/ER-0046/16, Feb. 1984, 38-45.

7.0 Future Work

Density change data will continue to be accumulated on ternary and solute-modified Fe-Cr-Mn alloys. A series of Fe-Cr-Mn-Ni alloys is also being prepared for irradiation in FFTF-MOTA.

8.0 Publications

None.

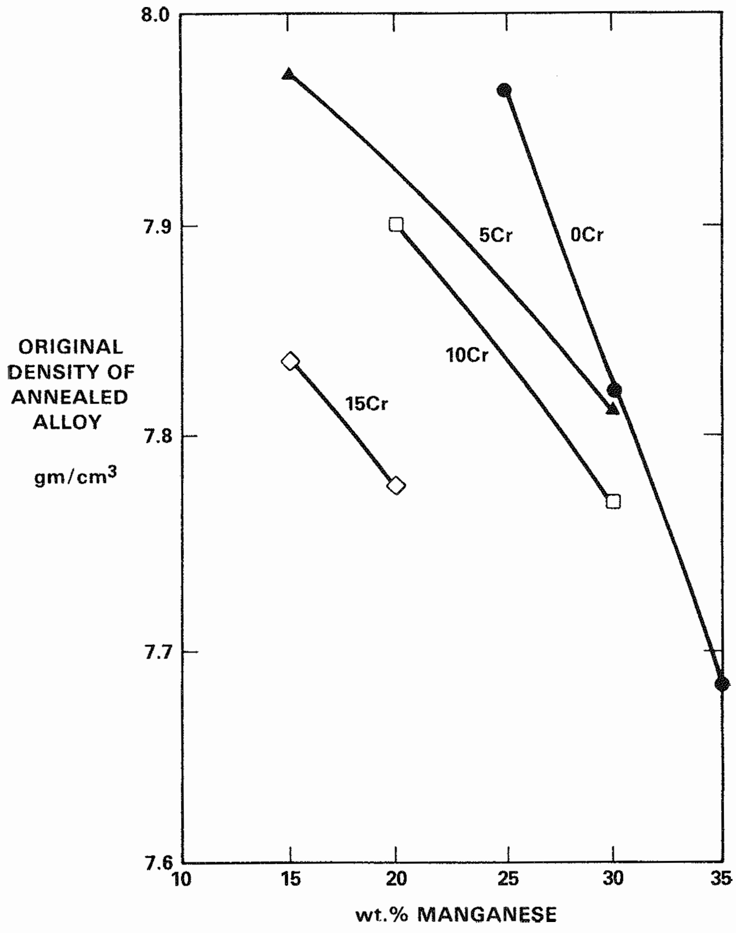

FIGURE 5. Dependence of pre-irradiation density on composition for annealed Fe-Cr-Mn alloys.

FUNDAMENTAL IRRADIATION STUDIES ON VANADIUM ALLOYS

B. A. Loomis (Argonne National Laboratory), F. A. Garner and A. M. Ermi (Hanford Engineering Development Laboratory)

1.0 Objective

The object of the effort is to study the response of simple vanadium alloys to fast reactor irradiation and thus provide a basis for the development of vanadium alloys which are suitable for fusion reactor service and which will also exhibit reduced long-term radio-activation.

2.0 Summary

A joint experiment on the irradiation response of simple vanadium alloys has been initiated under the auspices of the DAFS and BES programs. Specimen fabrication is nearly complete and the alloys are expected to be irradiated in lithium in FFTF-MOTA Cycles 7 and 8.

3.0 Program

Title: Irradiation Effects Analysis (AKJ)
Principal Investigator: D. G. Doran
Affiliation: Hanford Engineering Development Laboratory

4.0 Relevant DAFS Program Plan Task/Subtask

Subtask II.C.1 Effects of Material Parameters on Microstructure

5.0 Accomplishments and Status

5.1 Introduction

Three commercial vanadium-base alloys (V-15Cr-5Ti, Vanstar-7 and V-3Ti-1Si) are currently being irradiated in the FFTF fast reactor in the Materials Open Test Assembly (MOTA).(1) In order to determine the role of each elemental constituent in the phase stability and irradiation response of these alloys, a joint experiment between the DAFS and BES (Basic Energy Science) programs has been initiated.

This experiment will use a series of simple alloys produced earlier in the BES program. No helium will be added to these alloys. Specimens will be primarily in the form of TEM disks although miniature SS-3 tensile specimens will also be irradiated for some of these alloys. Irradiation under static lithium in TZM capsules is planned for Cycles 7 and 8 in FFTF-MOTA. In this experiment three capsules are designated as DAFS/BES capsules. Two of these are at level 2 in MOTA (420° and 600°C) accumulating ∿26 dpa/year and one is at level 1 (520°C) at ∿14 dpa/year. In addition other specimen subsets will be included in the HEDL ADIP capsules in levels 1, 2 and 5. These capsules will also contain one-third size Charpy specimens constructed from V-15Cr-5Ti.

5.2 Alloy Descriptions

The alloys can be categorized in the following subsets.

Vanadium Impurity Series: These alloys study the effects of impurity levels and variations in relative amounts of major impurities (carbon, oxygen, nitrogen).

Vanadium-Chromium Series: Ion bombardment data already exist for these alloys which contain chromium levels of 10, 15 and 20%. In addition to phase stability and swelling data, this subset of specimens will provide a correlation between ion and neutron irradiation behavior in a simple vanadium alloy system.

Vanadium-Titanium Series: Ion bombardment experiments on this alloy series are currently in progress. In addition to providing a neutron-ion correlation it is desired to determine the composition of the precipitates that form before and during irradiation.

Vanadium-Other Solute Series: In addition to chromium and titanium, three other solutes were chosen (Ni, W, Mo) to provide a range of elements varying from slow to fast-diffusing species. Both solute segregation and the diffusion relationship to swelling and other property changes will be studied.

V-15Cr-xTi and V-Cr-Ti-Zr Series: These alloys will be used to study the interplay between titanium's role in both fabricability and swelling and also to study the consequences of total or partial substitution of zirconium for titanium.

Reference Alloy Series: The three ADIP alloys described earlier will be included for comparison with the results of on-going ADIP studies.

5.3 Status of Experiment

All of the alloys shown in Table 1 have been prepared as TEM disks and delivered to HEDL for engraving and encapsulation. A total of 546 disks is currently available for irradiation. Some alloys (V-20Cr, V-Cr-Ti-Zn series) are still being prepared. Preparation of miniature tensile specimens is also in progress.

6.0 References

1. A. M. Ermi, "FFTF Fusion Irradiations-FFTF Cycles 4-6," Alloy Development for Irradiation Performance Semiannual Progress Report for Period Ending September 30, 1984, DOE/ER-0045/13 p. 21.

7.0 Future Work

Preparation of tensile specimens will continue.

8.0 Publications

None.

TABLE 1

Vanadium-Base Alloys for Irradiation in FFTF

Reference No.	Alloy Composition	Facility	DAFS	ADIP	ADIP	ADIP	ADIP	DAFS	ADIP	ADIP	ADIP	DAFS	Total No.	Primary Purpose for Irradiation
		Temp.(^{o}C)	420	420	420	420	420	520	520	600	600	600		
		DPA	26	26	26	52	78	14	28	10	30	78		
			Number of 3-mm Discs in Irradiation Facility											
BL-1	V-2.5Mo		2		3	2	2	2	2	2	2	2	19	Solid state parameters for swelling and solute segregation
BL-2	V-8.5W		2		3	5	5	2	2	2	2	2	25	Solid state parameters for swelling and solute segregation
BL-3	V-10Ni		2		3	2	2	2	2	2	2	2	19	Solid state parameters for swelling and solute segregation
BL-4	V-10Cr		2		3	2	2	3	2	2	2	2	20	Neutron/ion comparison
BL-5	V-15Cr		5					1	2	2	2	2	14	Neutron/ion comparison
BL-8	V-20Ti-5Y			2					2	2	2		8	Corrosion; surface spallation
BL-10	V-15Ti-7.5Cr		5			5	5	3	2	2	2	2	26	DBTT; swelling; candidate alloy
BL-11	V-5Ti-0.13O_2		3			3	3	2	2	2	2	2	19	DBTT; precipitates; high O_2
BL-12	V-10Ti-0.13O_2		3			3	3	2	2	2	2	2	19	DBTT; precipitates; high O_2
BL-13	V-15Ti-0.13O_2		3			3	3	2	2	2	2	2	19	DBTT; precipitates; high O_2
BL-15	V-20Ti			3				3	2	2	2	2	14	High O, N, C; DBTT; candidate alloy; precipitates
BL-16	V-20Ti		5			5	5		2	2	2	2	23	Low O, N, C; DBTT; candidate alloy; precipitates
BL-19	V				3				2	2	2	2	11	Neutron/ion comparison; high O, N, C
BL-20	V		5			5	5	3	2	2	2	2	26	Neutron/ion comparison; low O, N, C
BL-21	V-15Cr-5Ti		3	2		5	5		2	2	2	5	26	Reference alloy; O, N, C level; neutron/ion comparison; DBTT
BL-22	V-15Cr-5Ti		5			5	5		2	2	2	5	26	Reference alloy; O, N, C level; neutron/ion comparison; DBTT
BL-23	V-15Cr-5Ti		5			5	5		2	2	2	5	26	Reference alloy; O, N, C level; neutron/ion comparison; DBTT
BL-24	V-15Cr-5Ti		5			5	5	3	2	2	2	5	29	Reference alloy; O, N, C level; neutron/ion comparison; DBTT
BL-25	V-15Cr-0.3Ti		5						2	2	2	2	13	Fabricability; swelling; neutron/ion comparison; DBTT
BL-26	V-15Cr-1Ti		5			5	5	1	2	2	2	2	24	Fabricability; swelling; neutron/ion comparison; DBTT
BL-27	V-3Ti-1Si		5			5	5	3	2	2	2	5	29	Candidate alloy; corrosion resistance; DBTT
BL-28	VANSTAR-7		5			5	5	1	2	2	2	2	24	Candidate alloy; swelling; DBTT
BL-34	V-5Ti		5		1	5	5	3	2	2	2	2	27	Precipitates; low O, N, C; DBTT
BL-35	V-10Ti		2		3	5	5	3	2	2	2	2	26	Precipitates; low O, N, C; DBTT
BL-37	V-15Cr-5Ti(20%CW)			2	2	5	5	3	4	4	4	5	34	Thermo-mechanical; DBTT; neutron/ion comparison
											Total		546	

CHAPTER 4

FUNDAMENTAL MECHANICAL BEHAVIOR

YIELD STRESS DETERMINATION FROM MINIATURIZED DISK BEND TEST DATA

D. S. Sohn, G. Kohse and O. K. Harling (Massachusetts Institute of Technology)

1.0 Objective

The research described was aimed at establishing an analysis methodology for estimating yield stress from bend test data of 3.0 mm diameter by 0.25 mm thick disks.

2.0 Summary

Methodology for testing 3.0 mm diameter by 0.25 mm thick disks by bending in a punch and die has been described previously. This paper describes the analysis of load/deflection data from such miniaturized disk bend tests (MDBT) using a finite element simulation. Good simulation has been achieved up to a point just beyond the predominantly elastic response, linear initial region. The load at which deviation from linearity begins has been found to correlate with yield stress, and yield stress has been successfully extracted from disk bend tests of a number of known materials. Although finite element codes capable of dealing with large strains and large rotations have been used, simulation of the entire load/deflection curve up to fracture of the specimen has not yet been achieved.

3.0 Program

Title: Alloy Development for Irradiation Performance in Fusion Reactors
Principal Investigators: O. K. Harling and N. J. Grant
Affiliation: Nuclear Reactor Laboratory and Department of Materials Science and Engineering, Massachusetts Institute of Technology

4.0 Relevant DAFS Program Plan Task/Subtask

Task II.C.7	Effects of Helium and Displacements on Flow
II.C.8	Effects of Helium and Displacements on Fracture
II.C.9	Effects of Hydrogen on Fracture
II.C.10	Effects of Solid Transmutation Products on Fracture Behavior
II.C.11	Effects of Cascades and Flux on Flow
II.C.12	Effects of Cycling on Flow and Fracture
II.C.13	Effects of Helium and Displacements on Crack Initiation and Propagation
II.C.15	Effect of Near Surface Damage on Fatigue
II.C.19	Comparison of *In Situ* and Postirradiation Fracture Behavior

5.0 Accomplishments and Status

5.1 Introduction

Previous DAFS reports and other publications have described the MDBT experimental methodology.[1,2,3] A load/deflection curve is generated by bending the 3.0 mm diameter by 0.25 mm thick specimen in a punch and die. The punch and die geometry of the MIT version of the MDBT is such that fracture is achieved even in ductile materials. It should be possible, as discussed in References 1-3, to extract such data as yield stress, ultimate tensile stress, and elongation to fracture by comparing experimental load/deflection curves to simulation curves generated by the finite element code ABAQUS.[4] A first step toward this goal has been achieved through successfully simulating the initial portion of the load/deflection curve. The basis of this yield stress estimation method and an indication of the accuracies achieved with a range of test materials are briefly described here. Full details are available in Reference 5. Progress toward simulating the load/deflection curve up to the onset of fracture is also briefly summarized.

5.2 Yield Stress Estimation

As has been extensively discussed elsewhere,[1-3,5] the load/deflection curve of the MDBT has an initial region which is dominated by elastic deformation of the disk, as demonstrated by load/unload tests and confirmed by finite element stress/strain calculations. Figure 1 shows the linear regime for a ductile material, and also indicates the accuracy of finite element simulation which has been achieved. (Known material properties were input to the finite element code for this comparison.) Once eight to ten punch/specimen finite element nodes are in contact, the finite element solution falls within the envelope of the experimental curve, and continues to do so beyond the point of deviation from linearity. The load at measurable deviation from linearity has been termed the "yield load."

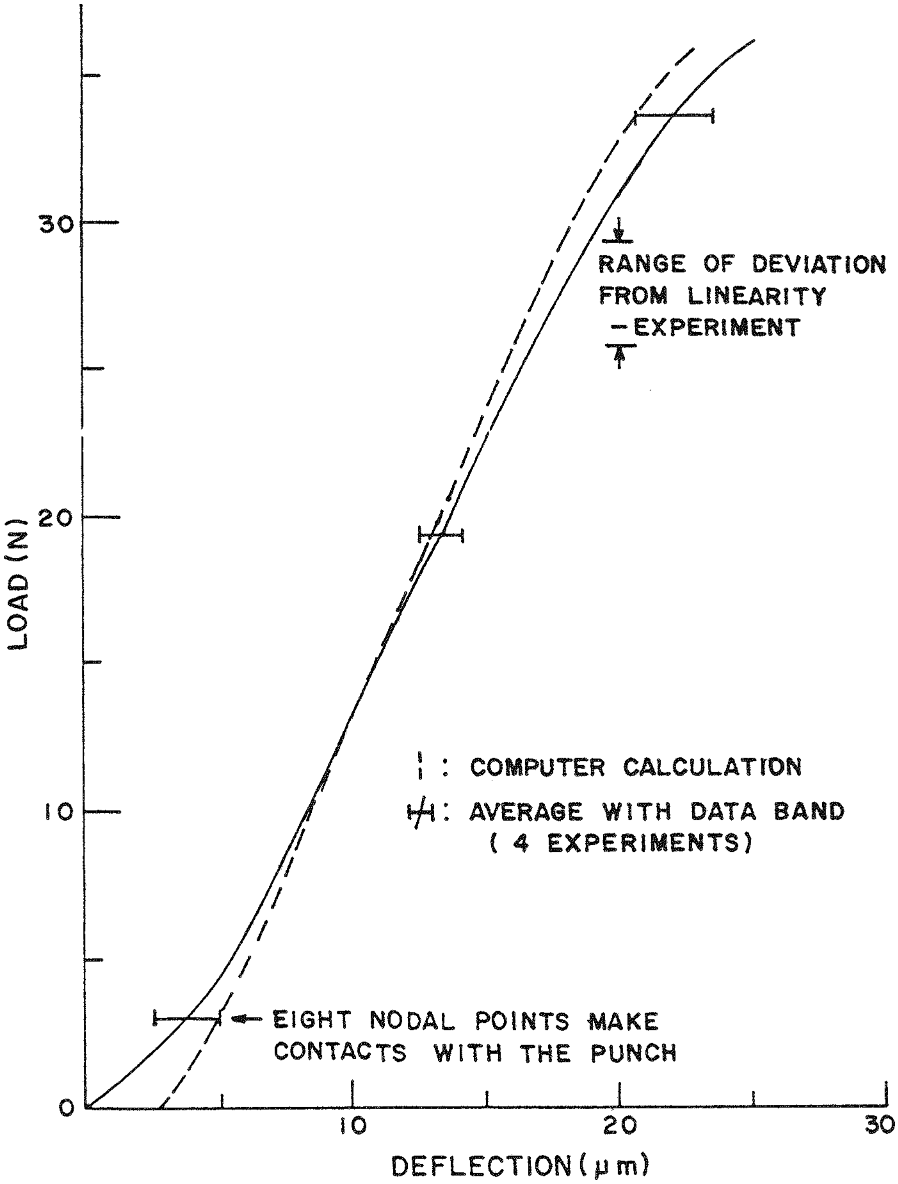

FIGURE 1. Comparison of a computer generated load/deflection curve with the results of four MDBT experiments for a Cu-Ni alloy at room temperature. Data from uniaxial tensile tests was used for the computer calculation.

Although a small fraction (~1%) of the disk volume has experienced plastic deformation by the time the yield load is reached, strain hardening behavior has been shown to have little effect on the yield load. In fact, yield load correlates strongly and monotonically, although non-linearly, with yield stress as shown in Figure 2. It is therefore possible, by varying the yield stress input to the finite element simulation, to produce a simulated curve which matches any experimental curve up to the yield load. The yield stress input which produces a simulation yield load equal to the experimental yield load is a good estimate of the yield stress for an unknown material. In practice, the nature of the yield load/yield stress relationship permits interpolation between well-chosen cases, minimizing the amount of finite element simulation which is required. This is particularly true where, as in postirradiation testing for example, the elastic modulus of a material is known.

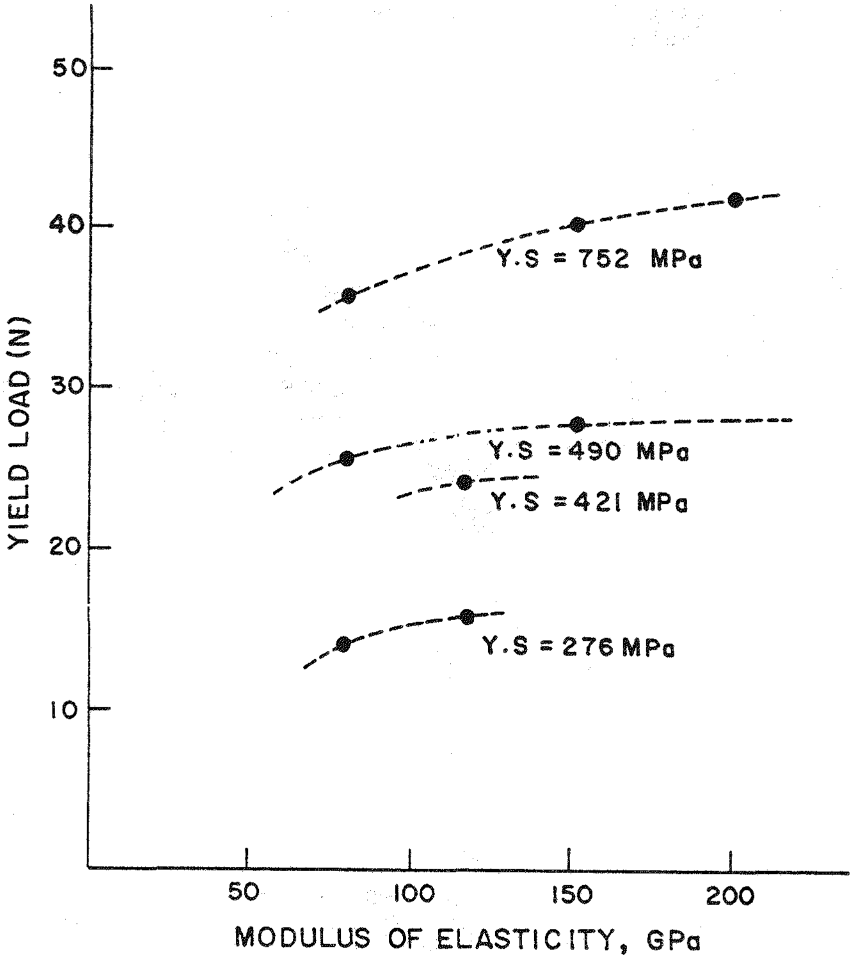

FIGURE 2. Dependence of yield load on yield stress and modulus of elasticity from computer simulations. The solid points represent cases calculated for interpretation of experimental curves.

Using this yield load simulation method and interpolating between six finite element simulation cases, yield stresses were estimated for a group of well-characterized materials. MDBT test specimens were cut from the undeformed ends of uniaxial tensile test specimens, and the MDBT estimated yield stresses are compared with the uniaxially determined values in Figure 3. Over this range of properties, the maximum difference between the MDBT test average and the uniaxial result is 10%.

5.3 Simulation to Fracture

Despite the application of a version of ABAQUS which is designed to accommodate large strains and large rotations, accurate simulation of the experimental curve up to the onset of fracture has not yet been achieved. A typical result is illustrated in Figure 4. Possible reasons for the discrepancy include

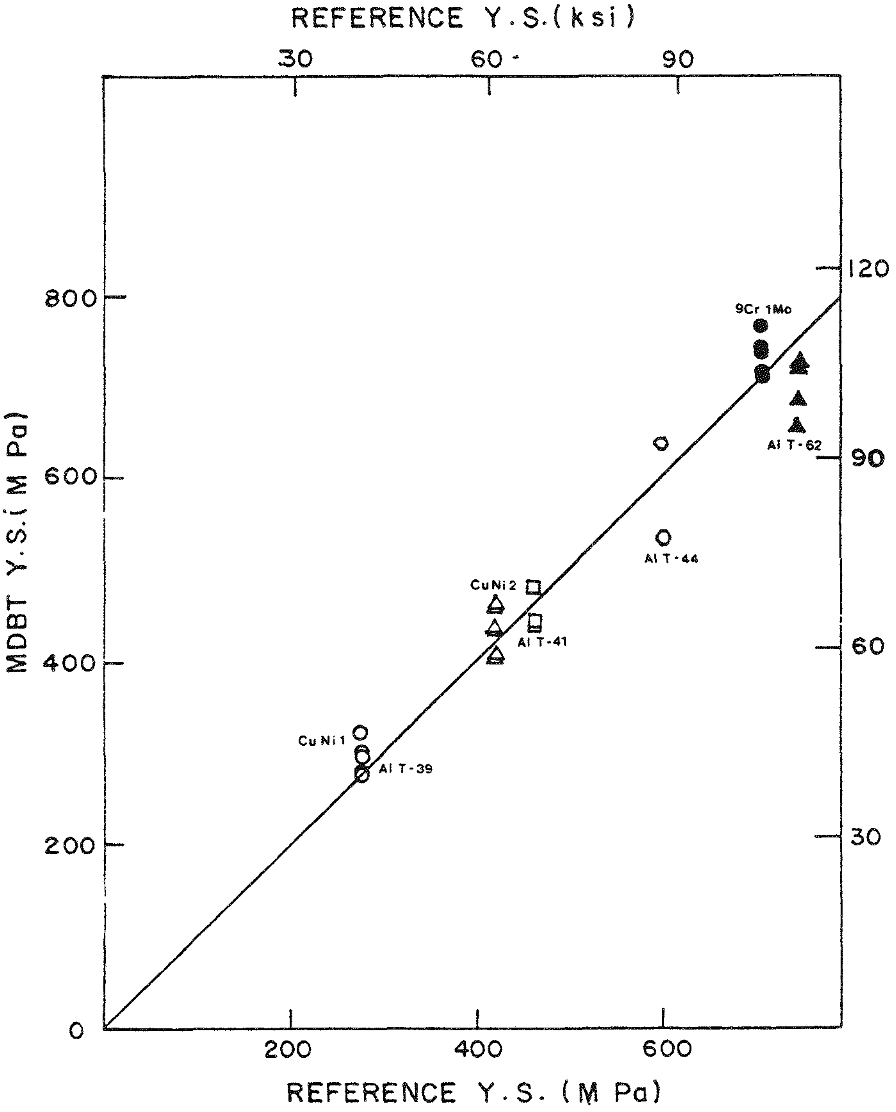

FIGURE 3. Comparison of MDBT-derived and uniaxial yield stress values for a number of alloys.

inadequacy of the boundary condition model and insufficient refinement of the finite element mesh in the region of the disk which undergoes pronounced deformation (thinning) in the later stages of the test. If the simulation can be improved, given that yield stresses can be obtained as described above, extraction of ultimate tensile strength and ductility information may be possible.

5.4 Summary

A method of extracting yield stress values from MDBT data has been described and has been shown to produce useful results over a range of material properties.

6.0 References

1. M. P. Manahan, A. S. Argon and O. K. Harling, "Mechanical Behavior Evaluation Using the Miniaturized Disk Bend Test," DAFS Quarterly Progress Report, DOE/ER-0046/8, Vol. 1, pp. 82-103, February 1982.

2. M. P. Manahan, "The Development of a Miniaturized Disk Bend Test for the Determination of Post-Irradiation Mechanical Behavior," Sc.D. Thesis, MIT, May 1982.

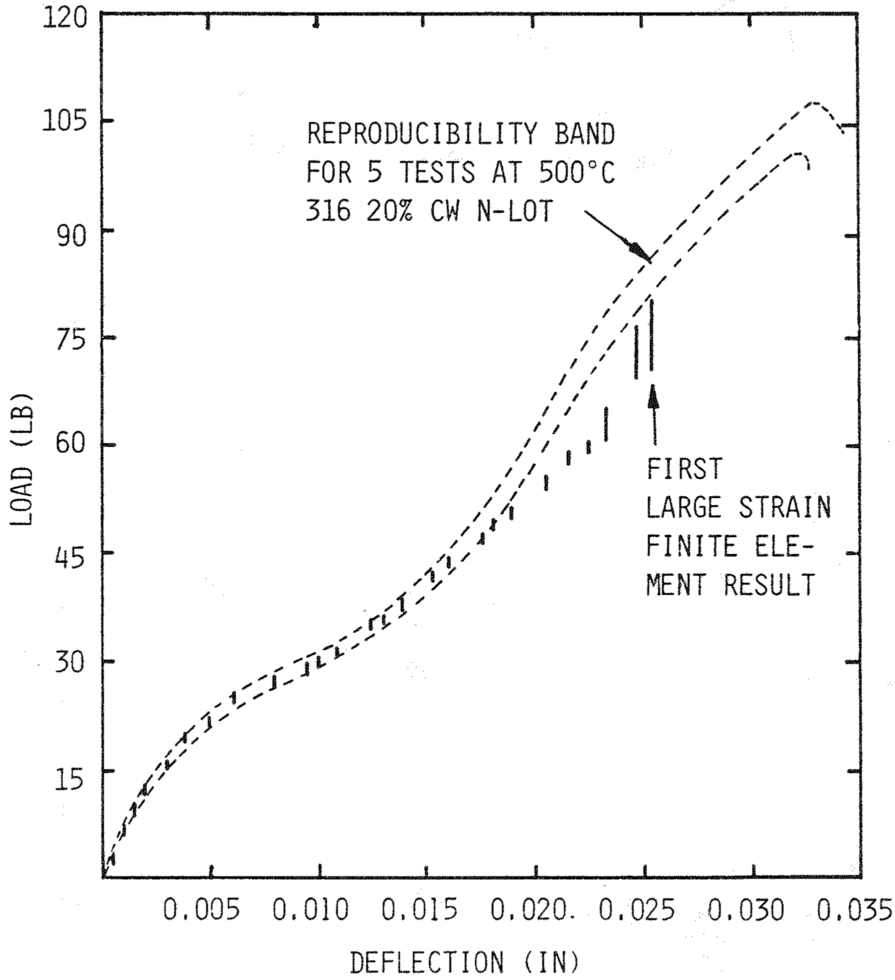

FIGURE 4. Comparison of experimental results and finite element simulation of MDBT test.

3. O. K. Harling, M. Lee, D. S. Sohn, G. Kohse and C. W. Lau, "The Miniaturized Disk Bend Test," presented at ASTM Symposium on the Use of Nonstandard Subsized Specimens for Irradiation Testing, Albuquerque, New Mexico, September 1983 (to be published).

4. ABAQUS was developed by Hibbitt, Karlsson and Sorensen, Inc., Providence, Rhode Island.

5. D. S. Sohn, "Further Development of the Miniaturized Disk Bend Test Approach for Post-Irradiation Mechanical Property Testing," Ph.D. Thesis, MIT, August 1984.

CHAPTER 5

RADIATION EFFECTS MECHANISMS AND CORRELATIONS

THE INFLUENCE OF THERMAL ANNEALING ON THE MICROSTRUCTURAL EVOLUTION IN HT-9 FERRITIC STEEL

J.J. Kai, G.L. Kulcinski and R.A. Dodd (University of Wisconsin-Madison)

1.0 Objective

The purpose of this study is to understand the microstructural evolution of the HT-9 ferritic steel under thermal effect. The results of this work will be used as a background to further investigate the heavy ion irradiation effects in HT-9 with and without helium preimplantation.

2.0 Summary

The as-received material and a set of thermal annealed specimens of HT-9 were carefully studied by using a JEOL-200CX II TEM/SCAN microscope equipped with x-ray EDS system. The dislocation density and the precipitate distribution and number density were studied by using conventional 3 mm TEM discs. The morphology, the crystal structure and the chemical composition of the precipitate were studied by utilizing a carbon extraction replica technique. The thermal annealed specimens were annealed in a temperature range between 300 and 900°C for 2 hrs and/or 24 hrs.

3.0 Program

Title: Radiation Effects to Reactor Materials
Principal Investigators: G.L. Kulcinski and R.A. Dodd
Affiliation: University of Wisconsin-Madison

4.0 Relevant DAFS Program Plan Task/Subtask

Subtask II.B.3.2 Experimental Characterization of Primary Damage State; Studies of Metals
Subtask II.C.1.1 Phase Stability Mechanics

5.0 Accomplishments and Status

5.1 Introduction

Ferritic steels are being considered as a candidate for the first wall structural material in a fusion reactor. HT-9 is one of the most attractive ferritic steels both in the mechanical strength and the swelling resistance under elevated temperature irradiation.

The present study is one in a series that intend to characterize the heavy ion irradiation effects in HT-9. Because of the complicated microstructure of HT-9, it is necessary to first understand the microstructure of as-received material and the microstructural evolution during thermal annealing without irradiation. Thereafter, the microstructure evolution induced (or enhanced) by irradiation can be addressed by examining the differences among the as-received condition, the thermal annealed condition, and the irradiated condition.

5.2 Experimental Procedures

5.2.1 Material and Annealing

The HT-9 ferritic steel used in this study has been described previously.[1] Two forms of specimen were prepared for the study. Several 3 mm discs were used for examining the microstructures under the transmission electron microscope and 5 mm × 10 mm foils were used for preparing carbon extraction replicas and for microhardness tests.

The specimens were mechanically polished with 0.3 μm Al_2O_3 powder. Thermal annealing was performed in a high vacuum furnace with a background pressure of 10^{-7} torr or lower. The temperature was measured by using two pairs of thermocouples which were attached to the specimen holder. The temperature measurements in all cases were within ±20°C.

5.2.2 Specimen Preparation and Analysis

The 3 mm TEM discs were electrothinned by utilizing a commercial twin-jet electropolisher with a solution of 10% $HClO_4$ and 90% ethanol at the condition of -20°C and 20 mA.

The carbon extraction replicas were produced from the foils by etching in a picral solution (1 gm picric acid + 100 ml ethanol + 5 ml hydrochloric acid) for about 30 seconds. The specimens were then coated with a thin layer of carbon film by using a carbon evaporator and re-etched in the same solution for about 10 minutes to loosen the carbides on the surface.

Both the carbon replicas and the TEM specimens were examined by using a JEOL-200CX II TEM/SCAN microscope operated at 200 KV. The x-ray energy dispersive spectra (EDS) were detected by a Si(Li) detector attached to the microscope and processed by a Tracor Northern TN-2000 system. Precipitate identification was done by combining the following information:

a. The crystal structure which is determined by the selected area diffraction pattern (SADP).
b. The qualitative EDS results.
c. The morphology of precipitate which is related to the results in (a) and (b).

The microhardness test was accomplished by using a Buehler Micromet microhardness tester. Every specimen was tested 20 spots at different areas and measured twice for each spot. The Vicker hardness number was obtained by using the average diagonal length of the indented spots.

5.3 Results

5.3.1 As-Received Material

The general TEM microstructure of as-received HT-9 is given in Fig. 1. A low magnification picture is shown in Fig. 1(a) which gives a rough idea of how complicated this material is in its original form. Figure 1(b), (c) and (d) are at three times higher magnification of certain specific regions in Fig. 1(a). The tempered lath martensite is the predominant phase in as-received HT-9, it occupies about 80% or more of the total volume of the material. The rest of the volume in HT-9 is equally divided by the heavily tempered carbide region and the ferrite region with some needle-like precipitates in it.

The dislocation density in HT-9 is always high. Figure 1 also indicates the high dislocation density in various regions. Figure 2 shows a well recovered region which still has a dislocation density about 1 x 10^{11} cm^{-2}. The dislocation density measurement is accomplished by using the $(\vec{g},3\vec{g})$ weak beam dark field (WBDF) technique. The specimen thickness is determined by examining an inclined dislocation running through the specimen from top to bottom and counting the number of segments of the dislocation in the matrix and also double checked by focusing the electron beam to produce a pair of contamination spots and measuring the distance between the two spots after tilting a large angle.

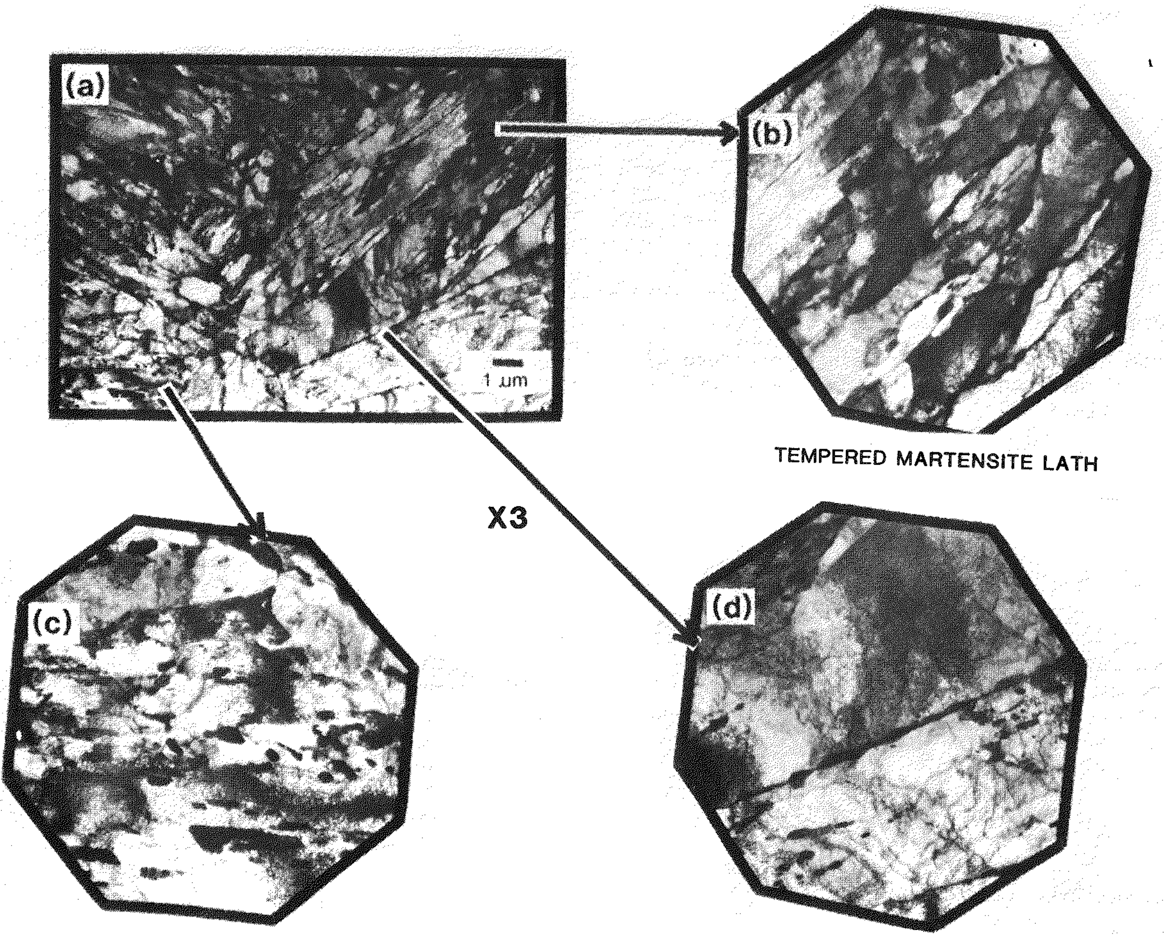

FIGURE 1. The general microstructure of as-received HT-9.

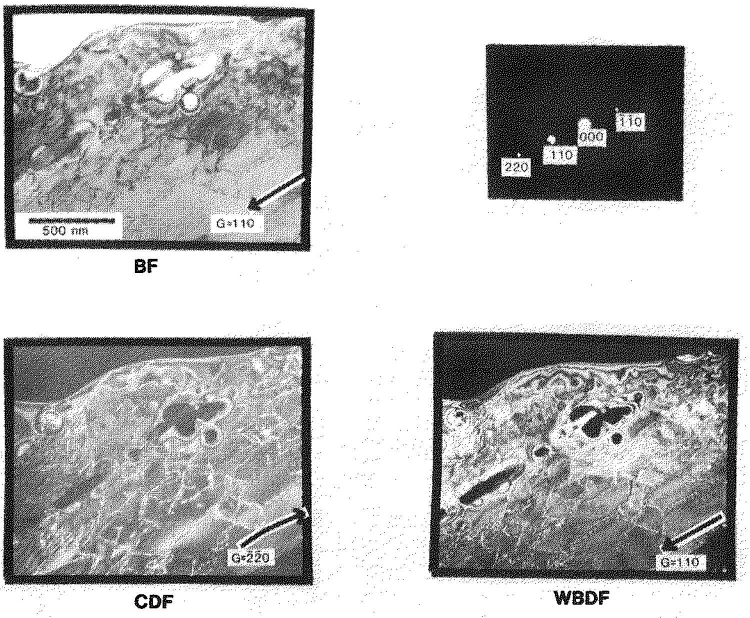

FIGURE 2. Dislocation density measurement in as-received HT-9.

In all, four types of precipitates were identified by the individual precipitate electron diffraction patterns and the x-ray EDS microanalysis. Figure 3 shows a carbon extraction replica which indicates the various precipitates and regions in HT-9.

The most predominant second phase in HT-9 is the equiaxed $M_{23}C_6$ particles which are distributed along the residual austenite grain boundaries and in the matrix. The size of this type precipitate varies from 0.1 µm to about 1.0 µm in diameter. The $M_{23}C_6$ phase has a complex fcc crystal structure with a lattice parameter of 1.062 nm. An example of an $M_{23}C_6$ particle in the matrix is shown in Fig. 4. Figure 5 shows a similar particle in a carbon replica. Both the bright field and dark field images and the diffraction patterns are shown as well as the qualitative EDS results. It is clearly shown that the $M_{23}C_6$ is Cr-enriched and also has noticeable Mo and W peaks. It is also found that the matrix does have a significant effect on the EDS results.[2] Therefore, for a more accurate quantitative EDS study, the carbon extraction replica must be used. Figure 6 shows the lattice image fringes of the {111} planes in an $M_{23}C_6$ particle that was protruding from the matrix at the edges of the hole in the HT-9 specimen.

The precipitates along the tempered martensite lath boundary, which had irregular elongated morphology, were also identified as $M_{23}C_6$. Although these precipitates have rather different morphology and composition with respect to the equiaxed $M_{23}C_6$ particles, the individual precipitate SADP shows that they are indeed the $M_{23}C_6$ phase. Figure 7 shows the phase both in the matrix and in the carbon extraction replica. The qualitative EDS result shows that this phase is enriched in Cr and V and depleted in Fe.

The third type precipitate, which can be easily distinguished from others, is the needle-like particles appearing in the ferrite region. The SADP shows that this phase is M_2X and has an hcp crystal structure with a_o = 0.27 nm, C_o = 0.44 nm. Figure 8 shows the morphology, the diffraction pattern, and the EDS result. This phase is highly enriched in Cr, therefore, it could be Cr_2N precipitate. The size of this type precipitate is about 0.2 µm to 1.0 µm long and 20 nm to 50 nm wide.

The fourth type precipitate is the MX phase (M = V, Cr and X = C, N). This type precipitate is characterized by thin plates and laths with edge dimensions from 50 nm to 300 nm.

The MX phase has an fcc crystal structure with a lattice parameter of 0.417 nm. Gelles and Thomas[3] reported this phase as a nitride in their neutron irradiation study. By using EELS (electron energy loss spectrometry), they found that this phase is (V,Cr)N with no carbon, oxygen or boron. However, in earlier thermal tempering study by Smith,[4] the V_4C_3 phase was a transient phase in a material that is quite similar to HT-9. At this time, the present authors would prefer to keep open the possibility that the MX phase could be both a nitride or a carbide. Figure 9 shows two MX precipitates with rather different chemical composition. Both of them are V and Cr enriched, but the one on the left hand side has a higher V peak and the one on the right hand side has a higher Cr peak. The total number density of all the precipitates in the as-received HT-9 ferritic steel is on the order of 10^{15} cm^{-3} or more. Most of them are equiaxed and irregular elongated $M_{23}C_6$ particles. The detailed quantitative studies of the precipitate number density, the volume fraction of each type precipitate, and the composition are underway.

5.3.2 Thermal Annealing Effects

A sequence of TEM micrographs that were taken from the various thermal annealed specimens and the relevant carbon extraction replicas are shown in Figs. 10-13. Figures 10 and 12 show the micrographs of the specimens annealed for 2 hrs. Figures 11 and 13 show the micrographics of the specimens annealed for 24 hrs. From the universal parameter equation for thermal annealing, P (Larson-Miller parameter) = T (20 + log t) x 10^{-3}, where t is the time in hours and T is the temperature in °K, it is clearly seen that the temperature has much greater effect than the time. In the following descriptions of the results, the thermal annealing effect is increased in the following order: (1) 300°C, 2 hrs (P = 11.6),; (2) 300°C, 24 hrs (P = 12.3); (3) 400°C, 2 hrs (P = 13.7); (4) 400°C, 24 hrs (P = 14.4); (5) 500°C, 2 hrs (P = 15.7); (6) 500°C, 24 hrs (P = 16.5): (7) 600°C, 2 hrs (P = 17.7); (8) 600°C, 24 hrs (P = 18.7); (9) 700°C, 2 hrs (P = 19.8);

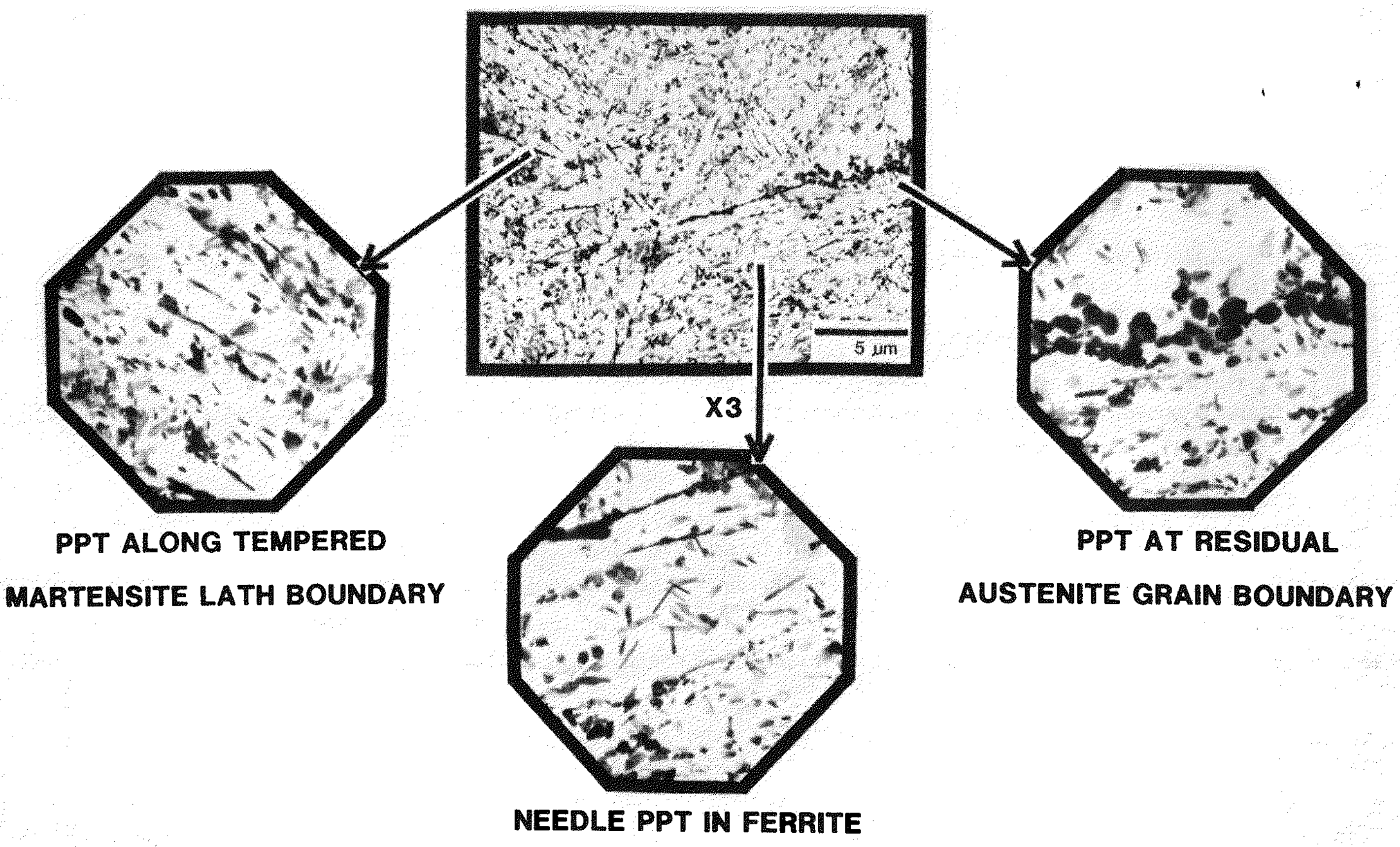

FIGURE 3. The carbon extraction replica shows the precipitate distribution in as-received HT-9.

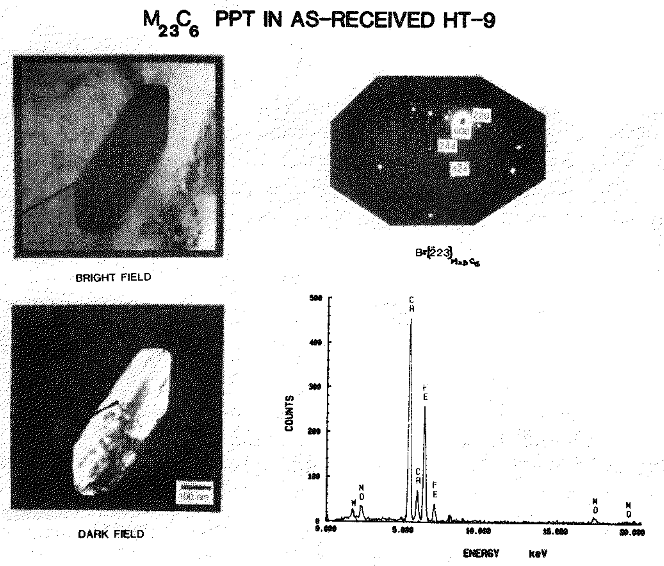

FIGURE 4. The $M_{23}C_6$ particle in HT-9 matrix.

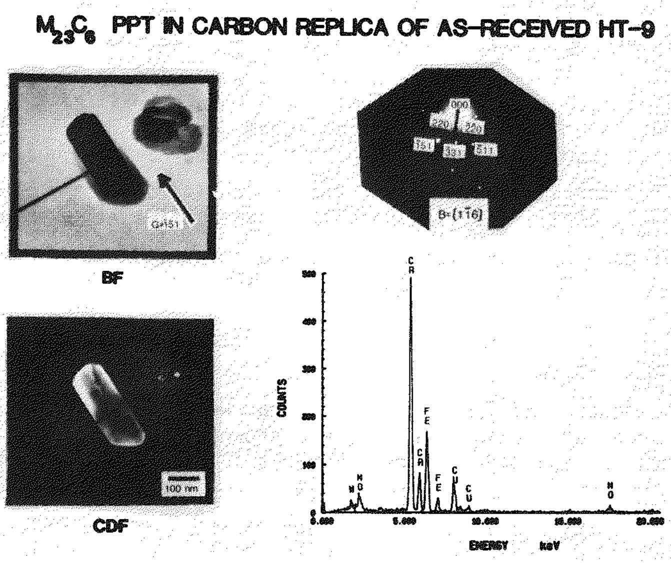

FIGURE 5. The $M_{23}C_6$ particle in the carbon extraction replica of as-received HT-9.

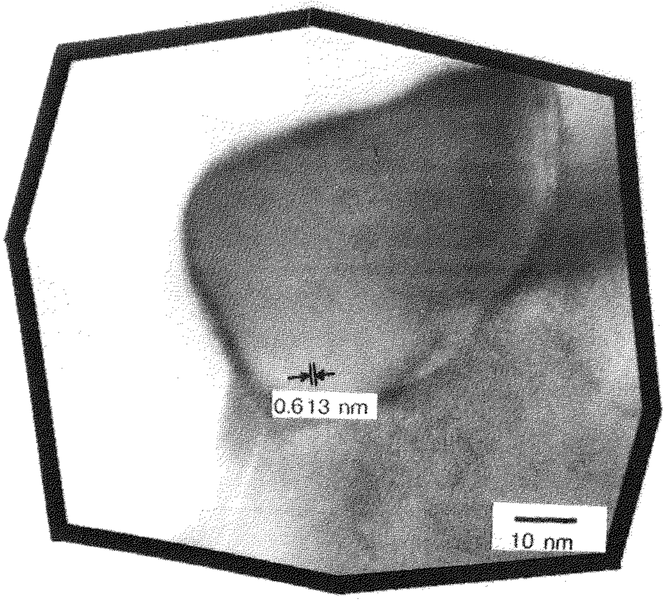

FIGURE 6. The lattice fringe of (111) planes in a $M_{23}C_6$ particle.

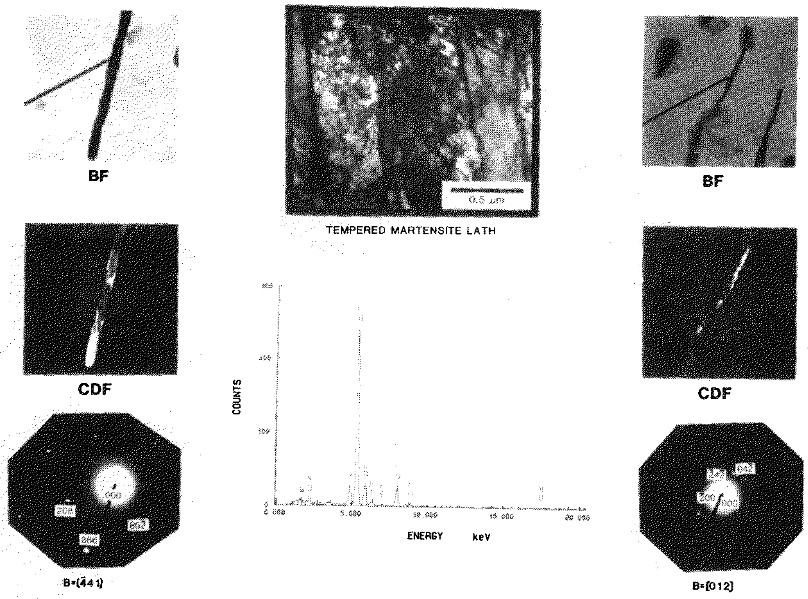

FIGURE 7. The irregular elongated $M_{23}C_6$ along the tempered martensite lath boundary.

(10) 700°C, 24 hrs (P = 20.8); (11) 800°C, 2 hrs (P = 21.8); (12) 800°C, 24 hrs (P = 22.9); and (13) 900°C, 2 hrs (P = 23.8).

Since the tempered lath martensite is the predominant phase in HT-9, it is used for the comparison of the thermal annealing effect. Figures 10 and 11 show the TEM microstructures of the thermal annealed specimens. There is no major microstructural change up to 600°C for 24 hrs (P = 18.7) except for a small amount of dislocation recovery in some laths. After 700°C for 2 hrs (P = 19.8), the subgrain of the tempered martensite lath started to recrystallize and the precipitate number density was gradually decreased. After 800°C for 24 hrs (P = 22.9), the microstructure was changed to martensite on cooling without any blocky precipitates in the matrix or on the grain boundary. The martensite is formed by the re-austenitizing process and the

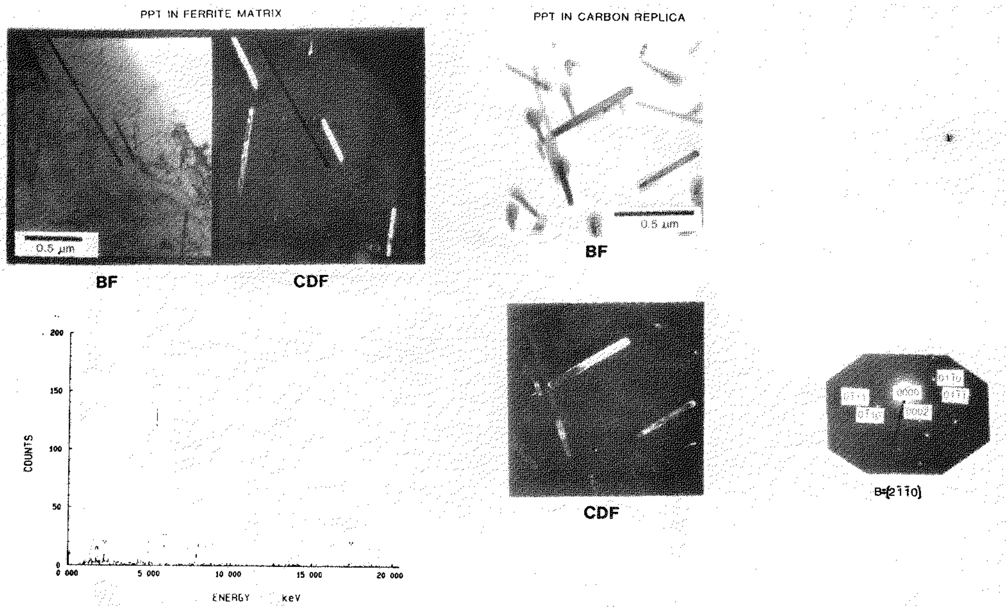

FIGURE 8. The M_2X phase in ferrite region of as-received HT-9.

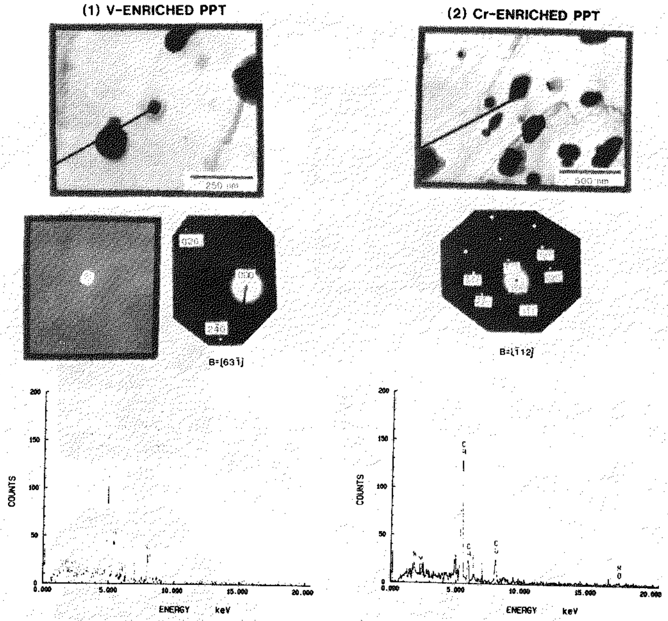

FIGURE 9. The MX phase in the carbon replica of as-received HT-9.

austenite to martensite transformation.

This austenite to martensite transformation is also shown in the microhardness tests. Figure 14 shows the curve of Vicker hardness number (VHN) versus the universal parameter P. It is shown that the hardness is gradually reduced up to 600°C due to the recovery of dislocation density. After 700°C or higher temperatures, the hardness goes up quickly due to the austenite to martensite transformation and finally saturates at the maximum hardness which is the Vicker hardness number of lath martensite.

The precipitate evolution under thermal annealing was studied by using the carbon extraction replica technique. Figures 12 and 13 show the micrographs that were taken from the carbon replicas of the thermal annealed specimens which were annealed for 2 hrs and 24 hrs, respectively. The types of precipitate and the chemical composition of each type of precipitate remained unchanged compared to the as-received material.

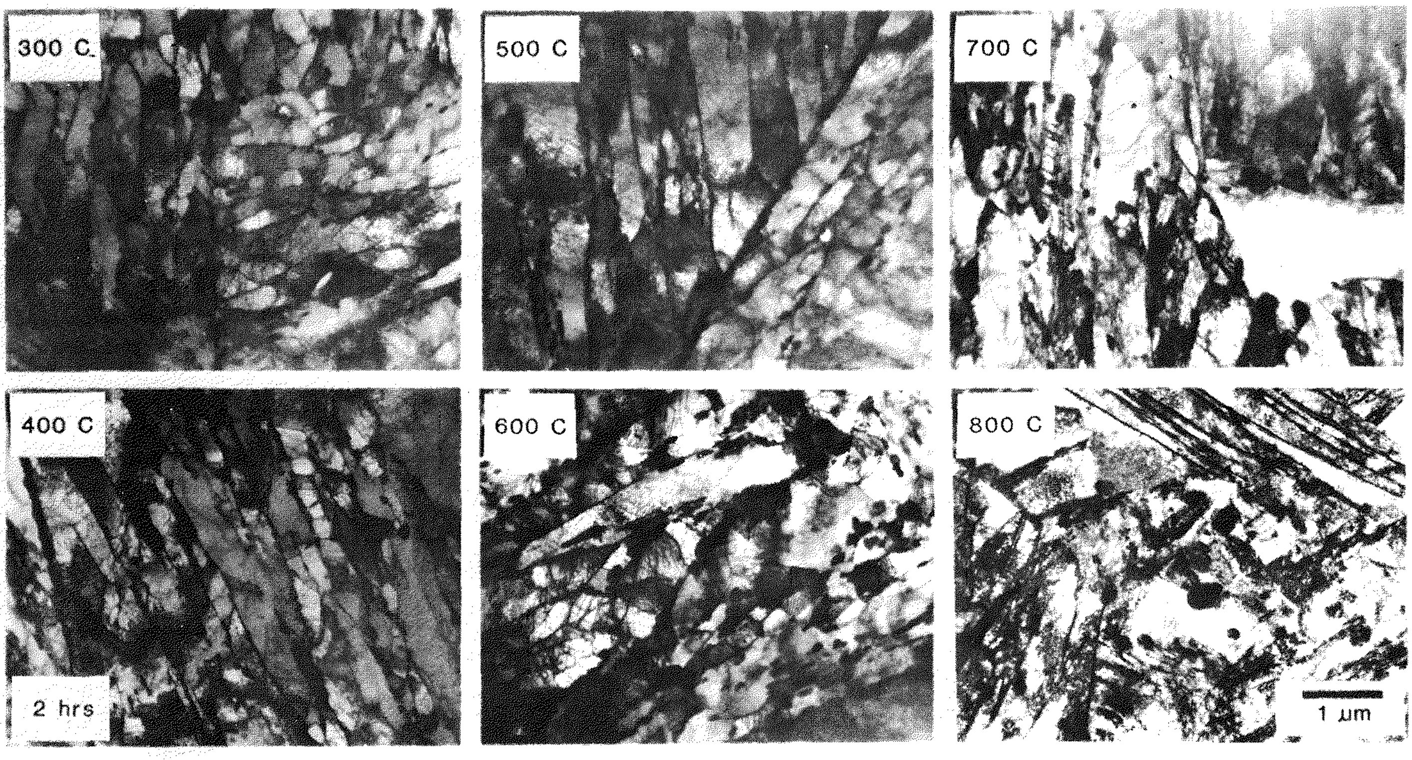

FIGURE 10. The tempered lath martensite of thermal annealed HT-9.

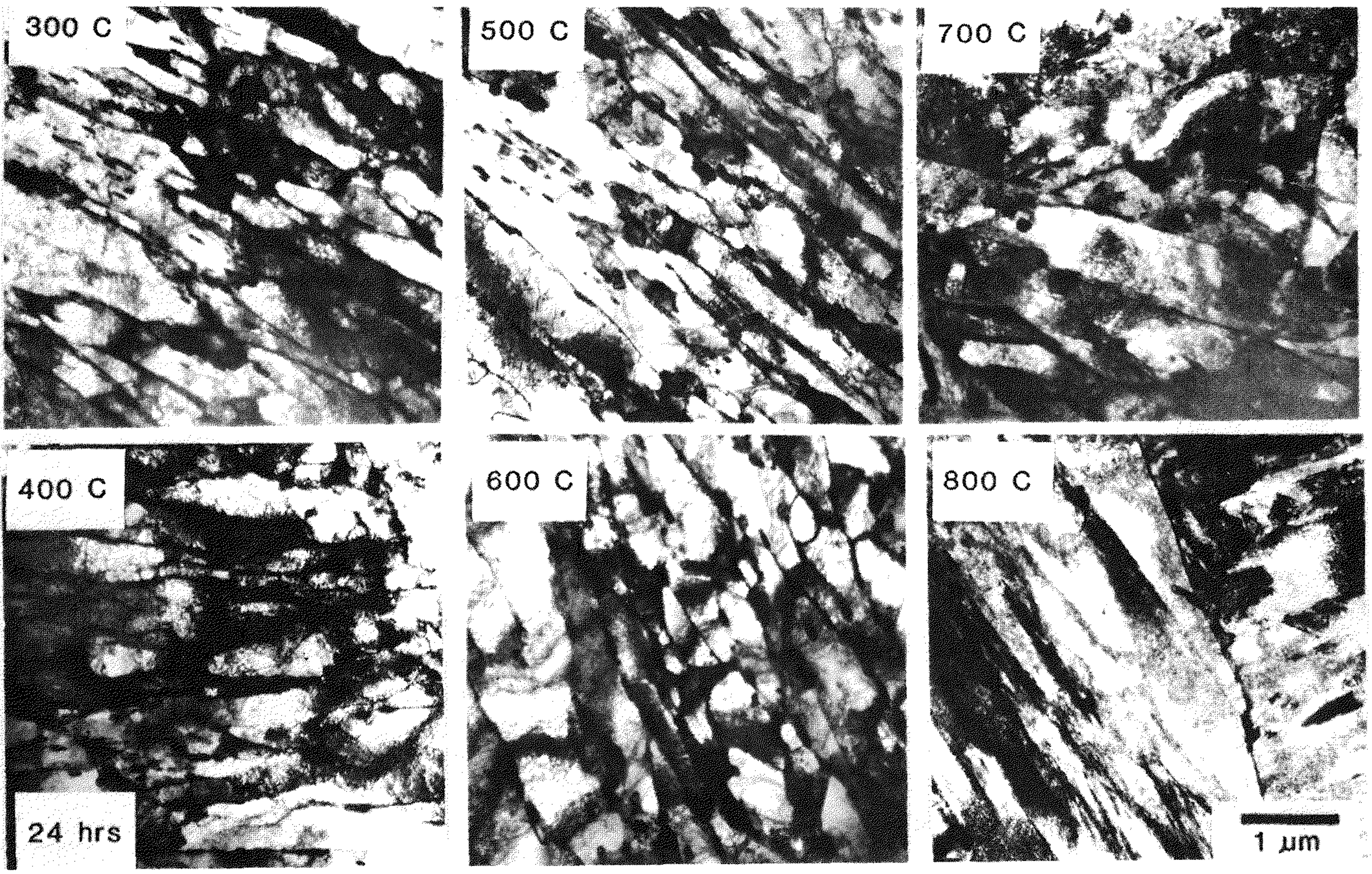

FIGURE 11. The tempered lath martensite of thermal annealed HT-9.

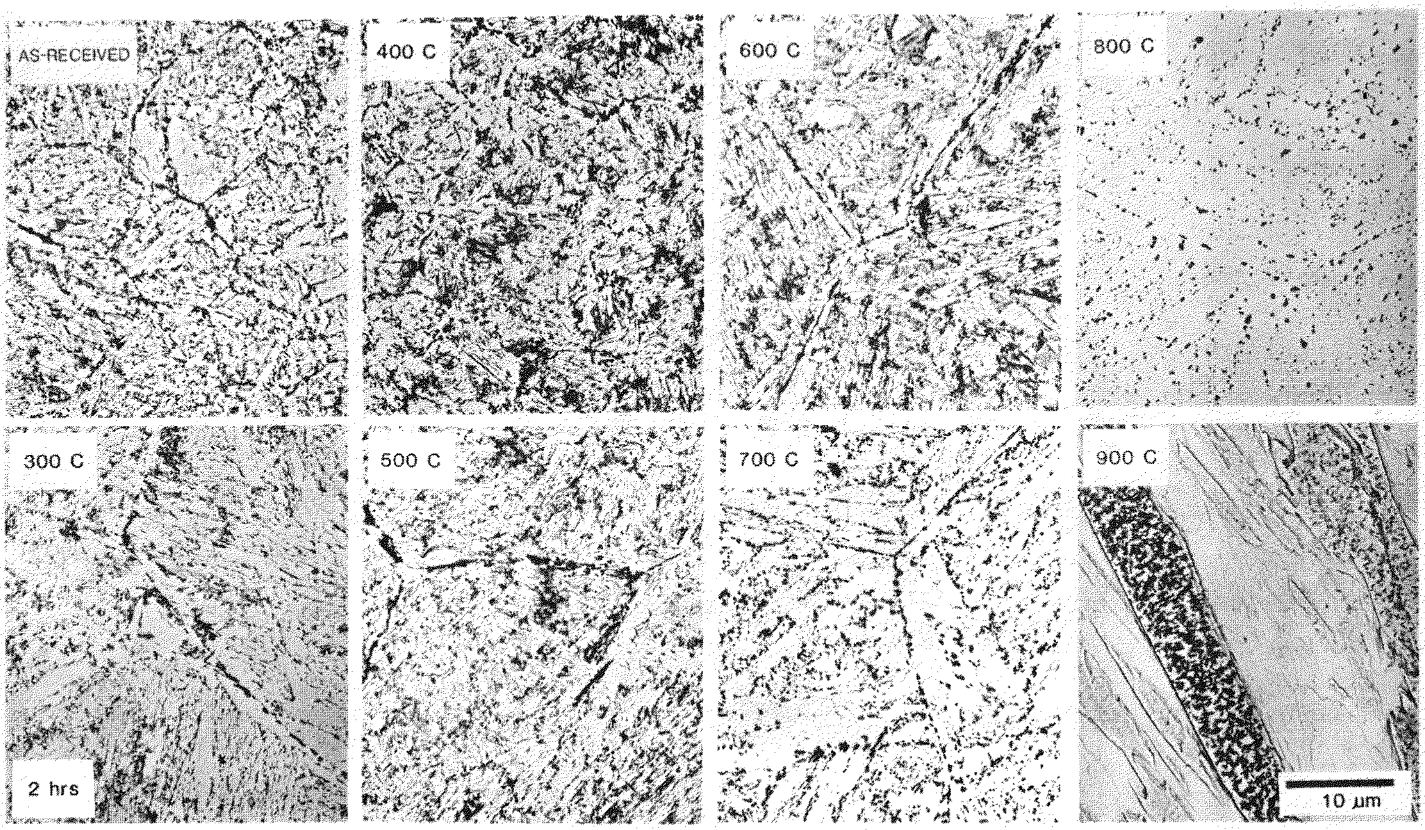

FIGURE 12. The carbon extraction replicas of thermal annealed HT-9.

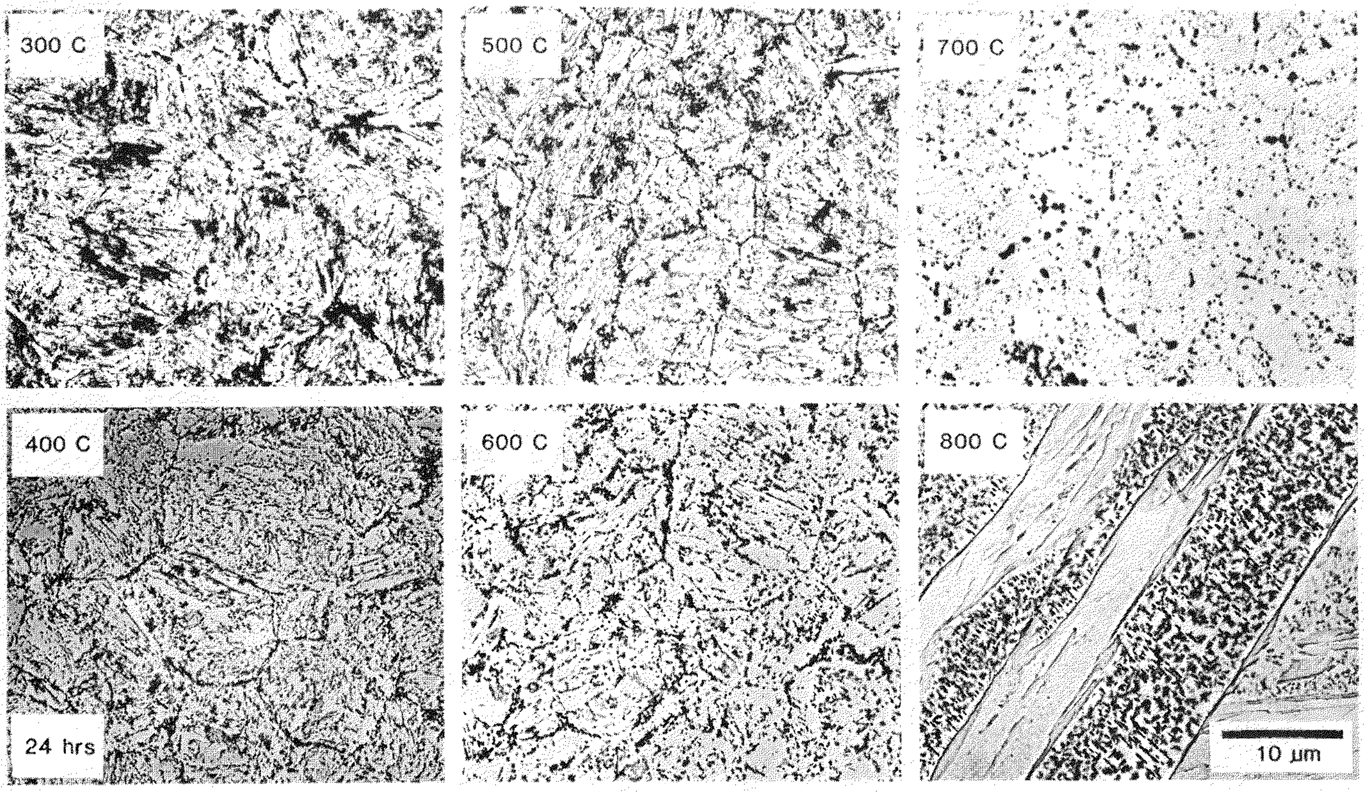

FIGURE 13. The carbon extraction replicas of thermal annealed HT-9.

However, the number density of each phase did change with temperature and time at high temperature annealing.

The distribution and the structure of precipitate were roughly unchanged during thermal annealings up to 600°C for 2 hrs (P = 17.7). The M_2X needle-like phase disappeared after 600°C for 24 hrs (P = 18.7). The irregular elongated $M_{23}C_6$ phase along the tempered martensite lath boundary started to dissolve after 700°C for 2 hrs (P = 19.8) and disappeared after 700°C for 24 hrs (P = 20.8). After the 800°C for 2 hrs (P = 21.8), the MX type phase was dissolved and some M_3C carbides were formed due to autotempering. The most stable second phase in thermal annealed HT-9 is the equiaxed $M_{23}C_6$ particles which are the only precipitates still found in the 800°C (2 hrs) (P = 21.8) specimen. After 800°C for 24 hrs (P = 22.9) and 900°C for 2 hrs (P = 23.8), the original precipitates were gone and a new generation of M_3C type phase was formed. This is consistent with the microstructure evolution in Figs. 10 and 11.

The x-ray EDS qualitative results showed that the chemical composition of each type precipitate was roughly unchanged and the M_3C phase had a high Fe peak with some Cr (Fig. 15a). However, in the higher temperature annealing (700°C, 24 hrs and 800°C, 2 hrs), the $M_{23}C_6$ phase has a V-peak which is about 3 wt.% (see Fig. 15b). This is due to the dissolution of other phases and the vanadium must be incorporated into the $M_{23}C_6$ phase.

5.4 Discussion

The dislocation density in HT-9 is always high ($\gtrsim 1 \times 10^{11}$ cm^{-2}). This can be explained by the special heat treatment response of this material. At lower temperature annealings ($T \leq 600$°C), the small subgrain size and the original high number density of precipitate slowed down the recovery of the dislocation density. At the higher temperature anneals ($T \geq 700$°C), certain portions of the material are transferred to austenite phase and the austenite to martensite transformation occurs during the cooling process producing the high dislocation density.

The microhardness test results can also be explained by the austenite to martensite transformation. Irvine et al.[5] have pointed out that the Ac_1 (re-austeniting) and M_S (martensite starting) temperatures are both affected by the minor alloy elements. According to their data, the calculated Ac_1 temperature of the HT-9 material used in this study is about 756°C which indicates that there should be no austenite reforming during annealing less than 700°C. However, the Ac_1 temperature is affected by local concentration of alloy elements so that the austenite to martensite transformation after 700°C annealing is reasonable. Since the TTT diagram (Fig. 16)[6] of a similar material shows that the nose is pushed to longer times, the cooling rate is not crucial for austenite to martensite transformation. All the reformed austenite will transform to martensite during the cooling process even during the slow cooling in the high vacuum furnace.

The precipitate evolution results are explained as follows. For lower temperature (≤ 600°C) anneals, the precipitate structure remained unchanged due to the slow diffusion rate of the alloy elements in the material. For higher temperatures (≥ 700°C) anneals, a portion of the matrix is re-austenitized and therefore, the smaller precipitates or the relatively unstable precipitates started to dissolve into the matrix.

The precipitate dissolution sequence can be explained by other studies.[4,7] For example, the M_2X phase has a relatively higher formation enthalpy[7] and also smaller size, therefore, it disappears first. The elongated $M_{23}C_6$ dissolves due to the tempered martensite laths which no longer exist at high temperature annealing. From Smith's[4] work, the equiaxed $M_{23}C_6$ is the final equilibrium phase at 700°C annealing in this material. Therefore, it is the last second phase which disappeared from the matrix.

The qualitative EDS results showed that most of the precipitates were Cr-enriched. It is understandable because the material contains about 12 wt.% Cr and only 3 wt.% of other alloy elements. Woodhead and Quarrell[8] reviewed the possible precipitates in thermal annealing alloy steels. They stated that often the

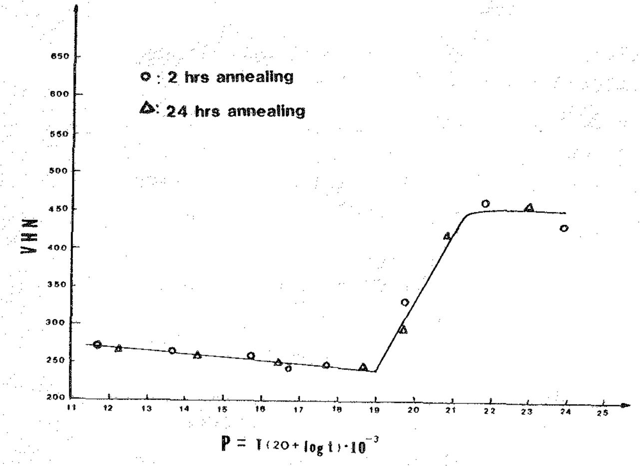

FIGURE 14. The microhardness test result of thermal annealed HT-9.

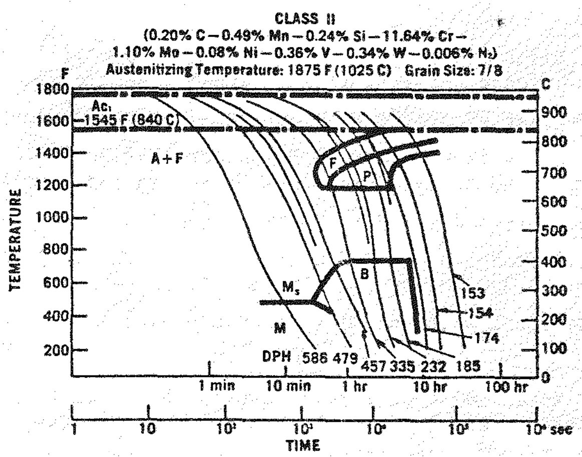

FIGURE 16. The TTT diagram for an alloy of chemical composition similar to HT-9.

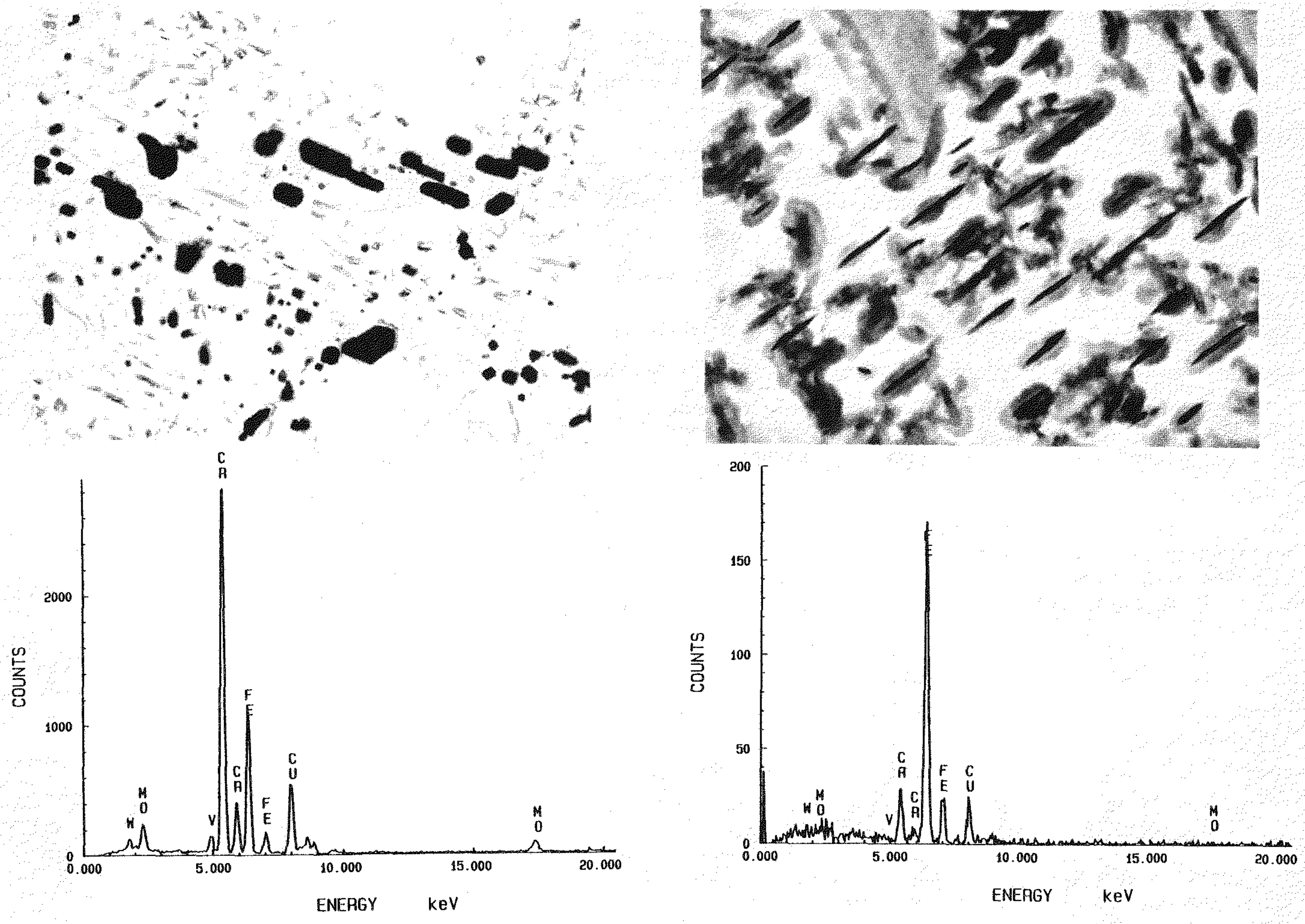

FIGURE 15. The morphology and qualitative EDS result of (a) $M_{23}C_6$, (b) M_3C.

precipitates were stable over an appreciable composition range, i.e. they were not stoichiometric and the general formulae (such as $M_{23}C_6$, MX, etc.) should be regarded as representing certain structural types rather than specific chemical species. There is sometimes appreciable solubility for nitrogen in precipitates; this is particularly true of the cubic carbides of formula MC and the hexagonal carbides of formula M_2C for which they are usually isomorphous with nitrides. Therefore, at the present time, the MX and M_2X phase is the best way to describe the platelet and the needle-like precipitates, respectively.

5.5 Conclusions

- The dislocation density in HT-9 is always high ($\geqslant 1 \times 10^{11}$ cm^{-2}).
- Four types of precipitates (2 types of $M_{23}C_6$, M_2X, MX) were identified in as-received HT-9 and most of the precipitates were Cr-enriched.
- Thermal annealing studies showed that some major microstructural changes occur after annealing above 600°C. Therefore, it is not practical to use this material above 600°C.
- Annealing at the temperature above 800°C will reform austenite in the matrix and the austenite will transform to martensite during the cooling process.
- The M_3C precipitate formed after the austenite to martensite transformation is due to the autotemping.

6.0 Acknowledgements

This work was supported by the U.S. Department of Energy, Office of Fusion Energy.

7.0 References

1. J.J. Kai, G.L. Kulcinski and R.A. Dodd, DAFS Quarterly Report DOE/ER-0046/20, Jan. 1985, pp. 63-67.
2. N.J. Zaluzec, "Quantitative X-Ray Microanalysis: Instrumental Considerations and Applications to Materials Science," in Introduction to Analytical Electron Microscopy, Edited by J.J. Hren, J.I. Goldstein and D.C. Joy (1979), Plenum Press, NY.
3. D.S. Gelles and L.E. Thomas, "Microstructural Examination of HT-9 Irradiated in the HFIR-CTR-32 Experiment," ADIP Quarterly Report (1982) DOE/ER-0045/9, p. 162.
4. R. Smith, in ISI Special Report No. 64, "Precipitation Processes in Steels," (1959) pp. 307-311.
5. K.J. Irvine, D.J. Crowe and F.B. Pickering, JISI 195, pp. 386-405, 1960.
6. E. Kauhausen and P. Kaesmacher, "The Metallurgy of Welded Heat-Resistant 12% Cr Steels + Mo-V-W," Schweissen and Schneiden 9, pp. 414-419, 1957.
7. H.L. Schick, Thermodynamics of Certain Refractory Compounds, Academic Press, NY, 1966.
8. J.H. Woodhead and A.G. Quarrell, JISI 203, pp. 605-620, 1965.

8.0 Future Work

More detail quantitative work on the unirradiated precipitates is underway and will be reported in the near future. The effect of irradiation on the microstructural evolution of HT-9 is also being analyzed.

THE IDENTIFICATION OF CHI PHASE IN HEAVY ION IRRADIATED HT-9 FERRITIC STEEL

J.J. Kai, G.L. Kulcinski, and R.A. Dodd (University of Wisconsin-Madison)

1.0 Objective

The purpose of this study is to understand the microstructural/microchemical evolution of HT-9 ferritic steel under heavy ion irradiation.

2.0 Summary

A new phase was formed in HT-9 ferritic steel under 14 MeV Ni^{+3} ion irradiation which is not found in thermal annealing studies of this alloy.[1] The specimens were irradiated at 500°C for the total dose up to 100 dpa at the peak damage region. The phase was identified as chi phase which has been reported in neutron irradiated HT-9 by Gelles and Thomas.[2] The techniques used for identifying this phase are described. The qualitative analysis results are presented.

3.0 Program

Title: Radiation Effects to Reactor Material
Principal Investigators: G.L. Kulcinski and R.A. Dodd
Affiliation: University of Wisconsin-Madison

4.0 Relevant DAFS Program Task/Subtask

Subtask II.C.1.1 Phase Stability Mechanics

5.0 Accomplishments and Status

A group of HT-9 specimens were irradiated by 14 MeV Ni^{+3} ion at 500°C to a dose level of up to 100 dpa at the peak damage region. The specimens were prepared for TEM examination by using the cross-section technique. The material and the cross-section technique used in this study were described before.[3]

An ordered bcc phase, which has a cube-on-cube orientation relationship with the matrix, was found in the irradiated region of every specimen. The phase is similar to the chi phase that was found by Gelles and Thomas[2] in fast neutron irradiated (EBR-II) HT-9. It was also reported by Little and Stoter[11] in fast neutron irradiated (DFR) CRM-12 ferritic steel which has a chemical composition very similar to HT-9. This phase has a bcc crystal structure with a lattice parameter of 0.8878 nm and a composition of $M_{18}C$ (M = Fe, Cr, Mo, Ni, and Si).

The diameter of these precipitates varies from 6 nm to 30 nm. Figure 1 shows the bright field and dark field images and the diffraction pattern of two dose level regions which represent the 40 dpa and 100 dpa, respectively. The superlattice diffraction pattern shows that the phase has a bcc crystal structure with a unit cell parameter about 0.89 nm and a cube-on-cube orientation relationship with the matrix.

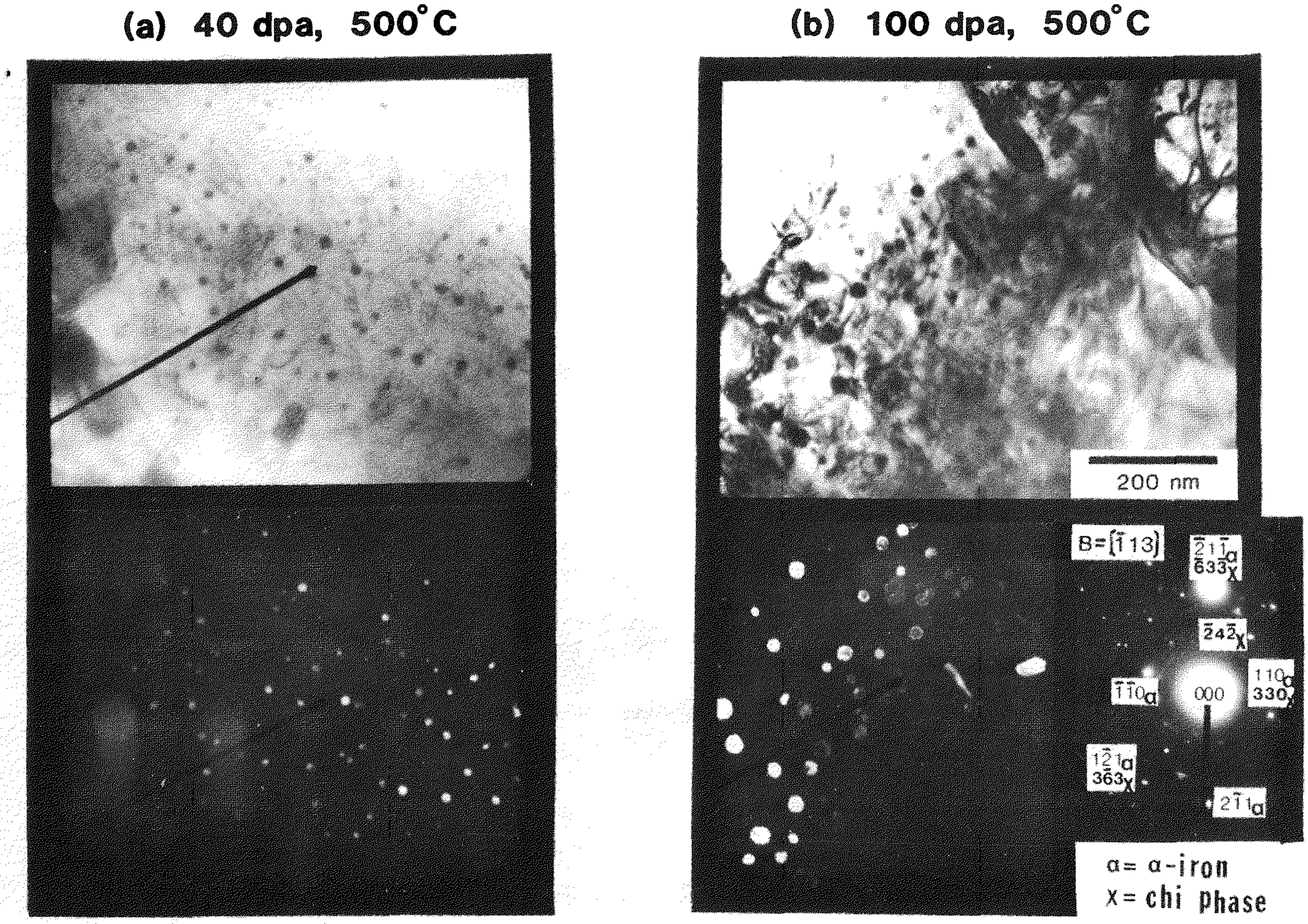

FIGURE 1. Examples of chi phase particles in 14 MeV Ni ion irradiated HT-9.

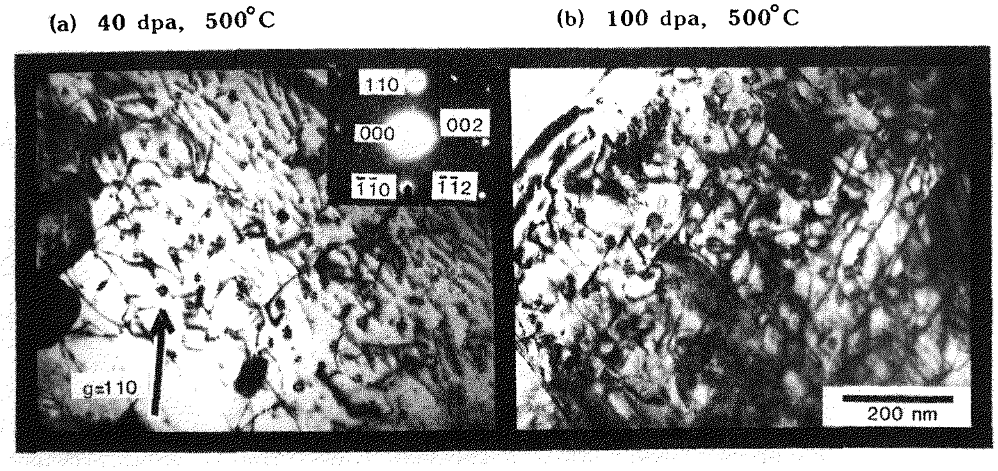

FIGURE 2. Same regions as in Fig. 1 shows the parallel type moiré fringe contrast in chi phase particles.

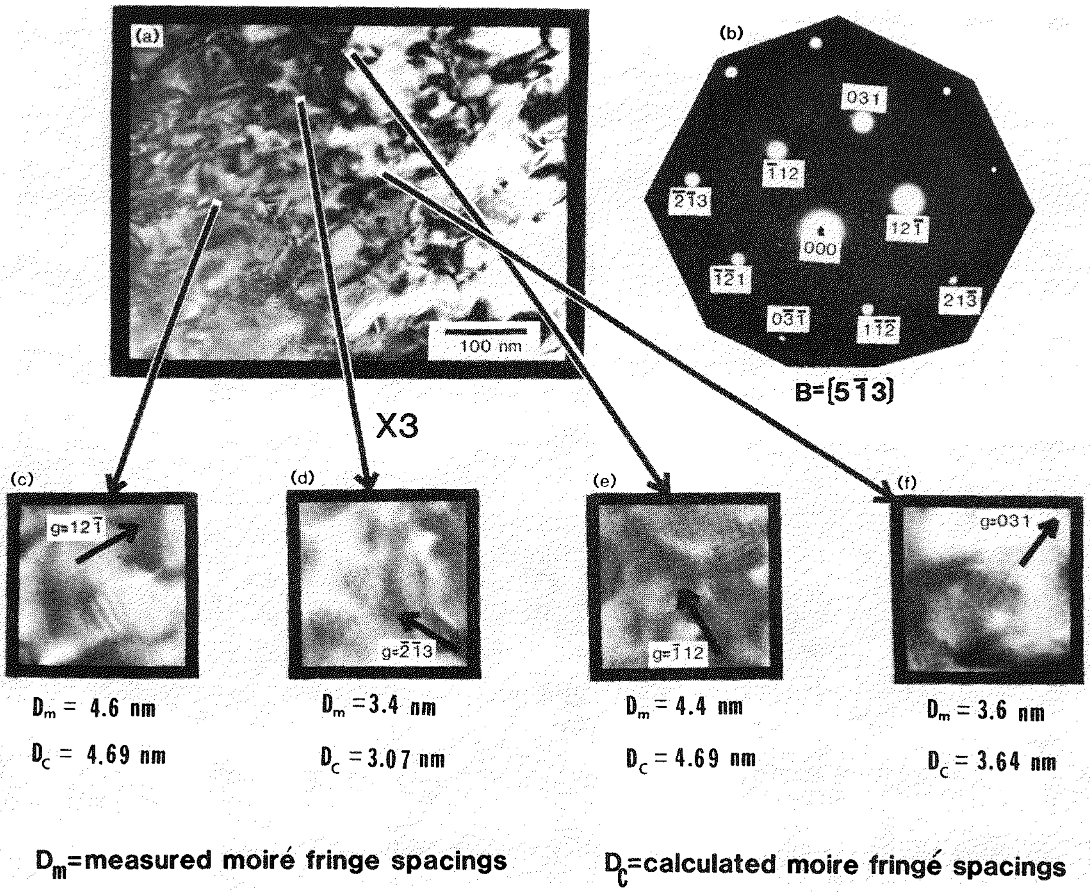

$$\Delta D = (d_1-d_2)/d_1 = \text{lattice mismatch} \approx 2.57\%$$

d_1 = d-spacing of the matrix d_2 = d-spacing of the ppt.

FIGURE 3. Identification of chi phase by using the moiré fringe spacings in 14 MeV Ni ion irradiated HT-9 at 500°C, 100 dpa.

Figure 2 shows the precipitates, which were in the same two regions of Fig. 1, that have the moiré fringe contrast on them. The diffraction pattern (insert) shows that these fringes are perpendicular to the $\bar{g}$ vector. This fact indicates that the moiré pattern is a parallel type and hence the spacing between the fringes, D, is given by:[4,5]

$$D = \frac{d_1 d_2}{d_1 - d_2} \qquad (1)$$

where d_1 and d_2 are the spacings of specified planes in the matrix and the precipitate, respectively.

Figure 3 gives a very clear demonstration of the relationship between the spacing of these moiré fringes and the lattice mismatch of Fe (α) and chi phase (χ) in certain $\bar{g}$ vectors.

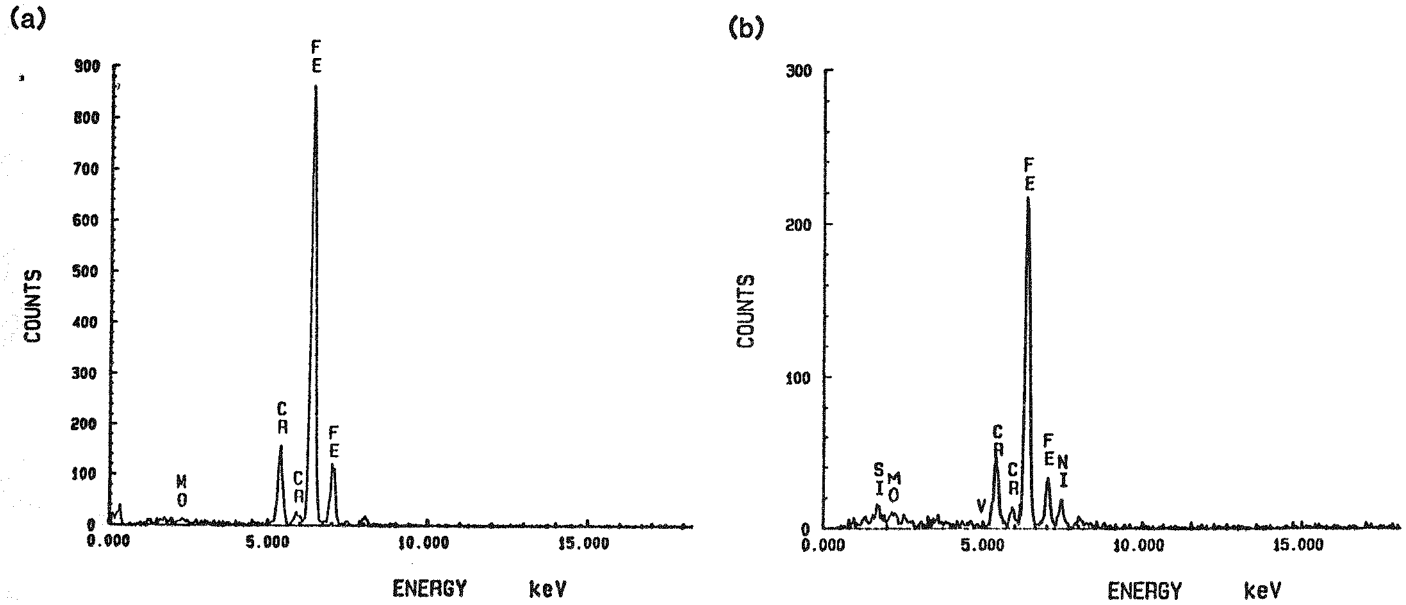

FIGURE 4. The qualitative EDS results of (a) the HT-9 matrix, and (b) the chi phase embedded in the matrix.

For example, in Fig. 3(c), $\bar{g} = 12\bar{1}_\alpha \sim 36\bar{3}_x$, the measured moiré fringe spacing (D_m) is 4.6 nm and the calculated moiré fringe spacing (D_c) is 4.69 nm. The consistent result is also true for other $\bar{g}$ vectors as shown in Figs. 3(d), 3(e), and 3(f). The moiré fringe pattern further proves that the new phase found in this study is indeed the chi phase.

The qualitative x-ray EDS spectra of the matrix and the chi phase embedded in the matrix are shown in Fig. 4. It is clearly indicated that the phase is enriched in Cr, Ni, and Si.

The number density and the average size of these precipitates are different in various dose levels. For example, in the 40 dpa dose level, the number density of the precipitate is about 3×10^{15} #/cm^3 and the average size is about 10 nm. In the 100 dpa dose level, the number density has dropped to about 1.5×10^{15} #/cm^3 but the average size is increased to about 18 nm. The volume fraction of the chi phase in the matrix is about 0.1% and 0.4% for 40 dpa and 100 dpa, respectively.

This phase was not reported by other heavy ion irradiation studies[6,7] and it was also not found in author's thermal annealing study.[1] From the equilibrium phase diagram of 12% Cr steel[8] and the carbides formed in alloy steels,[9] this phase is not one of the stable phases and also not a transient phase. From Smith's[10] 2000 hrs annealing at 700°C study, there is no sign that chi phase will form (this is equivalent to annealing at 500°C for about 2×10^5 years). Therefore, it is very possible that the chi phase is radiation induced in heavy ion irradiated HT-9.

6.0 Acknowledgements

The authors wish to express thanks to Dr. T.F. Kelly for his helpful information. This research is sponsored by the Department of Energy.

7.0 References

1. J.J. Kai, G.L. Kulcinski and R.A. Dodd, "The Influence of Thermal Annealing on the Microstructural Evolution in HT-9 Ferritic Steel," to be published in DAFS Quarterly Report DOE/ER-0046/21 (this volume).

2. D.S. Gelles and L.E. Thomas, "Effects of Neutron Irradiation on Microstructure in Experimental and Commercial Alloys", in the Proc. of the Top. Conf. on "Ferritic Alloys for Use in Nuclear Energy Technologies," Snowbird, UT, pp. 559-568, 1983, (Eds. J.W. Davis and D.J. Michel).

3. J.J. Kai, G.L. Kulcinski and R.A. Dodd, in DAFS Quarterly Report DOE/ER-0046/20, pp. 63-67, 1985.

4. P. Hirsch, A. Howie, R.B. Nicholson, D.W. Pashley and M.J. Whelan, "Electron Microscopy of Thin Crystals", Chapter 14, R.E. Krieger Publishing Co., New York, 1977.

5. J.W. Edington, "Interpretation of Transmission Electron Micrographs", in "Practical Electron Microscopy in Materials Science", Volume 3, 1975, Phillips, Northern Ireland.

6. F.A. Smidt, Jr., P.R. Malmberg, J.A. Sprague, and J.E. Westmoreland, in "Irradiation Effects on the Microstructure and Properties of Metals", ASTM-STP-611, pp. 227-241, 1976.

7. G. Ayrault, in DAFS Quarterly Report Oct.-Dec. 1981, DOE/ER-0046/8, pp. 182-190.

8. K.J. Irvine, D.J. Crowe, and F.B. Pickering, "The Physical Metallurgy of 12% Cr Steels," JISI 195, pp. 386-405, 1980.

9. J.H. Woodhead and A.G. Quarrell, JISI 203, pp. 605-620, 1965.

10. R. Smith, ISI Spec. Rep. No. 64, "Precipitation Processes in Steels," pp. 307-311, 1959.

11. E.A. Little and L.P. Stoter, "Microstructural Stability of Fast Reactor Irradiated 10-12% Cr Ferritic-Martensitic Stainless Steels," in Effects of Radiation Materials: 11th Conf., ASTM-STP-782, H.R. Brager and J.S. Perrin, Eds., pp. 207-233, 1982.

APPLICATION OF HIGH FLUENCE FAST REACTOR DATA TO FUSION-RELEVANT MATERIALS PROBLEMS

F. A. Garner (Hanford Engineering Development Laboratory)

1.0 Objective

The object of this effort is reassess the utility of fast reactors to fusion materials studies in light of recent insights on the response of materials to radiation exposure at different levels of helium.

2.0 Summary

In three recent comparative studies in HFIR and EBR-II where the effect of helium and solid transmutants could be assessed, it was found that in each case there was no significant perturbation of the macroscopic property change under consideration. These findings reinforce the belief that fast reactors can serve as a major tool for fusion materials studies and that the effects of helium and other transmutants can be treated as second-order perturbations to be studied by other methods. A number of new fusion-relevant insights derived from fast reactor studies are presented.

3.0 Program

Title: Irradiation Effects Analysis (AKJ)
Principal Investigator: D. G. Doran
Affiliation: Hanford Engineering Development Laboratory

4.0 Relevant DAFS Program Plan Task/Subtask

Subtask II.C.1 Effects of Material Parameters on Microstructure
Subtask II.C.2 Effects of He on Microstructure
Subtask II.C.7 Effects of He and Displacement on Flow
Subtask II.C.8 Effects of He and Displacement on Fracture

5.0 Accomplishments and Status

5.1 Introduction

The design of fusion devices requires the capability to predict radiation-induced changes in the properties and dimensions of structural materials. In the absence of a test device with a fusion-typical neutron spectrum this objective necessitates three types of activities. First, a sufficiently large data base at high neutron fluence must be derived from existing fission reactors for each property of interest. Second, a correct perception must be attained of the operating damage mechanisms and their response in the fission reactor to material and environmental variables. Finally, one must identify the consequences of differences in neutron spectra and operational variables between anticipated fusion environments and the fission environment from which the data were derived. Currently, we can only assume that the use of displacements per atom adequately describes the damaging characteristics of neutrons at fusion-relevant energies and only limited data are available concerning the potential impact of spectrum-dependent transmutants.(1)

Until a high flux fusion neutron facility is available, the U.S. materials community is using a variety of neutron sources to conduct experimental studies. The nature of the differences between fission and fusion neutrons is being studied in comparative low flux irradiations in RTNS-II and low power thermal reactors.(1) Although we anticipate the eventual use of the FMIT facility at high displacement rates, we must at this time rely on fast reactors and high flux mixed-spectrum reactors. While the latter have very high gamma heating rates and space limitations, they have been quite useful in investigating the impact of large amounts of helium on damage evolution in alloys that contain nickel.

The question of helium's influence in altering the response of materials to displacive irradiation is the subject of intensive world-wide investigation, but in three cases where a clear comparison can be made at both high and low helium levels, it was found that large levels of helium did not significantly perturb the macroscopic property change under consideration. It was found that the post-transient swelling rate of annealed AISI 316 stainless steel was not altered by the large differences in helium/dpa ratio obtained in EBR-II and HFIR; nor was it influenced by the much higher cavity density generated in HFIR(2,3). It was later determined that the tensile properties of 20% cold-worked AISI 316 stainless steel irradiated below 575°C were also insensitive to the large difference in helium generation rates in these two reactors.(4) Finally, the ductility loss exhibited by high nickel precipitation-hardened austenitic alloys in HFIR(5) was identical to that observed in EBR-II.(6,7) Thus, the response of these alloys to displacement damage and environmental variables overwhelmed the effect of large amounts of helium. These findings reinforce our decision to use fast reactors as a major tool for fusion materials studies and to treat helium effects as a second-order perturbation to be studied separately.

It is recognized, however, that this approach may not be valid for all alloys and all property changes of interest. Therefore studies are being continued in mixed spectrum reactors. Another approach is also being employed which concentrates on fast reactor irradiations and which introduces helium prior to or during irradiation.

The first of these techniques involves the use of the "tritium trick" to introduce helium into a portion of the specimen matrix prior to irradiation.(8) This technique is valuable for materials such as vanadium alloys that do not contain nickel and therefore will not produce significant amounts of helium in mixed spectrum reactors. The second approach involves the reirradiation in FFTF of a series of specimens previously irradiated in HFIR to different displacement levels and helium levels.(9) The most unique approach involves enrichment of the ^{59}Ni isotope prior to irradiation in FFTF.(10) This approach allows helium to be generated during fast-reactor irradiation at fusion-relevant rates. Approximately 50 grams of nickel enriched to ∿2% in ^{59}Ni have been extracted from Inconel 600 which was irradiated to a high fluence in ETR. Experiments utilizing this material are now being planned to study the synergistic effect of helium on void, dislocation, precipitate and spinodal evolution.

The EBR-II fast reactor was previously the major U.S. source of fusion-relevant data in the range of 400-700°C and reached exposures as large as 100 dpa in some experiments. EBR-II has now been supplanted by FFTF as the major irradiation facility. It has a much larger experimental volume, a higher displacement rate and on-line temperature control to ±5°C. On-line stress rupture detection using isotopic tagging of fill gases is also a feature of current FFTF fusion-related studies(11). The materials open test assembly (MOTA) in FFTF is the major experimental vehicle and is currently discharging specimens at increments of ∿30 dpa each year.

5.2 New Insights Derived from Fast Reactor Irradiations

Since the validity of any fission-fusion correlation is strongly dependent on the soundness of the property-change description in the fission environment, an increased emphasis has been placed on examination of previously developed correlations for swelling, creep, mechanical properties and phase stability. This attention has led to important revisions in some of our perceptions of the various damage processes, their relative importance and their dependence on material and environmental parameters. One unanticipated major conclusion is that differences in environmental variables such as temperature history and displacement rate are at least as important as differences arising from neutron spectral considerations(2).

Perhaps the most far-reaching revision involves the realization that the steady-state or post-transient swelling rate of all austenitic alloys is ∿1%/dpa, essentially independent of composition, temperature, displacement rate, stress and helium.(2) This conclusion has led to a reduction of effort on austenitic PCA alloys and an enhanced interest in ferritic alloys. In the recent Blanket Comparison and Selection Study for instance, austenitic alloys were not recommended for high exposure applications.(12) This conclusion has also led to reassessments in the theoretical descriptions employed to describe swelling(13,14) and in the correlation of results between neutron and charged particle irradiation.(15,16)

Other recent conclusions for austenitic steels were that the primary influcence of all variables lay in the duration of the transient regime of swelling, that swelling did not saturate at engineering-relevant levels and that the sensitivities of the swelling transient regime would be reflected in the sensitivities of transient creep but not in the post-transient creep rate.(2)

Since these findings were published additional data have been acquired which confirm their validity. Exposures of simple Fe-Cr-Ni ternary alloys have now reached 110 dpa in EBR-II. It was found that 1%/dpa is eventually reached at all compositions in the range 12-75% nickel and 7-22% chromium.(16) Simple Fe-Cr-Mn ternaries and solute-modified Fe-Cr-Mn-Ni alloys also appear to reach 1%/dpa.(17,18) As shown in Figures 1 and 2, structural alloys such as OKh16N15M3B and AISI 316 have also been reported to develop temperature- independent swelling rates of 1%/dpa.(19,20) The addition of titanium, phosphorus and other solutes to AISI 316 have been shown to delay but not to preclude the inevitability of reaching this swelling rate.(21,22)

In Fe-Cr-Ni and possibly in the Fe-Cr-Mn systems there appears to be a minimum transient regime of $\sim$10 dpa that cannot be reduced by application of stress, off-normal temperature histories or variations in displacement rate.(16,23) The swelling of ternary alloys is independent of temperature from the lowest test temperature (400°C) to some composition-dependent upper limit as shown in Figure 3. Above this temperature the transient duration increases with temperature. In general the transient regime increases with decreasing chromium (Figure 4) and increasing nickel (Figure 5). At relatively high temperatures, however, swelling again increases with increasing nickel as shown in Figures 5 and 6.

The compositional dependence of swelling arises from the strong effect of nickel content on two competing processes. The first is the effect of solvent composition on the effective vacancy diffusion coefficient and on void nucleation.(13,24) The second is the tendency of Fe-Ni-Cr alloys to undergo spinodal decomposition during either neutron or ion irradiation(25,26) as shown in Figure 7. In Fe-35Ni-7Cr the alloy decomposes toward Fe_3Ni and FeNi. Both of these processes increase with irradiation temperature. Nickel enhances vacancy diffusion and increases the tendency toward decomposition. Chromium on the other hand decreases vacancy diffusion and appears to be relatively inert in spinodal formation. The micro-oscillations in composition produce large areas which favor void nucleation since they are relatively low in nickel and high in chromium. Associated with the spinodal formation are a decrease in lattice parameter, a loss of the anomalous properties characteristic of the Invar compositional regime and a significant increase in yield strength.(25,27)

5.3 Consequences of Swelling

It is sometimes proposed that some fusion components can be relatively tolerant of swelling. There are newly discovered consequences, however, that mitigate against such a philosophy. First of all, there will be significant changes in thermal conductivity and elastic moduli.(28) Second, it appears that at swelling levels on the order of 5-10% there are significant changes in both irradiation creep and fail-

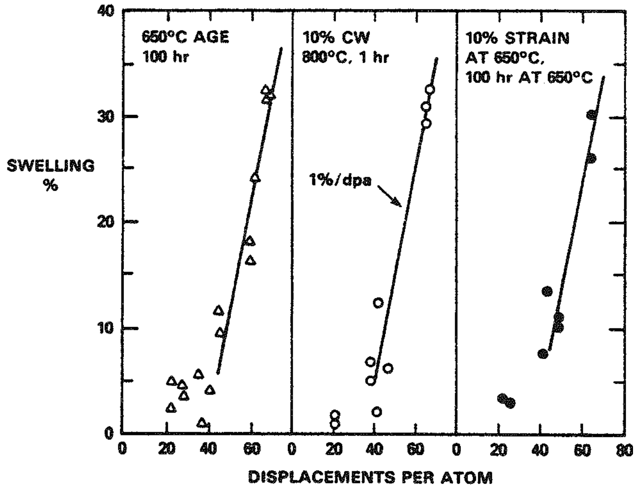

FIGURE 1. Swelling of OKh16N15M3B steel in BOR-60 Fast Reactor at 400-550°C.(19)

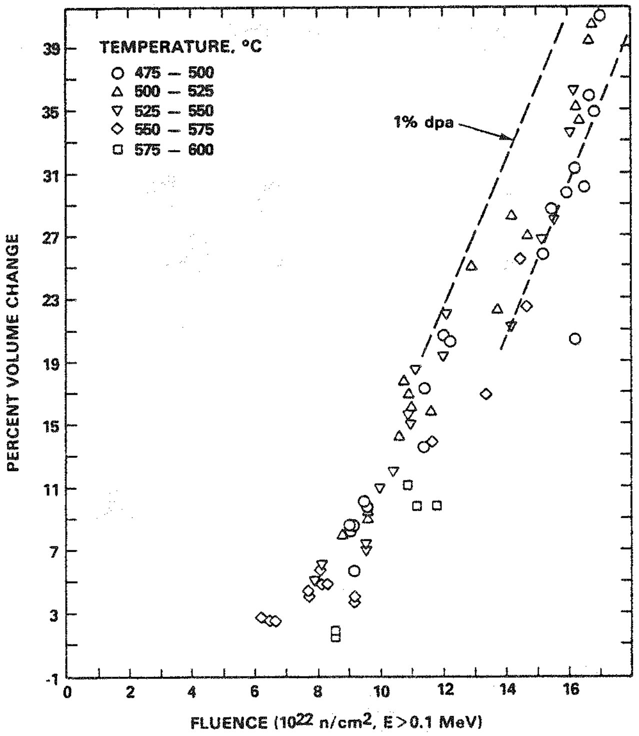

FIGURE 2. Swelling of 20% cold-worked AISI 316 fuel pin cladding.(20)

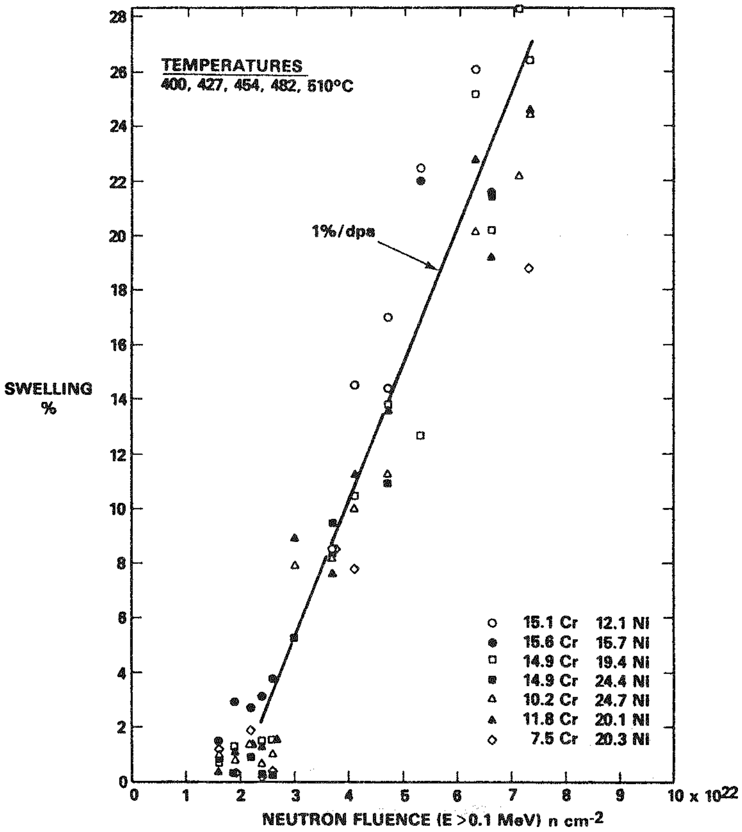

FIGURE 3. Swelling of seven Fe-Cr-Ni alloys in EBR-II at five temperatures in the range 400-510°C.(16)

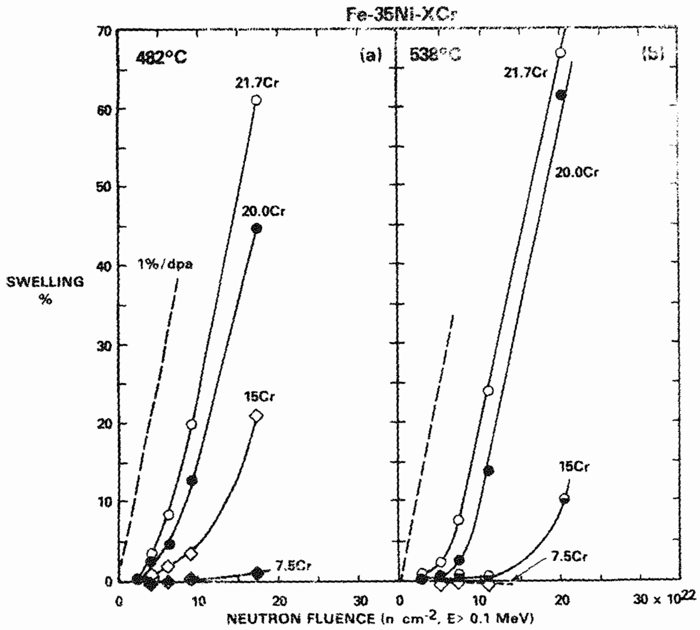

FIGURE 4. Influence of chromium level and temperature on the swelling of Fe-35Ni-XCr alloys in EBR-II.(16)

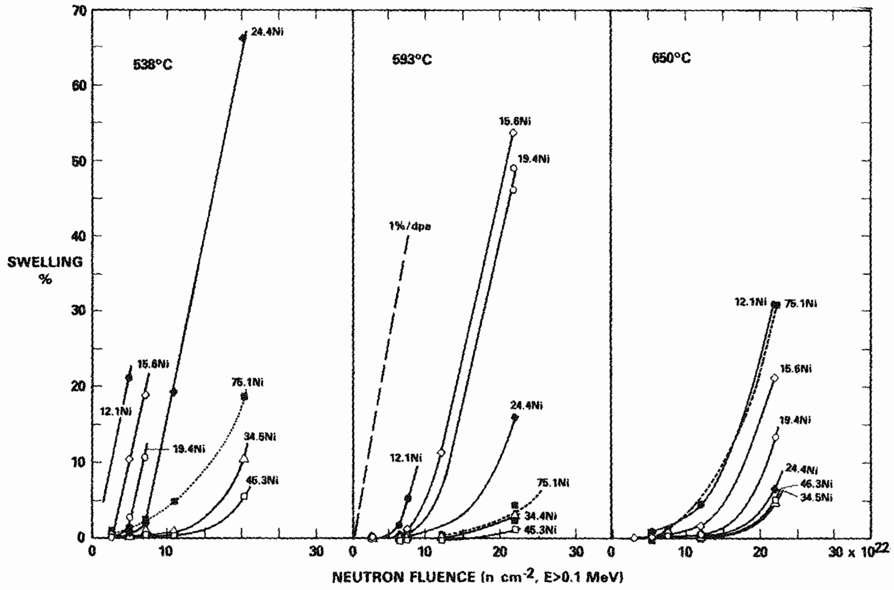

FIGURE 5. Influence of nickel level and temperature on the swelling of Fe-15Cr-XNi alloys in EBR-II.(16)

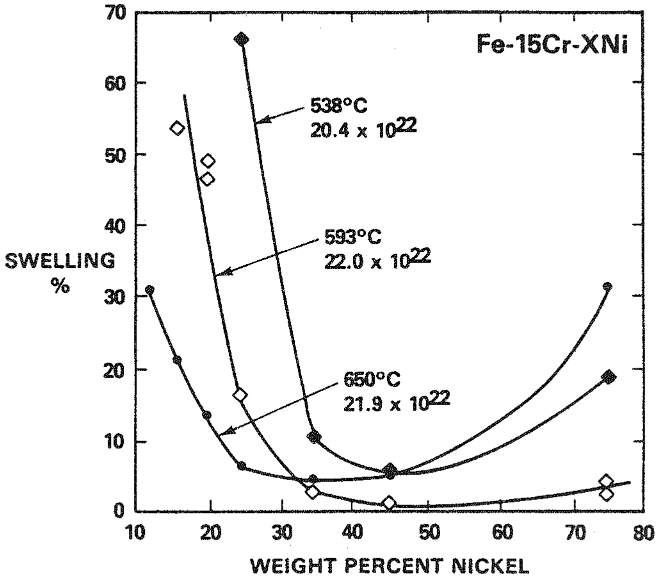

FIGURE 6. Dependence of swelling of Fe-15Cr-XNi alloys on temperature, neutron fluence and nickel content.(16)

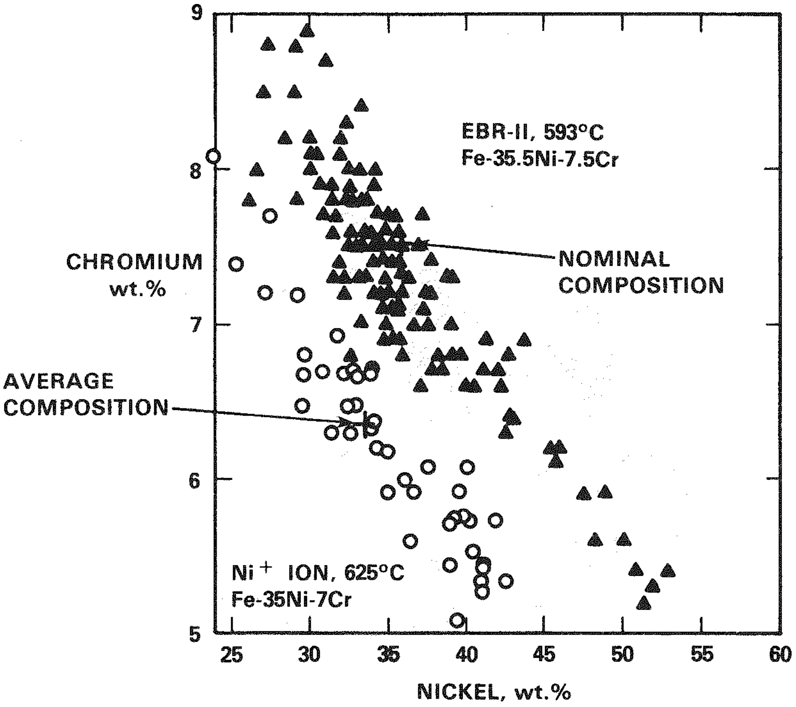

FIGURE 7. Local measurements of spinodal decomposition of Fe-Cr-Ni Invar alloys, illustrated by the tendency of nickel to separate from chromium and iron during irradiation by ions or neutrons.(26)

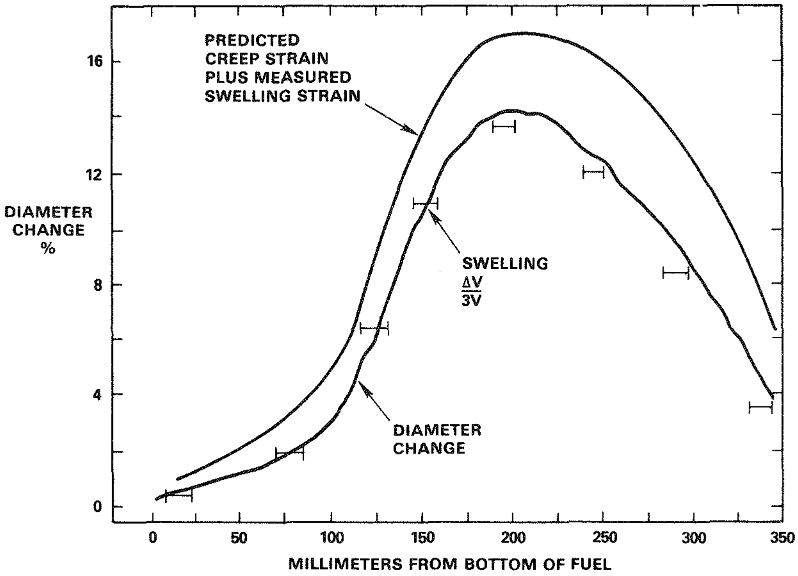

FIGURE 8. Comparison of predicted and measured diametral strains of 20% cold-worked AISI 316 cladding on a fuel pin irradiated to a peak fluence of 1.7×10^{23} n/cm^2 (E >0.1 MeV)(20). Note that the measured diameter change appears to arise primarily from the swelling-related strain.

ure modes. As shown in Figure 8 Makenas has recently found that large underpredictions of creep strain occur in fuel pins with significant levels of swelling. The results of on-going analyses of pressurized creep tubes irradiated in EBR-II show that creep strains appear to saturate coincident with 7-10% swelling. One consequence of this is that diameter changes at high fluence do not exceed 0.33%/dpa for any stress level. This strain rate therefore represents only post-transient swelling-induced deformation.

If large levels of void swelling tend to interfere with irradiation creep it might be expected that other deformation modes may also be affected. It has recently been found that the fracture modes in AISI 316 and titanium-modified AISI 316 undergo significant changes as swelling increases. There is a complete change in fracture mode from ductile to channel facture when swelling levels exceed 10% and when tensile tests are conducted at the irradiation temperature. As shown in Figure 9 a moderate amount of ductility remains and the fracture surfaces show significant ductility as evidenced by deformation of the sheared voids. When the tests are conducted at room temperature, however, there is a quasi-cleavage failure that occurs normal to the direction of applied stress and which shows the river patterns typical of cleavage fracture (Figure 10). The voids on the quasi-cleavage surface do not exhibit deformation. Although Huang(29) as well as Hamilton and coworkers(30) conclude that the fracture toughness of irradiated AISI 316 is sufficient for breeder and fusion applications, it appears that the tearing modulus at low temperatures is greatly reduced when significant swelling has occurred.

5.4 Conclusions

Based on the new insights discussed in this paper it appears that there are radiation-induced phenomena yet to be discovered. It is felt that most of these phenomena represent the response of the material to displacement damage and that neutron spectral considerations such a helium can be treated as second-order perturbations. Fast reactors will therefore continue to be a valuable tool for fusion materials studies.

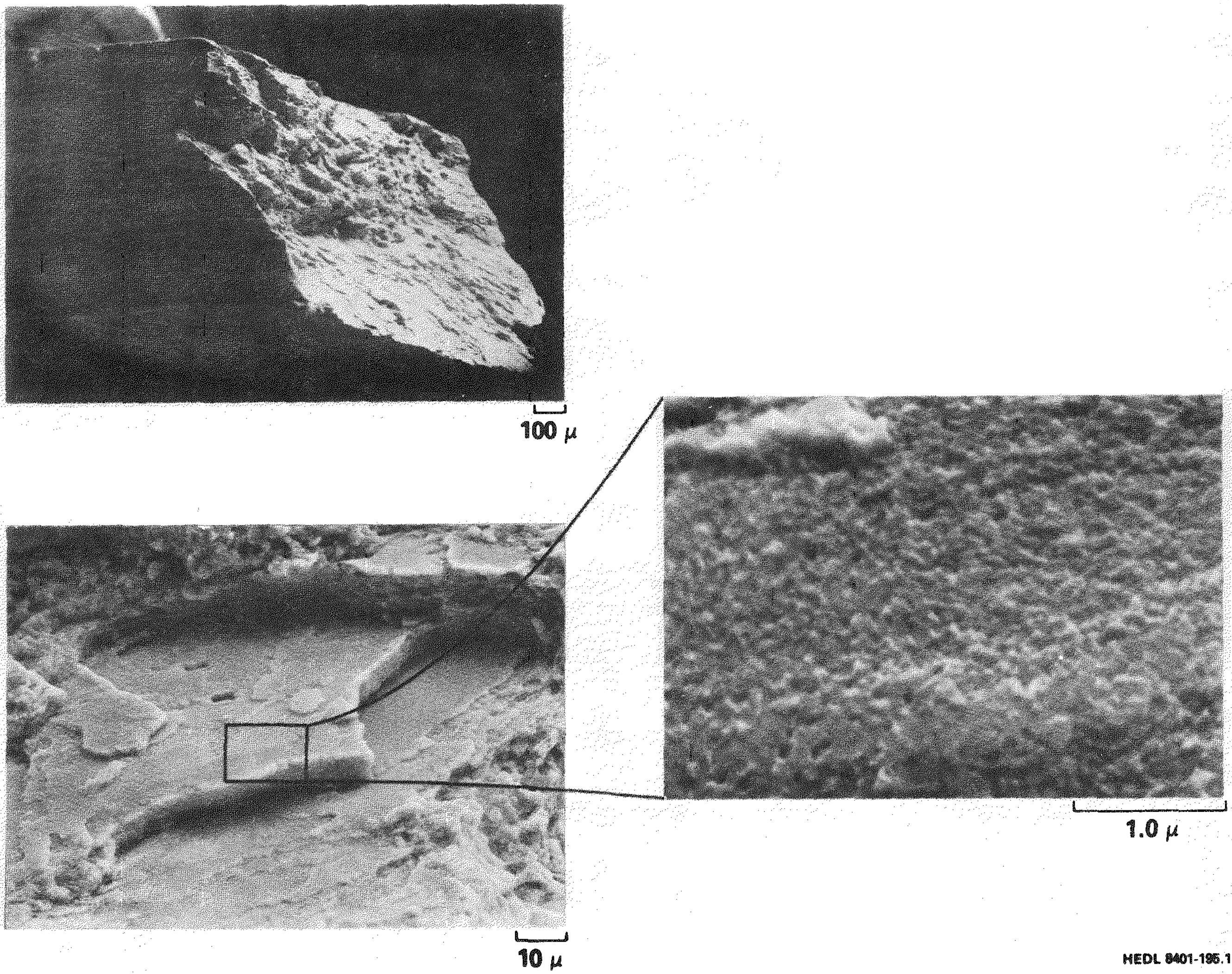

HEDL 8401-195.1

FIGURE 9. Channel fracture of 20% cold-worked AISI 316 duct irradiated at 460°C and tested at the same temperature. (Courtesy of M. L. Hamilton of HEDL) This material was irradiated to 15.5 x 10^{22} n/cm^2 (E > 0.1 MeV) and accumulated 7.2% strain before failure occurred.

6.0 References

1. D. G. Doran, J. Nucl. Mater. 117 (1983) 1.

2. F. A. Garner, J. Nucl. Mater. 122 and 123 (1984) 459.

3. H. R. Brager and F. A. Garner, J. Nucl. Mater. 117 (1983) 159.

4. A. F. Rowcliffe and M. L. Grossbeck, J. Nucl. Mater. 122 and 123 (1984) 181.

5. W. J. S. Yang and M. L. Hamilton, J. Nucl. Mater. 122 and 123 (1984) 748.

6. S. Vaidyanathan, W. C. Bell and T. Lauritzen, Effects of Radiation on Materials: Eleventh Conf., ASTM STP 782, Eds., H. R. Brager and J. S. Perrin (American Society for Testing and Materials, 1982) p. 619.

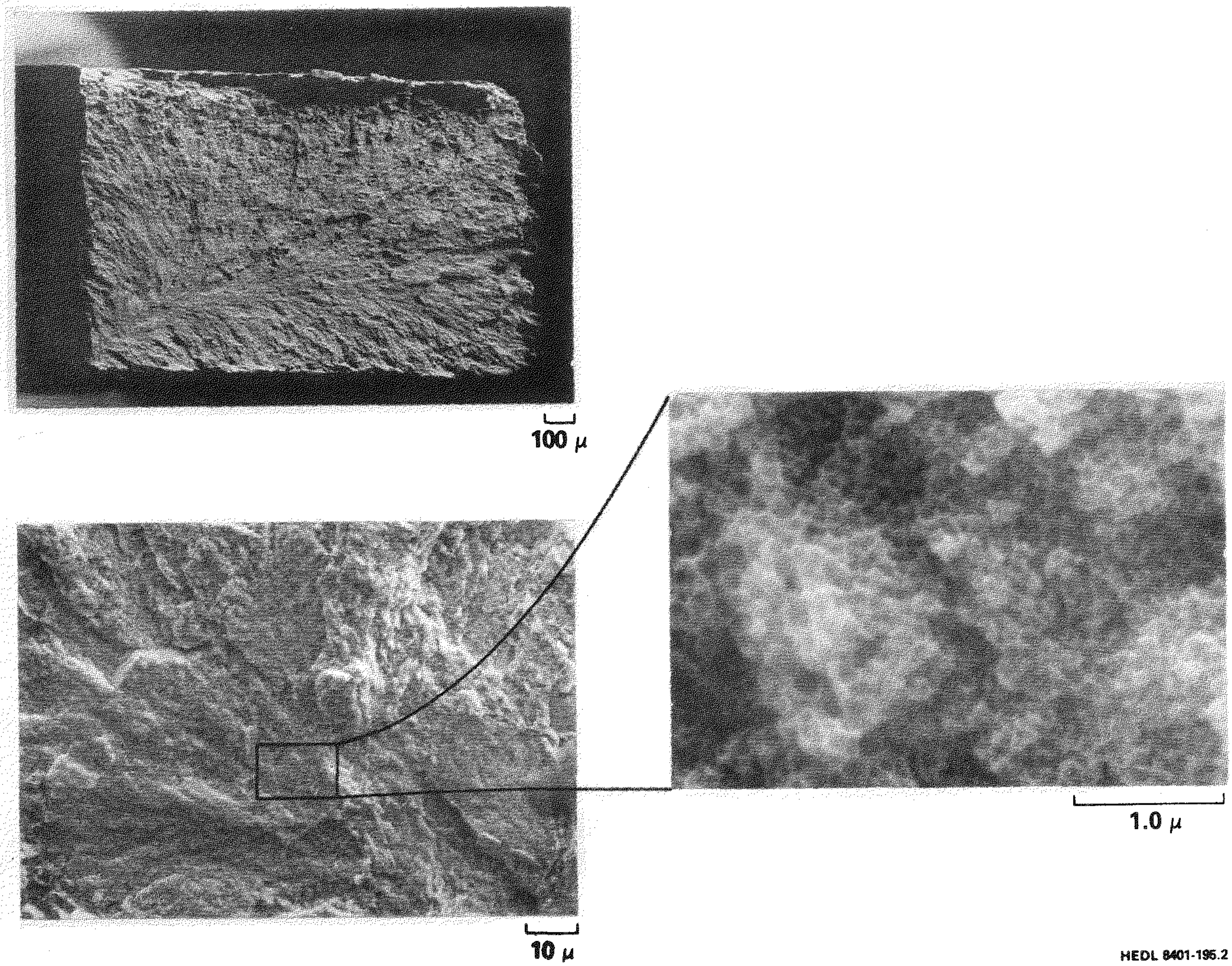

FIGURE 10. Quasi-cleavage fracture of 20% cold-worked AISI 316 duct irradiated to 15.5 n/cm^2 (E >0.1 MeV) at 460°C and tested at 20°C. (Courtesy of M. L. Hamilton of HEDL). This material failed after 1.9% strain had occurred.

7. W. J. S. Yang, D. S. Gelles, J. L. Straalsund and R. Bajaj, "Post-irradiation Ductility Loss of Iron-Nickel Base Precipitation Hardenable Alloys," to be published in J. Nucl. Mater.

8. D. N. Brasky and D. W. Ramey, "A Modified Tritium Trick Technique for Doping Vanadium Alloys With Helium," to be published in Effects of Radiation on Materials: Twelfth Conf., ASTM STP 870, Eds., F. A. Garner and J. S. Perrin (American Society for Testing and Materials, 1985) in press.

9. H. R. Brager, F. A. Garner and P. J. Maziasz, DAFS Quarterly Progress Report DOE/ER-0046/19 (November 1984) 49.

10. R. L. Simons, DAFS Quarterly Progress Report DOE/ER-0046/12 (February 1983) 37.

11. R. J. Puigh and R. E. Schenter, "The In-Reactor Creep Rupture Experiment in MOTA," to be published in Effects of Radiation on Materials: Twelfth Conf., ASTM STP 870, Eds., F. A. Garner and J. S. Perrin (American Society for Testing and Materials, 1985) in press.

12. D. L. Smith et al., Blanket Comparison and Selection Study Final Report ANL/FPP-84-1, September 1984.

13. F. A. Garner and W. G. Wolfer, J. Nucl. Mater. 122 and 123 (1984) 201.

14. W. G. Wolfer, ibid., 367.

15. F. A. Garner, J. Nucl. Mater. 117 (1983) 177.

16. F. A. Garner and H. R. Brager, "Swelling of Austenitic Fe-Cr-Ni Ternary Alloys During Fast Neutron Irradiation," to be published in Effects of Radiation on Materials: Twelfth Conf., ASTM STP 870, Eds., F. A. Garner and J. S. Perrin (American Society for Testing and Materials, 1985) in press.

17. H. R. Brager, F. A. Garner, D. S. Gelles and M. L. Hamilton "Development of Reduced Activation alloys for Fusion Service," HEDL-SA-3181, to be published in J. Nucl. Mater.

18. D. S. Gelles and F. A. Garner, "Swelling Behavior of Manganese-Bearing AISI 216 Steel," HEDL-SA-3150, to be published in J. Nucl. Mater.

19. V. A. Krasnoselov, V. I. Prokhorov, A. N. Kolesnikov and Z. A. Ostrovskii, Atomnaya Energiya, 54, No. 2 (1983), 111.

20. B. J. Makenas, "Swelling of 316 SS 20% Cold Worked Fuel Pin Cladding and Ducts," to be published in Effects of Radiation on Materials: Twelfth Conf., ASTM STP 870, Eds., F. A. Garner and J. S. Perrin (American Society for Testing and Materials, 1985) in press.

21. F. A. Garner and H. R. Brager, "The Role of Phosphorus in the Swelling and Creep of Austenitic Alloys," HEDL-SA-3153, to be published in J. Nucl. Mater.

22. F. A. Garner, H. R. Brager and R. J. Puigh, "Swelling Behavior of Titanium-Modified AISI 316 Alloys," HEDL-SA-3149, to be published in J. Nucl. Mater.

23. D. L. Porter and F. A. Garner, "Swelling of AISI 340L in Response to Simultaneous Variations in Stress and Displacement Rates," to be published in Effects of Radiation on Materials: Twelfth Conf., ASTM STP 870, Eds., F. A. Garner and J. S. Perrin (American Society for Testing and Materials, 1985) in press.

24. F. A. Garner, "A Model Describing the Compositional Dependence of Void Nucleation in Irradiated Fe-Ni-Cr Alloys," HEDL-SA-3024 (1984) to be submitted to J. Nucl. Mater.

25. H. R. Brager and F. A. Garner, "Microsegregation Observed in Fe-35.5Ni-7.5Cr Irradiated in EBR-II," to be published in Effects of Radiation on Materials: Twelfth Conf., ASTM STP 870, Eds., F. A. Garner and J. S. Perrin (American Society for Testing and Materials, 1985) in press.

26. H. R. Brager, F. A. Garner and T. Lauritzen, DAFS Quarterly Progress Report DOE/ER-0046/19 (November 1984) 56.

27. H. R. Brager, F. A. Garner and M. L. Hamilton, "The Influence of Composition on the Microstructural Evolution and Mechanical Properties of Irradiated Fe-Cr-Ni Ternaries," this volume.

28. W. G. Wolfer and F. A. Garner, DAFS Quarterly Progress Report DOE/ER-0046/17 (May 1984) 58.

29. F. H. Huang, Inter. J. of Fracture, 25 (1984) 181.

30. M. L. Hamilton, F. A. Garner and W. J. S. Yang, DAFS Quarterly Progress Report DOE/ER-0046/20, (Feb. 1985) 33.

7.0 Future Work

The reassessment of the utility of fast and thermal reactor data to fusion-relevant studies will continue as additional data become available.

8.0 Publications

This report will be published in a slightly shorter version in the J. of Nuclear Materials, Proceedings of the First International Conference on Fusion Reactor Materials, Tokyo, Japan, Dec. 3-6, 1984.

EFFECTS OF TENSILE AND COMPRESSIVE STRESSES ON IRRADIATION-INDUCED SWELLING IN AISI 316

T. Lauritzen, W. L. Bell, G. M. Konze, J. M. Rosa and S. Vaidyanathan (General Electric Company)

F. A. Garner (Hanford Engineering Development Laboratory)

1.0 Objective

The object of this effort is to identify the effects of applied external or internal stresses on radiation-induced dimensional changes in metals and to predict the impact of these effects on fusion reactor design and performance.

2.0 Summary

The results of two recent experiments indicate that the current perception of stress-affected swelling needs revision. It appears that compressive stresses do not delay swelling as previously modeled but actually accelerate swelling at a rate comparable to that induced by tensile stresses.

3.0 Program

Title: Irradiation Effects Analysis (AKJ)
Principal Investigator: D. G. Doran
Affiliation: Hanford Engineering Development Laboratory

4.0 Relevant DAFS Program Plan Task/Subtask

Task II.C.2.1	Effects of Material Parameters on Microstructure
Task II.C.16	Composite Correlation Models and Experiments

5.0 Accomplishments and Status

5.1 Preface

This report is divided into two parts. The first summarizes earlier experimental and modeling efforts directed toward describing stress-affected swelling. It also describes the conclusions of two recent independent studies which contradict one major facet of the current stress-affected swelling model. The second part describes work by Lauritzen and coworkers at General Electric Company done under the sponsorship of the U.S. Breeder Reactor program; it is published here with the permission of that program.

5.2 Part I

In an earlier report(1) it was shown that many alloys exhibit an enhancement of irradiation-induced void swelling due to the application of biaxial tensile stresses during irradiation. For AISI 316 this enhancement was shown to arise from a shortening of the incubation period of void growth. No effect of stress was seen on the steady-state swelling rate. A correlation developed to describe this phenomenon is currently employed in the U.S. Breeder Reactor Program.(1)

Before this correlation can be employed in fusion reactor design studies, one must consider the impact of the differences in the two reactor environments and also make an assessment on how best to extrapolate the data into untested stress states. It is important to note that the total data base was developed from essentially isothermal irradiations of the walls of thin tubes subjected to a constant biaxial tensile stress. There were no previously published data on the effect of compressive or torsional stress states and no experiments which provided guidance on how to incorporate the effects of stress history. These considerations are potentially quite important for three reasons. First, the stresses anticipated in the first wall of Tokamak-type reactors will be time-dependent, cycling from tensile to compressive, and will not develop gradually like the fission gas loading typical of breeder reactor fuel pins. Second, there is some unpublished evidence which indicates that the current model (based only on microstructural concepts) incorrectly predicts that compressive stresses will delay swelling. These new data indicate that perhaps compressive or torsional stresses also accelerate swelling, particularly at higher temperatures. Third, the duration of the void incubation period of AISI 316 steel has been shown to be primarily determined by the microchemical evolution of the matrix, a process which is normally rather sluggish compared to the microstructural evolution.(2) The greatest sensitivities of the microchemical evolution appear to be associated with variations in flux, temperature and stress, all three of which will undergo pronounced simultaneous variations in the walls of pulsed reactors. The possible synergisms for such complex and sensitive histories may lead to substantial changes in the rate of the microchemical evolution. Additional data presented in later reports indicated that applied tensile stresses indeed accelerate the microchemical evolution at temperatures above 550°C by accelerating the formation of stress-sensitive intermetallic phases.(3-5)

A subsequent modelling effort of the effect of stress on phase formation indicated that the phases formed in AISI 316 would be sensitive only to the hydrostatic component and not the deviatoric component of the stress state.(6) Therefore one would expect that compressive stresses would delay intermetallic phase formation and thereby temporarily suppress swelling. There was some discomfort with this conclusion, however, since all data were derived in a tensile-shear environment and no data on deviatoric or compressive-hydrostatic conditions were available to confirm such a prediction.

Other experimenters were therefore encouraged to generate data for compressive stress environments. Kera and coworkers had earlier used 6 MeV deuteron bombardment at 550°C and demonstrated that tensile stresses accelerate void nucleation and shorten the duration of the transient regime in a Fe-Cr-Ni-Mo quaternary alloy representative of the base composition of AISI 316.(7) They have recently extended this study using 7 MeV protons and both compressive and tensile stresses of 100 MPa at 500°C.(8) They conclude that the irradiation creep rate is unaffected by the sign of the stress, a conclusion that might well be expected. They also find, however, that the swelling is accelerated equally by tensile and compressive stresses.

In another recent study, Lauritzen and coworkers examined the swelling across a bent beam specimen of 20% cold-worked AISI 316 strained in a four-point bending mode during fast neutron irradiation in EBR-II at 400-425°C.(9) They found that void nucleation and swelling at ∿40 dpa were accelerated equally on both the tensile and compressive sides of the beam when compared to the region of the beam encompassing the neutral stress axis. Lauritzen and coworkers have now extended this study to higher neutron fluence. This work is described in the next section.

5.3 Part II

5.3.1 Introduction

In a recent publication,(9) we presented experimental evidence that irradiation-induced swelling in AISI 316 is increased by an applied bending stress at irradiation temperatures representative of operating LMFBR fuel assembly ducts. The results further indicated that the observed swelling enhancement was due to an accelerated nucleation of voids in both tension and compression regions of bent beams relative to that of a zero stress region at the beam centerline. However, because the specimens examined in that study accumulated a moderately low fluence (8×10^{22} n/cm^2, E > 0.1 MeV), the swelling was rather small with correspondingly large uncertainties. Moreover, it was assumed, based on the current swelling data and design equations, that the swelling represented by this fluence level was still well within the incubation regime. As a result of the interest that these data generated and the implications of stress-enhanced swelling on core structural materials, the experimental and analytical program was extended to evaluate sibling specimens of AISI 316 which had been reconstituted for additional irradiation.

In the present work, three beams ranging in fluence from 11.2 to 14.9x10^{22} n/cm^2 were selected for examination. The results of those examinations along with summaries of the previous low-fluence data are presented below.

5.3.2 Description of Material

The 20 percent cold-worked 316 specimens examined in this program were prepared as 0.030-inch thick coupons from wrought stock of Carpenter Heat No. K81581. The specimens were irradiated as uniform beam creep specimens in the C1 irradiation creep experiment, details of which have been given in numerous progress reports. (See, for example, Reference 10 and the bibliography appended thereto.) The multiple-element specimen train used in this experiment was designed to permit the removal of the entire train, fully encapsulated in a sodium-filled duct, from the irradiation capsule at various irradiation intervals for nondestructive examination of the weighted beams by neutron radiography. At the completion of one of these examination periods (after the fifth interim examination and the accumulation of a peak fluence of roughly 8x10^{22} n/cm^2, E > 0.1 MeV), it was discovered that the 22-element train had extended to such a degree that further irradiation would have caused the deadweight loading the train to bottom-out at the base of the capsule. Since the train was arranged into four modules of five to seven elements per module, it was decided to remove the lower two modules from the train, reattach the deadweight to the upper modules and resume the irradiation. Having done this, the lower modules were available for destructive examination and subsequently provided beams 13 and 15 for the first swelling examination. The remaining two modules, containing a total of twelve beams, accumulated an additional peak fluence of 7x10^{22} n/cm^2 before the experiment was terminated at 15 x 10^{22} n/cm^2.

The three reconstituted beams selected for swelling examination included the highest fluence beam, the highest temperature beam and the beam estimated from the current swelling design equation to have undergone the largest swelling. These beams were numbered 12, 6 and 8, respectively. Their irradiation and stress-strain histories are given, along with data from the previously reported two beams, in Table 1.

TABLE 1

Irradiation Parameters and Loading/Strain Conditions of the LUB/LUM Uniform Beam Specimens Selected for TEM Examination

Beam No.	Irrad. Temp., °C	Fluence, n/cm^2 (E > 0.1)	Stress, MPa Initial	Stress, MPa Final	Final Strain, % Elastic	Final Strain, % Creep	Total
15	412	7.6x10^{22}	328	151	0.09	2.3	2.4
13	423	7.8x10^{22}	159	143	0.09	1.2	1.3
6	458	11.2x10^{22}	85	81	0.05	1.2	1.2
8	444	13.0x10^{22}	237	59	0.04	3.6	3.6
12	420	14.9x10^{22}	82	72	0.04	1.3	1.4

After removing the sodium from the specimen train, duplicate samples of each beam were cut astride the peak-curvature centerline of the beam, as shown in Figure 1, step 1. The samples were roughly 3/16-inch in width, 0.030-inch thick, and as long as the individual beams were wide. (This dimension varied from 0.17 inch in Beam 8 to 0.30 inch in Beam 12). Extreme care was exercised throughout the sample extraction procedure to minimize any extraneous stresses on the beams.

After extraction from the beam train, the samples were removed from the hot cell for the preparation of discs for TEM. The sequence of events followed in this phase of sample preparation is illustrated in steps 2 through 5, Figure 1. In step 2, the sodium-exposed surfaces (both concave and convex surfaces) were lightly buffed with 400-grit metallographic paper to remove scale and oxide films that have been found to interfere with subsequent electro-discharge machining and electropolishing. The buffed surfaces were then electropolished lightly to remove the superficial cold-worked layer produced by buffing. This procedure removed, on the average, approximately 0.001-inch of surface. In step 3, one of the two samples from each beam was sliced through its thickness with an 0.006-inch thick diamond-impregnated cutoff wheel to isolate the tension region from the compression region of the beam and to provide a more optimum foil thickness for single-jet electropolishing. While maintaining strict identification of surfaces and stress states, duplicate 3-mm diameter discs were cut by electrodischarge machining from each of the two slices, as shown in step 4. These discs were then perforated from the sliced surface by single-jet electropolishing to provide thin foils of the tension and compression regions of each beam at a depth from the original surface not substantially greater than the 0.001-inch depth removed in step 2.

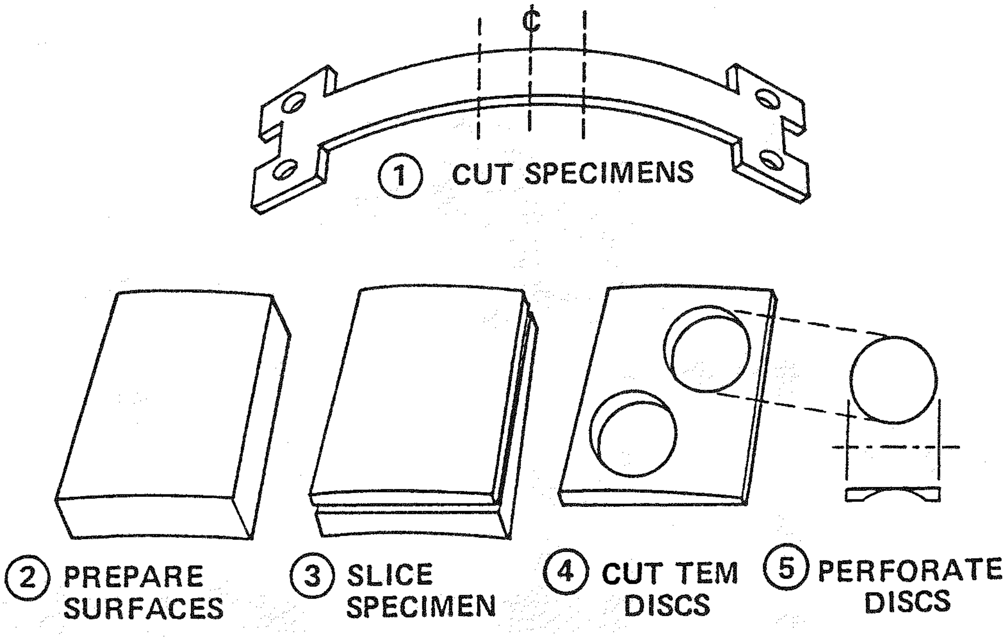

FIGURE 1. Sequence of Operations Followed in the Preparation of the TEM Foils of Cl Uniform Beam Specimens.

Foils of the neutral axis of the beams were prepared by twin-jet electropolishing of discs cut from the unsliced specimen of each beam. Since the polishing rates of the two jets in a twin-jet electropolisher are rarely the same, electropolishing was interrupted at measured intervals during preparation of the neutral axis foils to rotate the discs 180° in the polishing apparatus. This assured that the perforation occurred as close to the true centerline (i.e., the neutral axis) as possible. All electropolishing was performed with a Fischione twin-jet electropolisher; the electrolyte was a solution of 20 percent perchloric acid in ethanol maintained at -40°C. The foils were examined in a JEM-6A electron microscope operated at 100 kV.

5.3.3 Results and Discussion

Void images representative of the tension, compression and neutral regions of Beams 6, 8 and 12 are shown in Figures 2, 3 and 4 respectively. The three beams were extracted from the Cl creep assembly after the eighth and final discharge of the assembly from EBR-II. Although the in-reactor residence time of all beams was the same, the irradiation history of each is unique as the result of their different axial locations in the core. The differences in irradiation parameters (see Table 1 for details) are readily apparent when one compares the void images of the three beams. (To permit a one-to-one comparison of the three sets of images, plates with the same magnification and representing foils of similar thickness were selected for the figures.) Aside from the striking differences between the void distribution of Beam 6 and those of beams 8 and 12, the most significant observations one can make without benefit of quantitative void image analysis are that (1) a sharp difference in void density exists between stressed and unstressed regions and (2) there appears to be little difference in void density between tension and compression regions of the beams.

To more clearly demonstrate the effect of as much as a factor of two increase in fluence, these images can be compared with those collected from beams 13 and 15 (Figure 5) after their removal from the test assembly at the conclusion of interim examination No. 5. The sharp increases in both void size and void density are readily apparent.

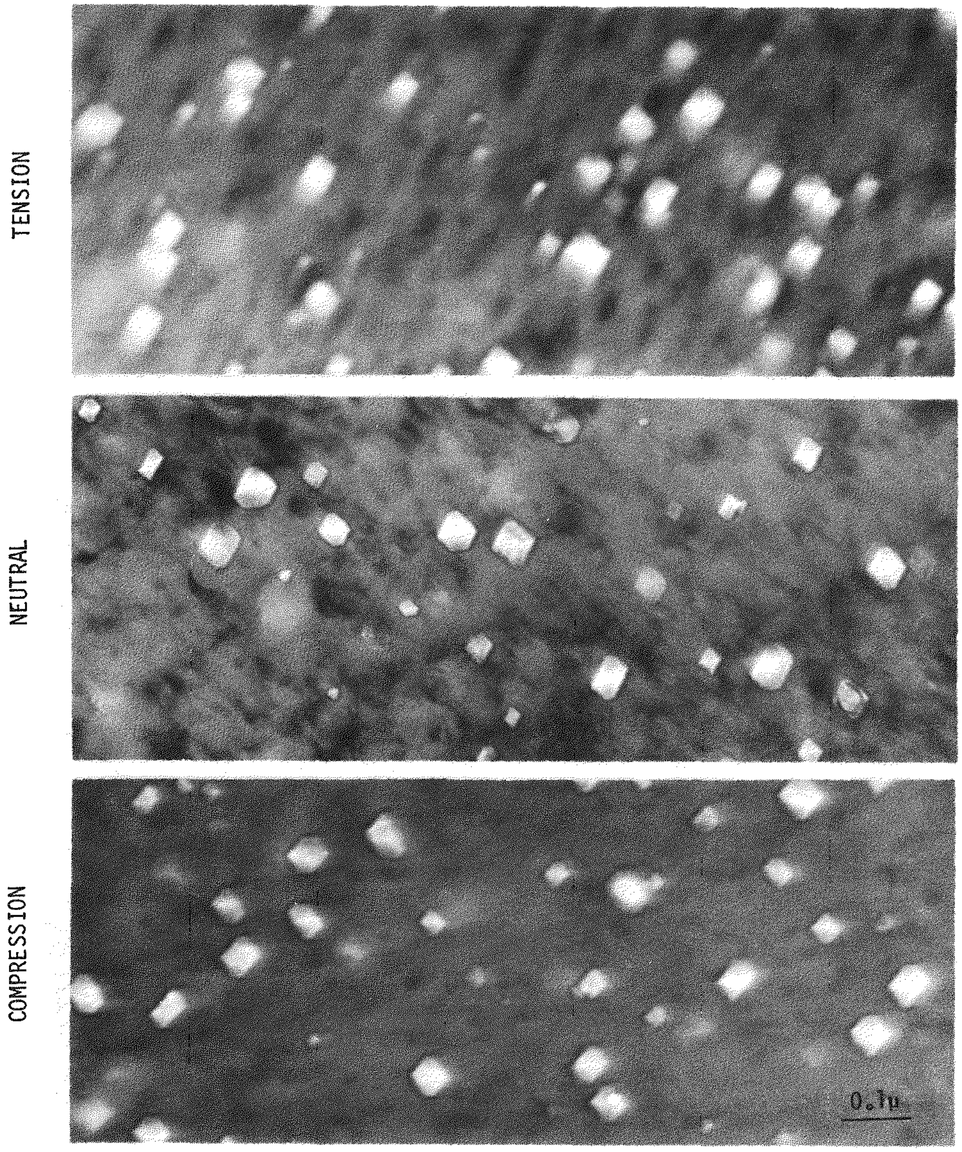

FIGURE 2. Void Images Representative of the Tension Side, the Neutral Axis and the Compression Side of AISI 316-CW Bent Beam Specimen 6. Beam 6 was irradiated at 450°C to 11.2×10^{22} n/cm^2 ($E > 0.1$ MeV) and sustained a total strain of 1.2 percent.

At least six regions of each foil were examined in detail and analyzed for void size, void density and percent void swelling. Weighted averages of the three types of data are summarized in Table 2 for the three beams examined in this program and the two low fluence beams examined earlier. The results show a clear effect of stress on swelling in the two highest fluence specimens, beams 8 and 12, with swelling levels in the tension and compression regions about a factor of two higher than in the unstressed central zone of the beams. These results corroborate the findings on Beam 13, as previously reported [9]. In the latter work, we proposed that the increase in swelling with stress was due to an accelerated void nucleation in the stressed material, as the data on both beams 12 and 13 seem to indicate. However, this explanation does not fit the trends shown by Beam 8 whose void densities are relatively uniform throughout the thickness of the beam, but whose void sizes are not only substantially higher than Beam 12 but show a sizeable increase in the stressed regions relative to that of the central unstressed zone. These increases in void sizes do not appear to reflect the slightly higher irradiation temperature, since Beam 6, with an even higher temperature exhibits void sizes comparable to those of Beam 12. Moreover, if this increase were a purely thermal effect, one would expect to see a corresponding increase in void size of the unstressed material. This clearly was not the case. Thus, the data seem to indicate that the stress-enhanced swelling observed in Beam 8 is the result of accelerated void growth rather than accelerated void nucleation as the Beam 12 and earlier data had indicated.

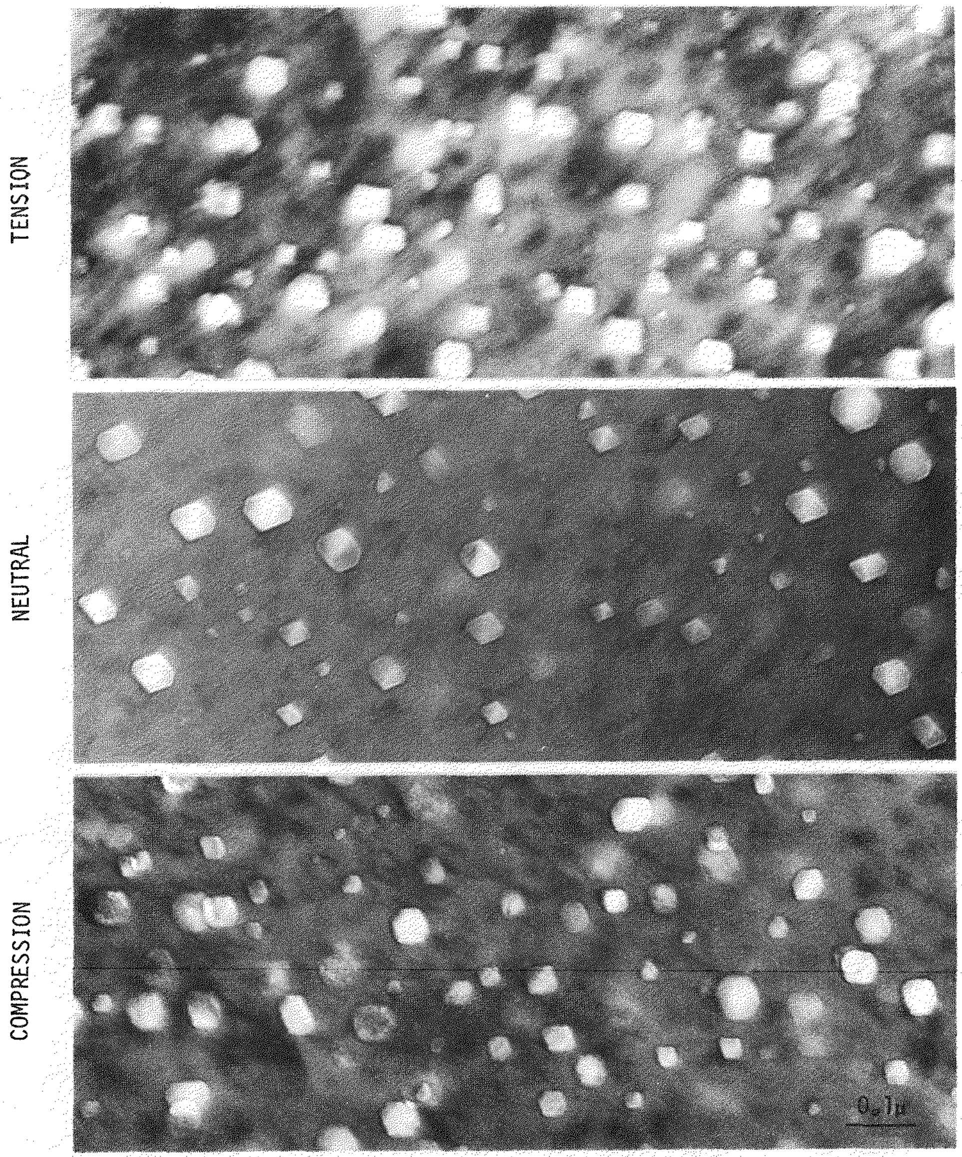

FIGURE 3. Void Images Representative of the Tension Side, the Neutral Axis and the Compression Side of AISI 316-CW Bent Beam Specimen 8. Beam 8 was irradiated at 444°C to 13.0×10^{22} n/cm^2 ($E > 0.1$ MeV) and sustained a total strain of 3.6 percent.

Except for a slightly higher fluence level in Beam 12 and a 24-degree higher temperature in Beam 8, the only significant difference between the two beams is their stress-strain histories. Beam 8 was originally loaded to a peak fiber stress of 237 MPa; the load on Beam 12 was 82 MPa. By the end of the irradiation, these stresses were reduced to 59 and 72 MPa, respectively, but the total strain accumulated by Beam 8 was more than twice that of Beam 12. These differences in stress-strain histories are clearly illustrated in Figure 6. Thus, the Beam 8 data showing accelerated void growth and the Beam 12 data showing accelerated void nucleation as a function of stress suggest that the mechanism for stress-enhanced swelling, although independent of the sign of the applied stress, may be a sensitive function of the magnitude of that stress.

6.0 References

1. F. A. Garner, E. R. Gilbert and D. L. Porter, "Stress-Enhanced Swelling of Metals During Irradiation," Proc. ASTM 10th International Symposium on Effects of Radiation on Materials, ASTM STP 725, Savannah, GA, June 3-5, 1980, 680-697.

2. F. A. Garner, "The Microchemical Evolution of Irradiated Stainless Steels," HEDL-SA-2159, Proceedings of AIME Symposium on Irradiation Phase Stability, October 5-9, 1980, Pittsburgh, PA, 165-189.

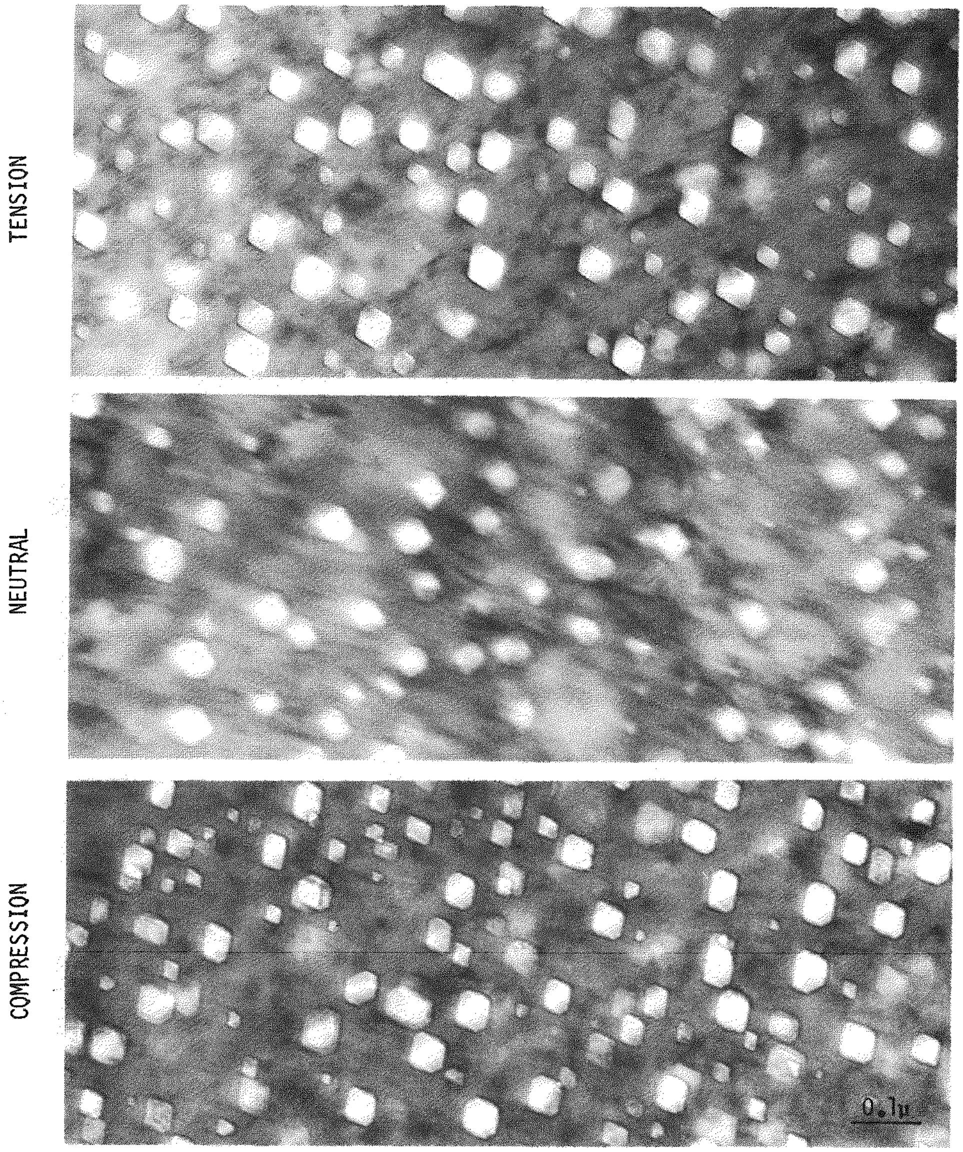

FIGURE 4. Void Images Representative of the Tension Side, the Neutral Axis and the Compression Side of AISI 316-CW Bent Beam Specimen 12. Beam 12 was irradiated at 420°C to 14.9x10^{22} n/cm^2 (E > 0.1 MeV) and sustained a total strain of 1.4 percent.

3. F. A. Garner, "Extrapolation of Stress-Affected Swelling Models Into Compressive and Cyclic Stress States," DAFS Quarterly Progress Report, DOE/ER-0046/5, 198-218.

4. F. A. Garner and D. L. Porter, "History Dependence and Consequences of the Microchemical Evolution of AISI 316," Effects of Radiation on Materials: Eleventh Conference, ASTM STP 782, H. R. Brager and J. S. Perrin, Eds., 1982, 295-309.

5. R. J. Puigh, A. J. Lovell and F. A. Garner, J. Nucl. Mater. 122 & 123 (1984), pp. 242-245.

6. K. C. Russell and F. A. Garner, "The Effect of Applied Stress on Precipitate Stability in Irradiated AISI 316," DAFS Quarterly Progress Report, DOE/ER-0046/7, 180-197.

7. S. K. Khera, C. Schwaiger and H. Ullmaier, J. Nucl. Mater. 92, 299-305, 1980.

8. P. Jung and H. K. Sahu, "Void Swelling and Irradiation Creep in Stainless Steel Under Compressive and Tensile Stress," presented at the First International Conference on Fusion Reactor Materials, Tokyo, Dec. 3-6, 1984.

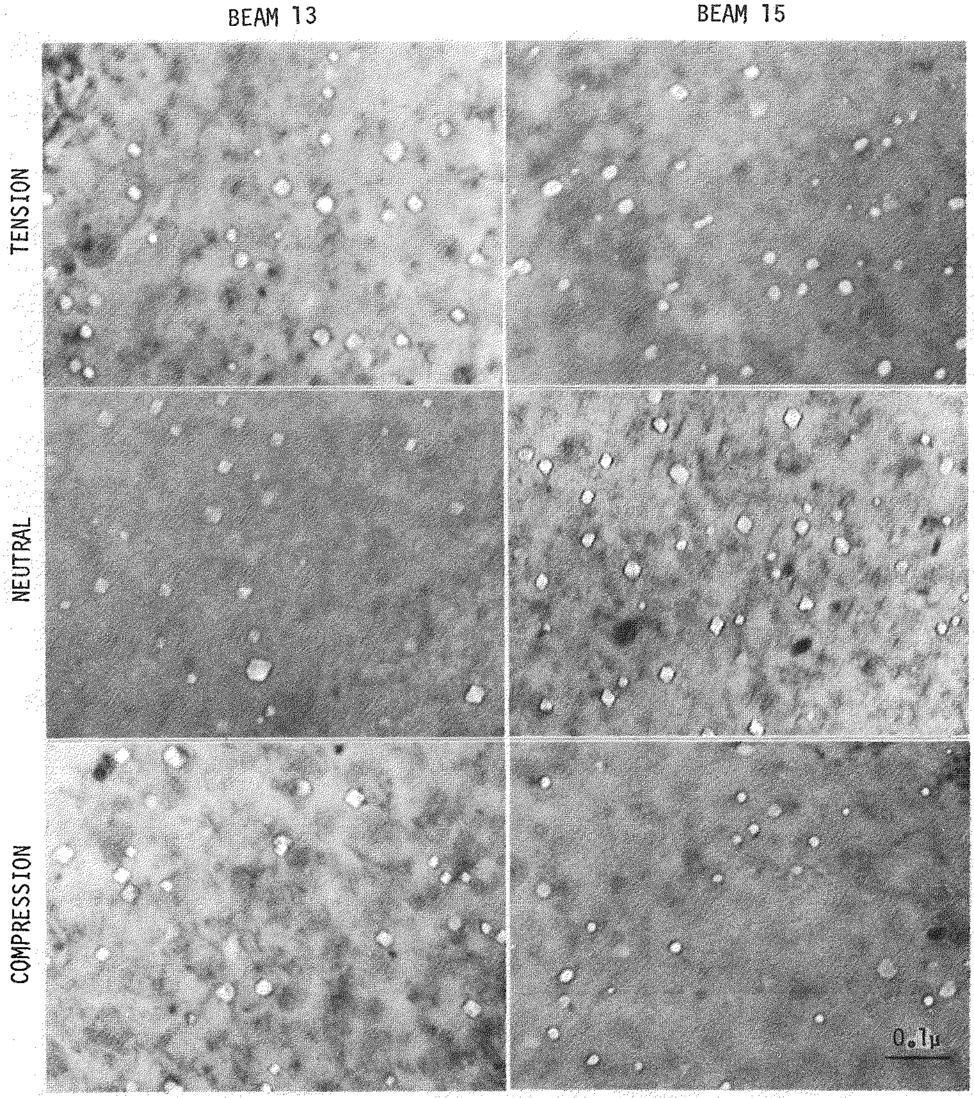

FIGURE 5. Void Images Representative of the Tension Side, the Neutral Axis and the Compression Side of AISI 316-CW Bent Beam Specimens 13 and 15. Beam 13 was irradiated at 423°C to 7.8×10^{22} n/cm^2 ($E > 0.1$ MeV) and sustained a total strain of 1.3 percent; Beam 15 was irradiated at 412°C to 7.6×10^{22} n/cm^2 and sustained a total strain of 2.4 percent.

9. T. Lauritzen, W. L. Bell, J. M. Rosa and S. Vaidyanathan, "Some Observations on the Effect of Stress on Irradiation-Induced Swelling in AISI 316," Effects of Radiation on Materials, 12th Conference, F. A. Garner and J. S. Perrin, Eds., American Society for Testing and Materials, 1984, in publication.

7.0 Future Work

These and other recent data on the stress-affected development of radiation-induced microstructure are being compiled prior to an extensive reanalysis of the models employed in creep and stress-affected swelling.

8.0 Publications

None.

TABLE 2

Void Swelling Data: Effect of Stress on Swelling in 20 Percent Cold Worked AISI 316

BEAM NO.	FLUENCE n/cm^2 (E > 0.1)	IRRAD. TEMP., °C	STRESS STATE	AVERAGE SWELLING PARAMETERS		
				VOID DIA., Å	VOID DENSITY cm^{-3}	SWELLING, %
12	14.9×10^{22}	420	TENSION	350	1.61×10^{15}	3.6
12	14.9×10^{22}	420	NEUTRAL	359	0.86×10^{15}	2.1
12	14.9×10^{22}	420	COMPRESSION	372	1.38×10^{15}	3.7
8	13.0×10^{22}	444	TENSION	432	0.84×10^{15}	3.5
8	13.0×10^{22}	444	NEUTRAL	342	0.71×10^{15}	1.6
8	13.0×10^{22}	444	COMPRESSION	423	0.74×10^{15}	3.1
6	11.2×10^{22}	458	TENSION	360	0.35×10^{15}	0.9
6	11.2×10^{22}	458	NEUTRAL	383	0.29×10^{15}	0.9
6	11.2×10^{22}	458	COMPRESSION	364	0.35×10^{15}	1.1
13	7.8×10^{22}	423	TENSION	215	0.71×10^{15}	0.4
13	7.8×10^{22}	423	NEUTRAL	211	0.40×10^{15}	0.2
13	7.8×10^{22}	423	COMPRESSION	191	0.83×10^{15}	0.3
15	7.6×10^{22}	412	TENSION	190	0.67×10^{15}	0.2
15	7.6×10^{22}	412	NEUTRAL	171	0.72×10^{15}	0.2
15	7.6×10^{22}	412	COMPRESSION	182	0.64×10^{15}	0.2

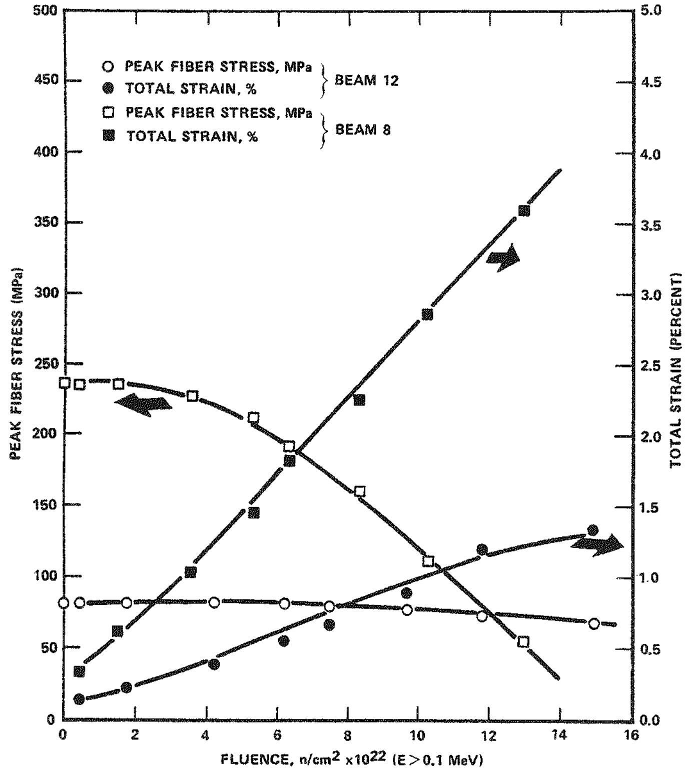

FIGURE 6. Stress-strain Histories of Irradiated AISI 316-CW Bent Beam Specimens 8 and 12.

EARLY DEVELOPMENT OF SPINODAL DECOMPOSITION IN NEUTRON-IRRADIATED Fe-35Ni-7.5Cr AT 550°C

H. R. Brager and F. A. Garner (Hanford Engineering Development Laboratory)

1.0 Objective

The object of this effort is to determine the microstructural and microchemical origins of radiation-induced changes in physical properties and dimensions.

2.0 Summary

In Fe-35Ni-7.5Cr irradiated at 550°C to 2.5×10^{22} n/cm^2 ($E > 0.1$ MeV) the spinodal decomposition observed at higher irradiation temperatures and higher neutron exposures is just beginning to form. The decomposition appears to begin very heterogeneously and may be assisted by the action of the inverse Kirkendall mechanism operating at various microstructural sinks.

3.0 Program

Title: Irradiation Effects Analysis (AKJ)
Principal Investigator: D. G. Doran
Affiliation: Hanford Engineering Development Laboratory

4.0 Relevant DAFS Program Plan Task/Subtask

Subtask II.C.1 Effects of Material Parameters on Microstructure

5.0 Accomplishments and Status

5.1 Introduction

In an earlier report it was shown that the radiation-induced changes in the tensile properties of annealed Fe-Cr-Ni alloys in the AD-1 experiment (irradiated at 450°C and 2.5×10^{22} n/cm^2 ($E > 0.1$ MeV) in FFTF-MOTA) were somewhat sensitive to nickel content in the range of 25 to 45 wt% but were not sensitive to chromium content.[1] It was also shown, however, that the component of radiation-induced hardening arising from microstructural components such as voids, Frank loops and network dislocations decreased relatively strongly with nickel content. The major effect was found to be the dependence of void density on nickel content.

This caused a disparity between the measured change in yield strength and that predicted from knowledge of the various microstructural densities. As shown in Figure 1, this disparity increases with nickel content and is attributed to the hardening that arises from spinodal decomposition. At the time it was considered infeasible to actually measure the spinodal period and confirm its presence because the wavelength at 450°C was expected to be on the order of the resolution of the x-ray analysis technique employed. It would also be difficult to measure because the large number of voids with their associated segregation would interfere with the measurement.

It was therefore decided to examine the E37 (Fe-35Ni-7.5Ci) specimen irradiated to the same fluence at 550°C. This specimen was chosen because the oscillation period should be larger and the void density should be lower than that obtained at 450°C. The oscillation period is still expected to be smaller than that observed at 593°C in EBR-II[2] and at 625°C with nickel ion irradiation.[3]

Based on the results of earlier studies, however, there was some concern that the spinodal process at this exposure level might not be very well advanced. Figure 2 shows the results of density measurements for this alloy over a range of irradiation temperatures from another experiment conducted in EBR-II. Note that the densification associated with spinodal decomposition does not appear to begin until exposures of 2 to 3 x 10^{22} n/cm^2 (E > 0.1 MeV). The density change of the E37 specimen chosen for examination is only -0.14% compared to the -0.9% maximum that can be realized by decomposition. The arrow in Figure 2 points to a measurement of the maximum densification at 593°C and 7.6 x 10^{22} n/cm^2 (E > 0.1 MeV).

5.2 Experimental Details

Microscopy disks were removed from the shoulder portion of a tensile specimen which had not been subjected to tensile testing. Standard specimen preparation, microscopy and EDX analysis techniques were employed. Due to their very low concentration, various microstructural features such as voids, dislocations or surface artifacts were used as markers from which to initiate compositional traverse measurements. The measurements were made on areas about 70 nm thick and were performed parallel to the edge of the central hole to reduce thickness gradients along the traverse line.

5.3 Results

As anticipated, the void density at this temperature and exposure level was very low (<10^{12} cm^{-3}) and the dislocation density was on the order of 10^{-9} cm^{-2}. No Frank loops or precipitates were observed.

Figures 3 and 4 show that, on the average, micro-oscillations exist, but they are less pronounced than those observed in earlier studies at higher exposure levels. As was also observed previously, nickel tends to flow in the opposite direction from that of iron and chromium.

Figure 5 shows much more pronounced ranges of variation were also found occasionally, however. The dominant feature in Run #7 of Figure 5 is the influence of a small ($\sim$50 nm) void which strongly alters the composition in its neighborhood, presumably by the action of the inverse-Kirkendall mechanism. The cause of the far-reaching gradient shown in Figure 5b was not determined and may be associated with a microstructural feature that originally lay outside the current foil volume.

Figure 6 contains a compilation of the data in Figures 3-5 showing the developing tendency of the spinodal decomposition to split toward Fe_3Ni and FeNi. More advanced levels of decomposition observed at higher temperatures and exposures are shown in Figure 7.

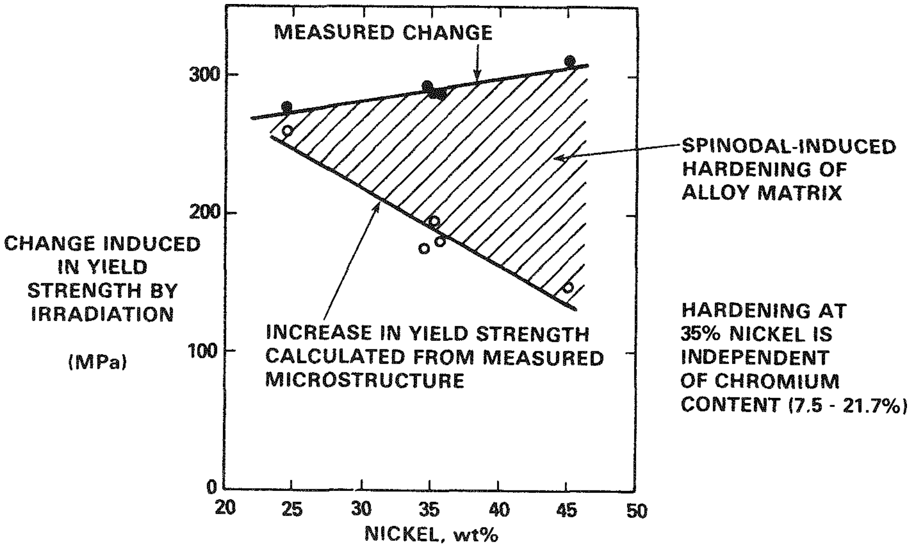

FIGURE 1. Disparity Observed in the AD-1 Experiment Between Measured and Calculated Increases in Yield Strength Due to Irradiation at 450°C to 2.5 x 10^{22} n/cm^2 (E > 0.1 MeV) or $\sim$12 dpa.[1]

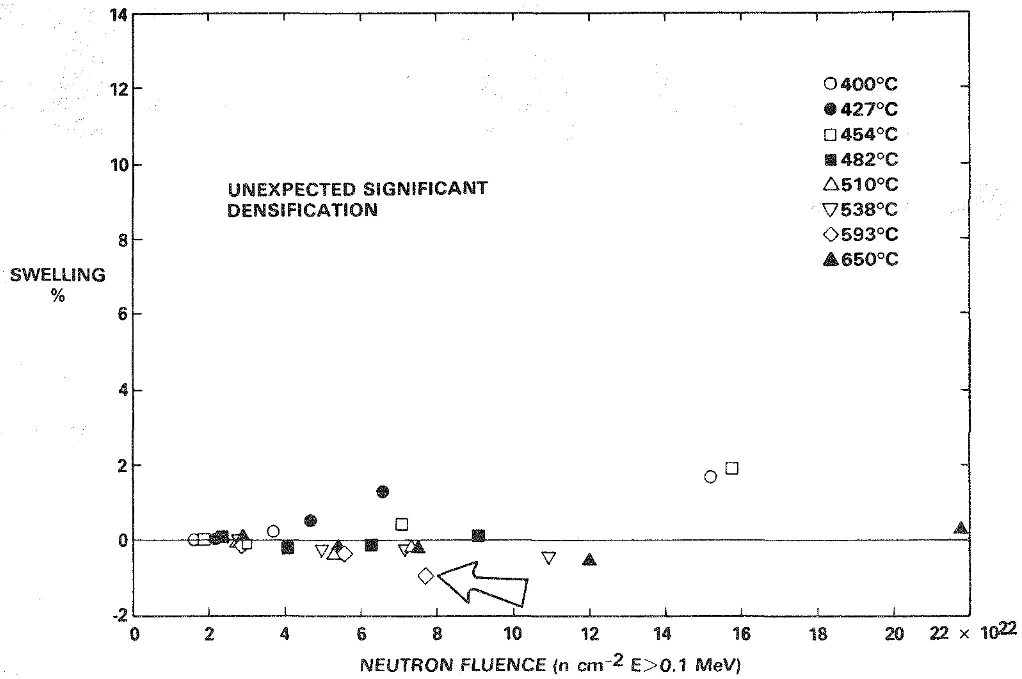

FIGURE 2. Swelling of Annealed Fe-35Ni-7.5Cr Ternary Alloy in EBR-II.[4]

5.4 Discussion and Conclusions

It appears that at 550°C and 2×10^{-6} dpa/s, the evolution of the spinodal process in Fe-35.5Ni-7.5Cr requires $\sim$10 dpa prior to the onset of measurable micro-oscillations or significant densification. The onset of the process is very heterogeneous and may be accelerated locally by the action of the inverse-Kirkendall mechanism at microstructural sinks such as voids.

6.0 References

1. H. R. Brager, F. A. Garner and M. L. Hamilton, "The Influence of Composition on Microstructural Evolution and Mechanical Properties of Irradiated Fe-Ni-Cr Ternaries," DAFS Quarterly Report DOE/ER-0046/20, (Feb. 1985) 41-47. To be published in the J. of Nuclear Materials.

2. H. R. Brager and F. A. Garner, "Microsegregation Observed in Fe-35.5Ni-7.5Cr Irradiated in EBR-II," DAFS Quarterly Report DOE/ER-0046/18, (Aug. 1984) 98-106.

3. H. R. Brager, F. A. Garner and T. Lauritzen, "Compositional Micro-Oscillations in Ion-Bombarded Fe-35.0Ni-7.0Cr," DAFS Quarterly Report DOE/ER-0046/19, (Nov. 1984) 56-61.

4. F. A. Garner and H. R. Brager, "Swelling of Austenitic Fe-Ni-Cr Ternary Alloys During Fast Neutron Irradiation," DAFS Quarterly Report DOE/ER-0046/14, (Aug. 1983) 152-159.

7.0 Future Work

Tensile tests will continue on the AD-1 specimens irradiated at 550°C and also at 395°C. Small angle neutron scattering and 2 1/2-D microscopy studies on these specimens are also planned.

8.0 Publications

None.

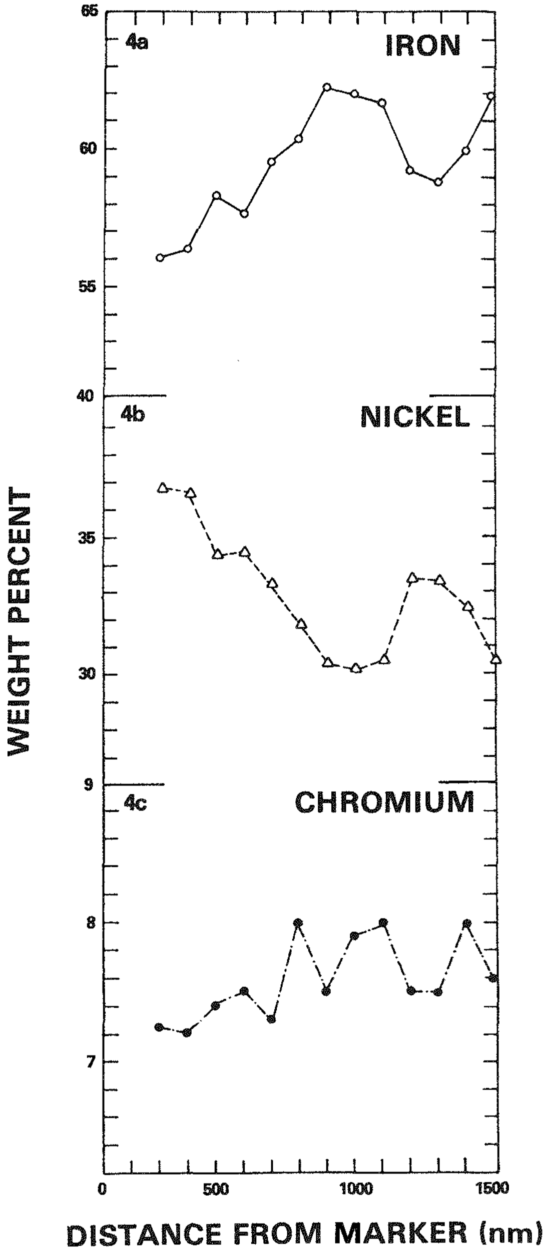

Figure 3. Compositional Traverse of E37 Alloy After Irradiation in FFTF-MOTA at 550°C and 2.5 x 10^{22} n/cm^2 (E > 0.1 Mev). The number in the left upper corner of each graph is the traverse identification number.

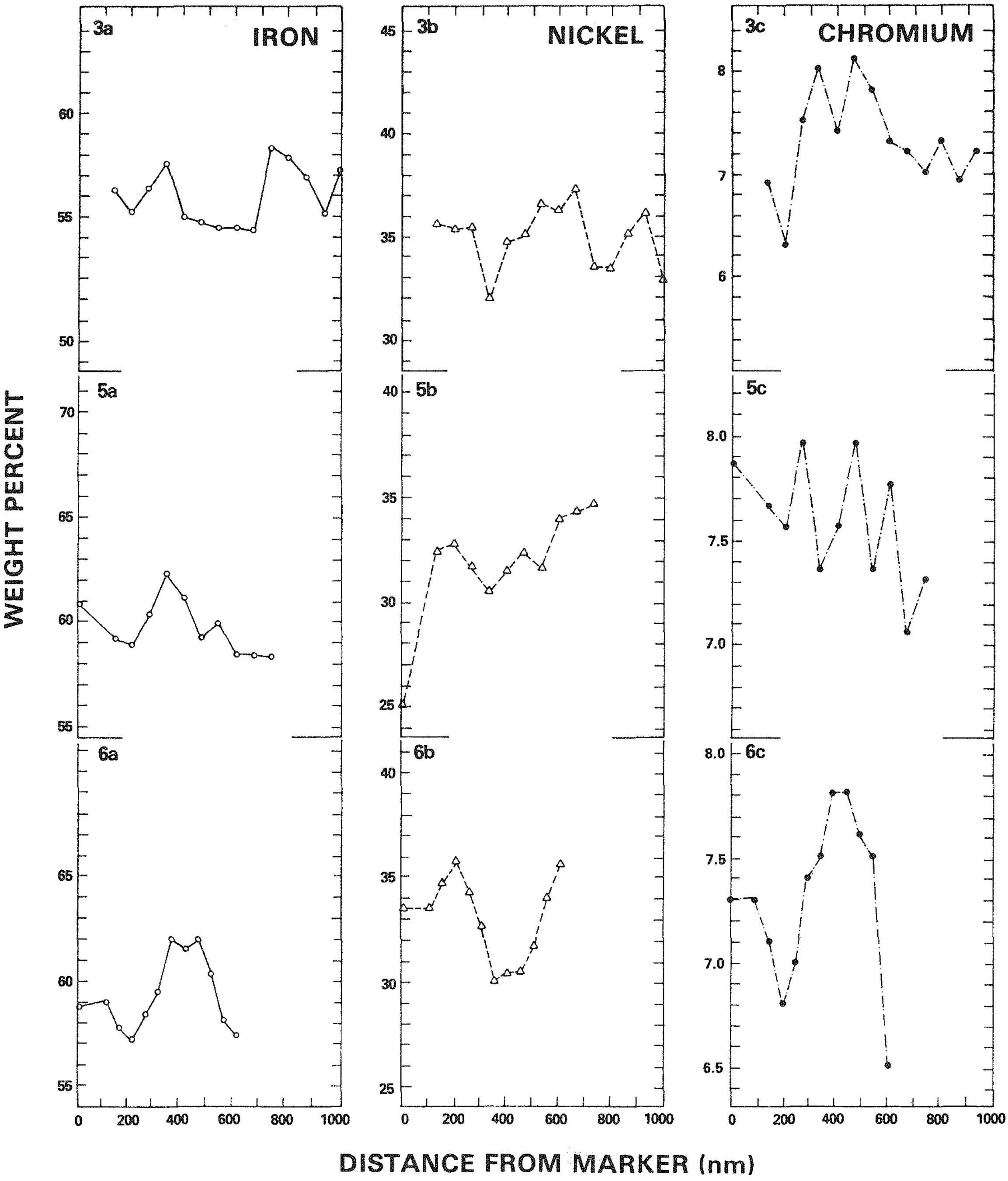

FIGURE 4. Compositional Traverses of E37 Alloy After Irradiation in FFTF-MOTA at 550°C and 2.5 x 10^{22} n/cm^2 (E > 0.1 MeV).

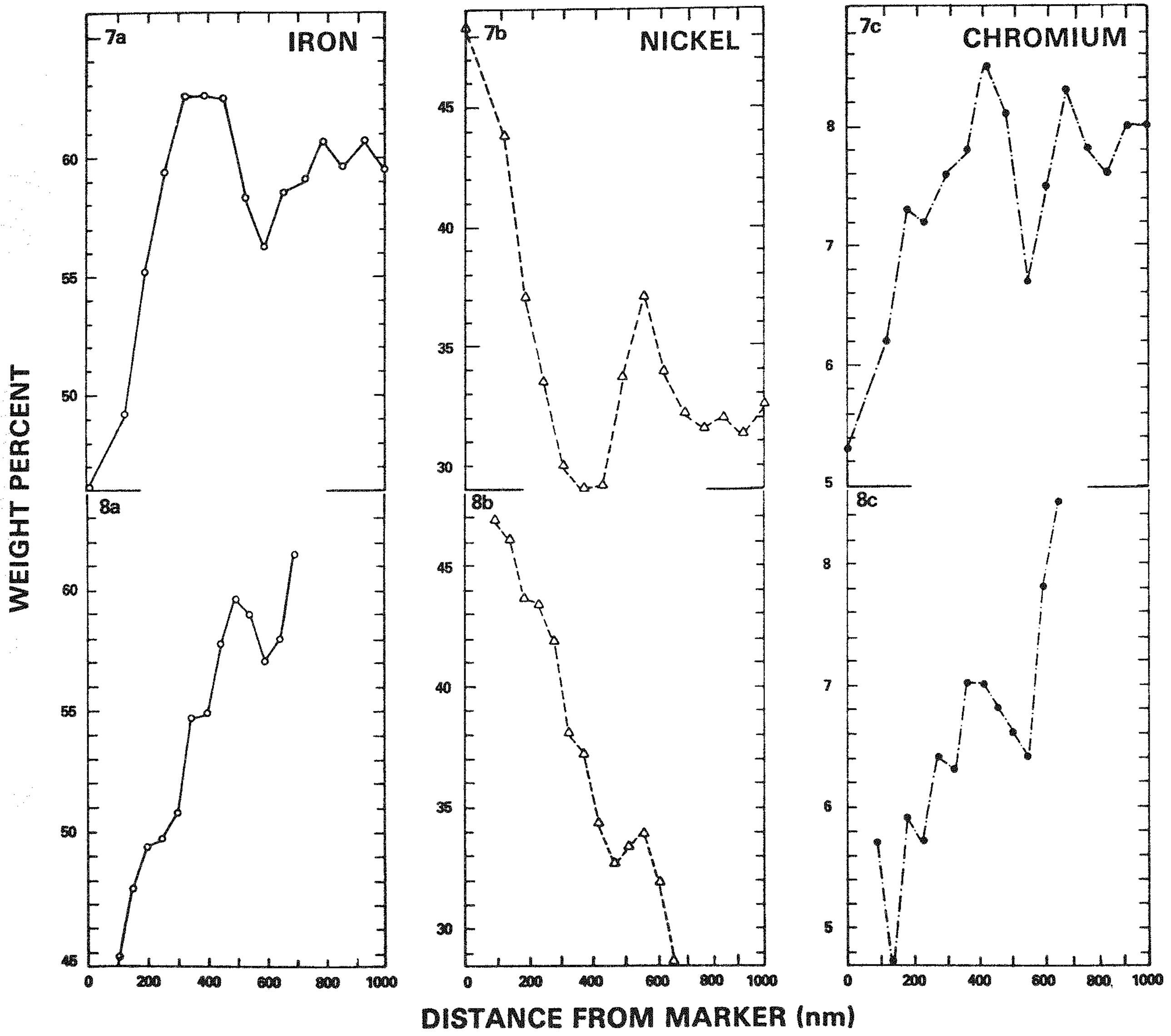

FIGURE 5. Additional Compositional Traverses of E37 Alloy After Irradiation in FFTF-MOTA at 550°C and 2.5×10^{22} n/cm^2 (E > 0.1 MeV).

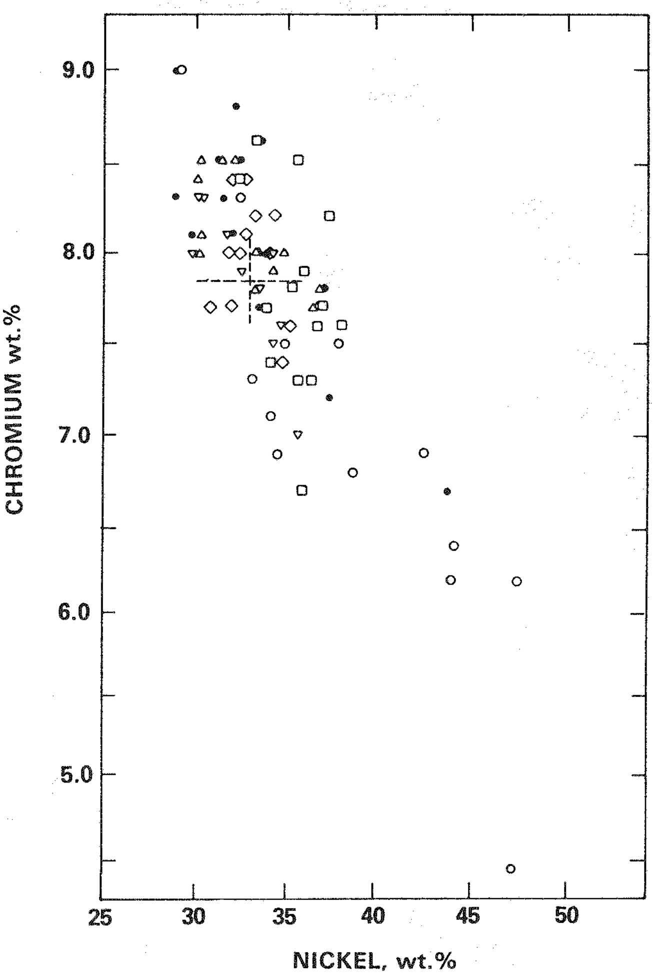

FIGURE 6. Compilation of Radiation-Induced Decomposition Data for Alloy E37 at 550°C and 2.5 x 10^{22} n cm^{-2} (E > 0.1 MeV), Showing the Tendency of Nickel to Flow in the Opposite Direction From That of Chromium. Iron Exhibits the Same Behavior as Chromium.

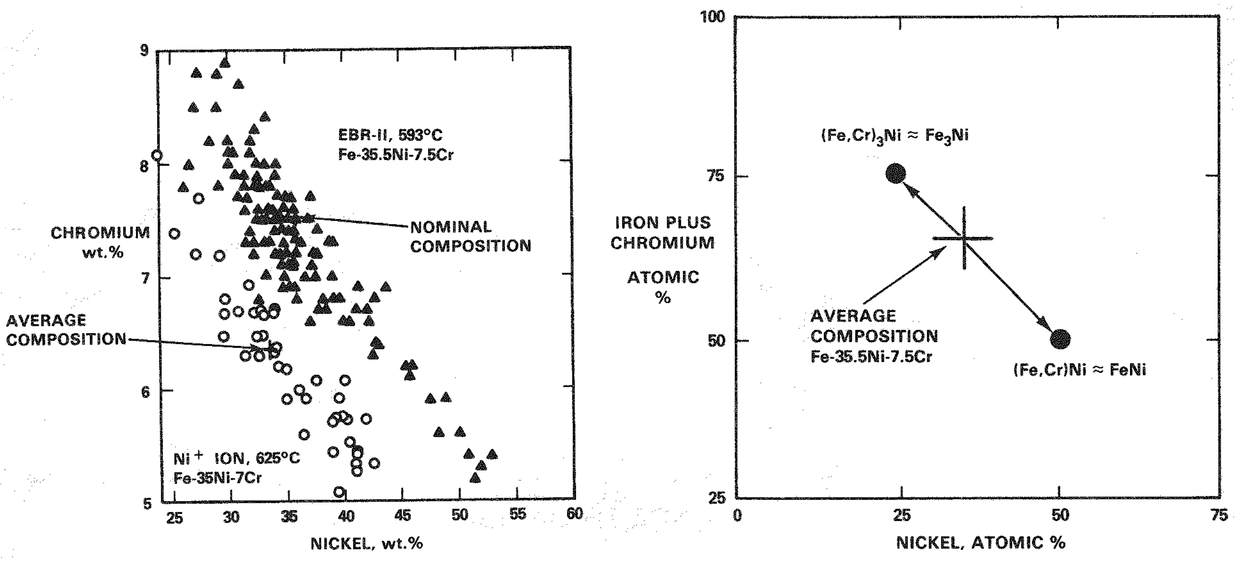

Figure 7. (a) Data Similar to That of Figure 9 From Earlier Studies at Higher Temperature,[2,3] and (b) Schematic Diagram Showing End-Points of Spinodal Decomposition of E37 Alloy.

OWR/RTNS-II LOW EXPOSURE SPECTRAL EFFECTS EXPERIMENT

H.L. Heinisch (Westinghouse Hanford Company)

1.0 Objective

The objective of this experiment is to determine the effect of the neutron spectrum on radiation-induced changes in mechanical properties for metals irradiated with fission and fusion neutrons.

2.0 Summary

The first RTNS-II irradiation of the Low Exposure Spectral Effects Experiment has been completed. The dosimetry has been analyzed, and expressions have been determined that fit the data very well. The effects of including the angular variation of the neutron spectrum were investigated.

3.0 Program

Title: Irradiation Effects Analysis
Principal Investigator: D. G. Doran
Affiliation: Hanford Engineering Development Laboratory

4.0 Relevant DAFS Program Plan Task/Subtask

Subtask II.B.3.2	Experimental Characterization of Primary Damage State; Studies of Metals
Subtask II.C.6.3	Effects of Damage Rate and Cascade Structure on Microstructure; Low-Energy/High-Energy Neutron Correlations
Subtask II.C.16.1	14-MeV Neutron Damage Correlation

5.0 Accomplishments and Status

5.1 Irradiations

The HEDL Low Exposure Spectral Effects Experiment is described in detail in an earlier report.(1) The irradiations consist of two primary RTNS-II irradiations (R-1 and R-2) and eight irradiations at the Omega West Reactor (O-1 through O-8). R-1, to a peak fluence of 2.4 x 10^{18} n/cm^2, has been completed, and R-2, scheduled for a peak fluence of 1 x 10^{19} n/cm^2, is in progress. The Omega West irradiations will begin immediately after installation of the In-core Reactor Furnace is completed.

R-1 and R-2 have been parts of joint US/Japan irradiations using the HEDL dual-temperature vacuum insulated furnace. These irradiations contain specimens for several other US experiments as well as specimens for approximately twelve Japanese experimenters.

5.2 R-1 Dosimetry

Dosimetry foils from R-1 have been analyzed, and the information has been used to determine neutron doses for the tensile specimens. The dosimeters in the main irradiation volume of the furnace consisted of Fe foils, utilizing the ^{54}Fe(n,p)^{54}Mn reaction. The 18 foils (9 in each temperature zone) were 0.025 mm thick with an area equal to the cross section of the specimen volume in each zone, 10.2 x 12.7 mm.

After loading the sample holders, the position of each dosimetry foil relative to the front foil (the first specimen in each zone) was measured directly using a traveling microscope at 10X.

After irradiation, the foils were analyzed by Ruth Nuckolls at LLNL. Each of the rectangular foils was cut into 9 equal pieces (a 3 x 3 rectangular array). The mass and ^{54}Mn gamma activity of each small piece was measured, and neutron fluences were determined from the activity and the facility operating time history information.

Expressions for the flux intensity from a radiating circular Gaussian source were fitted to the dosimetry data. The fluences supplied by the dosimetry analysis at LLNL were assumed to be the values at the center of each small rectangle. The position of each piece was determined relative to the centerline of the furnace and the plane of the front foils, which was assumed to be perpendicular to the deuteron beam.

Two expressions for the flux intensity at a point due to a circular Gaussian source were fitted to the data: one in which the ^{54}Fe(n,p) cross section is assumed constant, and one in which the spectrally averaged cross section varies due to the change in the neutron spectrum with the angle of the neutron from the beam direction. The cross section varies linearly with the cosine of the angle,$^{(2)}$ increasing by 23% from 0 to 90 degrees. Attenuation of the neutron field by the specimens and furnace was not considered.

The expressions have the general form

$$\Phi t\ (r,\phi,z) = \frac{Y}{4\pi^2(.3607A^2)} \int\!\!\int_{-\infty}^{\infty} \frac{\sigma(z',R)}{R^2}\, e^{-(x^2+y^2)/(.3607A^2)} dxdy$$

with $R^2 = (r'-x)^2 + y^2 + z'^2$

$z' = z + \Delta z$

$r'^2 = (r\cos\phi - \Delta x)^2 + (r\sin\phi - \Delta y)^2$

and $\sigma(z',R) = [a - b\,(z'/R)]$;

where r, ϕ, and z are coordinates of the point relative to the front center of the furnace, with z lying along the beam axis, and Δx, Δy, and Δz are the coordinates of the front center of the furnace relative to the center of the source; and where A is the beam spot size (FWHM) and Y is the source strength (total neutrons). For the case including angular variation a = 1.21 and b = 0.23. If the angular variation is not included, a = 1 and b = 0.

Each equation has five adjustable parameters, Δx, Δy, Δz, A, and Y, which were evaluated by non-linear least-squares fitting of the equations to 161 dosimetry values. With b = 0 the double integral reduces easily to a single integral, which results in more than an order of magnitude less computing time. Table 1 contains values of these parameters for the two expressions.

TABLE 1

	With Angular Variation	Without
Δx	1.22 mm	1.21 mm
Δy	4.06 mm	4.04 mm
Δz	6.62 mm	5.48 mm
A (Spot Size)	1.74 cm	1.95 cm
Y (Strength)	3.00×10^{19}	2.88×10^{19}

The functions fit the dosimetry data about equally well. In each case the fit was slightly better for the foils closer to the source. The measured and calculated values of the fluences at the dosimetry foils were within 3% of each other for all but the most distant foils. The most distant foils in both zones (approximately 53 mm from the source) had calculated values 10% to 12% less than measured, due perhaps to scattering of the neutrons by intermediate material.

The deviation in the alignment of the beam and furnace ($\Delta x, \Delta y$) was the same by both analyses, and the values of Δx and Δy are consistent with the beam deviations systematically experienced in other runs. The spot size was larger for the case in which the angular dependence of the neutron spectrum was neglected. This appears to be consistent behavior of the two models, since in order to match the gradient in the data, the case with the larger spot size has a correspondingly smaller source-furnace separation (Δz) and a lower source strength. In the furnace the specimens are close to the beam center line, thus the effect of the angular variation is small except near the source.

The value of $\Delta z = 6.62$ mm is about 2 mm greater than the nominal value of the source-to-foil distance, which is the sum of the target thickness, target-furnace gap, and foil location within the furnace. The target-furnace gap, which varies as the target is scanned, is measured at the distance of minimum separation, so the average separation will be larger. The irradiation consumed several targets, adding an additional source of scatter in the data.

The parameter values are also consistent with the neutron source position and size estimated from dosimetry foils fastened to the outside of the furnace during the run. The flux gradient within the furnace was less steep than the example in the RTNS-II Guide for Experimenters,(3) because the spot size was larger than assumed for that example.

As with the dosimetry foils, the positions of the tensile specimens within the volume were accurately measured prior to irradiation. Thus, either function will give very accurate values for the fluences seen by the specimens in this irradiation, especially in the front part of the specimen volume where the steeper gradients usually make an accurate representation more difficult to achieve.

6.0 References

1. H. L. Heinisch and S. D. Atkin, DAFS Quarterly Progress Report, January-March, 1984, DOE/ER-0046/17, 76 (1984).
2. L. R. Greenwood, "Activation Cross-Section Measurements at RTNS-II," this volume.
3. Guide for Experimenters, Rotating Target Neutron Source-II, LLNL-M-094 Rev. 1, Lawrence Livermore National Laboratory, (1982).

7.0 Future Work

Tensile testing of the miniature tensile specimens irradiated in R-1 has begun. The various parts of the experiment will continue as planned.

RADIATION INDUCED PRECIPITATION IN Ti-64

D.L. Plumton, G.L. Kulcinski and R.A. Dodd (University of Wisconsin-Madison)

1.0 Objective

The dominant radiation response in several titanium alloy systems is a phase separation. Previous studies have shown that a thermally unstable bcc phase precipitates out in the hcp matrix during irradiation. In this paper, the extent of this phase separation in Ti-64 is examined as a function of temperature for low dose ion irradiations.

2.0 Summary

The alloy Ti-64 was heavy ion irradiated to 2 dpa at a 2 μm depth over a 500-700°C temperature range. The densities of the radiation induced β precipitate were found to decrease for the high temperatures while the size increased. The as-received grain boundary β phase shows no radiation effect until 650°C when it undergoes a transformation to a Widmanstätten morphology. An EDS analysis of the radiation induced β phase indicates it is 50% enriched in vanadium compared to thermally predicted vanadium concentration. The total fraction of bcc phase present in a specimen is drastically altered by irradiation.

3.0 Programs

Title: Radiation Damage Studies
Principal Investigator: G.L. Kulcinski and R.A. Dodd
Affiliation: University of Wisconsin-Madison

4.0 Relevant DAFS Program Task/Subtask

Task Number I.C.4 Microstructures and Swelling in Reactive/Refractory Alloys (Path C)

5.0 Accomplishments and Status

5.1 Introduction

Titanium alloys are among the materials being considered for use in a fusion reactor.[1-4] The strength to weight ratio and creep rupture properties of Ti alloys are equal to or superior than those of stainless steel in the 400-500°C temperature range. The high electrical resistivity, heat capacity, and low coefficient of thermal expansion are all advantageous. Titanium is also compatible with coolants such as lithium, helium and water, and it has a low long-term residual radioactivity. However, the radiation damage resistance of titanium alloys, specifically the phase stability, is an area that needs to be examined.

The titanium alloy Ti-64 exhibits an extensive phase redistribution under irradiation. Wilkes and Kulcinski[5] first noted, in 1978, that ion irradiation of Ti-64 resulted in copious precipitation of a fine bcc phase in the alpha matrix. Subsequent work using both dual-ion irradiation[6,7] and neutron irradiation[8,9] has confirmed that the beta precipitates are an irradiation-induced phenomenon, and that they dissolve upon thermal annealing below the $\alpha/(\alpha + \beta)$ phase boundary transition temperature.[7,8,10] The alloy Ti-64 is an α/β alloy. Titanium alloys are divided into three major classes determined by phase constituency. These classes are the alpha (α), beta (β) and alpha/beta (α/β) where the α phase is hcp and the β phase is bcc. The alloying elements used in the titanium system can be divided into two classes upon the basis of which phase the element stabilizes.[11] The substitutional α stabilizers are Al, Zr and Sn while the beta stabilizers are V, Cr, Mn, Fe, Co, Ni and Mo. It has been noted that vanadium and aluminum are both undersize in titanium[12] and that this corresponds well with the radiation induced segregation (RIS) theory of Okamoto and Wiedersich[13] which predicts RIS of undersize solutes to sinks. Wang et al.,[14] using Auger depth profiling on Ti-64, found that vanadium and aluminum both segregate to a free surface under irradiation but the relative magnitude of the segregation could not be explained by the size of the misfit parameter. Vanadium segregated more than aluminum although aluminum has the larger misfit parameter. The strong segregation of V, a beta stabilizer, can be used to explain the β precipitation in the alpha matrix.

In this paper the extent of this phase redistribution in Ti-64 is examined as a function of temperature for low dose ion-irradiations. The density and size of the irradiation-induced β precipitates (β_i) are examined for each irradiated sample. The chemical composition of the hcp matrix, the bcc as-received grain boundary phase (β_G) and the β_i precipitates are analyzed using energy dispersive x-ray analysis on TEM foils.

5.2 Experimental Procedure

The composition and impurity content of the Ti-64, nominally Ti-6Al-4V, is presented in Table I.[15] The alloy was obtained from McDonnell Douglas Astronautics Company in the form of 0.9 mm sheet in the mill anneal condition. The mill anneal heat treatment consisted of 790°C for 15 min followed by an air cool, then 720° for 4 hours in a vacuum followed by an argon cool. Preparation of the alloy for irradiation consisted of punching out disc specimens 3 mm in diameter. These specimens were then mechanically polished to a thickness of 0.4 mm.

Irradiation of these specimens was performed at the University of Wisconsin Heavy-Ion Irradiation Facility using 9 MeV Al ions. Figure 1 shows a BRICE code damage calculation for 9 MeV Al on Ti-64 using the LSS[16] electronic stopping power (esp), a displacement efficiency of K = 0.8, and a displacement energy of 32 eV. Aluminum ions were used to avoid any chemical alterations in the alloy. Furthermore all the microscopy was carried out at the 2 μm depth to avoid any excess interstitial effects and any altered phase stability effects due to the additional aluminum deposited by the incident ions. The specimens were irradiated to a total dose of 2 dpa at 2 μm for temperatures from 500 to 700°C.

Post-irradiation specimen preparation for TEM analysis involved electrochemical removal of 1.8 μm of the front surface and then electrochemical jet polishing from the back to perforation. The surface removal was done in a solution of 5% H_2SO_4 in methanol at -35°C and 11 volts. The jet polish was accomplished using the standard solution[17] of 6% perchloric acid, 35% n-butyl alcohol and 59% methanol at -28°C and 20 volts. The low temperature polish avoids the chance of hydride formation in the TEM metal foils. TEM and EDS was performed using a JEOL TEMSCAN-200CX electron microscope equipped with a Tracor Northern TN-2000 x-ray analysis system.

5.3 Results

The results are presented in two parts. The TEM data is considered first where Table II summarizes the precipitate density and size measurements. The data from the EDS analysis is presented in Tables III-V and is considered after the TEM results.

Figure 2 is a TEM micrograph showing the microstructure of the as-received Ti-64 alloy. The α grains are equiaxed while the β phase forms intergranularly (β_G). The polishing conditions used result in enhanced attack on the β_G grains. After 2 dpa at 500°C the Ti-64 microstructure is illustrated in Fig. 3. It can be observed that the radiation-induced β precipitates (β_i) dominate the microstructure. The density of β_i is 1.2×10^{15} #/cm^3 with an average length of 65 nm. It can also be noted that the β_G phase shows no signs of radiation damage. To illustrate the high density of β_i in the α grains and the lack of damage in the β_G

TABLE I

	Composition (Weight Percent)		
Ti-64	Al-6.4	V-3.9	C-0.01
(Heat 891352)	N-0.01	O-0.12	Fe-0.21

TABLE II. Ti-64 2 dpa β_i Precipitate Response

Temperature (°C)	Length (nm)	Density (#/cm^3)
500	65	1.2×10^{15}
550	87	2.0×10^{15}
600	140	5.3×10^{14}
650	400	6×10^{12}
700	NONE	NONE

TABLE III. Alpha Phase Concentrations (Weight Percent)

Irradiated				Unirradiated			
dpa/temp	C^{α}_{Ti}	C^{α}_{V}	C^{α}_{Al}	dpa/temp	C^{α}_{Ti}	C^{α}_{V}	C^{α}_{Al}
				0/0 (720)	91.90 ± 1.39	1.34 ± 1.62	6.76 ± 1.07
2/500	94.34 ± 4.96	0 ± 4.43	5.66 ± 3.08	0/500	92.83 ± 1.88	0.44 ± 1.21	6.73 ± 1.05
2/550	94.00 ± 2.25	0 ± 1.73	6.00 ± 1.33				
2/600	93.63 ± 2.49	0 ± 1.52	6.37 ± 1.21				
2/650	92.51 ± 1.65	0.90 ± 1.38	6.60 ± 0.41	0/650	91.82 ± 0.79	1.61 ± 0.73	6.57 ± 0.93
2/700	91.96 ± 1.39	1.82 ± 1.73	6.22 ± 1.13				

TABLE IV. Beta G Phase Concentrations (Weight Percent)

Irradiated				Unirradiated			
dpa/temp	$C^{\beta_G}_{Ti}$	$C^{\beta_G}_{V}$	$C^{\beta_G}_{Al}$	dpa/temp	$C^{\beta_G}_{Ti}$	$C^{\beta_G}_{V}$	$C^{\beta_G}_{Al}$
				0/0 (720)	86.54 ± 5.66	10.06 ± 5.05	3.39 ± 2.15
2/500	79.19 ± 3.34	18.22 ± 2.68	2.59 ± 1.94	0/500	78.75 ± 4.27	18.14 ± 4.06	3.11 ± 1.52
2/550	78.69 ± 2.60	16.66 ± 3.40	4.65 ± 1.64				
2/600	80.58 ± 4.26	15.84 ± 3.84	3.58 ± 1.70				
2/650 (β_{GT})	86.92 ± 0.9	8.13 ± 0.85	4.94 ± 0.87	0/650	86.01 ± 1.64	10.26 ± 1.94	3.73 ± 0.86
2/700	84.66 ± 3.16	11.03 ± 2.88	4.30 ± 1.26				

TABLE V. Beta i Phase Concentrations (Weight Percent)

dpa/temp	$C_{Ti}^{\beta_i}$	$C_V^{\beta_i}$	$C_{Al}^{\beta_i}$
2/500	82.70 ± 6.19	11.65 ± 6.22	5.64 ± 3.75
2/550	87.29 ± 5.33	5.79 ± 5.76	6.92 ± 1.25
2/600	69.66 ± 4.70	24.50 ± 5.20	5.83 ± 2.06
2/650	87.07 ± 1.82	7.42 ± 2.12	5.51 ± 1.29
2/700		NONE	

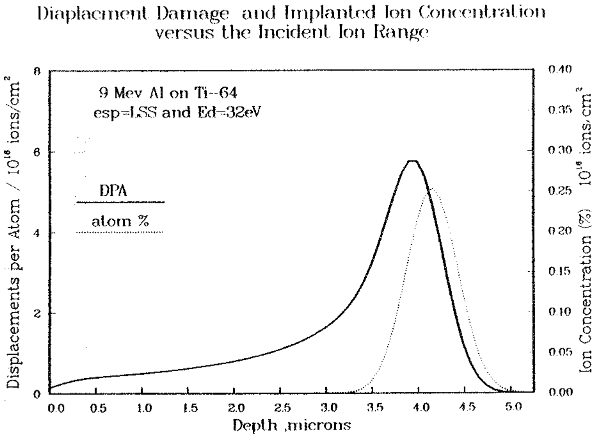

FIGURE 1. Displacement damage and implanted ion concentration for 9 MeV Al incident on Ti-64.

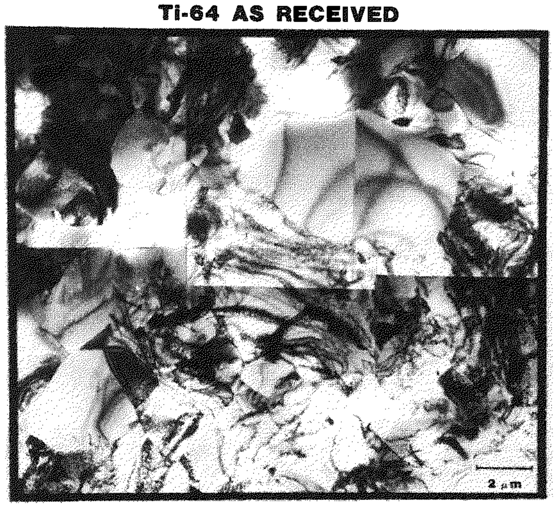

FIGURE 2. TEM micrograph showing the as-received Ti-64 grain structure. Note the enhanced attack on the grain boundary β_G phase.

grains, Fig. 4 shows a bright field/dark field pair. In Fig. 4a several orientations of the 6 possible[10] β_i orientations are shown in an α grain with a β_G grain at the top of the picture exhibiting a clear microstructure. In Fig. 4b one of the 6 possible orientations is imaged showing the high density of β_i and the large distribution in size. To obtain the 2 dpa damage level this specimen was irradiated for 1-1/2 hours at 500°C. If one anneals an as-received specimen for 8 hr at 500°C, no readily apparent difference is observed between the annealed and as-received specimens. This point is illustrated by Fig. 5 which shows a Ti-64 specimen annealed at 500°C for 8 hr.

Similarly, examination of specimens irradiated at 550-600°C shows the β_i precipitation response dominating the microstructure. Figure 6 shows two bright field/dark field pairs again illustrating the high density and large size distribution of the β_i precipitates. The density of β_i at 2 dpa and 550°C is 2×10^{15} #/cm^2 with an average length of 87 nm. Figure 7 shows the 2 dpa 600°C sample and illustrates how the β_i precipitates are drastically increasing in average size for just a 50°C temperature increase. The average length of the 2 dpa 600°C β_i precipitates is 140 nm with a density of 5.4×10^{14} #/cm^3. To fully appreciate the magnitude of this precipitation effect, Fig. 8 shows two micrographs at slightly different matrix orientations showing all 6 β_i precipitate orientations. Again it should be pointed out that the β_G grains display no sign of radiation damage. This can be seen in Fig. 9 which shows a clean β_G grain next to some obviously radiation-affected α grains.

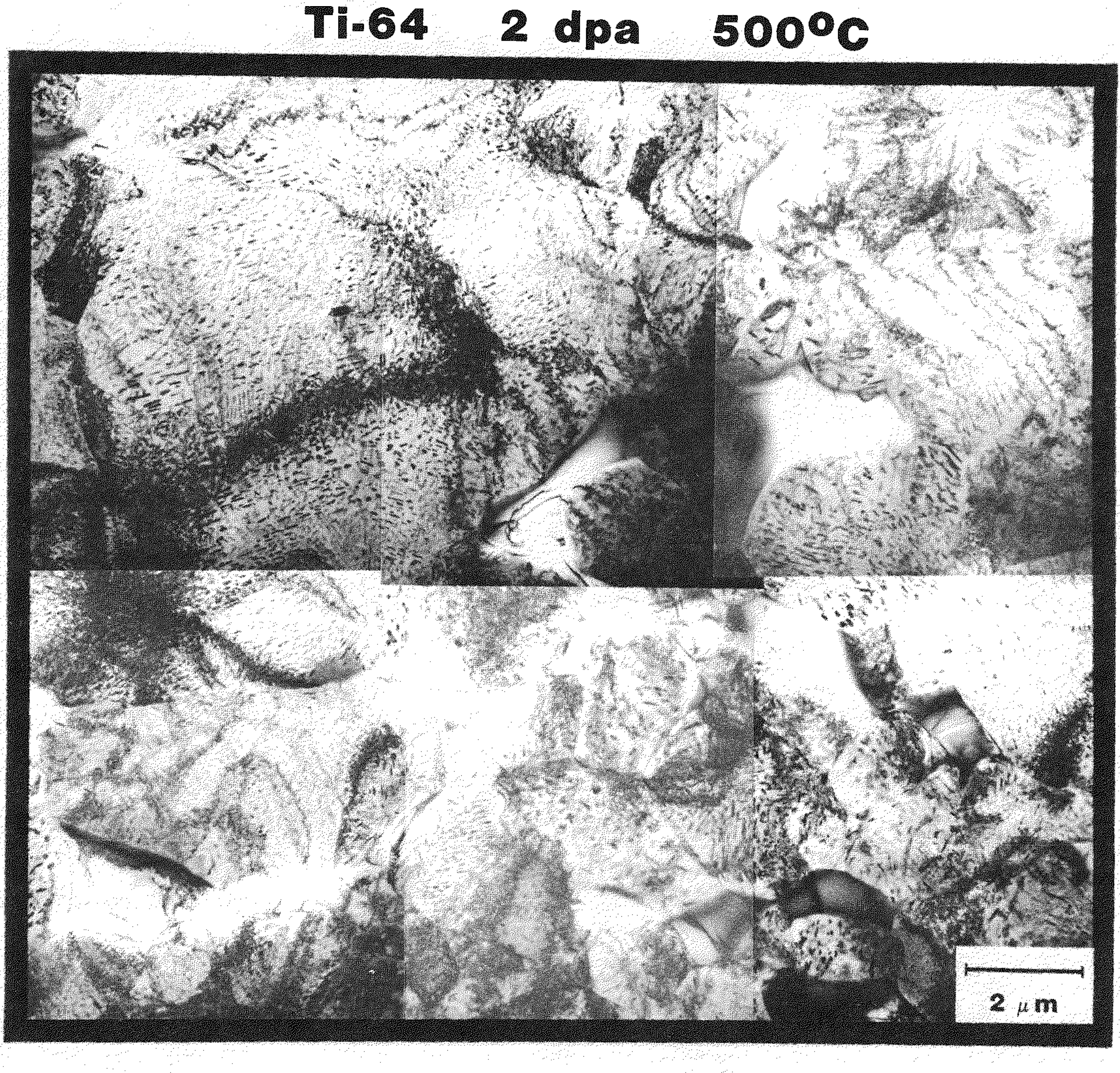

FIGURE 3. TEM micrograph showing the extensive β_i precipitation.

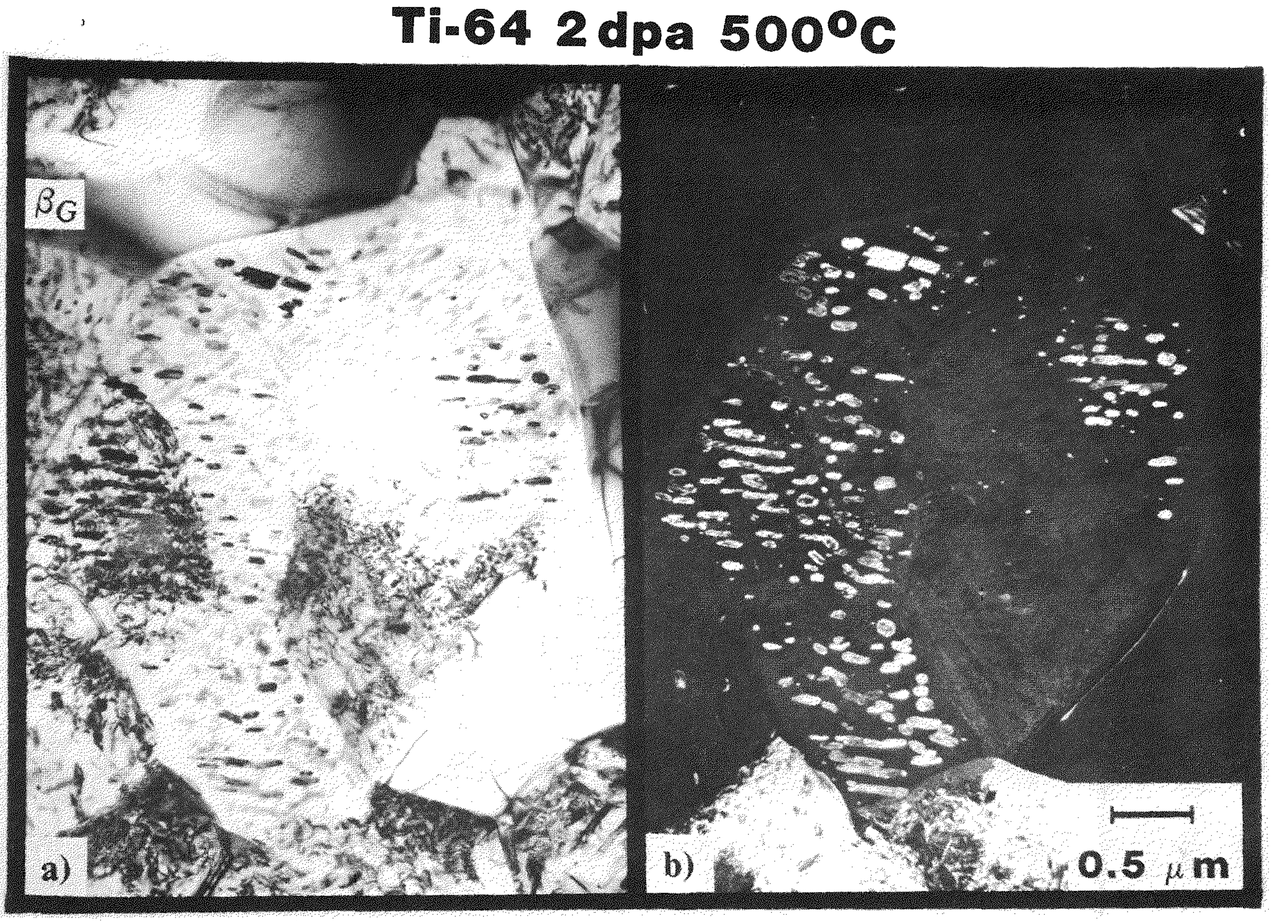

FIGURE 4. a) Bright field TEM micrograph showing β_i in an α grain adjacent to a β_G grain which appears unaffected.
b) Dark field TEM micrograph using $\vec{g}(\beta)$ = [110].

In the specimens irradiated at higher temperatures an effect is observed in the β_G grains. Figure 10 shows a 2 dpa 650°C specimen which displays a very low density of β_i precipitates in the α grain. However, the adjacent β_G grain has the morphology of a transformed beta grain composed of Widmanstätten alpha-beta plates. The precipitates in the alpha grains are β_i precipitates. This is shown in Fig. 11 which is a bright field/dark field pair imaging the β_i precipitates. The density of β_i is 6 x 10^{12} with an average length of 400 nm. To examine the anomaly of β_G becoming a transformed grain (β_{GT}) a Ti-64 as-received specimen was annealed at 650°C for 8 hours. Figure 12 shows the annealed specimen which appears to have undergone some recovery and a little grain growth in the α phase, while the β_G phase appears unaffected and certainly not transformed. Examination of the 2 dpa 700°C sample reveals no radiation-induced β_i precipitates. This is shown in Fig. 13 where no indication of the β_i precipitation response is found. However, the β_G grains again appear to be transformed (β_{GT}). A closeup of a β_{GT} grain, Fig. 14, shows the lamellar plate structure of a transformed grain.

The EDS analysis of this titanium alloy is complicated by the fact that the TiK_β characteristic x-ray peak lies on top of the VK_α peak. This was overcome by finding the ratio of TiK_β to TiK_α in pure titanium which was then used to separate the TiK_β component from the VK_α component in the Ti-64 alloy.

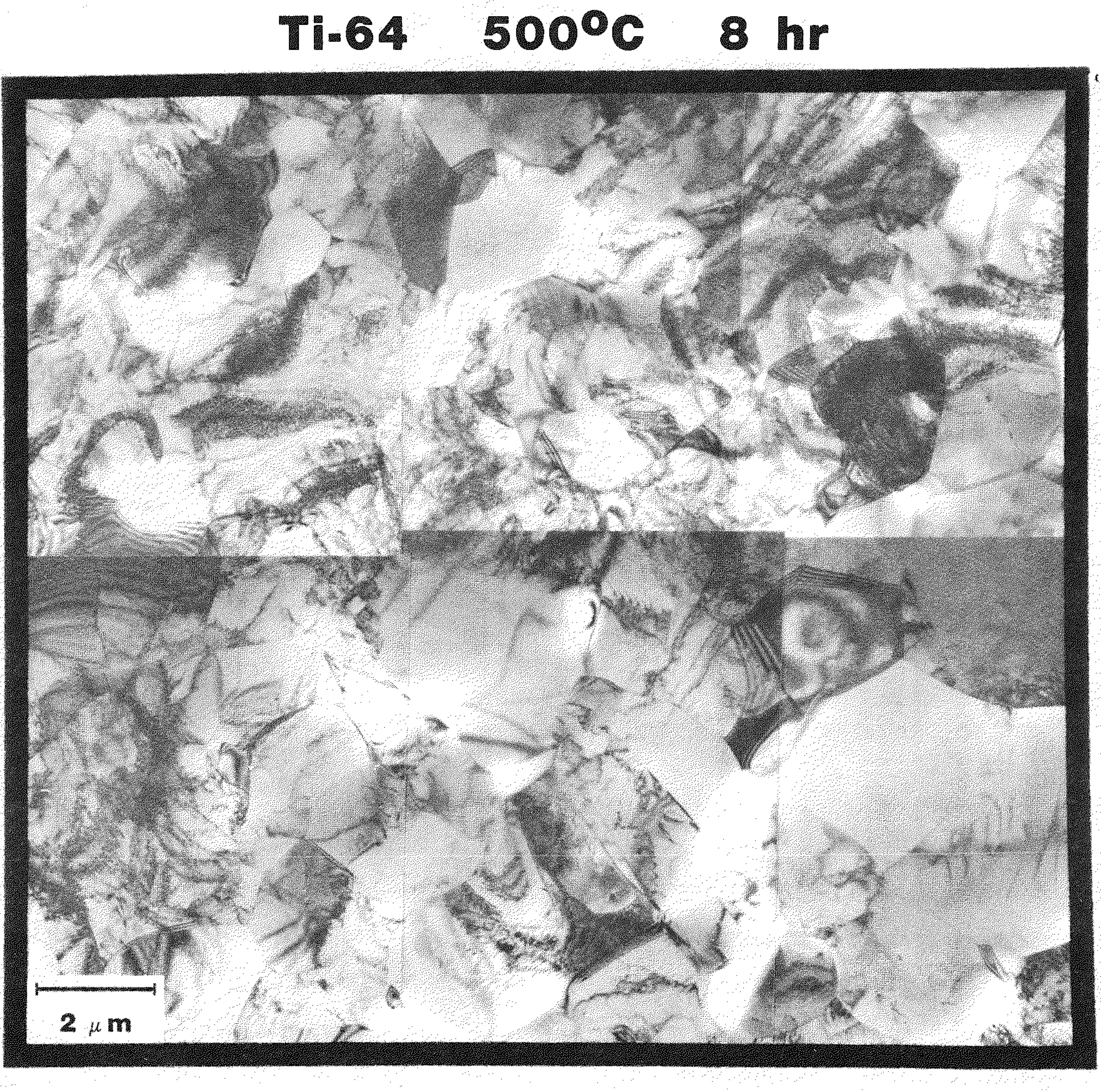

FIGURE 5. TEM micrograph showing the grain structure and dislocation distribution in Ti-64 annealed at 500°C for 8 hours.

The concentrations in weight percent of the α phase, β_G phase and β_i phase are shown in Tables III-V. In Table III the α phase concentrations are presented and illustrate that under irradiation no V is left free in the α matrix except in the 650°C case. For the β_G phase, Table IV shows that a 500-600°C temperature for annealing or irradiation results in significant increase in V concentration.

Comparison of aluminum concentration between the α and β_G phases indicates a preference for the α phase. The phase concentrations of the β_i precipitates are presented in Table V and show a large variance in vanadium values and a large error. The large variance and error results from taking spectra from small precipitates embedded in a matrix, so these values are not an accurate indication of the precipitate concentration. However, they do show a large vanadium concentration in the α matrix which has a low V concentration. In one case, β_i 2/600, the electropolish resulted in the β_i precipitates being suspended in a very thin α matrix. Therefore, the concentrations from the β_i 2/600 case are accurate. These β_i results indicate a V concentration higher than that found in the β_G phase. Also it should be noted that the Al concentration was not reduced to the same extent in the β_i phase as in the β_G phase.

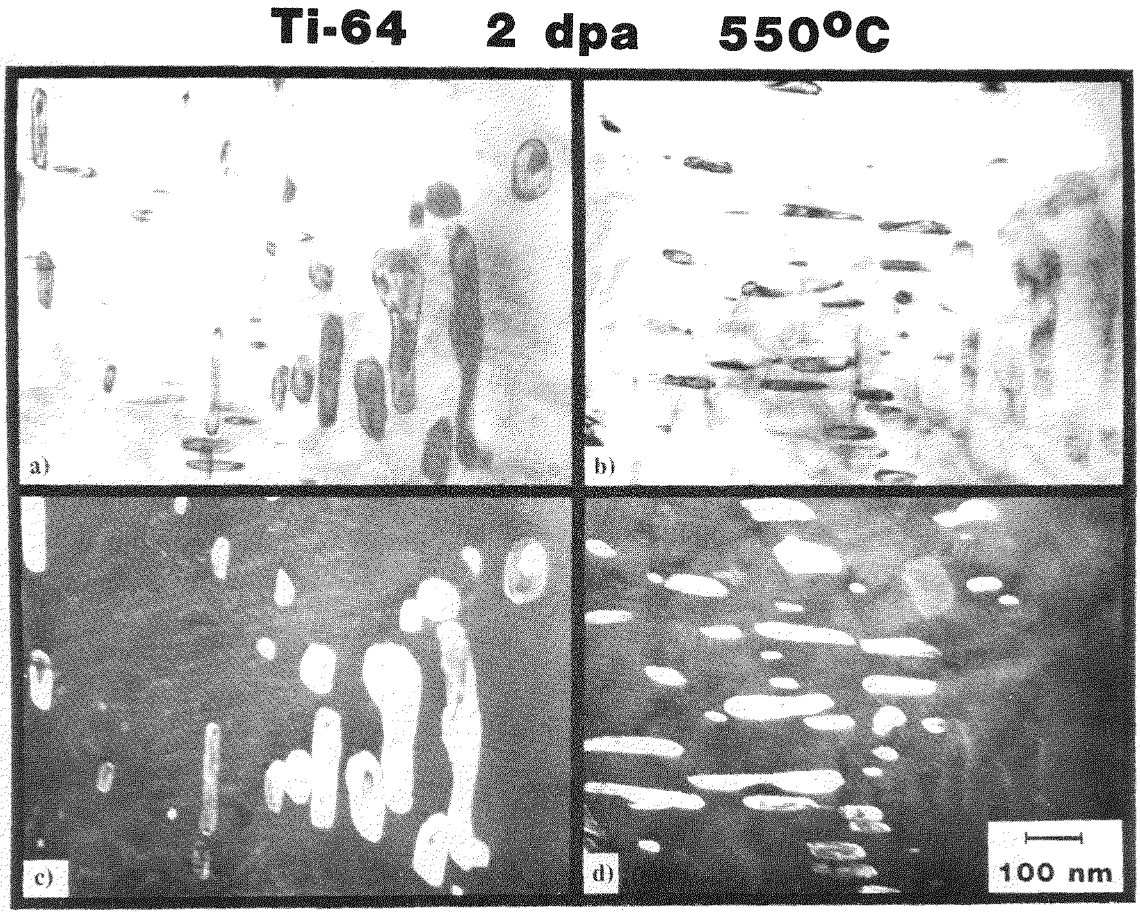

FIGURE 6. a) & b) Bright field TEM micrographs showing the radiation induced β_i precipitates using $\vec{g}(\alpha) = [3\overline{12}1]$ while moving $\vec{g}(\beta)$ from $[1\bar{1}0]$ to $[110]$.
c) & d) Dark field TEM micrograph using $\vec{g}(\beta) = [1\bar{1}0]$ and $\vec{g}(\beta) = [110]$.

5.4 Discussion

The radiation-induced precipitation (β_i) follows a fairly well expected pattern where the precipitate density decreases at high temperature while the precipitate size increases. The data is shown graphically in Fig. 15, the one anomaly being the small increase in density going from 500 to 550°C. This fluctuation is well within a 30% error but might indicate a flattening in the low temperature part of the curve that does not correspond well with the rest of the trend. The large amount of β_i precipitation makes the Ti-64 system an interesting model to examine two proposed mechanisms that account for radiation-induced precipitation.

The kinetic mechanism is based on radiation induced segregation (RIS)[13] which postulates undersize solutes segregating to sinks. In the area of the sink the solubility limit for the undersize solute is exceeded, resulting in precipitation. Wang et al.[14] noted that vanadium segregated more than aluminum to an irradiated free surface even though Al has the larger misfit parameter. They pointed out that diffusion data indicated that Al diffuses faster than V in Ti so that Al could be diffusing away from sinks via the inverse Kirkendall effect. This argument supports RIS; however, the EDS results presented here for Ti-64 2 dpa 600°C do raise a question. The vanadium concentration for the β_i precipitates is 24.5 wt.% which is ~ 50% higher than the concentration for the β_G grains. This implies a radiation induced shift in the $(\alpha + \beta)/\beta$ phase boundary.

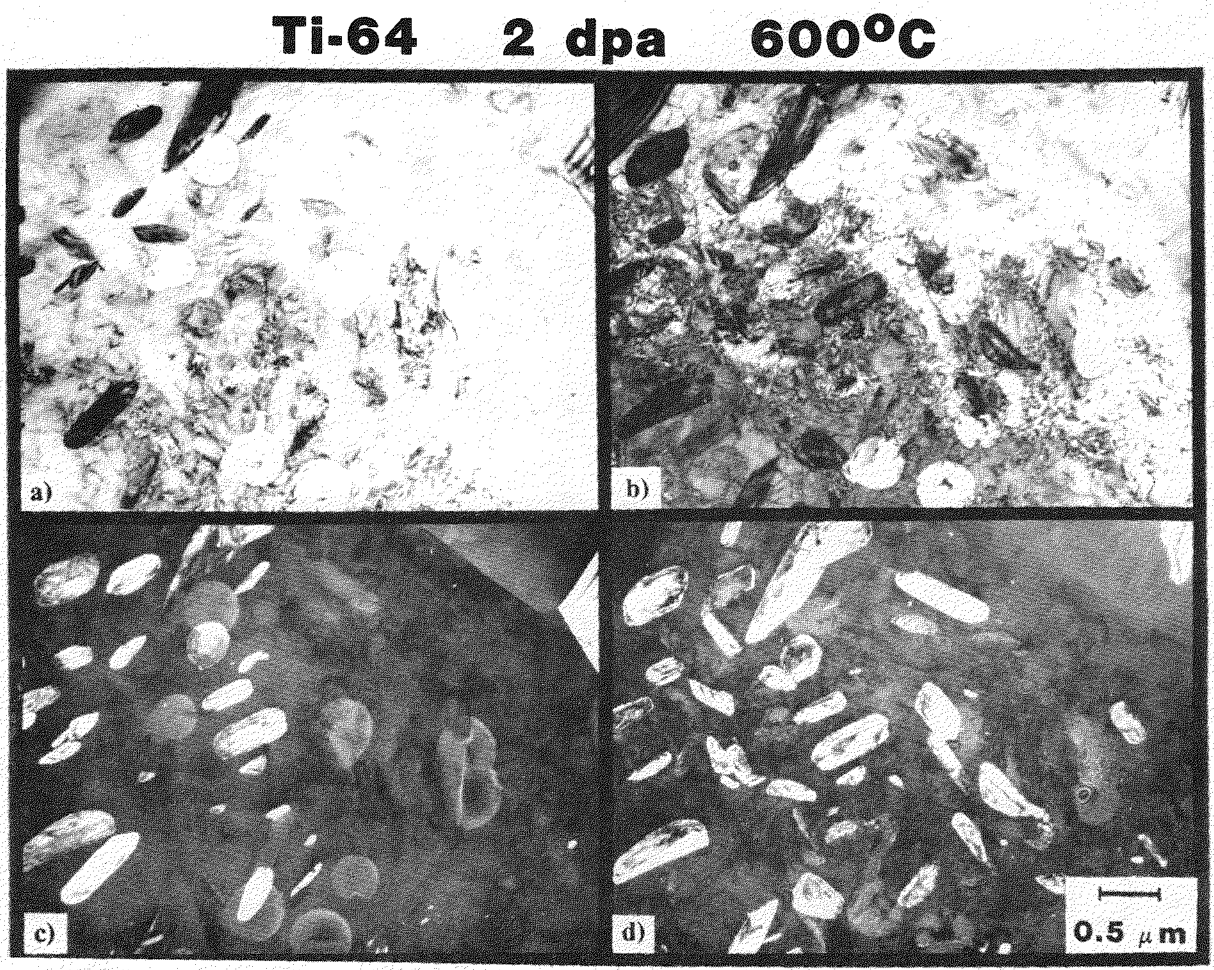

FIGURE 7. a) & b) Bright field TEM micrographs at orientations $\vec{g}(\alpha) = [01\bar{1}2]$ and $\vec{g}(\alpha) = [11\bar{2}0]$ showing the radiation induced β_i precipitate.
c) & d) Dark field TEM micrographs using $\vec{g}(\beta) = [011]$.

The second mechanism is based on thermodynamic reasoning. It postulates that if a material is in a nonequilibrium state, then radiation may promote nucleation in incoherent precipitates.[18] The as-received material is in a nonequilibrium state for the 500-600°C temperature range as is indicated by the increase in V concentration for a 500°C anneal. However, the irradiation-induced precipitates are not incoherent so this theory would also require modification to fit the results. The EDS results presented here can be used to sketch an irradiation modified phase diagram to further assess the phase stability under irradiation.

The relative amounts of the phases present can be calculated. Additionally, this gives an estimate on the accuracy of the EDS results. In the case of the annealed specimens and the 2 dpa 700°C specimen there are only 2 phases present, α and β_G (or β_{GT} in the latter case). By solving the following equations

$$C_V^\beta f_\beta + C_V^\alpha f_\alpha = 3.9$$

$$C_{Al}^\beta f_\beta + C_{Al}^\alpha f_\beta = 6.4$$

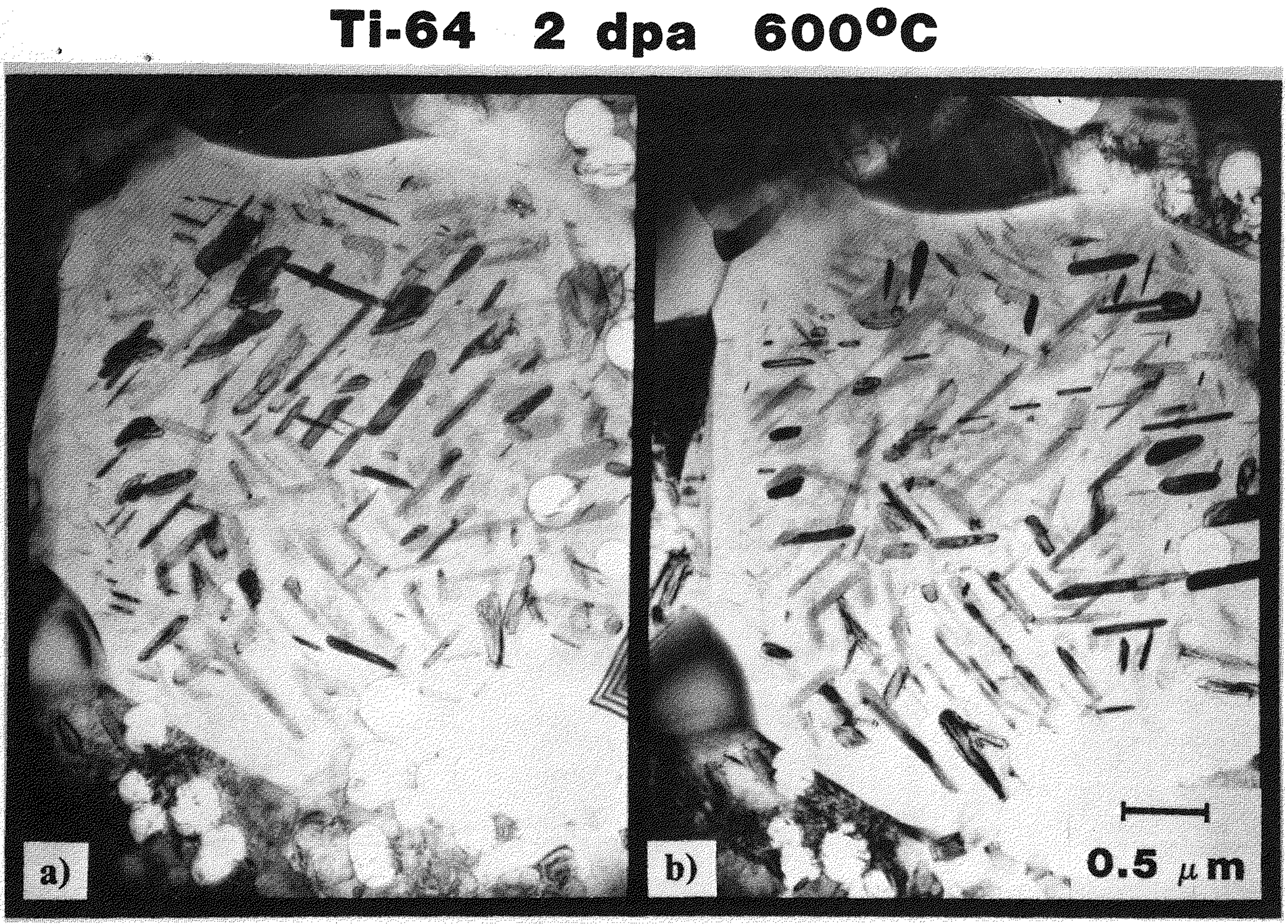

FIGURE 8. a) & b) Bright field TEM micrographs showing all 6 β_i precipitate orientations in varying amounts of contrast.

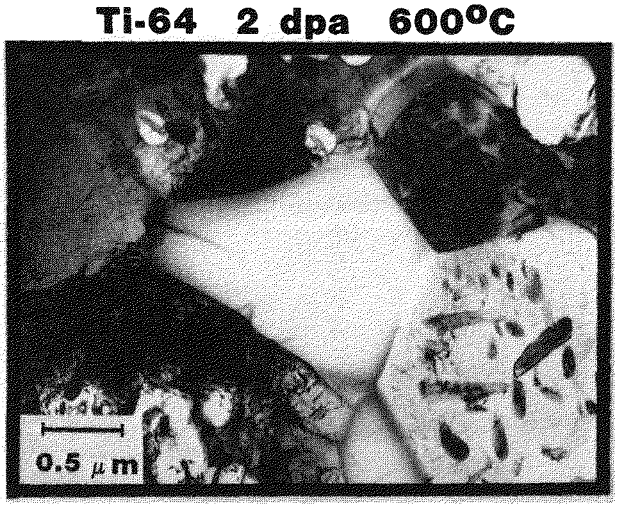

FIGURE 9. TEM micrograph showing a β_G grain which has no observable damage.

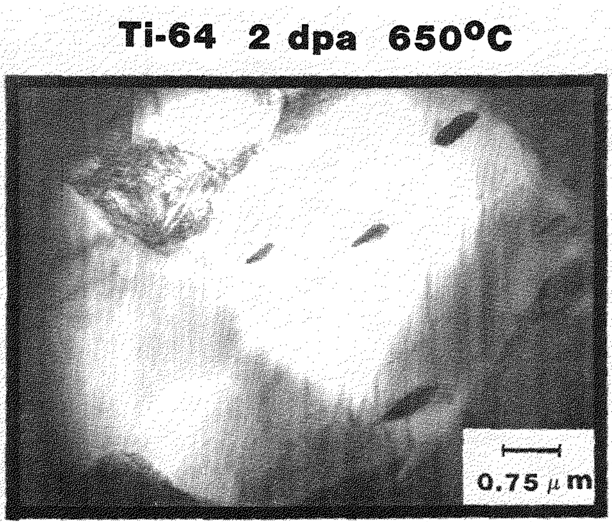

FIGURE 10. TEM micrograph showing the low density of β_i precipitates and how the β_G has become a transformed β grain.

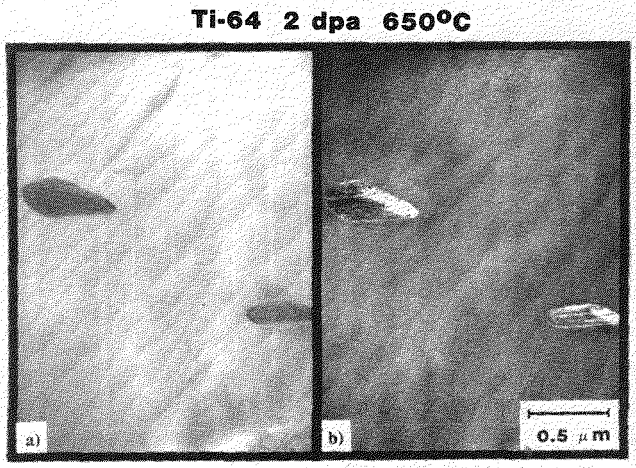

FIGURE 11. a) Bright field TEM micrograph showing the low density and large size of the β_i precipitates.
b) Dark field TEM micrograph using $\vec{g}(\beta)[110]$.

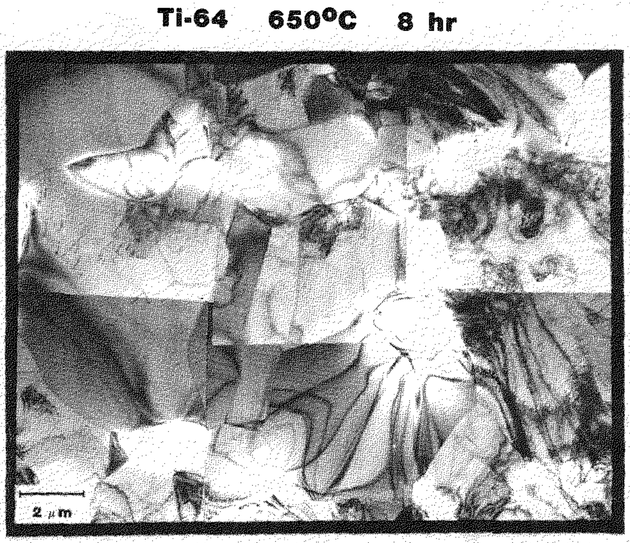

FIGURE 12. TEM micrograph showing some grain growth and recovery for Ti-64 annealed at 650°C for 8 hours.

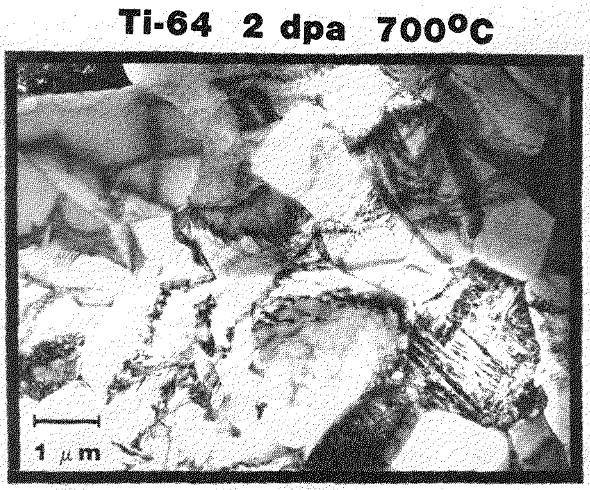

FIGURE 13. TEM micrograph illustrating the absence of β_i precipitates and the presence of a transformed β_G grain (β_{GT}).

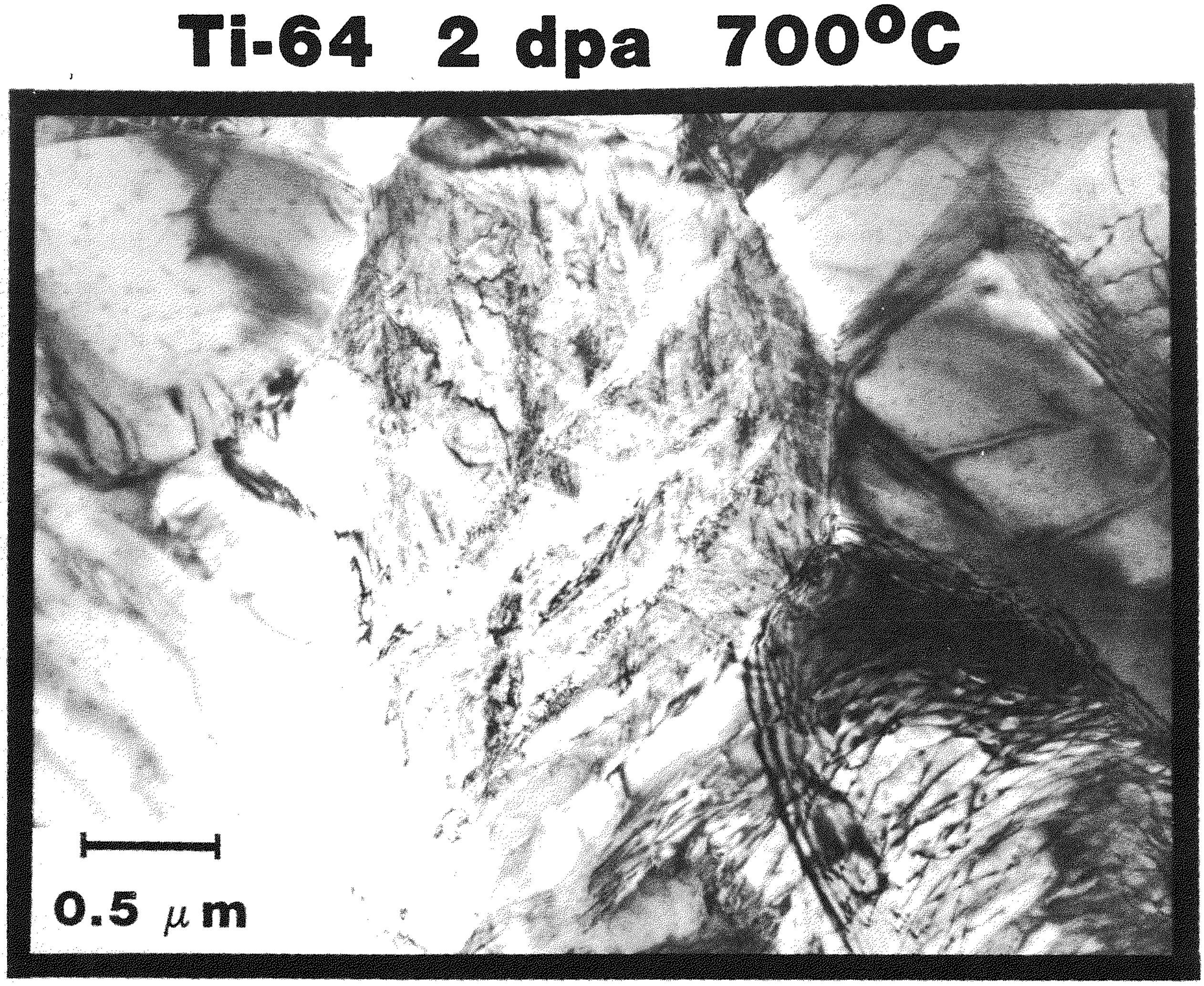

FIGURE 14. TEM micrograph showing a transformed β_G grain (β_{GT}).

the relative fraction of the phases, f_α and f_β, can be obtained. The results are presented in Table VI. It can be noted that a higher temperature anneal gives a higher fraction of β with a lower V concentration. Since the above two equations are not constrained to give $f_\alpha + f_\beta = 1.0$ any deviation from 1.0 is an estimate of the error. As can be seen, the error in each case is less than 10%. A little more difficult analysis is necessary for the irradiated specimens where three phases, α, β_G and β_i, are present. Solving

$$C^{\alpha}_{Ti} f_\alpha + C^{\beta_G}_{Ti} f_{\beta_G} + C^{\beta_i}_{Ti} f_{\beta_i} = 89.7$$

$$C^{\alpha}_{V} f_\alpha + C^{\beta_G}_{V} f_{\beta_G} + C^{\beta_i}_{V} f_{\beta_i} = 3.9$$

$$C^{\alpha}_{Al} f_\alpha + C^{\beta_G}_{Al} f_{\beta_G} + C^{\beta_i}_{Al} f_{Al} = 6.4$$

gives the appropriate fractions after normalization. The results are presented in two parts in Table VII. The first part, (a), takes the values of $C_V^{\beta_i}$ experimentally obtained, ignoring the fact that all but the 2 dpa 600°C results also average over a large part of the α matrix. From these results we can see that the $C_V^{\beta_i}$ must be higher, on the order of the 2/600 data, to give a reasonable f_{β_i} fraction (~ 20%) that qualitatively agrees with the TEM observations.

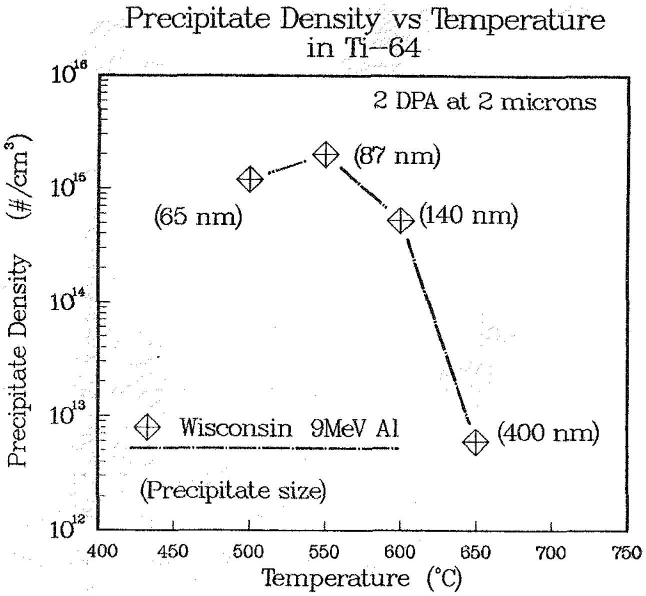

FIGURE 15. β_i precipitate density versus temperature.

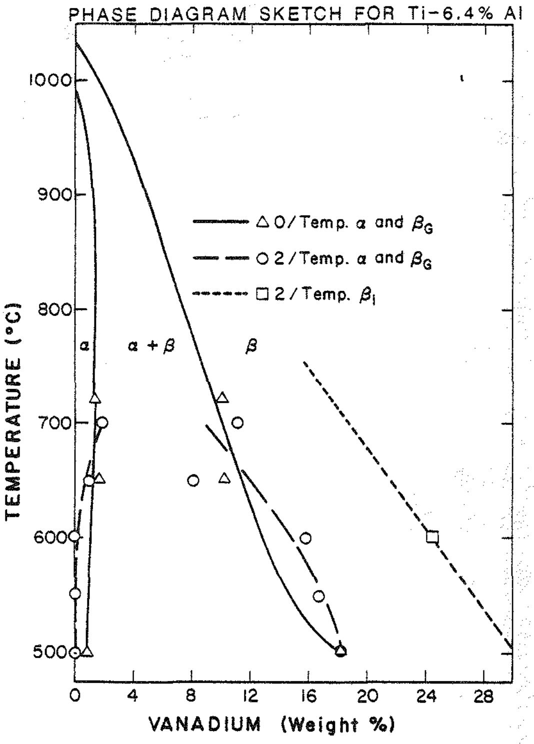

FIGURE 16. Sketch of the phase diagram for Ti-6.4% Al as a function of temperature and V concentration.

TABLE VI. f_α and f_β

dpa/temp	f_α	f_β	% error
0/500	0.861	0.194	9.2
0/650	0.832	0.25	5.5
0/0 (720)	0.806	0.28	8.2
2/700	0.885	0.21	9.3

TABLE VII. f_α, f_{β_G} and f_{β_i}

	dpa/temp	f_α	f_{β_G}	f_{β_i}
a)	2/500	0.353	0.164	0.482
	2/550	0.43	0.55	0.515
	2/600	0.784	0.043	0.174
	2/650	0.20	0.286	0.514
b)	2/500	0.651	0.164	0.186
	2/550	0.712	0.110	0.178
	2/600	0.783	0.044	0.173
	2/650	0.834	0.032	0.134

An irradiation modified phase diagram is presented in Fig. 16. This diagram is based on the EDS results presented in Tables III to V and on the higher temperature (~ 1000°C) work of Rausch et al.[19] in the Ti7% Al system. All the data on α and β_G is plotted. Only the 2/600 data for $C_V^{\beta_i}$ is plotted. The $\alpha + \beta_i/\beta_i$ transus is extrapolated by drawing a straight line through the $C_V^{\beta_i}$ 2/600 point and the $C_V = 0$ point. The irradiated β_G is a problem in presentation since at ~ 650°C there appears to be some form of phase transition ($\beta_G \rightarrow \beta_{GT}$). This transition to a β transformed morphology is seen in the $\alpha + \beta_G/\beta_G$ transus as a reduction in $C_V^{\beta_G}$ at 650°C (i.e., a pinching in or off of the $\alpha + \beta$ region). From Fig. 16 the $C_V^{\beta_i}$ data can then be taken for different temperatures and used to calculate f_α, f_{β_G} and f_{β_i}. This data is presented in part (b) of Table VII. This data agrees qualitatively with the TEM observation in that for low temperature irradiations the β_G fraction does not appear markedly reduced yet there is a significant β_i fraction. For T = 500°C and 2 dpa the total bcc fraction is 35% compared to 19% in the unirradiated case. This is a significant redistribution in the phase fractions which is difficult to ascribe solely to RIS. RIS should result in precipitation of the equilibrium precipitate, not a precipitate with 50% more vanadium. The accuracy of drawing a line through the one $C_V^{\beta_i}$ 2/600 data point can be questioned. However, it has been noted experimentally that in those few cases, at other temperatures, where the β_i precipitate hung over the edge of the foil, or was in very thin section of foil, that $C_V^{\beta_i}$ approached 20 + %.

The high temperature (650-700°C) irradiation response in the as-received β grain (β_G) resembles the morphology of a β_{anneal}. A beta anneal[20] is achieved by an anneal above the $\beta/(\alpha + \beta)$ transition temperature (at ~ 1040°) followed by an air cool and a reanneal at 700°C. This results in Widmanstätten alpha-beta plates. It seems reasonable to assume that even under irradiation the Widmanstätten morphology will not occur until the temperature is reduced. Under heavy ion irradiation conditions the temperature is not reduced until the irradiation ceases. Therefore, in the β_G grains as the vacancy concentration decays to equilibrium while the temperature is concomitantly reduced, here exists enough solute mobility for the Al and V to segregate to their respective α and β plates.

6.0 Conclusions

1. The densities and lengths of the radiation induced precipitates in Ti-64 are given as a function of temperature.
2. Observation of the first irradiation effect in the grain boundary β phase in Ti-64 at and above 650°C.
3. EDS analysis of Ti-64 resulted in:
   a. Observation that the radiation induced β precipitate has a vanadium concentration ~ 50% greater than thermally predicted.
   b. The fraction of bcc phase present at 500°C after a 2 dpa irradiation is 35% which is 80% more than predicted thermally, whereas the fraction of bcc phase present at 650°C after 2 dpa irradiation is 16% which is only 60% of the thermal prediction.

7.0 References

1. J.W. Davis and G.L. Kulcinski, EPRI, ER-386 (1977).
2. R.W. Conn, J. Nucl. Mater. 76 & 77, pp. 103-111, 1978.
3. E.E. Bloom, J. Nucl. Mater. 85 & 86, pp. 795-804, 1979.
4. R.H. Jones, B.R. Leonard and A.B. Johnson, EPRI-AP-1433, 1980.
5. P. Wilkes and G.L. Kulcinski, J. Nucl. Mater. 78, pp. 427-430, 1978.
6. S.C. Agarwal, G. Ayrault, D.I. Potter, A. Taylor and F.V. Nolfi, Jr., J. Nucl. Mater. 85 & 86, pp. 653-657, 1979.

7. R.H. Jones and L.A. Charlot, J. Nucl. Mater. 91, pp.329-335, 1980.

8. S.M.L. Sastry, J.E. O'Neal and J.W. Davis, Titanium '80, Eds. H. Kimwra and O. Izumi, pp. 651-662, 1980.

9. D.T. Peterson, Effects of Radiation on Materials: Eleventh Conference, ASTM STP 782, H.R. Brager and J.S. Perrin, Eds., 1982, pp. 260-274.

10. G. Ayrault, J. Nucl. Mater. 113, pp. 1-13, 1983.

11. C. Hamond and J. Nutting, Metal. Sci., pp. 474-490, 1977.

12. H.W. King, J. Mater. Sci. 1, pp. 79-90, 1966.

13. P.R. Okamoto and H. Wiedersich, J. Nucl. Mater. 53, pp. 336-345, 1974.

14. Z. Wang, G. Ayrault and H. Wiedersich, J. Nucl. Mater. 108 & 109, pp. 331-338 (1982).

15. D.R. Duncan, R.J. Puigh and E.K. Opperman, J. Nucl. Mater. 103 & 104, pp. 919-924, 1981.

16. J. Linhard and M. Scharff, Phys. Rev. 124, p. 128, 1961.

17. M.J. Blackburn and J.C. Williams, TMS-AIME 239, pp. 287-288, 1967.

18. S.I. Maydet and K.C. Russell, J. Nucl. Mater. 64, p. 101, 1977.

19. J.J. Rausch, F.A. Crossley and H.D. Kessler, Trans. AIME J. of Metals, pp. 211-214, 1956.

20. J.W. Davis, S.M.L. Sastry and L.J. Poinke, DOE/ET/0058/2, pp. 85-99, May 1979.

8.0 Future Work

Further characterization of the chemical composition of the radiation induced β precipitate.

HEAVY ION IRRADIATION OF Ti-6242S

D.L. Plumton, G.L. Kulcinski and R.A. Dodd (University of Wisconsin-Madison)

1.0 Objective

Previous work on Ti-64 has demonstrated that this titanium alloy system has phase instabilities under irradiation. Neutron results on Ti-6242S indicate this alloy may have a stable phase microstructure. The present study was undertaken to examine the microstructure and phase stability of Ti-6242S after 2 dpa of heavy ion irradiation over a 450-700°C temperature range.

2.0 Summary

After 2 dpa of 9 MeV Al ion irradiation, Ti-6242S displayed extensive precipitation at all temperatures in the range 450-700°C. The precipitate was identified as a bcc phase similar to that observed in Ti-64. The morphology of the precipitation response for 450-600°C was highly unusual. It consisted of the apparent agglomeration of small (~ 20 nm) precipitates into some form of array or cluster. The high temperature precipitate response (650-700°C) was normal where the precipitate morphology was that of an elongated platelet. A low void density was observed between 550-650°C with the voids preferentially located near grain boundaries.

3.0 Program

Title: Radiation Damage Studies
Principal Investigator: G.L. Kulcinski and R.A. Dodd
Affiliation: University of Wisconsin-Madison

4.0 Relevant DAFS Program Task/Subtask

Task Number I.C.4 Microstructures and Swelling in Reactive/Refractory Alloys (Path C)

5.0 Accomplishments and Status

5.1 Introduction

Titanium alloys are among the structural materials being considered for use in a fusion reactor.[1-4] Titanium is compatible with several coolants and it has a low long-term residual radioactivity. The strength to weight ratio and creep rupture properties of titanium alloys are equal to or superior to those of stainless steel in the 400-500°C temperature range. The high electrical resistivity, heat capacity and low coefficient of thermal expansion are all advantageous. However, the radiation damage resistance of titanium alloys, specifically the phase stability, is an area that needs to be examined.

Titanium alloys are divided into three major classes determined by phase constituency. These classes are the alpha (α), beta (β) and alpha/beta (α/β) where the alpha phase is hcp and the beta phase is bcc. The alloying elements used in the titanium system can be divided into two classes depending on which phase is stabilized.[5] The substitutional α stabilizers are Al, Zr and Sn while the beta stabilizers are V, Cr, Mn, Fe, Co, Ni and Mo.

Previous work on irradiated Ti-6Al-4V,[6-11] an α/β alloy, has shown an extensive radiation-induced β precipitation response. Wang et al.,[12] using Auger depth profiling, found that V, Mo and Al all segregate to a free surface under irradiation. However, the relative magnitude of this segregation could not be explained by the size of the solute misfit parameter alone. Radiation-induced segregation (RIS)[13] predicts the segregation of undersize solutes via interstitial complexes to sinks. In the titanium system, the relative magnitudes of the segregation effects for V, Mo and Al are exactly the opposite of what one would expect from just considering the size of the misfit parameter. Vanadium segregates the most and Al the least.

Irradiation studies of near α alloys are sparse. Ayrault[14] performed heavy ion irradiation of Ti-811 (8Al-1V-1Mo) and found the radiation-induced β precipitate. Neutron work[9,10] on Ti-6242S (6Al-2Sn-4Zr-2Mo-0.08Si) and on Ti-6242S (5Al-6Sn-2Zr-1Mo-0.3Si) has not revealed any radiation-induced β precipitate. Comparing the solute content of these alloys shows that vanadium is present in all the alloys where the radiation-induced β precipitate is observed.

In this paper the microstructure of the near α alloy, Ti-6242S, is examined as a function of temperature for low dose ion-irradiations. The morphology and distribution of a possible radiation-induced phase is examined over the temperature range of 500-700°C.

5.2 Experimental Procedure

The titanium alloy which was irradiated, Ti-6242S, has the nominal composition of 6Al-2Sn-4Zr-2Mo-0.08Si. The alloy was obtained from the McDonnell Douglas Astronautics Company in the form of 0.9 mm sheet in the duplex annealed condition. The duplex anneal heat treatment consists of 1/2 hr at 900°C, air cool, 1/4 hr at 790°C, air cool, then a 4 hr vacuum anneal at 720°C and an argon cool. This results in equiaxed α grains with grain boundary transformed β grains. Preparation of the alloy for irradiation consisted of punching out disc specimens 3 mm in diameter. These specimens were then mechanically polished to a thickness of 0.4 mm.

Irradiation of these specimens was performed at the University of Wisconsin Heavy-Ion Irradiation Facility using 9 MeV Al ions. Figure 1 shows a BRICE code damage calculation for 9 MeV Al on Ti-64 (~ Ti-6242S) using the LSS[15] electronic stopping power (esp), and a displacement energy of 32 eV. Aluminum ions were used to avoid any chemical alterations in the alloy. Furthermore, all the microscopy was carried out at the 2 μm depth to avoid any excess interstitial effects and any altered phase stability effects due to the additional aluminum deposited by the incident ions. The specimens were irradiated to a total dose of 2 dpa at a 2 μm depth for temperatures from 500-700°C.

Post-irradiation specimen preparation for TEM analysis involved electrochemical removal of 2.4 μm of the front surface and then electrochemical jet polishing from the back to perforation. The surface removal was done in a solution of 5% H_2SO_4 in methanol at -35°C and 11 volts. The jet polish was accomplished using the standard solution[16] of 6% perchloric acid, 35% n-butyl alcohol and 59% methanol at -28°C and 20 volts. The low temperature polishing avoids the chance of hydride formation in the TEM foils. Transmission electron microscopy (TEM) was performed on a JEOL TEMSCAN-200CX electron microscope.

5.3 Results

These results present a preliminary survey of the morphology and distribution of precipitates which are suspected of being radiation-induced. The results range from low temperatures, where the precipitate morphology is unusual, to high temperatures where a normal appearing precipitate is observed. A precipitate response is observed in all irradiated samples from 450 to 700°C, while samples annealed for longer times at similar temperatures show no precipitation.

Figure 2 shows a Ti-6242S specimen annealed for 8 hours at 500°C. There is little difference between this microstructure and the as-received microstructure. The alpha grains are fairly equiaxed and the as-received bcc β phase can be observed at α grain boundaries as a transformed β phase. The transformed β phase (β_T)

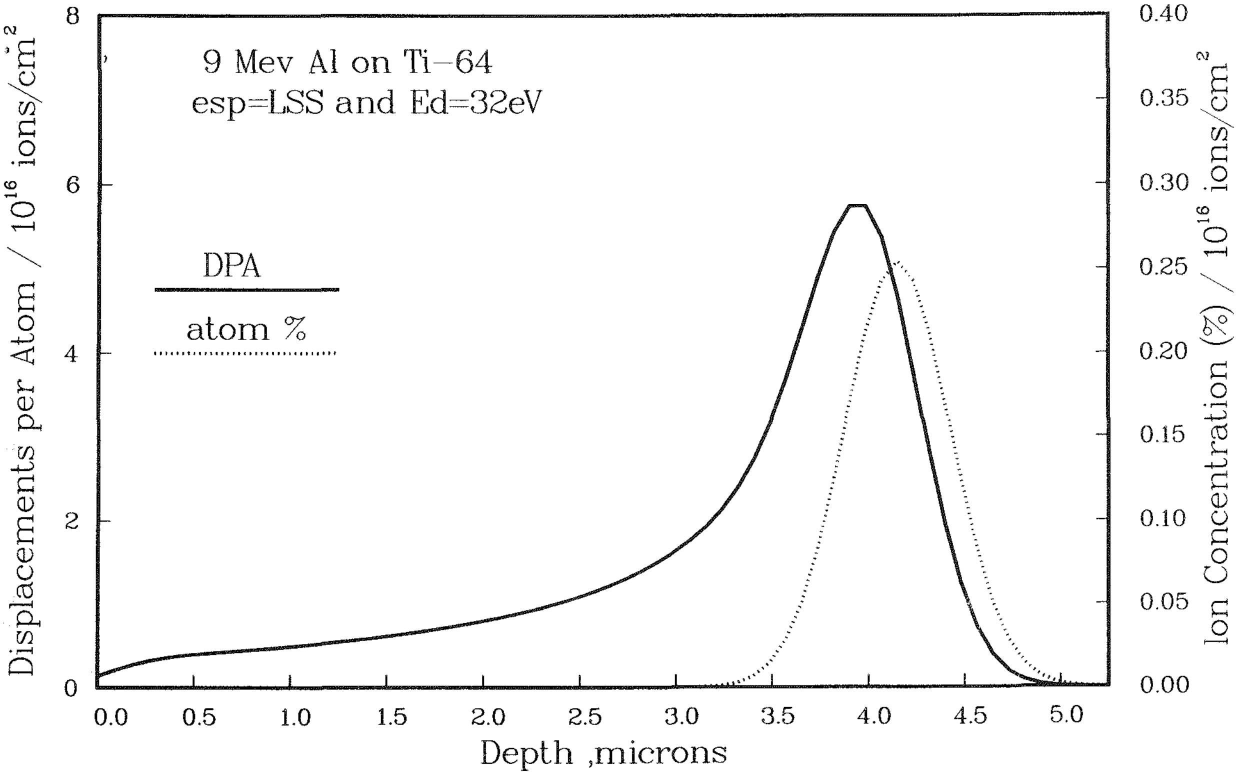

FIGURE 1. Displacement damage and implanted ion concentration versus the incident ion range for 9 MeV Al on Ti-6Al-4V.

FIGURE 2. TEM micrograph illustrating grain structure and dislocation distribution in Ti-6242S annealed at 500°C for 8 hours.

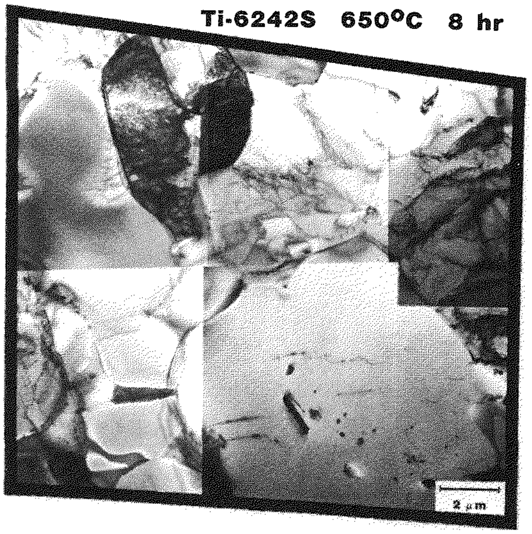

FIGURE 3. TEM micrograph illustrating some grain growth and recovery in Ti-6242S annealed at 650°C for 8 hours.

consists of alternating plates of α and β phase. Figure 3 shows the alloy microstructure after an 8 hr anneal at 650°C. It appears that some grain growth has occurred. The β_T appears to have consolidated from many plates to at most a few β plates and in some instances a small β grain. The precipitates in the large α grain have been qualitatively identified, using EDS, as Sn rich particles. It should be pointed out that in this titanium alloy system the dislocations often align into arrays, examples of which can be observed in both previous micrographs. This point will be important later as it will be shown that the irradiation precipitate response appears to be associated with these arrays.

A typical example of the microstructure of Ti-6242S irradiated to 2 dpa at 450°C is shown in Fig. 4(a). The alpha grain is full of a fine dislocation microstructure while the β_T visible in the lower left corner appears unaffected. Examination of the corresponding diffraction pattern, 4(d), shows what appears to be overlapping spots with the indexing given adjacent to the pattern. Figure 4(b) is a centered dark field micrograph using $g(\alpha) = [\bar{1}101]/g(\beta) = [110]$ which appears to be a strongly diffracting α reflection. This results in the imaging of the dislocation structure and possibly some precipitates aligned on the dislocation network. Figure 4(c) uses $g(\beta) = [\bar{1}10]/g(\alpha) = [\bar{1}011]$ which shows a double spot identity indicating a strongly diffracting β reflection, and indeed the image shows small precipitates arranged along dislocation lines. Further evidence that these precipitates are heterogeneously precipitating on dislocation lines is given in Fig. 5 where the bright field image shows some strongly diffracting precipitates arranged along lines. The dark field image shows how these precipitates are strongly imaged. The diffraction patterns associated with these precipitates indicate a bcc structure, similar to that reported previously for the radiation-induced β phase in Ti-64. For the present, these precipitates will be called β_i. A high magnification view of these β_i is shown in Fig. 6 where the high density and small size of these precipitates is imaged in a homogeneous distribution. Only in this type of homogeneous distribution is it possible to obtain a number density (8.8×10^{15}) and an average size (16 nm).

Figure 7 shows the β_i morphology at 550°C and 2 dpa. It appears that the β_i precipitation is occurring on dislocation arrays. This can be seen in the central portion of both (a) and (b). There is, however, a cluster morphology which is starting to occur and can be seen in the upper left corner. All of this precipitation appears to be small β_i precipitates which agglomerate at some sinks. A clearer illustration of this point is seen in Fig. 8. This is a bright field/dark field pair which distinctly shows the small individual β_i precipitates lined up in arrays.

At higher irradiation temperature (600°C) the β_i precipitate clusters predominate and are more uniformly distributed. Figure 9 illustrates this phenomenon. While much of the precipitation is occurring in the clusters, the Fig. 9(b) dark field view shows some small precipitates in the matrix away from clusters. The size of the β_i precipitates still appears very small and the clusters do seem to consist of these small β_i precipitates in several short linear agglomerations per cluster. In a few cases these clusters look distinctly globular. This is shown in Fig. 10.

Occasional voids are observed, Fig. 11, and in most cases they are adjacent to a grain boundary. The two voids in the upper right hand corner of Fig. 11 are next to a retained β grain and associated with a β_i cluster as the dark field micrograph indicates. Not all the β_i precipitates are in cluster form. Figures 12(a) and (b) show a β_i distribution that is a denser version of the linear array morphology. In all cases, at 600°C and 2 dpa, the density of small β_i precipitates in a cluster appears higher than at the lower temperatures in the linear arrays.

At 650°C and 2 dpa the precipitate morphology is of a more normal appearance and in fact resembles the radiation-induced precipitation that occurs in Ti-64 at lower temperatures. Figure 13 shows an α grain with all 6 β_i precipitate orientations. The β_i precipitates are elongated platelets with an average size of 150 nm and a density of 6×10^{13} #/cm^3. At this temperature there is dislocation movement and grain growth occurring. Also shown are faulted loops pinned on precipitates. The precipitates are not drastically reducing microstructural evolution, in terms of grain growth, as is indicated by the large retained β grain near the center of Fig. 13. That this alpha grain has grown around one of its former grain boundary β grains is indicated in Fig. 14. This shows that the retained β grain has no orientation relation with the β_i precipitates present in the α grain. Further indication of the extensive dislocation annealing, occurring during irradiation at 650°C, is shown in Fig. 15. Here the dislocations display long faulted traces.

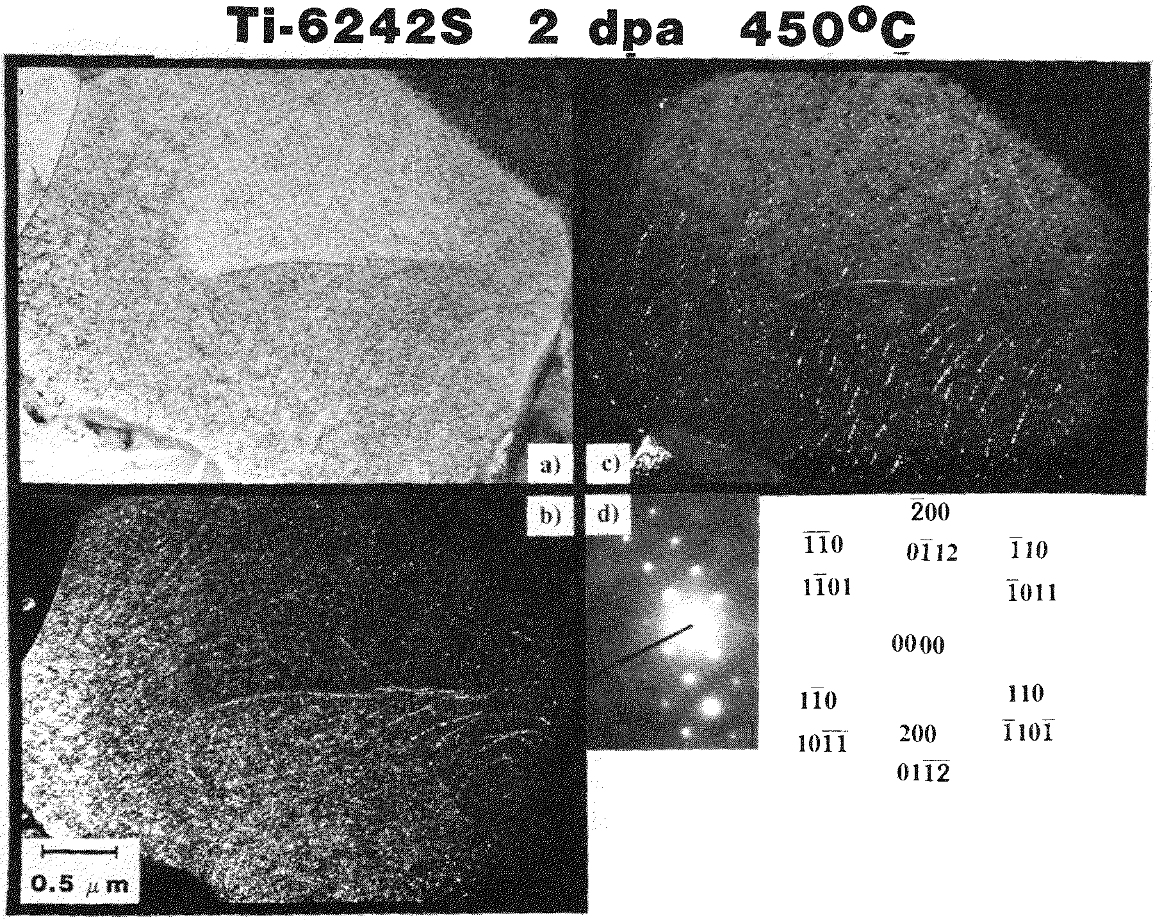

FIGURE 4. a) Bright field TEM micrograph showing a heterogeneous distribution of radiation-induced β precipitates.

b) & c) Dark field TEM micrograph using $\vec{g}(\beta)$ = [110] and [$\bar{1}$10].

d) Selected area diffraction pattern illustrating the overlap of $B_Z(\alpha)$ = [01$\bar{1}$1] and $B_Z(\beta)$ = [001].

While Fig. 13 showed the β_i precipitates, produced at 650°C, from near an edge-on perspective they can also be imaged from a top view orientation. Figure 16 shows the width of the β_i precipitates and also indicates that there is some small amount of clustering remaining in their distribution. An overall view of several grains is shown in Fig. 17. There are many items to note in this figure. In the large α grain on the left side, the view of the aligned β_i precipitates is their topside. However, the β_i density of the aligned precipitate arrays is not as high as it was for the lower temperature clusters. Beneath this grain in the lower left corner, the β_i precipitates are imaged from edge on. Another item to note is that the average α grain size has increased (i.e., compared to Fig. 2) while the as-received, transformed β grains appear to have consolidated into β grain boundary regions. The void density appears higher than in the 600°C case yet voids still are mainly associated with grain boundaries.

Finally after 2 dpa at 700°C, the β_i precipitates have grown to ~ 360 nm while the density has remained about the same at 5×10^{13} #/cms. Figure 18 shows the precipitates from edge on. While still slightly clustered, the distribution was fairly uniform. Unfortunately the sample preparation of this specimen was such that a void distribution was impossible to determine. The sizes and precipitate densities are summarized in Table I.

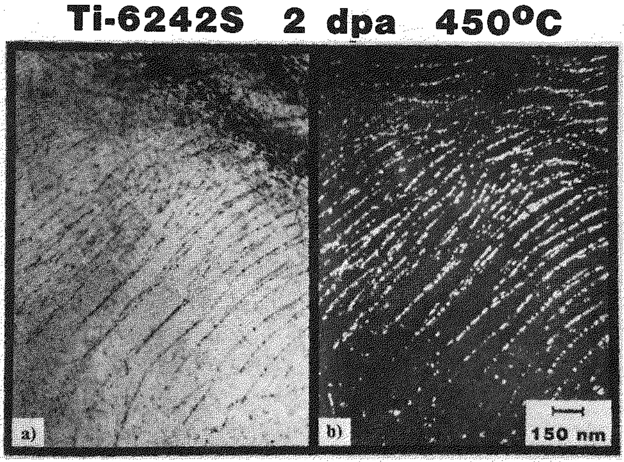

FIGURE 5. a) Bright field TEM micrograph showing a heterogeneous distribution of small β_i precipitation.
b) Dark field TEM micrograph using $\vec{g}(\beta)$ = [110].

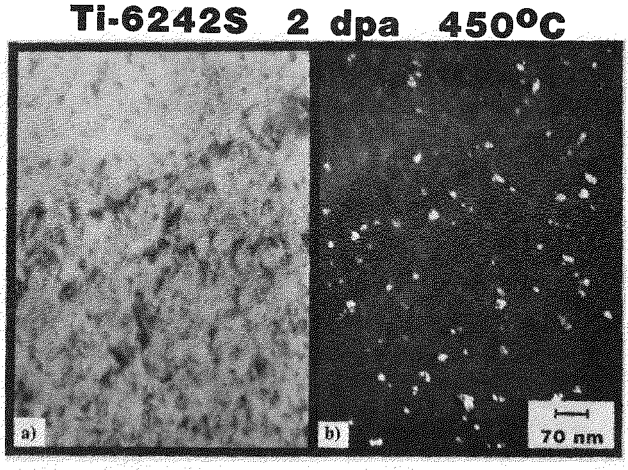

FIGURE 6. a) Bright field TEM micrograph showing the high density and small size of β_i precipitates in a homogeneous distribution.
b) Dark field TEM micrograph using $\vec{g}(\beta)$ = [011].

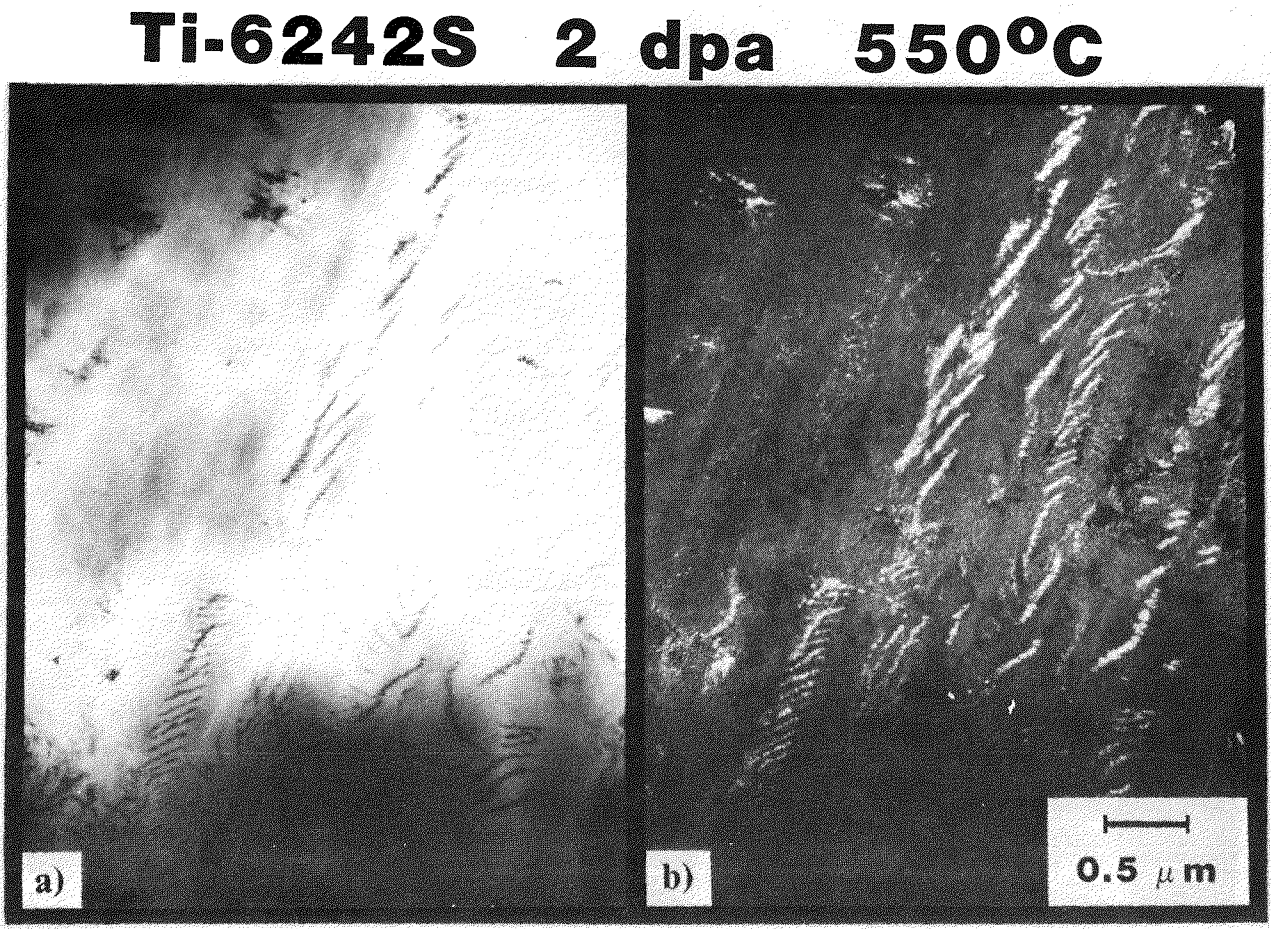

FIGURE 7. a) Bright field TEM micrographs showing both globular and linear array morphologies of the β_i precipitate agglomerations.
b) Dark field TEM micrograph using $\vec{g}(\beta)$ = [200].

5.4 Discussion

To positively identify these bcc precipitates as radiation-induced one must observe dissolution of the precipitate upon annealing at a temperature in the α phase field. This has not yet been done so a qualitative argument must be used. This near-α alloy, Ti-6242S, has much more α stabilizing solutes than Ti-6Al-4V and fewer β stabilizing solutes. Therefore it would seem reasonable that if the bcc radiation-induced precipitates (β_i) in Ti-64 dissolve, then so should those in Ti-6242S. The β_i precipitates probably are Mo enriched. As noted previously Wang et al.[12] did observe Mo segregation to a free surface after irradiation. They, however, noted some ambiguity in the interpretation of their results. They examined Ti-8Al-1V-1Mo and the binary alloys Ti-3V and Ti-8.7Al, and while they could state that V and Al do segregate to a free surface by consideration of the binary alloy results, there exists another possibility for Mo. This is that if vanadium-rich bcc precipitates form at the free surface, then this bcc phase might preferentially incorporate Mo. This would produce a driving force for Mo to diffuse into the depleted area. The fact that bcc radiation-induced precipitates are occurring in Ti-6242S without vanadium being present indicates that Mo is undoubtedly segregating to a sink, then precipitating out in a bcc phase. This point is further advanced by the work of Erck et al.[17] who irradiated Ti-8.5Al with ions and found no irradiation-induced β phase. They did note the Al segregated to sinks, precipitating out as α_2, the Ti_3Al ordered phase. Therefore, it appears that some form of bcc stabilizing solute is necessary for the radiation-induced beta phase to form.

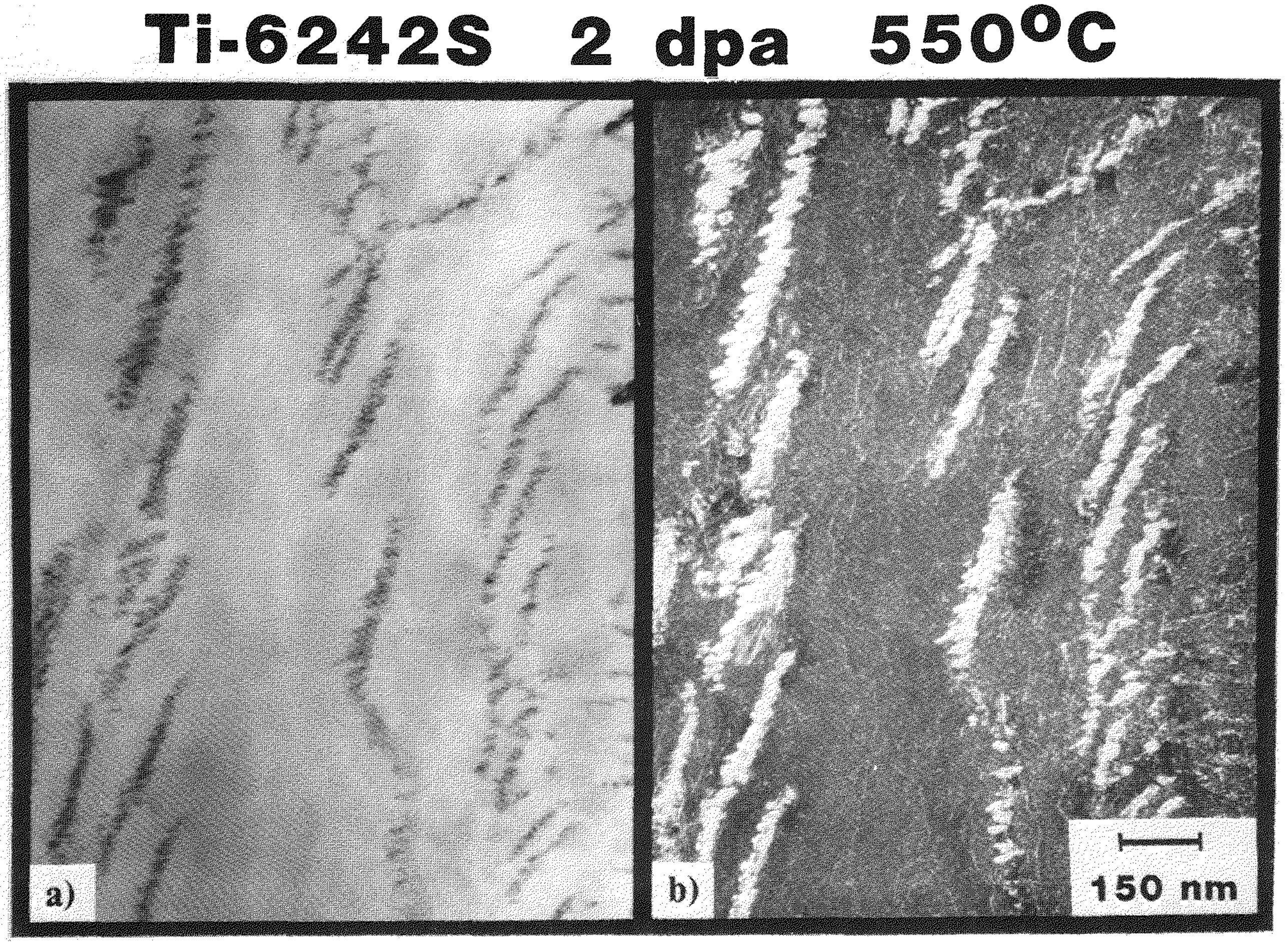

FIGURE 8. a) Bright field TEM micrograph showing a heterogeneous agglomeration of β_i precipitates.
b) Dark field TEM micrograph using $\vec{g}(\beta)$ = [200].

The neutron work on Ti-6242S[9,10] examined both 2 and 32 dpa at 450 and 450/550°C, respectively. In both cases no bcc precipitates were observed. A fine dislocation structure was produced with small loops and heterogeneous void distribution for the higher fluence. Two possible explanations for this behavior are immediately apparent. The different damage rates between neutron (1×10^{-6} dpa/s) and ion (2×10^{-3} dpa/s) irradiations might cause more solute segregation to occur under ion irradiation conditions. Neutron irradiations do confirm β_i precipitation in Ti-6Al-4V, but Ti-64 has more beta stabilizer (4 to 2) and a much more pronounced segregating solute[12] (i.e., V compared to Mo). The other explanation involves the presence of He in neutron irradiations retarding the microstructural evolution of the alloy. At 650°C, Figs. 13-15 and 17 show that under ion irradiation considerable dislocation annealing and grain growth is occurring. If one uses a "temperature shift" of 40°C for every decade increase in displacement rate,[18] one would have an equivalent neutron irradiation temperature of ~ 520°C. The fact that the neutron results did not indicate any evidence of grain growth at 550°C suggests that He may play a role in inhibiting dislocation and solute mobility.

Whether or not the radiation-induced phase observed in this study results from RIS of undersize solutes via interstitial complexes or from a shift in the potential energy of a phase resulting in a shift of phase boundaries, is a difficult question. The fact that the β_i phase occurs only with a β stabilizing solute present that has demonstrated radiation-induced segregation seems clear (i.e., V and Mo). However, in recent work[19] on Ti-64 using EDS analysis, the β_i precipitates occurring at 2 dpa and 600°C have been shown to have a vanadium concentration ~ 50% higher than what would be expected from an equilibrium phase diagram. Therefore one might expect both solute segregation and phase boundary shifts are occurring.

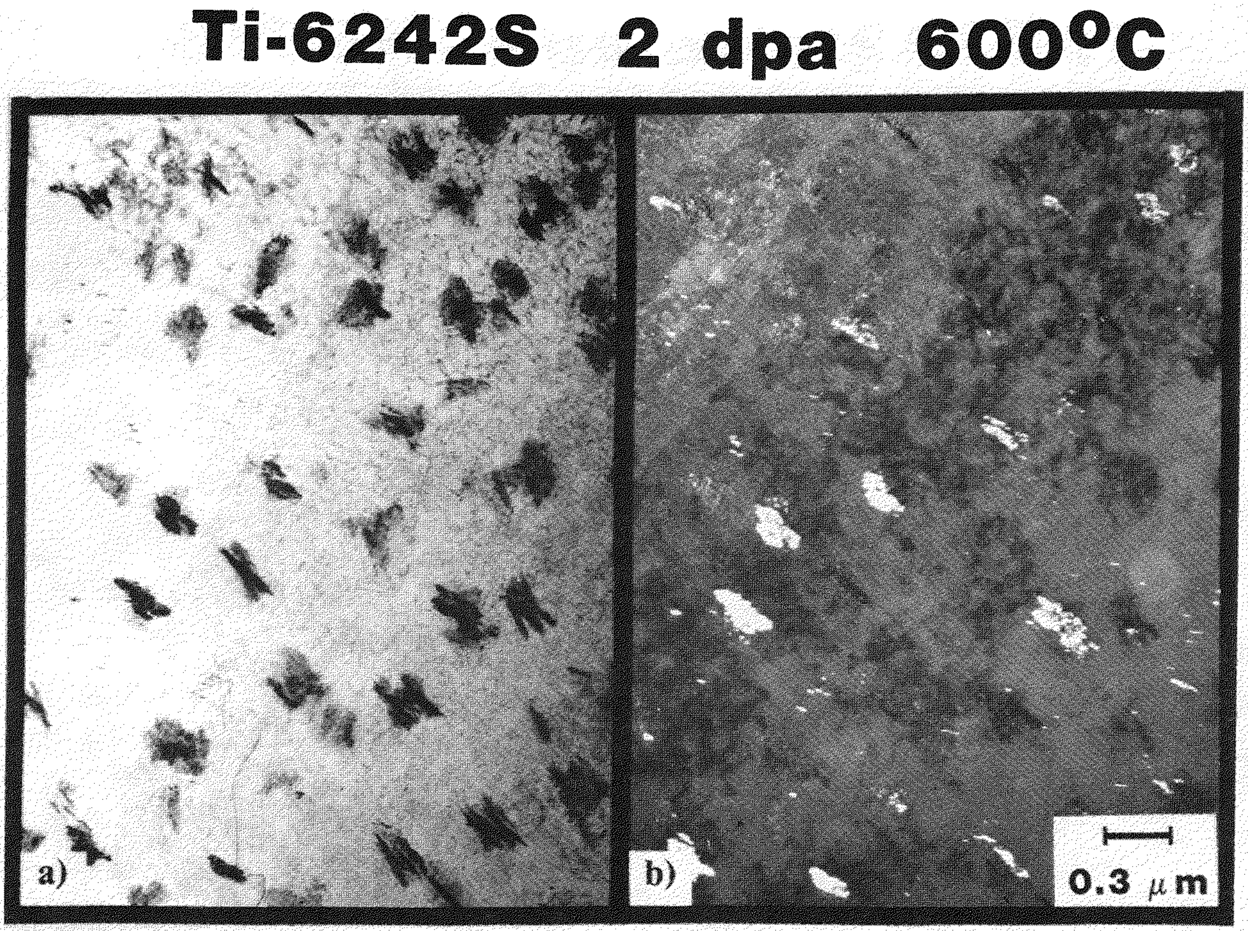

FIGURE 9. a) Bright field TEM micrograph illustrating a uniform distribution of β_i precipitate clusters.
b) Dark field TEM micrograph using $\vec{g}(\beta) = [011]$.

5.5 Conclusions

1. A bcc precipitate is observed in Ti-6242S after 2 dpa at temperatures from 450-700°C.
2. The low temperature (450-600°C) morphology of the β precipitate is unusual. It consists of small (~ 20 nm) β precipitates clustering into different shaped agglomerations. At 450°C the agglomerations were linear arrays while at 600°C the agglomerations had become "homogeneously" distributed clusters composed of short arrays.
3. The high temperature irradiations (650-700°C) produced precipitates that were normal in appearance and they consisted of elongated platelets similar to those seen in irradiated Ti-6Al-4V.
4. A low density of voids ($< 10^{12}$ #/cm^3) is observed between 550-650°C and the voids are heterogeneously distributed, usually adjacent to a grain boundary.

5.6 Future Work

The magnitude of the void swelling and the composition of the β_i precipitates will be quantitatively measured.

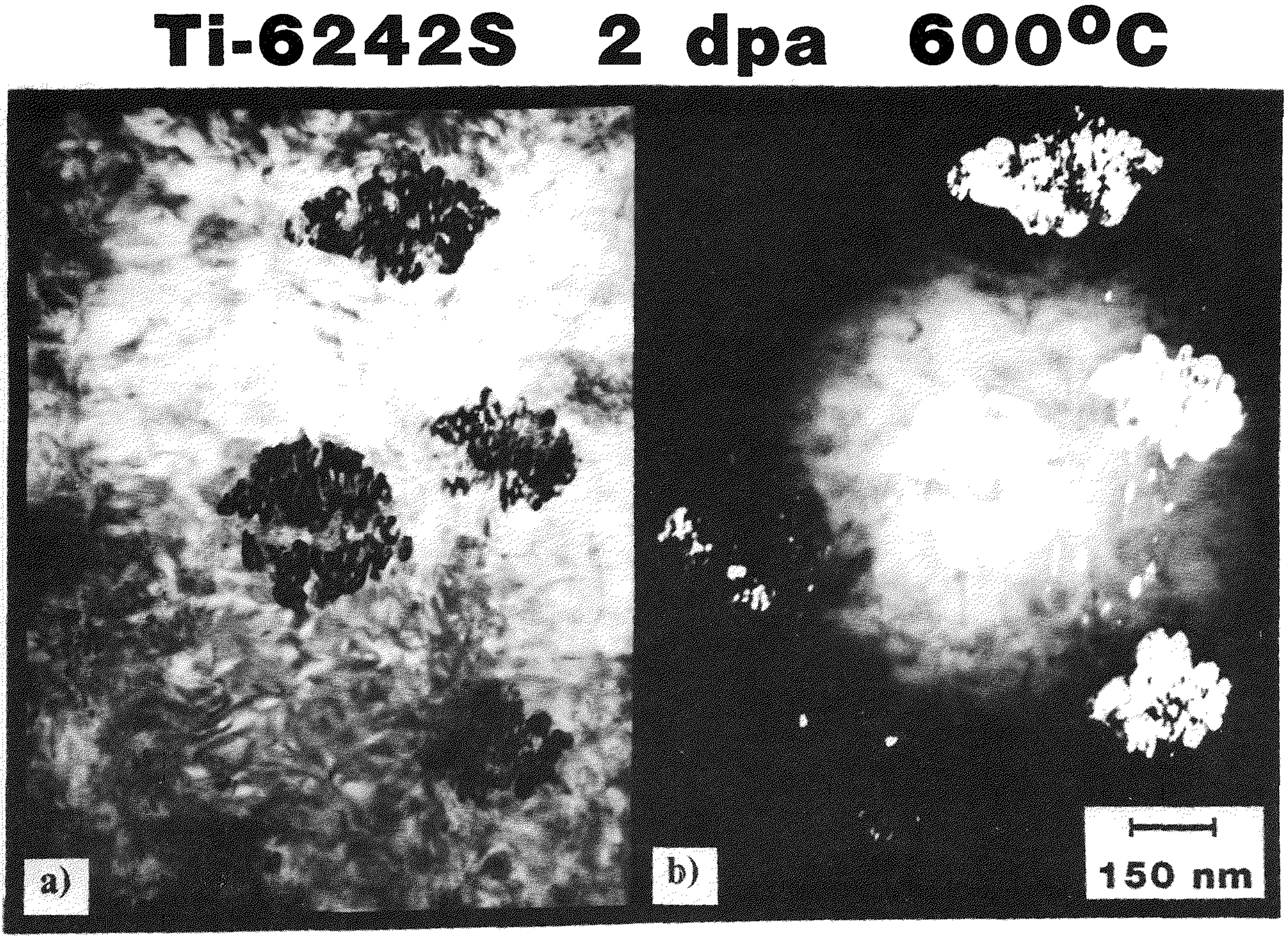

FIGURE 10. a) Bright field TEM micrograph showing several globular shaped β_i precipitate clusters.
b) Dark field TEM micrograph using $\vec{g}(\beta)$ = [110].

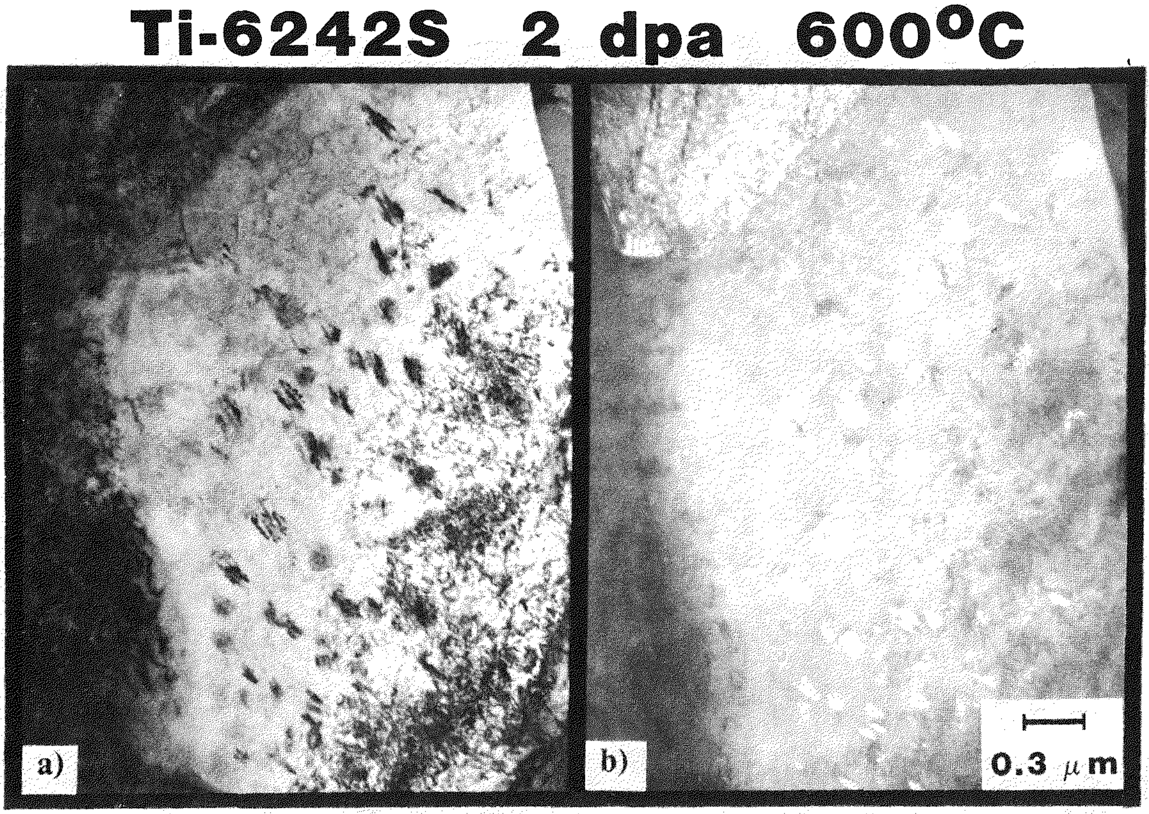

FIGURE 11. a) Bright field TEM micrograph illustrating a "homogeneous" distribution of β_i clusters and two voids next to a grain boundary.
b) Dark field TEM micrograph using $\vec{g}(\beta) = [110]$, and showing β_i precipitate/void association.

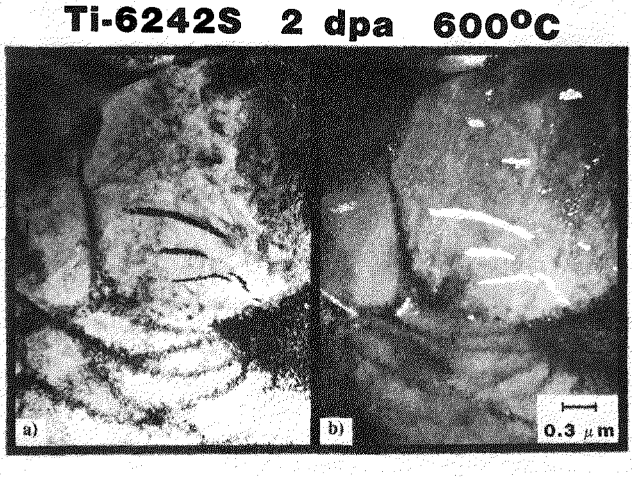

FIGURE 12. a) Bright field TEM micrograph illustrating the heterogeneous nature of β_i precipitation.
b) Dark field TEM micrograph using $\vec{g}(\beta) = [110]$.

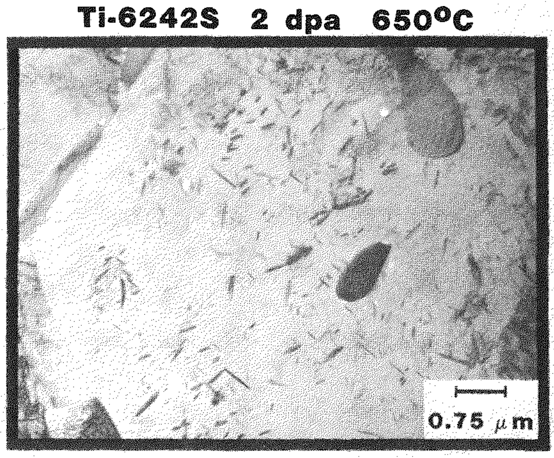

FIGURE 13. TEM micrograph showing all 6 β_i precipitate orientations. Also shown are faulted loops pinned on β_i precipitates.

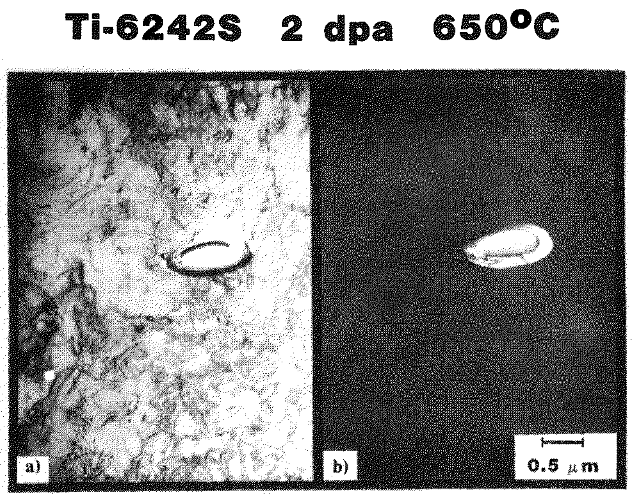

FIGURE 14. a) Bright field TEM micrograph showing a void and a retained grain boundary, β_G, precipitate, $\vec{g}(\alpha) = [11\bar{2}0]$.
b) Dark field TEM micrograph using $\vec{g}(\beta) = [200]$.

FIGURE 15. TEM micrograph showing stacking faults, an indication of the extensive recovery that has occurred.

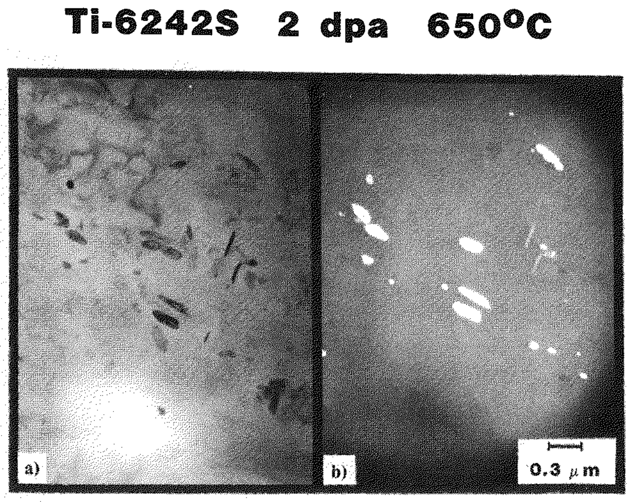

FIGURE 16. a) Bright field TEM micrograph showing β_i precipitates in a slightly clustered distribution.
b) Dark field TEM micrograph using $\vec{g}(\beta) = [112]$.

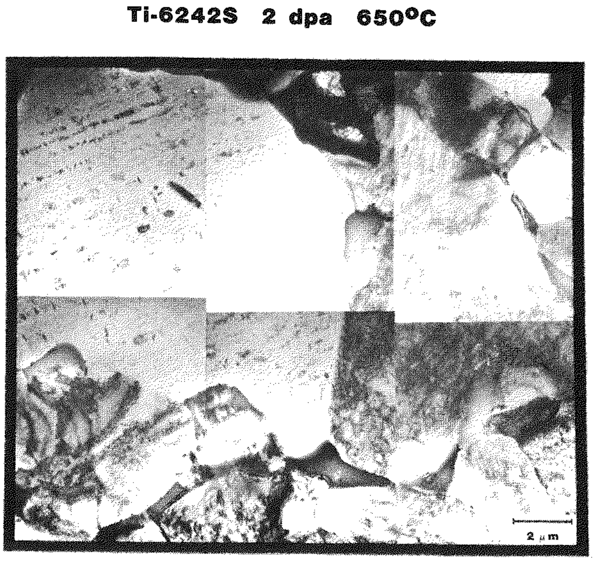

FIGURE 17. TEM micrograph showing a typical grain size distribution and the radiation-induced β precipitates (β_i).

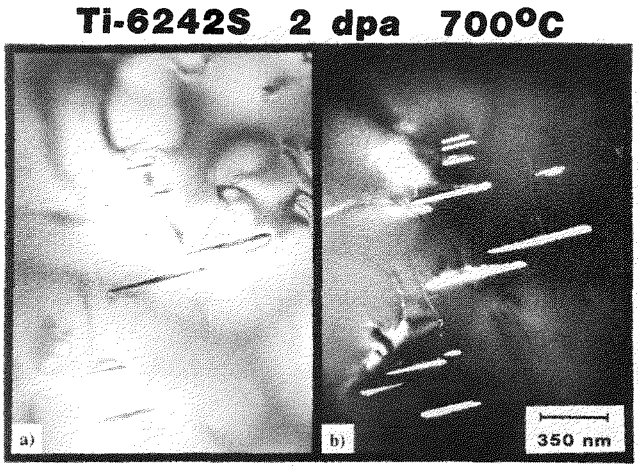

FIGURE 18. a) Bright field TEM micrograph showing the large size, 350 nm, and low density, 5×10^{19} #/m^3, of β_i precipitates.
b) Dark field TEM micrograph using $\vec{g}(\beta) = [112]$.

TABLE I. β_i Precipitate Sizes and Densities for Ti-6242S

Temperature (°C)	Density #/cm^3	Size (nm)
450	8.8×10^{15}	16
600	6.0×10^{13}	170
650	6.1×10^{13}	150
700	5.0×10^{13}	360

6.0 References

1. J.W. Davis and G.L. Kulcinski, EPRI, ER-386 (1977).

2. R.W. Conn, J. Nucl. Mater. 76 & 77, pp. 103-111, 1978.

3. E.E. Bloom, J. Nucl. Mater. 85 & 86, pp. 795-804, 1979.

4. R.H. Jones, B.R. Leonard and A.B. Johnson, EPRI-AP-1433 (1980).

5. C. Hammond and J. Nutting, Metal Sci., pp. 474-490, 1977.

6. P. Wilkes and G.L. Kulcinski, J. Nucl. Mater. 78, pp. 427-430, 1978.

7. S.C. Agarwal, G. Ayrault, D.I. Potter, A. Taylor and F.V. Nolfi, Jr., J. Nucl. Mater. 85 & 86, pp. 653-657, 1979.

8. R.H. Jones and L.A. Charlot, J. Nucl. Mater. 91, pp. 329-335, 1980.

9. S.M.L. Sastry, J.E. O'Neal and J.W. Davis, Titanium '80, Eds. H. Kimura and O. Izumi, pp. 651-662, 1980.

10. D.T. Peterson, Effects of Radiation on Materials: Eleventh Conference, Eds. H.R. Brager and J.S. Perrin, ASTM STP 782, pp. 260-274, 1982.

11. G. Ayrault, J. Nucl. Mater. 113, pp. 1-13, 1983.

12. Z. Wang, G. Ayrault and H. Wiedersich, J. Nucl. Mater. 108 & 109, pp. 331-338, 1982.

13. P.R. Okamoto and H. Wiedersich, J. Nucl. Mater. 53, pp. 336-345, 1974.

14. G. Ayrault, Phase Stability During Irradiation, Proc. Fall Meeting, Pittsburgh, PA, TMS-AIME, 1980.

15. J. Lindhard and M. Scharf, Phys. Rev., 124, p. 128, 1961.

16. M.J. Blackburn and J.C. Williams, TMS-AIME 239, pp. 287-288, 1967.

17. R.A. Erck, D.I. Potter and H. Wiedersich, J. Nucl. Mater. 80, pp. 120-125, 1979.

18. F.A. Garner and J.J. Laidler, Proc. Workshop on Correlation of Neutron and Charged Particle Damage, CONF-760673, ORNL, p. 177, 1976.

19. D.L. Plumton, G.L. Kulcinski and R.A. Dodd, DAFS Quarterly Report, April 15, 1985.

THE EFFECT OF DENSITY CHANGES ON THE ENERGY AND ION DEPOSITION PROFILES

W.G. Wolfer and M.E. Benchikh-Lehocine (University of Wisconsin-Madison)

1.0 Objective

Ion bombardment of solid surfaces produces density changes in the surface layer which subsequently affects the ion range. A correction procedure is developed to evaluate the modified ion range.

2.0 Summary

Using the transport theory for the distribution of deposited energy or deposited ions, it is shown that the effect of density changes on these distribution profiles can be obtained from the distribution profiles in a medium with constant density by a simple coordinate transformation, provided the distribution functions depend only on one spatial coordinate.

3.0 Program

Title: Effect of Radiation and High Heat Flux on the Performance of First-Wall Components
Principal Investigator: W.G. Wolfer

4.0 Relevant DAFS Program Plan Task/Subtask

Subtask III.B.2.3 Correlation Methodology

5.0 Accomplishments and Status

5.1 Introduction

In studies of sputtering, blistering, radiation damage, and ion implantation of solids, the range distribution of both deposited ions and deposited energy are of primary interest. These distribution profiles are commonly computed according to the transport theory developed by Sigmund and Sanders.[1,2] In their original formulation, the density of atoms in the solid was considered to be constant. It is a trivial matter, however, to generalize it to include nonuniform atom densities.

Variations in density and composition with depth are often encountered in ion bombardment studies. These variations may be due to the initial surface contamination and segregation of alloying elements to the surface. Or, more often, the variations are due to void and bubble formation as a result of the ion bombardment itself.

The effect of density variations as caused by radiation-induced voids on the range of ions and damage was earlier considered by Odette et al.[3] in an ad hoc fashion. They argued that the effect of voids can simply be included into the range by adding the distance traveled through the voids to the distance traveled through the void-free solid. They considered this procedure an approximate one, however, since void-induced straggling was not accounted for.

In the present paper we prove rigorously, starting from the transport theory, that density correction to the entire profiles for both ion and damage distribution can be made immediately if one knows these profiles in the solid with constant density and if one knows the density variation with depth. This can be achieved by a simple transformation of the depth coordinate. It follows further from the proof that density corrections can be made in this manner whenever the transport problem can be formulated as a one-dimensional one, be it planar, cylindrical or spherical.

5.2 Transport Equation for Range and Damage Distribution

Let $F(\vec{r},\vec{v})$ denote the distribution function for either the deposited energy (damage) or the deposited ions (range). More specifically, $F(\vec{r},\vec{v})\,d^3r$ is either the recoil energy or the ions deposited in the volume element d^3r about $\vec{r}$ when these ions enter the solid at $\vec{r} = 0$ and with initial velocity $\vec{v}$.

This distribution function satisfies the following transport equation:

$$-\frac{\vec{v}}{|v|}\cdot\vec{\nabla}_r F(\vec{r},\vec{v}) - N(\vec{r})\,\frac{S_e}{|v|}\,\frac{\partial}{\partial|v|}F(\vec{r},\vec{v}) = \int N(\vec{r})\,d\sigma\,\{F(\vec{r},\vec{v}) - F(\vec{r},\vec{v}\,') - \xi\bar{F}(\vec{r},\vec{v}\,'')\}\quad . \tag{1}$$

Here, $N(r)$ is the local atom density, $d\sigma(\vec{v}\,',\vec{v}\,'')$ is the differential cross section for elastic nuclear scattering, the integration being carried out over all velocities $\vec{v}\,'$ of the scattered ion and over all velocities $\vec{v}\,''$ of the recoiling target atom, and S_e is the electronic stopping power per target atom. The parameter $\xi = 0$ for the range distribution, and $\xi = 1$ for the damage distribution, respectively. $\bar{F}(\vec{r},\vec{v})$ is the recoil distribution. If the target atoms differ from the projectile atoms, then $\bar{F}(\vec{r},\vec{v})$ satisfies an equation like Eq. (1) in which all the distribution functions refer now to target atoms.

Equation (1) is identical to those derived by Sigmund and Sanders[1,2] and others[4,5,6] with the trivial modification that the number density of target atoms, $N(\vec{r})$, is a function of the position.

5.3 Transformation to Constant Density

For a plane ion source with a lateral ion flux profile that changes little over distances of the order of the ion range, the transport problem becomes one-dimensional. Then F depends only on the depth coordinate x if the density is also only a function of x. Let us then define a new space coordinate

$$\bar{x} = \frac{1}{\bar{N}}\int_0^x N(x')\,dx' \tag{2}$$

where

$$\bar{N} = \frac{1}{R}\int_0^R N(x')\,dx' \tag{3}$$

is the number density of atoms averaged over at least the entire range or beyond.

Assuming that the function $\bar{x}(x)$ can be inverted in principle to obtain $x(\bar{x})$, the distribution function becomes now a function of $\bar{x}$. Since

$$\frac{\partial F}{\partial x} = \frac{d\bar{x}}{dx}\,\frac{\partial F}{\partial\bar{x}} = \frac{N(x)}{\bar{N}}\,\frac{\partial F}{\partial\bar{x}}\quad , \tag{4}$$

the transport Eq. (1) for the one-dimensional case can now be written as

$$-\frac{v_x}{|v|}\,\frac{N(x)}{\bar{N}}\,\frac{\partial}{\partial\bar{x}}F(\bar{x},r^{\rightarrow}) - N(x)\,\frac{S_e}{|v|}\,\frac{\partial}{\partial|v|}F(\bar{x},\vec{r}) = \int N(x)\,d\sigma\,\{F(\bar{x},\vec{r}) - F(\bar{x},\vec{v}:) - \xi\bar{F}(\bar{x},\vec{v}\,'')\}\quad . \tag{5}$$

If this equation is multiplied by $\overline{N}/N(x)$ we obtain a transport equation for $F(\overline{x},\vec{v})$ in a medium with constant atom density $\overline{N}$.

Therefore, we have shown, that if the transport equation is solved for a constant uniform atom density $\overline{N}$ and the solution is $F(\overline{x},\vec{v})$, then the distribution function in a medium with nonuniform atom density $N(x)$ is given by $F[x(\overline{x}),\vec{v}]$, where $x(\overline{x})$ can either be obtained from the inversion of the function defined in Eq. (2), or from the equation

$$x = \overline{N} \int_0^{\overline{x}} \frac{d\overline{x}}{N(\overline{x})} \quad . \tag{6}$$

When we apply these results to density changes caused by void or bubble swelling, it is more convenient to employ the number density N_0 in the theoretically dense material rather than $\overline{N}$. If $S(x) = \Delta V/V$ and $S_0(\overline{x}) = \Delta V/V_0$ denote then the void volume fraction per unit volume of the voided and void-free material, respectively, then

$$N(x) = N_0(1 - S(x)) \tag{7}$$

and

$$N(\overline{x}) = N_0(1 - S_0(\overline{x})) \quad . \tag{8}$$

Hence, the depth coordinate transformation is given by

$$\overline{x} = x - \int_0^x S(x')\, dx' \tag{9}$$

or by

$$x = \int_0^{\overline{x}} \frac{d\overline{x}'}{[1 - S_0(\overline{x}')]} \quad . \tag{10}$$

Experimentally, the swelling is usually measured as a function of depth x, so that Eq. (9) is the more appropriate one to use.

5.4 Discussion

We have shown rigorously from the transport theory applicable to range and damage distribution as produced by a planar ion beam that density variations with depth can simply be accounted for once the distribution functions have been obtained for the fully dense and uniform material. Although this was shown explicitly only for the planar, one-dimensional distributions, the same result is obtained, whenever the transport equations depend only on one coordinate. It applies then also to ion-bombardment from a spherical or a cylindrical source in a solid. Spherical ion sources in the form of boron-rich precipitates have recently been considered by Gelles and Garner[7] as a tool to study void formation is steels under simultaneous production of damage and helium. The void density around the precipitate particles was found to depend only on the radial distance.

As mentioned in the discussion, a variation in the composition of alloys or compounds with depth may be produced by the ion bombardment due to preferential sputtering, radiation-induced segregation and recoil mixing. To compute the redistribution of the various elements in an alloy or compound as a result of ion bombardment, a set of transport equations for each species need to be solved simultaneously.[8] When electronic losses can be neglected each transport equation depends on only one number density. If the number densities for the various species depend on the depth we can again apply the above coordinate transformation for each species separately, and we obtain transport equations which depend only on an average constant density of one particular species.

Unfortunately, when electronic losses are included each transport equation depends now on all number densities, and the above transformation no longer generates equations for uniform atom densities.

6.0 References

1. P. Sigmund and J.B. Sanders, Proc. of the Intern. Conf. on "Application of Ion Beams to Semiconductor Technology," ed. by P. Glotin (Editious Oplinys, Paris, 1967), p. 215.
2. P. Sigmund, Phys. Rev. 184, p. 383, 1969.
3. G.R. Odette, D.M. Schwartz, and A.J. Ardell, Rad. Effects 22, p. 217, 1974.
4. K.B. Winterbon, P. Sigmund, and J.B. Sanders, Mat. Fys. Medd. Dan. Vid. Selsk. 37, No. 14, 1970.
5. P. Sigmund, M.T. Matthies, and D.L. Phillips, Rad. Effects 11, p. 39, 1971.
6. K.B. Winterbon, Rad. Effects 30, p. 199, 1976.
7. D.S. Gelles and F.A. Garner, J. Nucl. Materials 85 & 86, p. 689, 1979.
8. K.B. Winterbon, Rad. Effects 48, p. 97, 1980.

STABILITY OF VACANCY CLUSTERS IN COPPER AND OTHER METALS

S.J. Zinkle, L.E. Seitzman and W.G. Wolfer (University of Wisconsin-Madison)

1.0 Objectives

To examine the energies of various vacancy clusters both in the absence and presence of gas. From this analysis, we hope to determine experimental conditions that lead to void formation.

2.0 Summary

The energies of voids, stacking fault tetrahedra and vacancy loops in aluminum, copper, nickel and stainless steel have been determined as a function of size using established equations from elasticity theory. Stacking fault tetrahedra and vacancy loops were the most stable small cluster morphologies in all four metals in the absence of gas. A model is presented that determines the effect of oxygen and helium on the energies of vacancy clusters. The presence of small amounts of these gases causes the void to be the most stable cluster morphology.

3.0 Programs

Title: Radiation Effects to Reactor Materials
Principal Investigators: G.L. Kulcinski and R.A. Dodd
Affiliation: University of Wisconsin-Madison

Title: Effect of Radiation and High Flux on the Performance of First Wall Components
Principal Investigator: W.G. Wolfer
Affiliation: University of Wisconsin-Madison

4.0 Relevant DAFS Program Plan Task/Subtask

Subtask II.C.1.2 Modeling and Analysis of Effects of Materials Parameters on Microstructures

5.0 Accomplishments and Status

5.1 Introduction

Macroscopic swelling due to void formation is a major concern in radiation damage studies. Unfortunately, the physical mechanisms that comprise the void nucleation process are still not completely understood. In particular, the role of small amounts of gas on void nucleation is uncertain. It has been recognized for some time that helium can have a strong effect on the void microstructure.[1] Oxygen[2] and hydrogen[3] are also known to promote void swelling. Recent experimental work at the University of Wisconsin[4-6] and elsewhere has found that gas may be required for void formation.

This paper examines the relative energies of vacancy clusters in aluminum, copper, nickel, and stainless steel as determined from elasticity theory. A model is then presented for determining the effects of oxygen and helium on the vacancy cluster energies. Representative calculations are given for low concentrations of these gases in copper.

5.2 Energetics of Vacancy Cluster Formation

The relative stabilities of vacancy clusters may be determined using procedures given by previous workers.[7,8] Four types of vacancy cluster morphologies were considered, namely the void, the perfect circular dislocation loop, the faulted (Frank) loop, and the stacking fault tetrahedron. Various equations are available that describe the energy of a dislocation loop. We have chosen the expressions derived by Kroupa,[9] since they are valid for small sizes. The energy of a perfect dislocation loop is given by[9]

$$E_p = \frac{Gb^2}{2(1-\nu)} \{2R + (2R - \varepsilon) [(1 - 0.5 K^2) F(K) - E(K)]\} \tag{1}$$

where $K^2 = \frac{4R(R-\varepsilon)}{(2R-\varepsilon)^2}$

$$F(K) = \frac{2}{\pi} \int_0^{\pi/2} \frac{d\phi}{\sqrt{1-K^2\sin^2\phi}}$$

$$E(K) = \frac{2}{\pi} \int_0^{\pi/2} d\phi \sqrt{1-K^2\sin^2\phi}$$

and G = shear modulus, $b = a_o/\sqrt{2}$ = Burgers vector of a perfect loop, ν = Poisson's ratio, R = loop radius and ε = core radius, $\varepsilon \simeq b$. F(K) and E(K) are elliptical integrals of the first and second kind, respectively. They may be solved numerically using polynomial approximations.[10]

A faulted vacancy loop may be described by a similar equation[9]:

$$E_F = \frac{b_F^2}{b^2} E_p + A\gamma \tag{2}$$

where $b_F = a_o/\sqrt{3}$ = Burger's vector of a faulted loop, A = loop area and γ = stacking fault energy.

The energy of a stacking fault tetrahedron (SFT) is given by[11]

$$E_T = \frac{Gb^2L}{6\pi(1-\nu)} \{\ln \frac{4L}{b} + 1.017 + 0.97 \nu\} + \sqrt{3} L^2\gamma \tag{3}$$

where L = tetrahedron edge length. The energy of a void may be expressed as[12]

$$E_v = 4\pi R_v^2 \Gamma (1 - \frac{0.8}{N+2}) \tag{4}$$

where R_v = void radius, Γ = surface energy of a flat surface, and N = number of vacancies in the void. The term in parenthesis is an empirical correction to the surface energy due to curvature effects.

Values for the materials parameters[13-15] required in the energy calculations are given in Table 1. Calculations were performed on four representative fcc metals (aluminum, copper, nickel, and austenitic stainless steel) at homologous temperatures near the peak void swelling temperature, 0.45 T_M. The effect of temperature of the vacancy cluster energies is rather small, and the calculated results are reasonably valid over

TABLE 1. MATERIALS PARAMETERS

	Al	Cu	Ni	Stainless Steel	Ref
G (GPa)	26.1	48.3	76	72.8	13
ν	0.345	0.343	0.312	0.305	13
N (m^{-3})	6.0×10^{28}	8.45×10^{28}	9.14×10^{28}	8.6×10^{28}	13
a_o (nm)	0.405	0.361	0.352	0.360	13
γ (J/m^2)	0.2	0.055	0.250	0.040	14
Γ (J/m^2)	1.15 @ 150°C	1.7 @ 400°C	2.1 @ 500°C	2.2 @ 500°C$^{(a)}$	15

(a) value for γ-Fe

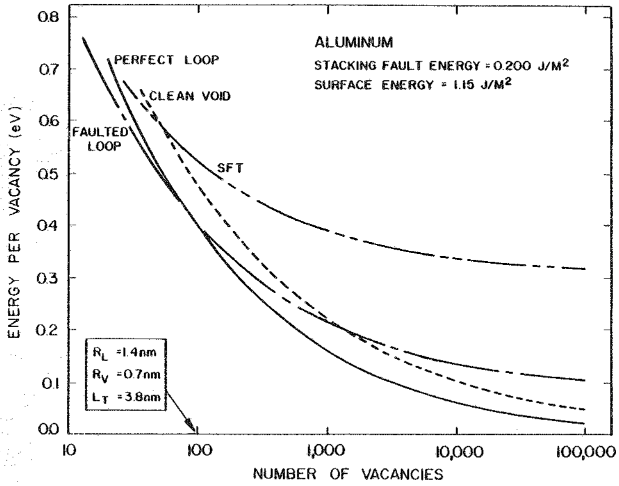

FIGURE 1. Calculated specific energies of vacancy clusters in pure aluminum.

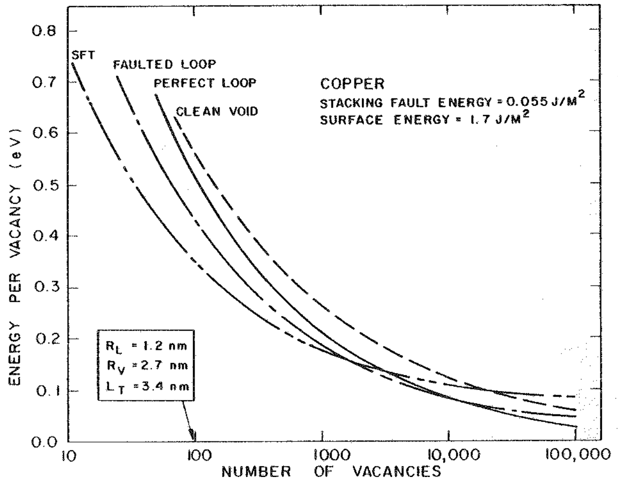

FIGURE 2. Calculated specific energies of vacancy clusters in pure copper.

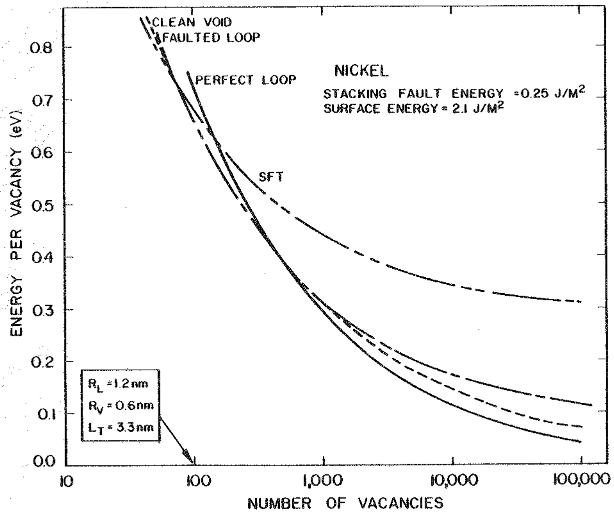

FIGURE 3. Calculated specific energies of vacancy clusters in pure nickel.

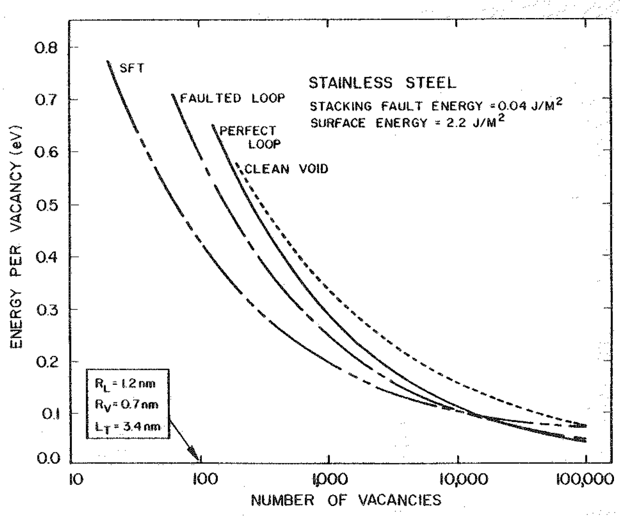

FIGURE 4. Calculated specific energies of vacancy clusters in 316 stainless steel.

the entire void swelling temperature regime. Figures 1-4 show the calculated energy per vacancy of the different cluster morphologies as a function of the number of vacancies in the cluster for the four metals. The stacking fault tetrahedron (SFT) is predicted to be the most stable configuration for small ($\lesssim$ 1000 vacancies) clusters in copper and stainless steel, whereas the faulted (smaller sizes) or perfect (larger sizes) vacancy loop is the most stable in aluminum. Void formation is predicted to never be energetically favorable in these three metals. The void and the faulted loop are equally stable as the lowest energy morphologies in nickel for small cluster sizes ($\lesssim$ 1000 vacancies). The perfect loop is the most stable configuration for all four metals at very large vacancy cluster sizes. Since vacancy cluster nucleation necessarily occurs at small sizes, the stability of the small clusters ($\lesssim$ 1000 vacancies) is expected to exert the dominant effect on the final observed morphology. (As discussed later, there is an appreciable activation energy barrier that inhibits conversion of vacancy clusters between planar and three-dimensional morphologies). The most interesting aspect of the calculations presented in Figs. 1-4 is that void formation is not expected to occur in any of the metals investigated, with the exception of nickel.

Elasticity theory is not strictly valid for very small defect clusters,[8] and it would be more appropriate to use atomistic calculations to determine the most stable morphology at cluster sizes where void nucleation is expected to occur ($\lesssim$ 100 vacancies). Unfortunately, the interatomic potentials of most metals are not known at sufficient accuracy to allow this type of calculation to be performed. Atomistic calculations have recently been conducted on the stability of small vacancy clusters in pure copper.[16,17] Both investigations found that the vacancy loop[16,17] and SFT[17] (planar configurations) are more stable than the void, in agreement with the elasticity predictions (Fig. 2).

There have been several reported observations of SFT in irradiated or quenched copper and copper alloys (see, e.g., 6, 18-21), as predicted from Fig. 2. Faulted and perfect loops are commonly observed in irradiated aluminum.[5,21] McLaurin[5] observed that electron irradiation of high-purity aluminum initially resulted in the formation of faulted vacancy loops. Subsequent growth during continuous irradiation caused the faulted loops to shear and become perfect loops. No voids or SFT were observed, in agreement with Fig. 1. Vacancy loops, SFT and voids have all been observed in irradiated or quenched nickel.[21,22] This matches the predictions of Fig. 3. Figure 4 predicts that SFT are stable in stainless steel. Recent observations of SFT have been made in irradiated 316 type stainless steel and in some Fe-Cr-Ni alloys that are similar to 316 stainless steel.[23-25]

The general agreement between theory (Figs. 1-4) and experiment indicates that elasticity theory may be at least qualitatively correct in its predictions at small cluster sizes. However, a review of the literature reveals that void formation is commonly observed in quenched or irradiated aluminum,[21] copper,[21,26,27] and stainless steel.[28,29] These experimental findings are in conflict with the elasticity theoretical predictions (Figs. 1, 2, 4). In order to remedy this discrepancy between theory and experiment, it is necessary to examine the effect of impurities on the relative energies of vacancy clusters. A model is developed in the following sections that addresses the effect of oxygen and helium on the vacancy cluster energies. In the interest of brevity, calculations are only performed for the case of irradiated copper.

5.3 Role of Oxygen on Void Formation in Copper

It is well known that surface-active species such as oxygen or sulfur may chemisorb onto clean surfaces of metals and cause a reduction in the surface energy.[30-34] If the reduction in surface energy is sufficiently large, then void formation may become energetically favorable. The change in surface energy due to the chemisorption of oxygen at a constant temperature is given by the Gibbs adsorption isotherm:[33,34]

$$\frac{d\Gamma}{d \ln X} = - \frac{RT\,\theta_{sat}}{A_{cu}} \tag{5}$$

where θ_{sat} is the saturated fractional surface coverage, X is the mole fraction of oxygen in solution and A_{Cu} is the molar surface area of copper. The value of A_{Cu} depends upon crystallographic orientation and is 3.40×10^4 m^2/g-mol for the (111) close packed plane.[15] Experimental measurements of the surface energy[33-35] have found that the surface of copper becomes saturated with oxygen at a coverage level of

$\theta_{sat} \approx 0.25$. In the presence of higher partial pressures of oxygen, an oxide layer forms.[34,35] These findings on the oxidation sequence are in good agreement with surface studies of chemisorption and oxidation in copper.[36] However, Habraken et al.[36] reported that $\theta_{sat} \approx 0.5$ for oxygen chemisorption on copper.

The Langmuir-McLean isotherm[31,37] may be used to determine the temperature-dependent relationship between oxygen in solution in the matrix and the degree of surface coverage (θ) on a void.

$$\frac{\theta}{1-\theta} = x \exp\left(\frac{G_B-G_s}{RT}\right) = (X_o-X_{cs}) \exp \frac{G_B-G_s}{RT} \tag{6}$$

where X_o is the mole fraction of oxygen initially present in the matrix, X_{cs} is the mole fraction of oxygen chemisorbed onto void surfaces, and G_B and G_s are the Gibbs free energies for oxygen in the bulk and on the surface, respectively, relative to a single oxygen atom in vacuum. If entropy terms are neglected, then $G_B \approx (H_{cs} + E_D)/2$ where E_D is the dissociation energy of molecular oxygen and H_u and H_{cs} are the heat of solution and chemisorption for molecular oxygen. Using $E_D = 498.4$ KJ/mol,[38] $H_u = -47$ KJ/mol [39] and $H_{cs} = -167$ KJ/mol [31] yields the result, $G_B \approx 226$ KJ/mol and $G_s \approx 166$ KJ/mol. This approach implies that there is no effect of oxygen coverage on the heat of chemisorption. It is known that the magnitude of H_{cs} becomes appreciably smaller at high coverage levels.[31,40,41] However, it appears that there is little change in H_{cs} for coverage levels up to $\theta = 0.25$, which corresponds to the range of interest in the present case.

The change in surface energy due to oxygen chemisorption may be calculated using the method of Gallois and Lupis[33]

$$\Gamma - \Gamma(\theta) = \frac{RT}{A_{cu}} \left[\frac{\theta}{1-4\theta} + \frac{g\,\theta^2}{RT}\right] \tag{7}$$

where g corresponds to an interaction energy between neighboring adsorbed oxygen atoms. It has been empirically observed that g is negative,[33] but its exact value is uncertain. In the following, we will neglect interaction effects (i.e., $g = 0$). This will lead to an overestimate of the effectiveness of oxygen in lowering the surface energy. Simple calculations indicate that the magnitude of the error introduced by setting $g = 0$ is expected to be $\lesssim 20\%$ for surface coverage levels of $\theta \gtrsim 0.22$ (also see Fig. 7 of Ref. 33).

An evaluation of the energetics of vacancy cluster formation indicates that a surface energy of $\Gamma \lesssim 1.0$ J/m^2 is required in order for void formation to occur in copper (Fig. 5). Using Eq. (7), this corresponds to a surface coverage of $\theta \gtrsim 0.22$. This value is then inserted into Eq. (6) in order to compute the requisite matrix oxygen concentration. The amount of oxygen that is chemisorbed onto void surfaces, X_{cs}, depends on the average void size and density (n_v):

$$X_{cs} = \frac{4\pi\, R_v^2 N_A \theta\, n_v}{A_{Cu}\, n_{Cu}} \tag{8}$$

where N_A is Avogadro's number and n_{Cu} is the atom density of copper. Since we are interested in the stability of clusters at sizes where void nucleation occurs, it is appropriate to use values of n_v and R_v obtained from nucleation theory. Wehner and Wolfer[42,43] have recently developed a dynamic void nucleation theory based on a Fokker-Planck description that is in good agreement with experimental results. Table 2 lists the calculated temperature-dependent values of n_v and R_v obtained from their analysis of copper.

The calculated initial matrix oxygen content required to reduce the surface energy of voids in copper to 1.0 J/m^2 is plotted in Fig. 6. This oxygen concentration corresponds to the minimum amount of oxygen that is required to stabilize as voids all of the vacancy clusters that are nucleated during irradiation (Table 2). A lower oxygen concentration could result in partial stabilization of the void nuclei population. The critical oxygen concentration depends strongly on temperature, and exhibits a minimum value for intermediate temperatures. Relatively large amounts of oxygen are needed in order to stabilize void formation at low temperatures because of the high vacancy cluster density that is nucleated (Table 2). Large oxygen concen-

TABLE 2

CALCULATED CRITICAL VOID SIZE AND DENSITY IN COPPER AS A FUNCTION OF IRRADIATION TEMPERATURE (FROM REF. 43)

	Void Density (m^{-3})		
Temperature (°C)	10^{-3} dpa/s	10^{-6} dpa/s	Critical Void Radius (nm)
100	5×10^{23}	2×10^{22}	0.6
200	5×10^{22}	3×10^{21}	0.6
250	2.5×10^{22}	1.5×10^{21}	0.6
300	9×10^{21}	2.5×10^{20}	0.6
400	2.5×10^{21}		0.6
450	1×10^{20}		0.6

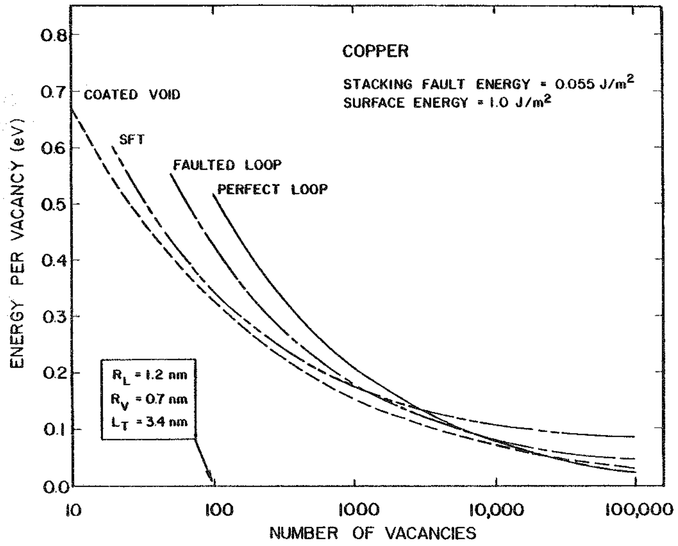

FIGURE 5. Specific energies of vacancy clusters in copper assuming a surface energy of 1.0 J/m².

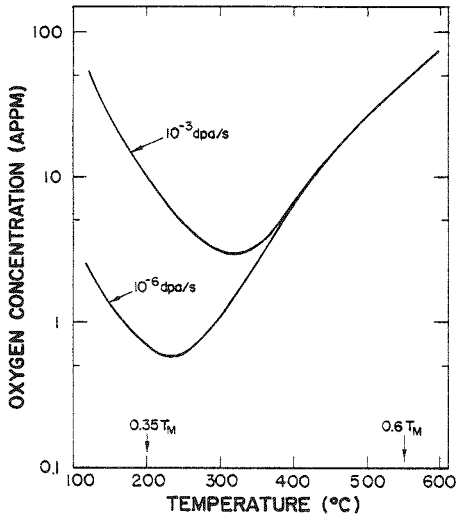

FIGURE 6. Minimum matrix oxygen concentration that is needed to make voids stable in pure copper.

trations are also necessary at high temperatures because there is a lowered driving force for oxygen to come out of solution and chemisorb onto void embryo surfaces.

The interpretation of Fig. 6 is as follows: Charged particle irradiation at 1×10^{-3} dpa/s of pure copper containing less then 3 appm oxygen (e.g., OFHC copper)[44] should not cause any substantial void formation at any temperature. On the other hand, irradiation of copper containing greater than 50 appm oxygen should result in void formation throughout the entire swelling temperature regime (0.3-0.6 T_M). At intermediate oxygen concentrations, void formation should occur over a limited temperature regime centered around 325° (0.45 T_M). In particular, void swelling will not occur at high temperatures and the void swelling regime will be restricted to the lower temperature range for partially outgassed copper. Neutron irradiation at copper (1×10^{-6} dpa/s) is more complicated than indicated in Fig. 6 because helium generated during irradiation greatly enhances void stability in addition to the oxygen stability effects (see following section). It should be noted that regular "high purity" copper that has not been deoxidized often contains $\gtrsim$ 200 appm oxygen.[44]

The predicted values of oxygen concentration required to stabilize void formation in copper at a given temperature are not expected to be exact due to the various approximations that were used to obtain the final result. For example, the assumption of $g = 0$ in Eq. (7) results in an underestimation of the critical matrix oxygen concentration necessary for void stability. Nevertheless, it is pleasing to note that the predictions are in good agreement with the limited amount of irradiation data that is available on copper containing known amounts of oxygen.[27] A 14-MeV Cu ion irradiation of high-purity copper containing < 5 ppm oxygen at a damage rate of 2×10^{-3} dpa/s did not result in any significant void formation over the temperature range of 100-500°C.[4,6] A very limited number of voids ($n_v \approx 10^{17}/m^3$) were observed[6] at one temperature, 400°C. There was no observable void formation at 300 or 450°C. Glowinski and coworkers found that copper containing 50 ppm oxygen (~ 200 appm O) formed voids easily following electron[45] and ion[46-48] irradiation. Outgassing of the foils in a high-vacuum furnace prior to irradiation shifted the swelling peak to lower temperatures and completely eliminated high-temperature void swelling. As noted earlier, Fig. 6 predicts that partial deoxidation of copper will preferentially eliminate void formation at the high temperature end of the void swelling regime. Sindelar et al.[49] have recently observed a similar temperature shift in ion-irradiated stainless steels which they attributed to oxygen effects.

The effect of oxygen gas existing in the void interior was neglected in the preceding analysis of void stability. Application of Sievert's Law data[39] at 400°C shows that 10 appm oxygen in solution is in equilibrium with a partial pressure of 2.6×10^{-6} atm. The contribution to void stability for these pressures is negligible. We have also neglected to include the oxygen atoms residing in the void interior in the oxygen mass balance. This contribution can also be shown to insignificant, i.e. $X \approx X_0 - X_{cs}$. It may be stated that void stabilization in copper in the presence of oxygen is solely due to the chemical surface interaction between oxygen and copper.

5.4 Role of Helium in Void Formation in Copper

Unlike oxygen, inert gases such as helium have no effect on the macroscopic surface energy of copper.[32] There have been several investigations of the energetics of cavities in the presence of helium (see, e.g., Refs. 50, 51). However, the derived energy equations contain several terms whose values are not well known. A simplistic estimate of the stability of vacancy clusters in the presence of helium may be obtained from the following:

$$E_v \approx E_v^o - [\sum_{i=1}^{m} (E_{He}^B)_i - pV] \tag{9}$$

$$E_x \approx E_x^o - m\, E_{He-D}^B \tag{10}$$

where E_v^o is the energy of a void in the absence of helium, E_x^o is the energy of a vacancy loop or SFT in the absence of helium, m is the number of helium atoms associated with the vacancy cluster, $E_{He}^B)_i$ is the binding energy of the ith helium atom to the cavity, and E_{He-D}^B is the binding energy of interstitial helium to a dislocation. In a sufficiently dilute system, (helium/vacancy << 1) the binding energies of helium atoms in a helium-vacancy cluster can be approximated by the formation energy of interstitial helium, E_{He}^F.

$$\sum_{i=1}^{m} (E_{He}^B)_i \lesssim m\, E_{He}^F$$

This approximation breaks down for concentrated helium-vacancy clusters (see, e.g., Table 6.53 in Ref. 52). The value of E_{He}^B/E_{He}^F decreases to about 0.5 as the helium to vacancy ratio approaches 1. The last term in Eq. (9) can be represented by the helium equation of state, $pV = zmkT$. The compressibility factor, z, is on the order of unity[53] for all cases considered in this paper. Therefore, $zkT \lesssim 0.1$ eV for temperatures in the void swelling regime. This factor is negligible compared to the uncertainties in E_{He}^F. From the above considerations, Eq. (9) may be approximated by

$$E_v \gtrsim E_v^o - m\,E_{He}^F \; . \tag{11}$$

The inequality sign serves as a reminder that the simplifications used to obtain Eq. (11) may result in an underestimation of the actual void energy, especially for high helium per vacancy ratios.

The values of E_{He}^F and E_{He-D}^B apparently have not yet been accurately determined for copper. Calculations of E_{He}^F for copper[54] indicate that it should be ~ 3 to 4 eV. The binding energy of helium to a dislocation is taken to be[55] $E_{He-D}^B \approx 0.3$ eV, which is the calculated value for nickel.

Figure 7 shows the calculated energies per vacancy of voids and stacking fault tetrahedra in copper in the presence of 3.5 and 35 He/vacancy cluster. This is equivalent to a helium concentration of 0.1 and 1 appm, respectively, for ion-irradiated copper at 400°C (Table 2) assuming that all of the helium initially present in the matrix is contained in the vacancy clusters. The presence of helium causes the void to be the most stable type of vacancy cluster for small cluster sizes. Previous atomistic calculations reached a similar conclusion -- addition of helium to copper causes the void to be energetically favorable compared to planar defect clusters.[16] Increasing concentrations of helium further enhance the stability of the void relative to the other vacancy cluster morphologies. The critical amount of helium required to make the void energetically stable compared to the stacking fault tetrahedron is given by

$$m_{crit} \approx \frac{E_v - E_T}{E_{He}^F - E_{He-D}^B} \tag{12}$$

where E_v and E_T are given by Eqs. (3) and (4) and depend on the cluster size. Table 3 gives the values of m_{crit} for two different void sizes that are appropriate for void nucleation. Values are tabulated for E_{He}^F = 2 eV and 4 eV, which represents the lower and upper estimates for this quantity. The helium per vacancy ratio is << 1 for a critical sized void nucleus, indicating that Eq. (11) may be a reasonable approximation.

Figure 8 gives the minimum helium concentration required for void stability during irradiation as a function of temperature, assuming that all of the helium initially present in the matrix precipitates into the vacancy clusters. Values relevant for neutron (1×10^{-6} dpa/s) and ion or electron irradiation (1×10^{-3} dpa/s) of copper were obtained from the data in Tables 2 and 3. The minimum helium concentration for void stability decreases rapidly with increasing temperature. Figure 8 predicts that less than 0.1 appm He will cause the void to be the most stable vacancy cluster morphology during neutron irradiation at all void swelling temperatures (0.35 - 0.6 T_M). Irradiation at a higher displacement rates requires a higher helium concentration. Small amounts of helium should greatly enhance the stability of voids at high temperatures, and may "shift" the void swelling temperature regime to higher temperatures. Such a shift has been observed in irradiated copper,[48] stainless steel[56] and nickel[57].

Figure 8 is in good agreement with the limited amount of experimental data on helium effects in copper -- no voids were observed in degassed copper following ion irradiation at 450°C. However, implantation of 1-100 appm He prior to irradiation resulted in void formation.[48] McLaurin[5] observed that high-purity aluminum irradiated with 9-MeV Al ions at 50°C (0.35 T_M) did not form voids, whereas preimplantation of as little as 0.1 appm He resulted in significant void swelling with a void concentration of $1 \times 10^{21}/m^3$. The corresponding He concentration per void in this case is $m_{He} \approx 6$, assuming that all of the implanted helium is contained in the voids. Application of Eq. (12) to the vacancy cluster energetics data for aluminum (Fig. 1) results in a calculated void stability criterion of $m_{crit} \lesssim 5$ He atoms per void. The preceding calculation used $E_{He}^F - E_{He-D}^B = 3.7$ eV and an average void nucleus size of 200 vacancies ($R_v = 0.7$ nm). Therefore, void formation is predicted to be stable in aluminum for implanted helium concentrations ~ 0.1 appm He, in agreement with the observations of McLaurin.[5]

The model developed to describe helium effects in metals contains several assumptions that may limit its applicability. First, it is assumed that all of the helium that was initially in the matrix migrates to the

TABLE 3

MINIMUM HELIUM CONCENTRATION FOR VOID STABILITY IN COPPER

	R_v = 0.6 nm		R_v = 1.0 nm	
	M_{crit}	He/vacancy	M_{crit}	He/vacancy
E^B_{He} = 2 eV	4.3	0.056	8.2	0.023
E^B_{He} = 4 eV	2.0	0.026	3.8	0.01

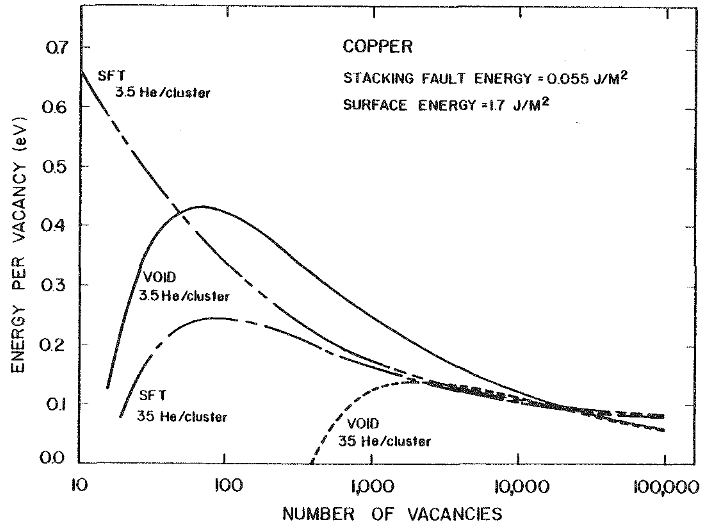

FIGURE 7. VOID and SFT energies in the presence of helium.

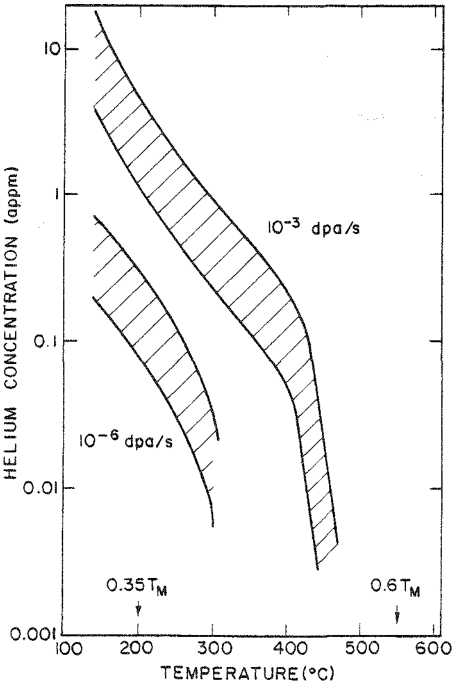

FIGURE 8. Minimum helium concentration that is needed to make voids stable in pure copper.

void embryos where it is equally partitioned. Helium has a relatively high mobility in most metals and tends to cluster at vacancies or other high-order vacancy clusters.[58,59] Therefore, the above assumption should be valid in the experimental cases where helium initially exists as isolated atoms in a metal containing vacancy clusters (neutron irradiation or subthreshold coimplantation studies). The case of helium preimplantation by ion bombardment prior to irradiation is not accurately modeled here -- the implanted helium tends to spontaneously cluster at the implantation-produced vacancies (forming He_6V clusters in copper)[59] and becomes relatively immobile. Also, the nucleation code used in the present treatment does not account for heterogeneous nucleation at helium clusters. The results may therefore be inappropriate for most preimplantation studies. However, Makin[60] found that the observed void density in irradiated stainless steel was not strongly affected by a 10 ppm He preinjection at room temperature. It is possible that the results obtained in this paper concerning helium effects may be valid for preinjection studies if low helium concentrations are involved (< 10 appm He).

5.5 Activation Energy for the Collapse of a Void

At very large sizes, the perfect loop is always the most energetically stable type of vacancy cluster. Therefore, voids which may have been energetically stable at small sizes may become unstable once they have grown larger than a critical size. It is important to determine what the probability is that a void of a given size will collapse into a planar defect cluster. An activation energy barrier exists that inhibits conversion of a void to a dislocation loop. An upper limit to this activation energy barrier is obtained by comparing the energy difference between a sphere and a disk (of thickness b) that are of equal volume.

$$\Delta E = E_v \left[\frac{2 R_v}{3b} - 1\right] \tag{13}$$

A more realistic estimate of the activation energy is obtained by comparing the energies between a sphere and an oblate spheroid (a "squashed" sphere).[61] The oblate spheroid accurately represents the geometry of a void that is in the process of collapsing to a planar configuration. The energy difference is given by

$$\Delta E = C \cdot E_v \tag{14}$$

where C is a constant that depends on the eccentricity of the spheroid. Values of C are given in Table 4 for various ratios of major to minor axis along with calculated activation energies for the collapse of a "typical" small void. A rule-of-thumb in void nucleation calculations is that energy barriers up to 30 kT may occasionally be surmounted by thermal energy processes. For temperatures applicable to void swelling in metals, this indicates that energy barriers $\gtrsim$ 2 eV will not allow void collapse to occur. Since the activation energy barrier is proportional to R_v^2 , it is apparent from Table 4 that void collapse will not occur except possibly for voids that have just nucleated and are, therefore, very small, $R_v \lesssim 2$ nm).

5.6 Discussion and Conclusions

Elasticity theory predicts that void formation is energetically unstable in many pure metals (Figs. 1-4). Incorporation of the effects of oxygen and helium on the stability at vacancy clusters modifies the relative energies of the cluster so as to favor void formation. The gas effects models presented in this paper appear to be in good agreement with the experimental data that is available on oxygen and helium. Small amounts of oxygen in copper tend to stabilize voids at low irradiation temperatures whereas small helium concentrations preferentially stabilize voids at high temperatures. The combination of minute quantities of oxygen and helium can stabilize void formation in copper at all temperatures relevant to void swelling. Figure 9 shows the minimum combined gas content that is needed to stabilize void formation in copper irradiated at a damage rate of 10^{-3} dpa/s. The combination of 10 appm oxygen and 0.01 appm helium in solution in the matrix is predicted to result in void stabilization at all temperatures in the void swelling regime. Even lower gas levels are sufficient for void stability in copper during neutron irradiation (1×10^{-6} dpa/s).

The elasticity calculations presented in this paper predict that void formation should not occur in aluminum, copper or austenitic stainless steel unless suitable impurities (such as gas atoms) are present. Previous researchers have similarly concluded that gas is necessary for void formation (see, e.g., Ref. 62). Recent experimental studies on high-purity aluminum and copper[4,6] have shown that these two metals do not exhibit any significant void formation following self-ion irradiation to high doses. In addition, ion irradiation of a "low-oxygen" (200 appm O) austenitic stainless steel resulted in greatly reduced swelling (and no observable void formation at high temperatures) compared to a "high-oxygen" (1000 appm O) alloy. It is not known whether stainless steel has ever been irradiated in a very low oxygen form (< 5 appm).

There have been many reported observations of void formation in high-purity aluminum and copper following irradiation with charged particles. For example there are more than twenty known reports of void formation in copper following electron or ion irradiation.[27] From the preceding discussion, it appears that some type of gas must have been present in the foil during the irradiation. Significant oxygen levels can be found in high-purity copper unless special deoxidation steps are taken.[44] Unfortunately, irradiation studies to date on copper have not kept close control of their oxygen content. It appears that all of the preceding charged particle irradiation studies on aluminum and copper that reported void formation should be reevaluated with respect to gas effects. These gas effects may have masked or distorted the effects of other irradiation parameters that were being studied.

TABLE 4

ENERGY BARRIER FOR COLLAPSE OF A VOID

	Oblate Spheroid			
	a/c = 2	a/c = 4	a/c = 6	Disk
Energy Barrier Constant, C*	0.095	0.43	0.88	$\frac{2R_v}{3b} - 1$
Activation Energy**	1 eV	4.4 eV	9.1 eV	24 eV

---

a/c = ratio of major/minor axis
*In terms of the initial void energy
** Assuming R_v = 5 b (1.8 nm) and Γ = 1 J/m^2

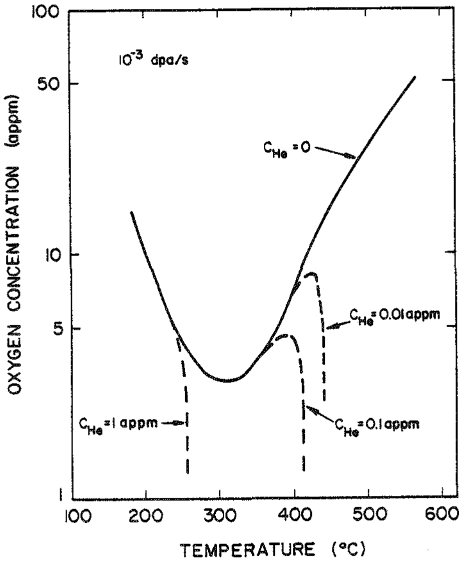

FIGURE 9. Minimum oxygen concentration that is needed to make voids stable in copper containing various amounts of helium.

The conclusion that gas is necessary for void formation is currently known to be valid only for aluminum and copper. However, it seems likely that many other metals may also be resistant to void formation in the absence of impurities (gaseous and otherwise). Future irradiation studies should be performed only on foils with a well-characterized and preferably low gas concentration.

Form a metallurgical point of view, the theoretical prediction (and experimental confirmation) that voids are not inherently stable in metals such as Al and Cu during irradiation raises hopes that alloy development research may be able to prevent deleterious levels of void swelling. At least two conditions are needed to minimize void swelling. First, the base metal should be oxygen-free ($\lesssim$ 1 appm O) . A second consideration is that helium generated during neutron irradiation cannot be allowed to freely interact with the embryonic vacancy clusters. Significant advances in this area have recently been made using microstructural tailoring of precipitates, etc. that directs the helium into a rather benign role.[63]

6.0 Acknowledgments

The authors would like to thank M.F. Wehner for supplying the void nucleation calculations prior to their publication.

7.0 References

1. K. Farrell, Rad. Effects 53 (1980) 175-194.
2. W.G. Wolfer, J. Nucl. Mater. 122 & 123 (1984) 367-378.
3. D.B. Bullen, G.L. Kulcinski and R.A. Dodd, "Effect of Hydrogen on Void Production in Nickel", 1st Intern. Conf. on Fusion Reactor Materials (ICFRM-1) Tokyo (Dec. 1984); to be publ. in J. Nucl. Mater.
4. R.W. Knoll, "Effects of Heavy Ion Irradiation on the Phase Stability of Several Copper-Base Alloys", Ph.D. Thesis, Nuclear Engineering Department, University of Wisconsin-Madison (1981), UWFDM-436.
5. S.K. McLaurin, "Radiation Damage from Heavy Ion Bombardment in High Purity Aluminum", Ph.D. Thesis, Nuclear Engineering Department, University of Wisconsin-Madison (Jan. 1984). Also see S.K. McLaurin et al., J. Nucl. Mater. 117 (1983) 208.
6. S.J. Zinkle and G.L. Kulcinski, "Ion Irradiation of Copper and Copper Alloys to 40 dpa at 100-400 °C", DAFS Quarterly Progress Report DOE/ER-0046/20 (Feb. 1985); also S.J. Zinkle, "Effects of Thermal Annealing and Ion Irradiation on the Microstructures of Copper Alloys", Ph.D. Thesis, Nuclear Engineering Department, University of Wisconsin-Madison (May 1985).
7. J.A. Sigler and D. Kuhlmann-Wilsdorf, in The Nature of Small Defect Clusters, Vol. 1 (Consultants Symp.), M.J. Makin, Ed., Harwell Report AERE R5269, July 1966, 125-143.
8. R.J.C. Cotterill, in The Nature of Small Defect Clusters, Vol. 1 (Consultants Symp.), M.J. Makin, Ed., Harwell Report AERE R5269, July 1966, 144-172.
9. F. Kroupa, Czech J. Phys. 10B (1960) 284.
10. M. Abramowitz and I.A. Stegun, Handbook of Mathematical Functions, Dover Publications, Inc., New York, 1972, 591-592.
11. T. Jossang and J.P. Hirth, Phil. Mag. 13 (1966) 657.
12. A. Si-Ahmed and W.G. Wolfer, in Effects of Radiation on Materials: 11th Conf., ASTM STP 782, H.R. Brager and J.S. Perrin, Eds. (1982) 1008.
13. G.W.C. Kaye and T.H. Laby, Tables of Physical and Chemical Constants, 14th Ed., (Longman Group, Ltd., London, 1973) p. 31, and Mark's Standard Handbook for Mechanical Engineers, T. Baumeister, et al., Eds. (McGraw-Hill) p. 5-5.
14. P.C.J. Gallagher, Met. Trans. 1 (1970) 2429.
15. W.R. Tyson, Can. Metall. Quart 14, 4 (1975) 307.
16. M.I. Baskes, Trans ANS 27 (1977) 320.
17. N.V. Doan, in Point Defects and Defect Interactions in Metals, J-I Takamura, M. Doyama and M. Kiritani, Eds. (Univ. of Tokyo Press, 1982) 722.
18. N. Yoshida, et al., J. Nucl. Mater. 122/123 (1984) 664-8; also see Y. Shimomura, et al., "Electron Microscopic Studies of Damage Evolution in Fission Neutron Irradiated Metals", and N. Yoshida et al., "Effect of Cascade Damage by 14 MeV Neutrons on Microstructure Evolution", 1st Intern. Conf. on Fusion Reactor Materials, Tokyo (Dec. 1984).
19. A.Y. Stathopoulos et al., Phil. Mag. A 44 (1981) 309-322.
20. H. Fujita, T. Sakata and H. Fukuyo, Jap. J. Appl. Phys. 21 (1981) L235-6.
21. B.L. Eyre, J. Phys. F: Metal Phys. 3, 2, (1973) 422-470.

22. D.B. Bullen, "The Effects of Implanted Hydrogen and Helium on Cavity Formation in Self-Ion Irradiated Nickel", Ph.D. Thesis, Nuclear Engineering Dept., University of Wisconsin-Madison (May 1984).

23. R.L. Sindelar, University of Wisconsin-Madison, private communication (1985).

24. T. Yoshiie, S. Kojima, Y. Sato and M. Kiritani, "A Study of Point Defect Processes in Candidate and Model Alloys for Fusion Reactor First Wall by HVEM", 1st Intern. Conf. on Fusion Reactor Materials, Tokyo (Dec. 1984).

25. N. Yoshida, et al., "D-T Neutron Irradiation of JPCA and Its Model Alloys", 1st Intern. Conf. on Fusion Reactor Materials, Tokyo (Dec. 1984).

26. H.G. Bowden and R.W. Ballufi, Phil. Mag. 19 (1969) 1001.

27. S.J. Zinkle and R.W. Knoll, "A Literature Review of Radiation Damage Data for Copper and Copper Alloys", University of Wisconsin Fusion Technology Institute Report UWFDM-578, June 1984 (94 pp.).

28. R.W. Ballufi and D.N. Seidman, in Radiation Induced Voids in Metals, J.W. Corbett and L.C. Ianniello, Eds. (AEC, 1972) CONF 710601, p. 563.

29. N.H. Packan and K. Farrell, in Effects of Radiation on Materials, 11th Conf., ASTM STP-782, H.R. Brager and J.S. Perrin, Eds. (1982) 885-894.

30. N. Eustathopoulos and J-C Joud, "Interfacial Tension and Adsorption of Metallic Systems", in Current Topics in Materials Science, Vol. 4, E. Kaldis, Ed. (North-Holland, 1980) Chpt. 6, 281-360.

31. G.A. Somorjai, Chemistry in Two Dimensions: Surfaces (Cornell Univ. Press, 1981) Chpts. 3,6.

32. M.F. Felsen and P. Regnier, Surf. Sci. 68 (1977) 410-418.

33. B. Gallois and C.H.P. Lupis, Met. Trans. 12B (1981) 549.

34. C.E. Bauer, R. Speiser and J.P. Hirth, Met. Trans. 7A (1976) 75.

35. M. McLean and E.D. Hondros, J. Mater. Sci. 8 (1973) 349.

36. F.H.P.M. Habraken et al., Surf. Sci. 97 (1980) 264.

37. R.H. Jones and W.G. Wolfer, J. Nucl. Mater. 122/123 (1984) 379.

38. R.C. Weast, Ed., CRC Handbook of Chemistry and Physics, 59th Ed. (CRC Press, 1978-79) p. F-236.

39. W. Dürrschnabel and H. Vosskühler, in Gase und Kohlenstoff in Metallen, E. Fromm and E. Gebhardt, Eds. (Springer-Verlag, 1976) 657-678.

40. D.O. Hayword, in Chemisorption and Reactions on Metallic Films, J.R. Anderson, Ed. (Academic Press, 1971) 225-326.

41. K-I. Tanaka and K. Tamaru, J. Catalysis 2 (1963) 366-370.

42. M.F. Wehner and W.G. Wolfer, "Vacancy Cluster Evolution in Metals under Irradiation", to be publ. in Phil. Mag. A (1985); also UWFDM-590.

43. W.G. Wolfer, M.F. Wehner and J.W. Davis, "Resistivity Contribution of Vacancy Clusters and Voids in Irradiated Copper", to be submitted to ADIP Progress Report DOE/ER-0045/15 (Sept. 1985).

44. Oxygen free copper designation requires an oxygen concentration of less than 10 ppm (40 appm) -- see ASTM Standard specification for oxygen-free electrolytic copper, 1983 ASTM standards Vol. 2.01, copper and copper alloys, B170-82. Electrolytic tough pitch copper has < 50 ppm total metallic impurities (99.995% Cu + O) but generally contains 200-400 ppm O (ASM Metals Handbook, Vol. 2, "Properties and Selection: Nonferrous Alloys and Pure Metals", 9th Ed., ASM, Metals Park, OH).

45. L.D. Glowinski, J. Nucl. Mater. 61 (1976) 8-21.

46. L.D. Glowinski, C. Fiche and M. Lott, J. Nucl. Mater. 47 (1973) 295-310.

47. L.D. Glowinski and C. Fiche, J. Nucl. Mater. 61 (1976) 22-28.

48. L.D. Glowinski and C. Fiche, J. Nucl. Mater. 61 (1976) 29-40.

49. R.L. Sindelar, G.L. Kulcinski and R.A. Dodd, "Heterogeneous Void Formation in 14-MeV Nickel Ion Irradiated 316 SS", 1st Intern. Conf. on Fusion Reactor Materials, Tokyo (Dec. 1984).

50. M.W. Finnis et al., Rad. Eff. 78 (1983) 121-132.

51. H. Trinkaus, Rad. Eff. 78 (1983) 189-211.

52. J.R. Beeler, Jr., Radiation Effects Computer Experiments, Vol. 13 of the series Defects in Solids, S. Amelinckx et al., Eds. (North-Holland, 1983).

53. B.B. Glasgow and W.G. Wolfer, DAFS Quarterly Progress Report DOE/ER-0046/16 (Feb. 1984) p. 68.

54. M.I. Baskes and C.F. Melius, Phys. Rev. B 20 (Oct. 1979) 3197.

55. H. Ullmaier, Nucl. Fusion 24 (1984) 1039.

56. N.H. Packan and K. Farrell, Nucl. Tech./Fusion 3 (1983) 392; also K. Farrell and N.H. Packan, J. Nucl. Mater. 85/86 (1979) 683-7.

57. N.H. Packan, K. Farrell and J.O. Stiegler, J. Nucl. Mater. 78 (1978) 143-155.

58. W.D. Wilson, C.L. Bisson and M.I. Baskes, Phys. Rev. B 24 (1981) 5616.

59. M.I. Baskes and W.D. Wilson, J. Nucl. Mater. 63 (1976) 126-131.

60. M.J. Makin, J. Nucl. Mater. 107 (1982) 133-147.

61. CRC Standard Mathematical Tables, 25th Ed., W.H. Bleyer, Ed. (CRC Press, 1978) p. 149.

62. J.M. Lanore, et al., in Fundamental Aspects of Radiation Damage in Metals, Vol. 2, M.T. Robinson and F.W. Young, Eds., Gatlinburg, TN (1975) CONF 751006-P2, 1169-1179.

63. P.J. Maziasz, J. Nucl. Mater. 122/123 (1984) 472-486.

A NOTE ON REACTIVE GAS CHARGING DURING PRE-IRRADIATION SPECIMEN PREPARATION

R.L. Sindelar, R.A. Dodd and G.L. Kulcinski (University of Wisconsin-Madison)

1.0 Objective

To clarify the nature and mechanisms of reactive gas charging during pre-irradiation electrochemical polishing of metallic specimens.

2.0 Summary

Reactive gases act as potent agents in void formation in many alloys during irradiation. In particular, the pre-irradiation implantation of hydrogen or oxygen into metals is known to cause the rapid onset of void swelling.

The common misconception of hydrogen introduction during the pre-irradiation specimen electropolish has been addressed. It is shown that hydrogen cannot enter the specimen, but that the ingress of oxygen may occur during the electropolishing step. Hydrogen can, however, enter the specimen in the absence of the applied voltage if the sample, without a passive film layer, remains in the electrolyte.

3.0 Program

Title: Radiation Effects to Reactor Materials
Principal Investigator: G.L. Kulcinski and R.A. Dodd
Affiliation: University of Wisconsin-Madison

4.0 Relevant DAFS Program Plan Task/Subtask

Subtask II.C.3.2 Effects of Hydrogen on Microstructural Evolution

5.0 Accomplishments and Status

5.1 Introduction

In 1972, Nelson et al.[1] reported the formation of voids in an 18/8/Ti stainless steel during ion irradiation only after a large amount of oxygen was pre-implanted into the material. Nitrogen pre-implantation, however, showed no effect. Oxygen has also been observed to promote a significant increase in void swelling in vanadium,[2] niobium,[3] copper[4] and nickel alloys.[5] Similarly, hydrogen pre-implantation has been reported to enhance the size and number density of voids in ion-irradiated nickel alloys.[5,6] Excessive implantation of oxygen, however, can actually reduce the amount of void swelling in some alloys.[2,3]

Zinkle et al.[7] give a mechanistic description of the effect of reactive and inert gases on the relative stability of various vacancy clusters. With a reduction in the surface energy through chemisorption of the reactive gas atoms, a three-dimensional vacancy cluster (void) can become the most stable cluster. This decrease in surface energy of voids with an increase in the matrix oxygen content was shown by an annealing experiment of voids in copper.[8]

It has been conjectured[9] that hydrogen can enter a sample during the common step[10] of a pre-irradiation electropolish. However, it is difficult to justify this argument.

5.2 Anodic Reactions

During electropolishing, the metallic components in the alloy undergo anodic dissolution, i.e. oxidation, according to

$$M \rightarrow M^{n+} + ne^- \ .$$

The corresponding cathodic reduction is likely to be

$$nH^+ + ne \rightarrow nH \rightarrow n/2\ H_2 \ .$$

The atomic hydrogen can diffuse into the cathode and/or hydrogen gas will be evolved from the cathode surface. The main point is that atomic hydrogen is not available at the surface of the specimen being electropolished (anode surface) because the anodic reactions are oxidations. Therefore, hydrogen charging of a metallic specimen is impossible during the period of time when the specimen is actually being electropolished. Of course, if the specimen is allowed to remain in the electrolyte after electropolishing has been completed (no applied current), a small amount of corrosion may occur, and atomic hydrogen generated at local cathodes may enter the metal. No doubt this is why titanium hydride sometimes occurs in thin foils of titanium electropolished for TEM, but it is not a likely mechanism for charging bulk samples with hydrogen.

On the other hand, if the anode potential is slightly more noble than needed to obtain an electropolished surface, oxygen may be evolved at the anode, and atomic oxygen may enter the specimen. Also, the instability of passive films (oxides) in electropolishing solutions suggests that oxygen may be available from this source. In metals such as nickel where the solubility of oxygen at room temperature approaches 0.1 at.%, it seems highly probable that it is oxygen which causes the enhanced swelling of alloys which have undergone a pre-irradiation electropolish.

5.3 Oxygen Charging

If the anodic potential is noble enough to generate oxygen at the specimen surface, and if in the absence of a passive surface layer it is possible for oxygen to diffuse into the specimen, simple application of Fick's second law[11] yields the expression for the depth-dependent oxygen concentration,

$$C_0^V\ (x,\tau) = C_{0,0}^V\ \mathrm{erfc}\ (x/2\sqrt{D\tau}) \qquad (1)$$

where $C_{0,0}^V$ is the oxygen concentration at the sample surface, x is the distance into the sample, τ is the charging time and D is a constant diffusion coefficient. The mass of O, m_0, that has entered the sample during τ can be found by integrating Eq. (1) with respect to x, thus,

$$m_0(\tau) = 2\ C_{0,0}^V (D\tau/\pi)^{1/2}\ . \qquad (2)$$

Atrens et al.[12] have considered the ingress of H during cathodic polarization of austenitic stainless steels along with the egress of H after the electrolytic charging. Their computer model based on diffusion control accurately described their experimental results of H motion during and after charging. In an analogous manner, a model for the ingress and egress of oxygen may be developed. The rapid formation of a passive oxide film after the electropolish may limit, however, the egress of oxygen from the sample.

5.4 Conclusions

It is postulated that hydrogen charging of the specimen is not possible during the electropolish step prior to irradiation. Anodic reactions may include the formation of atomic oxygen or oxygen gas and thus, in the absence of a passive surface film, allow the diffusion of oxygen into the specimen. Such oxygen must be taken into account when subsequent microstructures of irradiated specimens are analyzed.

6.0 References

1. R.S. Nelson et al., "Void Formation in Metals During Ion Bombardment," in Radiation-Induced Voids in Metals, J.W. Corbett and L.C. Ianniello, Eds (1972) pp. 430-448.
2. S.C. Agarwal, D.I. Potter and A. Taylor, Met. Trans A 9A, p. 569, 1978.
3. B.A. Loomis and S.B. Gerber, J. Nucl. Mater. 97, pp. 113-125, 1981.
4. L.D. Glowinski et al., J. Nucl. Mater. 61, p. 29, 1976.
5. M.J. Makin et al., in Radiation Effects in Breeder Reactor Structural Materials, M.L. Bleiberg and J.W. Bennett, Eds. (1977), pp. 645-664.
6. D.B. Bullen, Ph.D. Thesis, University of Wisconsin-Madison, 1984.
7. S.J. Zinkle, L.E. Seitzmann and G.L. Kulcinski, "Stability of Vacancy Clusters in Copper and Other Metals," DAFS Quarterly Report, this volume.
8. M.F. Felsen and P. Regnier, Surface Science 68, pp. 410-418, 1977.
9. J.R. Buswell, S.B. Fisher, J.E. Harbottle and D.I.R. Norris, in Physical Metallurgy of Reactor Fuel Elements, J.E. Harris and E.C. Sykes, Eds (1973), p. 170.
10. K.C. Thomson-Russell and J.W. Edington, Electron Microscope Specimen Preparation Techniques in Materials Science, Vol. 5 of Practical Electron Microscopy in Materials Science, Philips (1977).
11. J. Crank, The Mathematics of Diffusion, Clarendon Press, Oxford, 1956.
12. A. Atrens, J.J. Bellina, N.F. Fiore and R.J. Coyle, in The Metal Science of Stainless Steels, E.W. Collings and H.W. King, Eds (1979), TMS-AIME, p. 54.

CHAPTER 6

FUNDAMENTAL STUDIES OF SPECIAL PURPOSE MATERIALS

RADIATION ENHANCED RECRYSTALLIZATION IN COPPER ALLOYS

S.J. Zinkle and G.L. Kulcinski (University of Wisconsin-Madison)

1.0 Objective

To investigate the source of radiation-enhanced recrystallization in metals.

2.0 Summary

AMZIRC and AMAX-MZC have been found to exhibit signs of radiation-enhanced recrystallization following ion irradiation to 10 dpa at temperatures above 300°C. A simplified analysis of the results suggests that the accelerated recrystallization kinetics is due to radiation-enhanced diffusion. AMAX-MZC exhibits a more sluggish recrystallization response when compared to AMZIRC. This is attributed to Cr and Mg solute atoms retarding the grain boundary mobility.

3.0 Program

Title: Radiation Effects to Reactor Materials
Principal Investigators: G.L. Kulcinski and R.A. Dodd
Affiliation: University of Wisconsin-Madison

4.0 Relevant DAFS Program Plan Task/Subtask

Subtask II.C.1.1 Phase Stability Mechanics
Subtask II.C.1.2 Modeling and Analysis of Effects of Material Parameters on Microstructure

5.0 Accomplishments and Status

5.1 Introduction

Recent studies of some high-strength, high-conductivity copper alloys have shown that ion irradiation causes an acceleration of recovery and recrystallization processes.[1-3] It is important to determine what irradiation conditions are sufficient to induce recrystallization in the cold worked plus aged class of copper alloys because a large portion of their strength is lost when recrystallization occurs.[4] Recent neutron irradiation studies of some of these alloys have found that their strength following irradiation is less than their initial, nonirradiated value.[5,6] However, it is possible that this decrease in strength may be simply due to thermal recrystallization effects.

There have been several previous observations of radiation-enhanced recrystallization effects in metals (see, e.g., Refs. 7-13). The acceleration of the recrystallization process during irradiation has been proposed to be caused by an increase in the grain boundary mobility due to a supersaturation of vacancies (radiation-enhanced diffusion) or by an increase in the grain nucleation rate.[8,10,11,13] However, there has been relatively little effort devoted to making quantitative predictions of the magnitude of these effects.

Foils of two commercial copper alloys (AMZIRC and AMAX-MZC) in the cold worked plus aged condition were irradiated with 14-MeV Cu ions to a damage level of 10 dpa (1 µm depth) over the temperature range of 100 to 500°C (0.28-0.57 T_m). The calculated damage rate was 2 x 10^{-3} dpa/s and the corresponding irradiation time was about 1.5 hours. The irradiated specimens were examined in cross-section in a JEOL 200 CX electron microscope.

The degree of radiation-enhanced recrystallization as a function of irradiation temperature may be quantified by making appropriate measurements of the subgrain size in irradiated and nonirradiated regions of the foils. The most common procedure is to measure the grain size using the intercept method. In this paper we have made no distinction between the nucleation of subgrains (polygonization) and grains (primary recrystallization). Instead, we have adopted the approach of Vaidya and Ehrlich[12] where recrystallization is taken to start with the formation of subgrains and it proceeds until grain growth processes become important.

5.2 Results

Figure 1 shows the subgrain size in the longitudinal (rolling) direction as a function of irradiation temperature for AMZIRC and AMAX-MZC, as determined from TEM measurements. Figure 2 shows the dependence of subgrain area (as viewed in cross-section) on irradiation temperature. It has been proposed that the subgrain area is a better parameter for determining the degree of recrystallization.[12] Figures 1 and 2 show that the subgrain size and area are independent of the ion irradiation temperature over the interval 100-300°C for both AMZIRC and AMAX-MZC. The subgrain size in this temperature range is equal to the measured as-received (nonirradiated) value (0.4 µm, 0.34 µm for AMZIRC and AMAX-MZC, respectively).

The subgrain size and area increased above the as-received values following ion irradiation at temperatures greater than 300°C, indicating that recrystallization was occurring. Subgrain nucleation was visible in irradiated regions of the foils.[1,2] The subgrains were generally found along preexisting high angle grain boundaries. In the absence of irradiation, the subgrain size of both alloys was determined to be constant up to 475C for a 1 hour anneal, with a rapid increase at higher temperatures. Figure 1 (subgrain size) suggests that AMZIRC begins to recrystallize at ~ 350°C during ion irradiation, while AMAX-MZC does not start to recrystallize until irradiation temperatures of ~ 450°C are reached. Figure 2 (subgrain area) indicates that recrystallization has started to occur following ion irradiation at 300°C in AMZIRC and 400°C in AMAX-MZC. This represents an effective shift in the recrystallization temperature of these two alloys due to ion irradiation of ~ 75°C for AMAX-MZC and ~ 150°C for AMZIRC.

A quantitative prediction of the shift in the recrystallization temperature (ΔT_R) during irradiation may be made by assuming that the acceleration of recrystallization kinetics is solely due to radiation-enhanced diffusion. The radiation-enhanced diffusion coefficient was determined from a calculation of the vacancy concentration during irradiation based on steady state nucleation theory. Only monovacancy diffusion was considered to contribute to the radiation-enhanced diffusion. Figure 3 shows the calculated temperature-dependent self-diffusion coefficient of copper for conditions appropriate to ion irradiation (2 x 10^{-3} dpa/s), neutron irradiation (1 x 10^{-6} dpa/s) and thermal annealing. The predicted shift in recrystallization temperature during irradiation may be obtained as follows: The recrystallization temperature of AMZIRC and AMAX-MZC for a 1 hour thermal anneal[4] is about 475°C. This corresponds to a self-diffusion coefficient of 3 x 10^{-19} m^2/s. During ion irradiation at 2 x 10^{-3} dpa/s, the radiation-enhanced self-diffusion coefficient equals 3 x 10^{-19} m^2/s for an irradiation temperature of about 300°C. The shift in the recrystallization temperature due to ion irradiation is therefore predicted to be $\Delta T_R \approx 180°C$.

Neutron irradiation at 1 x 10^{-6} dpa/s has no effect on the self-diffusion coefficient for irradiation temperatures above 375°C due to a low vacancy supersaturation at high temperatures (Fig. 3). The extrapolated recrystallization temperature of AMZIRC and AMAX-MZC for a 2 year anneal[4] is $\lesssim$ 350°C, which corresponds to a self-diffusion coefficient of about 4 x 10^{-22} m^2/s. The predicted recrystallization temperature for a 10^{-6} dpa/s neutron irradiation is about 140°C ($\Delta T_R \approx 210°C$). Many of the proposed applications for high strength copper alloys in fusion devices require operation at irradiation temperatures of 100-350°C for several years.[1] The preceding calculations indicate that AMZIRC and AMAX-MZC will recrystallize in this type of an irradiation environment (probably with an accompanying loss of strength).

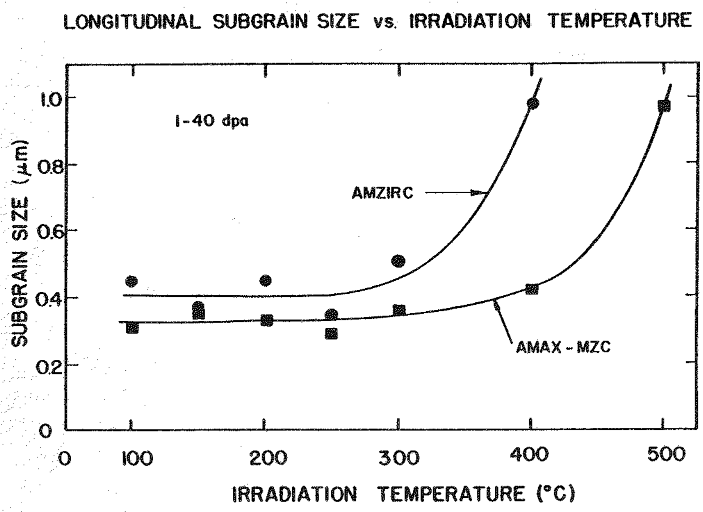

FIGURE 1. Longitudinal subgrain size of cold-worked plus aged copper alloys as a function of irradiation temperature.

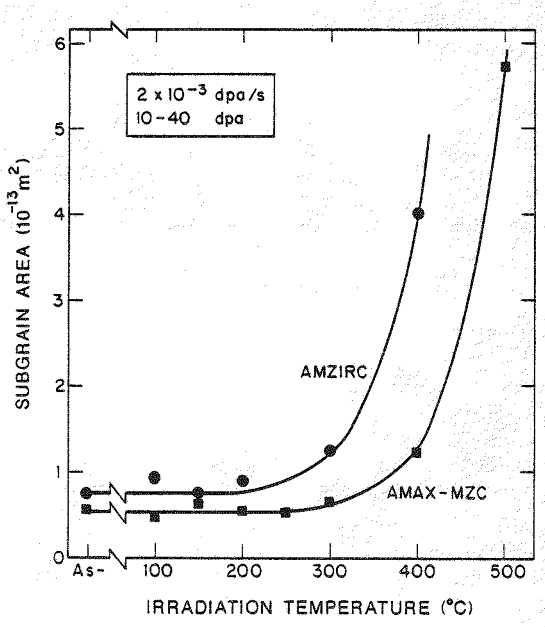

FIGURE 2. Subgrain area of cold-worked plus aged copper alloys as a function of irradiation temperature.

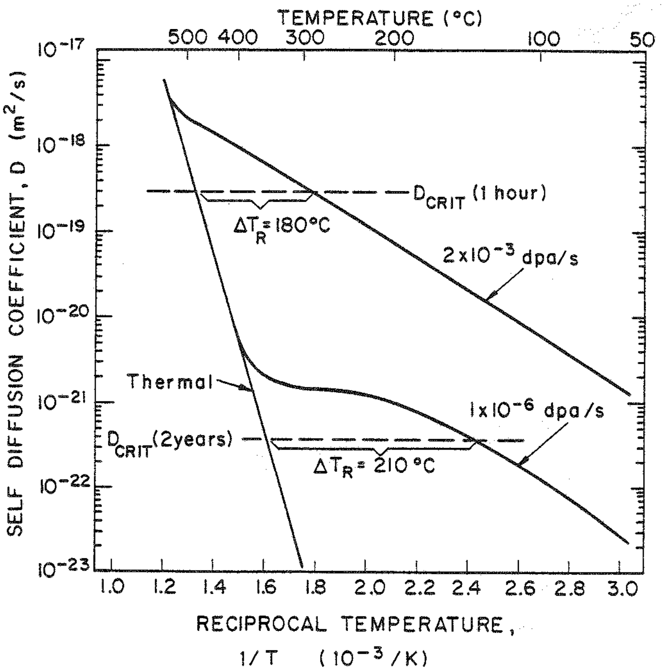

FIGURE 3. Predicted shift in the recrystallization temperature of copper alloys due to radiation-enhanced diffusion.

5.3 Discussion

It is well established that recrystallization requires a sufficiently large driving force in combination with adequate atomic mobility in order to proceed.[10,11,13] Irradiation tends to increase the driving force for recrystallization by creating defect clusters in the lattice. The atomic mobility is also increased during irradiation due to a supersaturation of point defects (radiation-enhanced diffusion). Previous studies have shown that grain boundary mobility is directly related to the vacancy concentration in the matrix.[8,10,13] In this regard, radiation-enhanced recrystallization differs from irradiation creep in the sense that creep has been shown to be independent of radiation-enhanced diffusion.[14,15] This may be due to the fact that irradiation creep involves a "directional flux" of defects whereas recrystallization simply requires adequate mobility in any direction.

The predicted shift in the recrystallization temperature of AMZIRC due to ion irradiation (Fig. 3) is in reasonable agreement with the actual observations (Fig. 2). In particular, the predicted and observed recrystallization temperatures for AMZIRC during ion irradiation are both about the same, 300°C. The results for AMAX-MZC are not in as close of agreement; the predicted and observed recrystallization temperatures are 300°C and 400°C, respectively.

The difference between the predicted and observed radiation-enhanced recrystallization temperature of AMAX-MZC is probably due to the neglect of solute/precipitate effects in the recrystallization calculations. Vaidya and Ehrlich[12] found that slight variations in the composition of irradiated stainless steel resulted in a spectrum of recrystallization stages that ranged from unrecrystallized to completely recrystallized. In the present case, AMZIRC is a simple binary alloy containing 0.15% Zr whereas AMAX-MZC is a quaternary alloy containing 0.65% Cr, 0.15% Zr and 0.04% Mg.

Examination of the damage microstructure of the two alloys following irradiation at different temperatures indicated that recrystallization is initiated in both AMZIRC and AMAX-MZC at temperatures of ~ 300°C, i.e. subgrain nucleation occurs. However, the coalescence and growth of these subgrains during irradiation is suppressed in AMAX-MZC relative to AMZIRC (Fig. 2). This results in a sluggish recrystallization response of AMAX-MZC that is maintained up to irradiation temperatures of 500°C. Chromium and magnesium are both oversized solutes in copper[16] and are expected to migrate away from vacancy sinks such as grain boundaries during irradiation (vacancy inverse Kirkendall effect). It has also been observed that solutes which are repelled from grain boundaries act to strongly retard grain growth.[13,17] Therefore, it appears that irradiation enhances the initiation of recrystallization in AMAX-MZC, but retards subgrain coalescence and subsequent grain growth. Irradiation enhances all phases of recrystallization in AMZIRC.

TEM examination of copper alloy foils that were irradiated at the same temperature but different dose levels indicated that the subgrain size was essentially independent of damage level over the dose range of 1-40 dpa (see Fig. 1). This is in agreement with another study[9] which found that recrystallization effects in cold-worked copper were independent of neutron fluence for damage levels $\gtrsim$ 0.01 dpa.

Neutron irradiation studies of AMZIRC and AMAX-MZC have found that their yield strengths decreased following irradiation to 10-15 dpa at temperatures of 450°C[5] and 385°C.[6] Since these irradiation temperatures are too high for radiation-enhanced diffusion processes to be important (Fig. 3), the observed softening is probably due to thermal annealing effects alone.

5.4 Conclusions

The shift in the recrystallization temperature of AMZIRC and AMAX-MZC during irradiation may be explained by considering the effect of radiation-enhanced diffusion. The recrystallization temperature of these alloys under long term neutron irradiation conditions is predicted to be ~ 100-200°C. This may limit their applicability in fusion devices, since their high strength is not retained following recrystallization. The solute and/or precipitates in irradiated AMAX-MZC tend to retard the growth of subgrains and grains, which leads to a higher recrystallization temperature when compared to AMZIRC.

6.0 Acknowledgments

The authors would like to thank D.L. Plumton for performing the computer calculations of the steady state vacancy concentrations during irradiation.

7.0 References

1. S.J. Zinkle, G.L. Kulcinski and R.A. Dodd, "Comparison of Thermal and Irradiated Behavior of High-Strength, High-Conductivity Copper Alloys," 12th Intern. Symp. on Effects of Radiation on Materials, June 1984, Williamsburg, VA, to be publ. in ASTM STP 870, F.A. Garner and J.S. Perrin, Eds.
2. S.J. Zinkle, R.A. Dodd and G.L. Kulcinski, "Ion Irradiation of High-Strength, High-Conductivity Copper Alloys at Fusion-Relevant Conditions," 1st Intern. Conf. on Fusion Reactor Materials, Tokyo, Dec. 1984.
3. J.A. Spitznagel and J.W. Davis, "Response of Selected High Strength, High Conductivity Copper Alloys to Simulated Fusion Irradiation and Temperature Conditions, ADIP Semi-Annual Progress Report, Fall 1984.
4. S.J. Zinkle, D.H. Plantz, A.E. Bair, R.A. Dodd and G.L. Kulcinski, "Correlation of the Yield Strength and Microhardness of High-Strength, High-Conductivity Copper Alloys," 1st Intern. Conf. on Fusion Reactor Materials, Tokyo, Dec. 1984.
5. H.R. Brager, H.L. Heinisch and F.A. Garner, "Effects of Neutron Irradiation at 450°C and 16 dpa on the Properties of Various Commercial Copper Alloys," 1st Intern. Conf. on Fusion Reactor Materials, Tokyo, Dec. 1984.
6. R.J. Livak and F.W. Clinard, Jr., "High-Dose Neutron Radiation Damage Study of Copper Alloys for the CRFPR First Wall," presented at EPRI, Palo Alto, CA, Feb. 1985; also to be presented at the ANS Annual Meeting, Boston, June 9-14, 1985.
7. W. Christ, K. Gschwendtner and F. Haessner, Phys. Stat. Sol. 10, p. 337, 1965.
8. K.R. Williams, S.B. Fisher and I.R. McLauchlin, Rad. Effects 7, p. 203, 1971.
9. V.V. Klyushin et al., Phys. Metals and Metallography 34, No. 5, p. 205, 1972.
10. F. Haessner and H.P. Holzer, Acta Met. 22, p. 695, 1974.
11. G. Das and T.E. Mitchell, Scripta Met. 8, p. 1135, 1974.
12. W.V. Vaidya and K. Ehrlich, J. Nucl. Mater. 113, p. 149, 1983.
13. H. Gleiter and B. Chalmers, High Angle Grain Boundaries, Prog. in Mat. Sci., Vol. 16, B. Chalmers, J.W. Christian and T.B. Massalski, Eds., Pergamon Press, 1972, pp. 127-178.
14. R.V. Hesketh, J. Nucl. Mater. 35, p. 253, 1970.
15. F.R.N. Nabarro, R. Bullough and J.R. Matthews, Acta Met. 30, p. 1761, 1982.
16. H.W. King, J. Mater. Sci. 1, pp. 79-90, 1966.
17. P. Niessen and W.C. Winegard, J. Inst. Met. 92, p. 300, 1963/64.

EXTERNAL DISTRIBUTION

UC-20 (107), 20c (66)

DOE-HQ/Office of Fusion Energy
ER-62
Washington, DC 20545

SE Parket

DOE-HQ/Office of
International Security Affairs
DP-33, Mail Stop 4C-024
Washington, DC 20585

DW Dorn

Argonne National Laboratory (3)
9700 South Cass Avenue
Argonne, IL 60439

LR Greenwood, CMT-205
A. Taylor, MST-212
BA Loomis, MST-212

Battelle
Pacific Northwest Laboratory (2)
P.O. Box 999
Richland, WA 99352

JL Brimhall 306W/210
TD Chikalla PSL/1277

Carnegie-Mellon University
Metallurgical Engineering
3325 Science Hall
Pittsburgh, PA 15213

WM Garrison Jr

Columbia University
School of Engineering & Applied Science
New York, NY 10027

RA Gross

Commission of the European Communities
Rue de la Loi 200
B-1049 Bruxelles, Belgium

J. Darvas

Commission of the European Communities
Joint Research Center
Materials Science Division
I-21020 Ispra, Varese, Italia

P. Schiller

Department of the Navy
Naval Research Laboratory (2)
Washington, DC 20375

JA Sprague, Code 6395
LE Steele, Code 6390

Energieonderzoek Centrum Nederland (2)
Netherlands Energy Research Foundation
Westerduinweg 3, Postbus 1
NL-1755 ZG, Petten (NH), The Netherlands

B. vanderSchaaf
W. vanWitzenburg, Materials Dept

GA Technologies Inc (3)
P.O. Box 85608
San Diego, CA 92138

JR Gilleland
GR Hopkins
T. Lechtenberg

General Dynamics/Convair
P.O. Box 85377
San Diego, CA 92138

H. Gurol, MZ 92-1072

General Electric
Advanced Nuclear Technology Operation (2)
310 DeGuign Drive
Sunnyvale, CA 94088

ANTO Library, M/C F-02
S. Vaidyanathan, M/C 5-53

Hahn-Meitner Institüt für Kernforschung Berlin GmbH
Arbeitsgruppe C2
Glienickerstrasse 100
D-1000 Berlin 39, Federal Republic of Germany

H. Wollenberger

Hokkaido University (2)
Facility of Engineering
Kita-hu, Sapporo, 060 Japan

Michio Kiritani, Precision Engineering
Taro Takeyama, Metals Research Institute

Institüt für Festkörperforschung der
Kernforschungsanlage Jülich GmbH
Postfach 1913
D-5170 Jülich 1, Federal Republic of Germany

P. Jung

Japan Atomic Energy Research Institute (2)
Physical Metallurgy Laboratory
Tokai Research Establishment
Tokai-mura, Naka-gun, Ibaraki-ken, 319-11 Japan

Tadao Iwata, Physics
Kensuke Shiraishi, Fuels Materials Research

Kernforschungszentrum Karlsruhe GmbH
Institüt für Material und Festkörperforschung II
Postfach 3640
D-7500 Karlsruhe 1, Federal Republic of Germany

K. Ehrlich

EXTERNAL DISTRIBUTION (Cont'd)

Kyushu University
Research Institute for Applied Mechanics
6 Kasuga-Koen, Kasuga-shi
Fukuoka, 816 Japan

Kazunori Kitajima

Lawrence Livermore National Laboratory (2)
P.O. Box 808
Livermore, CA 94550

MW Guinan, L-396
DW Heikkinen, L-397

Lawrence Livermore National Laboratory
P.O. Box 5511
Livermore, CA 94550

EC Dalder, L-643

Los Alamos National Laboratory
P.O. Box 1663
Los Alamos, NM 87544

DJ Dudziak, S-41F611

Massachusetts Institute of Technology (2)
77 Massachusetts Avenue
Cambridge, MA 02139

I-Wei Chen, 13-5118
NJ Grant, 8-407

Massachusetts Institute of Technology
Nuclear Reactor Laboratory
138 Albany St
Cambridge, MA 02139

OK Harling, NW12-204

Max-Planck-Institüt für Plasma Physik (2)
The NET Team, IPP/NET
D-8046 Garching bei München,
Federal Republic of Germany

DR Harries
R. Toschi

McDonnell-Douglas Astronautics Co
P.O. Box 516
St. Louis, MO 63166

JW Davis

Nagoya University
Institute of Plasma Physics
Furo-chyo, Chikusa-ku,
Nagoya, 464 Japan

Taijiro Uchida

National Research Institute for Metals
Tsukuba Laboratories
1-2-1 Sengen, Sakura-mura,
Nihari-gun, Ibaraki, 305 Japan

H. Shiraishi

North Carolina State University
Box 7907
Materials Engineering Department
Raleigh, NC 27695-7907

JR Beeler Jr

Oak Ridge National Laboratory (6)
P.O. Box X
Oak Ridge, TN 37831

ML Grossbeck
MCG Hall
LK Mansur
PJ Maziasz
NH Packan
RE Stoller

Oak Ridge National Laboratory (2)
P.O. Box Y
Oak Ridge, TN 37831

LA Berry
FW Wiffen, FEDC Bldg

Osaka University
2-1 Yamada-oka, Suita,
Osaka, 565 Japan

Kenji Sumita, Nuclear Engineering

Osaka University
8-1 Mihogaoka
Ibaraki, Osaka, 567 Japan

Toichi Okada, Institute of
Scientific & Industrial Research

Pacific Sierra Research Corp
1104B Camino Del Mar
Del Mar, CA 92014

RD Stevenson

Princeton University (2)
Plasma Physics Laboratory
Forrestal Campus
P.O. Box 451
Princeton, NJ 08544

JPF Conrads
Long-poe Ku

Risφ National Laboratory
Postfach 49
DK-4000 Roskilde, Denmark

BN Singh

EXTERNAL DISTRIBUTION (Cont'd)

Rockwell International Corp
Rocketdyne Division
6633 Canoga Avenue
Canoga Park, CA 91304

DW Kneff, NA02

Sandia National Laboratories
Livermore, CA 94550

WG Wolfer

Science University of Tokyo
Faculty of Engineering
Kagurazaka, Shinjuku-ku,
Tokyo, 162 Japan

RR Hasiguti

Studiecentrum voor Kernenergie
Centre d'Etude de l'Energie Nucleaire
Boeretang 200
B-2400 Mol, Belgium

J. Nihoul

Swiss Federal Institute
for Reactor Research (2)
CH-5303 Würenlingen, Switzerland

WV Green
M. Victoria

Tohoku University (2)
Research Institute for Iron,
Steel and Other Metals
2-1-1 Katahira, Sendai, 980 Japan

Katunori Abe
Hideki Matsui

Tokyo Institute of Technology
Research Laboratory for Nuclear Reactors
12-1, 2-chome, O-Okayama
Meguro-ku, Tokyo, 152 Japan

Kazutaka Kawamura

United Kingdom Atomic Energy Authority
Atomic Energy Research Establishment (2)
Oxfordshire OX11 ORA, UK

R. Bullough, Theoretical Physics

United Kingdom Atomic Energy Authority
Culham Laboratory
Applied Physics & Technology Division
Abingdon, Oxfordshire OX14 3OB, UK

GJ Butterworth

University of California (2)
School of Engineering and Applied Science
Boelter Hall
Los Angeles, CA 90024

RW Conn, KL-98
NM Ghoniem, KH-01

University of Michigan
Nuclear Engineering
Ann Arbor, MI 48109

T. Kammash

University of Missouri
Dept of Nuclear Engineering
Rolla, MO 65401

A. Kumar

University of Tokyo (3)
3-1, Hongo 7-chome,
Bunkyo-ku, Tokyo, 113 Japan

Naohira Igata, Met & Materials Science
Shiori Ishino, Nuclear Engineering
Shuichi Iwata, Nuclear Engineering

University of Virginia
Dept of Materials Science
Thornton Hall
Charlottesville, VA 22901

WA Jesser

Westinghouse
Advanced Energy Systems Division
Fuels Materials Technology
P.O. Box 10864
Pittsburgh, PA 15236

A. Boltax, Manager

Westinghouse
Research and Development Center
1310 Beulah Road
Pittsburgh, PA 15235

JA Spitznagel

INTERNAL DISTRIBUTION

DOE-RL/AME
Breeder Technology Division
Technology Development & Engineering Branches
FED/210

KR Absher, Chief

HEDL (28)

HR Brager	W/A-58	C. Martinez	W/A-58
LL Carter	W/B-47	WN McElroy	W/C-39
DG Doran (5)	W/A-57	EK Opperman	W/A-58
MJ Korenko	W/C-27	RW Powell	W/A-58
FA Garner	W/A-58	RJ Puigh	W/A-58
DS Gelles	W/A-58	FA Schmittroth	W/A-58
R. Gold	W/C-39	WF Sheely	W/C-20
HL Heinisch	W/A-58	RL Simons	W/A-65
DL Johnson	W/B-41	JL Straalsund	W/A-61
GD Johnson	W/A-65	HH Yoshikawa	W/C-44
NE Kenny	W/C-115	Central Files	W/C-110
FM Mann	W/A-58	Documentation Services	W/C-123

*GPO 593-083 (1985)